



University
of Glasgow

Clark, Louise (2022) *Hadron spectroscopy of pseudoscalar and vector meson photoproduction using linearly polarised photons at CLAS*. PhD thesis.

<https://theses.gla.ac.uk/83236/>

Copyright and moral rights for this work are retained by the author

A copy can be downloaded for personal non-commercial research or study,
without prior permission or charge

This work cannot be reproduced or quoted extensively from without first
obtaining permission from the author

The content must not be changed in any way or sold commercially in any
format or medium without the formal permission of the author

When referring to this work, full bibliographic details including the author,
title, awarding institution and date of the thesis must be given

Enlighten: Theses

<https://theses.gla.ac.uk/>
research-enlighten@glasgow.ac.uk

Hadron spectroscopy of pseudoscalar and vector meson photoproduction using linearly polarised photons at CLAS

Louise Clark

Submitted in fulfilment of the requirements for the
Degree of Doctor of Philosophy

School of Physics and Astronomy
College of Science and Engineering
University of Glasgow



University
of Glasgow

June 2022

Abstract

The field of hadron spectroscopy is informed by experiments which study excited states of the nucleon by detecting the decay products following excitation with a hadronic, leptonic or electromagnetic probe. Experiments using a polarised beam of photons provide an important contribution to the world data. This thesis describes the analysis of data from one such experiment, the CEBAF Large Acceptance Spectrometer at Jefferson Laboratory, Virginia, USA. In the experiment, an incident beam of electrons passes through a diamond radiator producing a linearly polarised photon beam of energy from 1.1 to 2.1 GeV on a liquid hydrogen target.

The analysis method and results for two reaction channels are presented. In the first analysis, the polarisation observables $\{\Sigma, P, T, O_x, O_z\}$ for the reaction $\vec{\gamma} p \rightarrow K_S^0 \Sigma^+$ are extracted simultaneously using likelihood sampling with Markov-Chain Monte-Carlo. The results are presented as angular distributions ($\cos \theta_{K_S^0}$) for bins in photon energy E_γ for a total of 21 bins. The values extracted for T , O_x and O_z are a first measurement of these quantities for this reaction and the beam asymmetry (Σ) measurement supplements the one previous measurement for this quantity and extends the energy range over which it has been extracted. The measurement of the recoil polarisation, P , is consistent with previous measurements.

In a second analysis, the spin density matrix elements (SDMEs) for $\gamma p \rightarrow p \phi$ are extracted using similar analysis techniques. The results are presented as angular distributions ($\cos \theta_\phi$) for bins in photon energy E_γ for a total of 24 bins. This work is the first to extract all nine SDMEs for the full angular range of the ϕ meson production. A comparison is made to the predictions of the Vector Meson Dominance (VMD) model and the results provide evidence for contributing processes other than VMD, particularly at more backward angles of the ϕ meson production. The data also indicate non-helicity conserving process in both the s-channel and the t-channel.

The results from the first analysis have been passed to the Juelich-Bonn theory group and the effect of including the new data within their dynamical coupled channel model is described. Several nucleon resonances are affected and the impact on the pole positions, widths and photon decay amplitudes of the affected resonances is described.

Contents

Abstract	i
Declaration	xiv
1 Introduction	1
1.1 Hadron Physics	1
1.2 QCD in the Low-energy Regime	3
1.3 Hadron Spectroscopy	5
1.3.1 Pseudoscalar Meson Photoproduction and Polarisation Observables	9
1.3.2 Vector Meson Photoproduction and Spin Density Matrix Elements	10
1.4 Theoretical Models	11
1.5 Current Status of Experimental Measurements	13
1.6 Summary	15
2 Thomas Jefferson National Accelerator Facility and CLAS	16
2.1 Continuous Electron Beam Accelerator Facility	16
2.2 Coherent Bremsstrahlung Facility and Photon Tagger	17
2.3 Target for g8 Experiment	20
2.4 Beamline Devices	20
2.5 CEBAF Large Acceptance Spectrometer	20
2.5.1 Start Counter	22
2.5.2 Superconducting Toroidal Magnet	23
2.5.3 Drift Chambers	26
2.5.4 Time-of-flight Scintillators	27
2.5.5 Čerenkov Counters	27
2.5.6 Electromagnetic Calorimeters	28
2.6 Trigger, Data Acquisition and Reconstruction	28
2.7 The CLAS12 upgrade	29
2.7.1 Overview	29
2.7.2 Time-of-flight Detectors	30

3	Analysis methods	32
3.1	Overview	32
3.1.1	The sPlots technique	33
3.1.2	Likelihood sampling with Markov Chain Monte Carlo	36
3.2	Summary	39
4	Extracting Polarisation Observables for $\vec{\gamma} p \rightarrow K_S^0 \Sigma^+$	40
4.1	Formalism	41
4.2	Event Selection	43
4.2.1	Initial Event Filter	43
4.2.2	Coherent Peak Selection	44
4.2.3	Particle Identification	45
4.2.4	Channel ID	54
4.2.5	Summary	56
4.3	Signal/Background Separation with sPlots	57
4.3.1	Binning	57
4.3.2	Signal and Background Shapes	58
4.3.3	Extraction of Weights	59
4.3.4	Weighted Mass Distributions	64
4.3.5	Summary	66
4.4	Simulation	67
4.4.1	Event Generation	67
4.4.2	g8 Simulation and Reconstruction	68
4.5	Extracting Observables	69
4.5.1	Data Model	69
4.5.2	Likelihood Sampling Using MCMC - Method	69
4.5.3	Results	76
4.5.4	Summary	81
4.6	Systematic and Validation Studies	82
4.6.1	Systematic Uncertainty Due to K^0 Fit Width	82
4.6.2	Systematic Uncertainty Due to Polarisation Degree	87
4.6.3	1-D Extraction of Σ	87
4.6.4	Toy Data Study	92
4.6.5	Conclusions from Systematic and Validation Studies	95
5	Extracting Spin Density Matrix Elements for $\vec{\gamma} p \rightarrow p \phi$	97
5.1	Formalism	98
5.2	Event Selection	99
5.2.1	Photon Energy Bins (Coherent Peak Settings)	100

5.2.2	Hit Multiplicity and TOF Mass Cuts	100
5.2.3	Z-Vertex Cut	102
5.2.4	Photon Selection	103
5.2.5	Energy Loss Corrections	103
5.2.6	Channel ID	105
5.2.7	Summary	107
5.3	Signal/Background Separation with sPlots	108
5.3.1	Binning	108
5.3.2	Extraction of Weights	108
5.3.3	Weighted Mass Distributions	112
5.4	Simulation	112
5.5	Extracting Spin Density Matrix Elements	113
5.5.1	MCMC Time Series and Posterior Distributions	113
5.5.2	Results	123
5.6	Systematic and Validation Studies	128
6	Comparison to Previous Measurements	130
6.1	Polarisation Observables for $\vec{\gamma} p \rightarrow K_S^0 \Sigma^+$	130
6.1.1	Recoil Polarisation	131
6.1.2	Beam Asymmetry	134
6.2	Spin Density Matrix Elements for $\vec{\gamma} p \rightarrow p \phi$	135
6.3	Summary	142
7	Impact on Models and Conclusion	143
7.1	Polarisation Observables for $\vec{\gamma} p \rightarrow K_S^0 \Sigma^+$	143
7.2	Spin Density Matrix Elements for $\vec{\gamma} p \rightarrow p \phi$	145
7.3	Next Steps	146
7.4	Conclusion	148
A	Time-of-flight calibration	149
A.1	Overview	149
A.2	Paddle status	152
A.3	Gain balancing	152
A.4	Left-right timing alignment	153
A.5	Attenuation length	154
A.6	Effective velocity	154
A.7	Time walk correction	155
A.8	RF offset	157
A.9	Paddle to paddle corrections	157

A.10 Calibration Graphical User Interface	158
A.11 Calibration results	158
B Run Numbers	160
C Tabulated Results for $K_0\Sigma^+$ Polarisation Observables	162
D Tabulated Results for ϕ-meson Spin Density Matrix Elements	166
D.1 Tabulated Results for ϕ -meson Spin Density Matrix Elements in the Helicity system	166
D.2 Tabulated Results for ϕ -meson Spin Density Matrix Elements in the Gottfried-Jackson system	171
D.3 Tabulated Results for ϕ -meson Spin Density Matrix Elements in the Adair system	176

List of Tables

1.1	Comparison of hadron and quark masses.	1
1.2	Properties of the particles involved in the reactions studied in this work as listed in the Particle Data Group.	9
3.1	Comparison of analysis steps for the Σ^+ and ϕ analyses.	34
4.1	The definition of the nominal coherent peak settings.	45
4.2	Analysis cuts applied and resulting number of events for all coherent peak settings.	56
4.3	Reaction vertices for event generation.	67
5.1	ϕ -meson decay modes from Particle Data Group.	98
5.2	z -axis orientations.	99
5.3	Analysis cuts applied and resulting number of events for all coherent peak settings.	107
6.1	Comparison of this work to previous measurements	131
7.1	Reduced χ^2 values before and after the inclusion of the new data.	144
7.2	Pole positions of resonances affected by the new data, before and after fitting. .	145
7.3	Pole positions of resonances affected by the new data, before and after fitting. .	145
B.1	Run numbers used for the $E_\gamma = 1.3, 1.5,$ and 1.7 GeV coherent peak settings. .	160
B.2	Run numbers used for the 1.9 and 2.1 GeV coherent peak settings, as well as the amorphous radiator runs. The "/" separators in the amorphous runs divide the runs into groups which were performed during the run period for each coherent peak setting.	161
C.1	Values characterising the probability density function for the each observable and bin for the $K_0\Sigma^+$ polarisation observables.	165
D.1	Values characterising the probability density function for each observable and bin for the ϕ -meson spin density matrix elements in the Helicity system.	171
D.2	Values characterising the probability density function for each observable and bin for the ϕ -meson spin density matrix elements in the Gottfried-Jackson system.	176

D.3 Values characterising the probability density function for each observable and bin for the ϕ -meson spin density matrix elements in the Adair system. 181

List of Figures

1.1	The dressed quark mass function and its dependence on momentum.	2
1.2	The baryon octet (spin 1/2) and decuplet (spin = 3/2).	3
1.3	Pseudoscalar (spin 0) and vector (spin 1) meson nonets.	3
1.4	QCD running coupling constant, α_s , and its dependence on momentum transfer, Q	5
1.5	Cross-section obtained from photoproduction on the proton.	6
1.6	Production mechanisms for photoproduction from the proton.	7
1.7	The predicted N^* resonances, their overall status, and status by channel.	8
1.8	The polarisation observables categorised by their accessibility via polarised photon beam, polarised target or measuring the recoil polarisation.	10
1.9	ϕ -meson photoproduction methods. a) The general case. b) In the vector meson dominance model. c,d) Direct knockout mechanism.	12
1.10	ϕ -meson decays showing the dominant kaon decay mode and OZI suppressed pion decay mode (right).	13
1.11	The number of measurements by year showing the split between cross-section measurements (light blue) and polarisation observable measurements (dark blue) for pion scattering (left) and single meson photoproduction (right).	14
1.12	The increase in the number of measurements since 2000 of the unpolarised cross-section (left) and polarisation observables (right)	15
2.1	Schematic diagram of the Continuous Electron Beam Accelerator Facility . . .	17
2.2	Example of coherent bremsstrahlung spectrum from g8b run period at CLAS . .	18
2.3	The layout of the coherent bremsstrahlung facility and photon tagger within Hall B.	19
2.4	Geometry of the photon tagging system in Hall B.	19
2.5	Schematic diagram of CLAS.	21
2.6	Cross-section of CLAS showing the layout of the detector components.	22
2.7	Diagram of the start counter showing the target cell within.	23
2.8	The CLAS torus prior to installation.	24
2.9	(A) Contours of magnetic field strength for a coil of the CLAS torus. (B) Magnetic field vectors for the CLAS torus.	25

2.10	Left: the position of Region 2 of the Drift Chamber between the torus coils. Right: Representation of the two superlayers of Region 3 of the Drift Chamber.	26
2.11	Time-of-flight scintillator paddles for one sector of CLAS.	27
2.12	Exploded view of a section of the Electromagnetic Calorimeter.	28
2.13	The CLAS12 detector showing the relative positions of the detector components.	30
2.14	The CLAS12 Forward Time-of-Flight detector.	31
2.15	The CLAS12 Central Time-of-Flight detector.	31
3.1	Overview of the analysis method used in both analyses.	33
3.2	Illustration of the calculation of sWeights.	36
3.3	Illustration of Markov Chain Monte Carlo sampling.	38
4.1	Schematic view of the $\gamma p \rightarrow K^0 \Sigma^+$ reaction and subsequent decay.	40
4.2	Kinematics of the $\gamma p \rightarrow K^0 \Sigma^+$ reaction.	41
4.3	β vs momentum for positive particles (top left) and negative particles (top right) and multiplicity (bottom) after event selection based on number of particles and the mass calculated from the time-of-flight system.	46
4.4	z-vertex distributions of the positive particles following initial skim (top) and with the applied cuts (bottom).	48
4.5	Tagger vertex time subtracted from the time-of-flight vertex time before best photon selection.	51
4.6	Total energy loss in target and start counter vs. momentum for the π^- (top), π^+ (middle) and proton (bottom).	53
4.7	Missing mass ($\pi^+ \pi^-$) versus Mass ($\pi^+ \pi^-$) at each stage of the invariant mass cuts. Top: after particle ID only. Bottom: after cut around π^0 mass.	55
4.8	Binning system used throughout this analysis.	58
4.9	π^0 mass fits for E_γ bin 1.23 GeV, $\cos \theta_{K^0}$ bins -0.81, -0.53 and -0.28.	60
4.10	π^0 mass fits for E_γ bin 1.23 GeV, $\cos \theta_{K^0}$ bins -0.03, 0.21 and 0.68.	61
4.11	K^0 mass fits for E_γ bin 1.23 GeV, $\cos \theta_{K^0}$ bins -0.81, -0.53 and -0.28.	62
4.12	K^0 mass fits for E_γ bin 1.23 GeV, $\cos \theta_{K^0}$ bins -0.03, 0.22 and 0.68.	63
4.13	Missing mass ($\pi^+ \pi^-$) for E_γ bin 1.23 GeV.	65
4.14	Mass ($\pi^+ \pi^- \pi^0$) for all events, background weights applied. The ω peak is visible at $783 \text{ MeV}/c^2$.	66
4.15	Distributions in E_γ (top row) and momentum transfer, t , (bottom row) showing from left to right, unweighted simulation, weighted simulation and data.	68
4.16	MCMC time series including the 50 burn-in steps	71
4.17	MCMC time series for a typical $\cos \theta_{K^0}$ bin within E_γ bin 1.23 GeV	72
4.18	Beam asymmetry, Σ , posterior probability density function for all $\cos \theta_{K^0}$ bins within E_γ bin 1.23 GeV	72

4.19 O_x posterior probability density function for all $\cos \theta_{K^0}$ bins within E_γ bin 1.23 GeV	73
4.20 O_z posterior probability density function for all $\cos \theta_{K^0}$ bins within E_γ bin 1.23 GeV	73
4.21 Recoil asymmetry, P , posterior probability density function for all $\cos \theta_{K^0}$ bins within E_γ bin 1.23 GeV	74
4.22 Target asymmetry, T , posterior probability density function for all $\cos \theta_{K^0}$ bins within E_γ bin 1.23 GeV	74
4.23 PDFs and correlations for all $\cos \theta_{K^0}$ bins within E_γ bin 1.23 GeV	75
4.24 Measurements obtained for beam asymmetry, Σ	76
4.25 Measurements obtained for O_x	77
4.26 Measurements obtained for O_z	78
4.27 Measurements obtained for recoil asymmetry, P	79
4.28 Measurements obtained for target asymmetry, T	80
4.29 Example PDF with KDE smoothing.	81
4.30 Correlations between $\cos \theta_x$ and Mass ($\pi^+ \pi^-$) for signal weighted events (left), background weighted events (centre) and all events (right).	83
4.31 Signal weighted $\cos \theta_x$ distributions for fit interval of 80 MeV/ c^2 (left) and 35 MeV/ c^2 (right).	83
4.32 sWeights fits around K^0 using varied interval widths.	84
4.33 Results of K^0 fitting systematic study for beam asymmetry, Σ	85
4.34 Results of K^0 fitting systematic study for O_x	85
4.35 Results of K^0 fitting systematic study for O_z	86
4.36 Results of K^0 fitting systematic study for recoil asymmetry, P	86
4.37 Results of K^0 fitting systematic study for target asymmetry, T	87
4.38 Signal weighted $K_S^0 \phi$ asymmetry for E_γ bin 1.23 GeV	89
4.39 Background weighted $K_S^0 \phi$ asymmetry for E_γ bin 1.23 GeV	90
4.40 Comparison of measured $K_S^0 \phi$ asymmetry	91
4.41 Comparison of results extracted for toy data (light blue circles) and real data (green triangles) for beam asymmetry, Σ	92
4.42 Comparison of results extracted for toy data (light blue circles) and real data (green triangles) for O_x	93
4.43 Comparison of results extracted for toy data (light blue circles) and real data (green triangles) for O_z	93
4.44 Comparison of results extracted for toy data (light blue circles) and real data (green triangles) for recoil asymmetry, P	94
4.45 Comparison of results extracted for toy data (light blue circles) and real data (green triangles) for target asymmetry, T	94

4.46	Distributions of (measured - true value) for each observable for toy data studies.	95
5.1	Schematic view of the $\gamma p \rightarrow p\phi$ reaction and subsequent decay.	98
5.2	Number of events per topology.	101
5.3	β vs momentum for positive particles after event selection based on number of particles and TOF mass.	102
5.4	z-vertex distributions of the positive particles following initial skim (top) and with the applied cuts (bottom).	102
5.5	Tagger vertex time subtracted from the time-of-flight vertex time before best photon selection.	103
5.6	Energy loss vs. momentum for the K^- (top), K^+ (middle) and proton (bottom).	104
5.7	Invariant mass of (K^+K^-) . The ϕ peak is apparent at $1.019 \text{ GeV}/c^2$	105
5.8	Schematic view of the $\gamma p \rightarrow \Lambda K^+$ reaction and subsequent decay.	106
5.9	Invariant mass of $(p K^-)$. The Λ peak is apparent at $1.520 \text{ GeV}/c^2$	106
5.10	Invariant mass of (K^+K^-) versus invariant mass of $(p K^-)$ showing the overlap of Λ production with ϕ production.	107
5.11	Binning system used throughout the ϕ -meson SDME analysis.	108
5.12	ϕ mass fits for E_γ bin 1.80 GeV, $\cos\theta_\phi$ bins -0.64, -0.10 and 0.19.	110
5.13	ϕ mass fits for E_γ bin 1.80 GeV, $\cos\theta_\phi$ bins 0.39, 0.54 and 0.81.	111
5.14	Signal and Background weighted distributions for the invariant mass of pK^-	112
5.15	Distributions in E_γ (top row) and t (bottom row) showing simulation (left) and data (right).	113
5.16	Posterior probability density functions for SDMEs extracted for a typical bin ($E_\gamma = 2.00 \text{ GeV}$, $\cos(\theta_\phi) = 0.26$) in the helicity system	114
5.17	Posterior probability density functions for SDMEs extracted for a typical bin ($E_\gamma = 2.00 \text{ GeV}$, $\cos(\theta_\phi) = 0.26$) in the Gottfried-Jackson system	115
5.18	Posterior probability density functions for SDMEs extracted for a typical bin ($E_\gamma = 2.00 \text{ GeV}$, $\cos(\theta_\phi) = 0.26$) in the Adair system	116
5.19	PDFs and correlations for a typical bin ($E_\gamma = 2.00 \text{ GeV}$, $\cos(\theta_\phi) = 0.26$) in the Helicity system	117
5.20	PDFs and correlations for a typical bin ($E_\gamma = 2.00 \text{ GeV}$, $\cos(\theta_\phi) = 0.26$) in the Gottfried-Jackson system	118
5.21	PDFs and correlations for a typical bin ($E_\gamma = 2.00 \text{ GeV}$, $\cos(\theta_\phi) = 0.26$) in the Adair system	119
5.22	MCMC time series for a typical bin ($E_\gamma = 2.00 \text{ GeV}$, $\cos(\theta_\phi) = 0.26$) in the Helicity system	120
5.23	MCMC time series for a typical bin ($E_\gamma = 2.00 \text{ GeV}$, $\cos(\theta_\phi) = 0.26$) in the Gottfried-Jackson system	121

5.24	MCMC time series for a typical bin ($E_\gamma = 2.00$ GeV, $\cos(\theta_\phi) = 0.26$) in the Adair system	122
5.25	Measurements obtained for SDMEs in the 1.6 GeV energy bin in the Helicity system.	123
5.26	Measurements obtained for SDMEs in the 1.8 GeV energy bin in the Helicity system.	124
5.27	Measurements obtained for SDMEs in the 2.0 GeV energy bin in the Helicity system.	124
5.28	Measurements obtained for SDMEs in the 1.6 GeV energy bin in the Gottfried-Jackson system.	125
5.29	Measurements obtained for SDMEs in the 1.8 GeV energy bin in the Gottfried-Jackson system.	125
5.30	Measurements obtained for SDMEs in the 2.0 GeV energy bin in the Gottfried-Jackson system.	126
5.31	Measurements obtained for SDMEs in the 1.6 GeV energy bin in the Adair system.	126
5.32	Measurements obtained for SDMEs in the 1.8 GeV energy bin in the Adair system.	127
5.33	Measurements obtained for SDMEs in the 2.0 GeV energy bin in the Adair system.	127
6.1	Definition of axes a) this work, and b) from Nepali et al. CLAS measurements.	131
6.2	Recoil polarisation measurements from Nepali et al. (red circles) and this work (green triangles).	132
6.3	Recoil polarisation measurements from the most recent CBELSA/TAPS (black circles), previous CBELSA/TAPS (red crosses), SAPHIR (blue squares) and this work (green triangles).	133
6.4	Recoil polarisation preliminary measurements from FSU (circles) and this work (black triangles).	134
6.5	Beam asymmetry measurements from Ewald et al. (black circles) and this work (green triangles).	135
6.6	Beam asymmetry cross-section modulations from Ewald thesis showing the cross-section angular distribution and the cross-section modulation fits for each bin.	135
6.7	Comparison of the ρ_{00}^0 SDME from this work (black) and from previous CLAS results (red) for Helicity system (top), Gottfried-Jackson system (middle) and Adair system (bottom).	137
6.8	Comparison of the $\text{Re}\rho_{10}^0$ SDME from this work (black) and from previous CLAS results (green) for Helicity system (top), Gottfried-Jackson system (middle) and Adair system (bottom).	138

6.9	Comparison of the ρ_{1-1}^0 SDME from this work (black) and from previous CLAS results (blue) for Helicity system (top), Gottfried-Jackson system (middle) and Adair system (bottom).	139
6.10	Comparison of the unpolarised SDMEs (ρ_{00}^0 , $\text{Re}\rho_{10}^0$, and ρ_{1-1}^0) from this work (black) and from previous CLAS results (red) and LEPS results (blue) for the Gottfried-Jackson system.	140
6.11	Comparison of this work ($E_\gamma = 1.8$ GeV) to LEPS-Spring8 results ($E_\gamma = 1.87$ GeV) for the Helicity system.	141
6.12	Comparison of this work ($E_\gamma = 2.0$ GeV) to LEPS-Spring8 results ($E_\gamma = 2.07$ GeV) for the Helicity system.	142
7.1	Comparison of results against the Juelich-Bonn dynamical coupled channels model.	144
7.2	Mass ($\pi^+ \pi^- \pi^0$) showing peak at the η' mass of $952 \text{ MeV}/c^2$	147
A.1	Calibration procedure for the Forward Time of Flight detector.	150
A.2	Calibration procedure for the Central Time of Flight detector.	151
A.3	Example of gain balancing plots for FTOF calibration showing histograms of ADC geometric mean (left) and ADC log ratio (right).	152
A.4	Time difference distributions for FTOF (left) and CTOF (right) for representative paddles.	153
A.5	Example of distribution used to extract attenuation length for FTOF calibration.	154
A.6	Example of distribution used to extract effective velocity for FTOF calibration.	155
A.7	Example of distribution used to extract time walk correction for FTOF calibration.	156
A.8	Example of distribution used to extract time walk correction position dependence for FTOF calibration.	157
A.9	Example of vertex time difference distribution for FTOF.	157
A.10	β vs momentum distribution for calibrated FTOF.	159
A.11	Timing resolution for CLAS12 time-of-flight detectors. CTOF (left) and an example of one sector in panel 1b for FTOF (right)	159

Declaration

The work in this thesis is based on research carried out at the Nuclear and Hadron Physics Group, School of Physics Astronomy, University of Glasgow, UK. No part of this thesis has been submitted elsewhere for any other degree or qualification and it is all my own work unless referenced to the contrary in the text.

Chapter 1

Introduction

1.1 Hadron Physics

Before expanding on the motivation behind the measurements in this thesis, we might first ask “Why study hadrons?”. Hadron physicists study the properties of baryons (for example, protons and neutrons) widely described as consisting of three quarks (qqq), and mesons (for example, pions) widely described as consisting of a quark and antiquark ($q\bar{q}$), held together by the strong force carrier, the gluon. However, a glance at the quark masses relative to the hadronic masses for the proton and neutron tells us there is much more to the story. In Table 1.1, we can see that the total mass of the “bare” quarks (or “valence” quarks), i.e. the mass which is attributed to the Higgs mechanism, contributes only about one percent of the total mass of the proton or neutron. Instead, we must also consider the contributions of “sea” quarks (quark-antiquark pairs constantly popping in and out of existence), the gluon cloud and the many possible interactions between the valence quarks, sea quarks and gluons within the hadron. The mass of the “constituent” quarks making up each baryon or meson arises from the interaction of the bare quarks with the gluon cloud as part of a process known as “dynamical chiral symmetry breaking”. Figure 1.1 shows theoretical predictions for the momentum dependence of the quark mass. At low momenta, typical of quarks inside a hadron, the quark becomes a so-called “dressed” quark and the mass is more in line with our initial simple picture of the qqq or $q\bar{q}$ make up of the hadron.

Particle	Approximate Mass (MeV/c^2)
proton (quark content uud)	938.3
neutron (quark content udd)	939.6
u quark	2.2
d quark	4.7

Table 1.1: Comparison of hadron and quark masses. Values taken from [1]

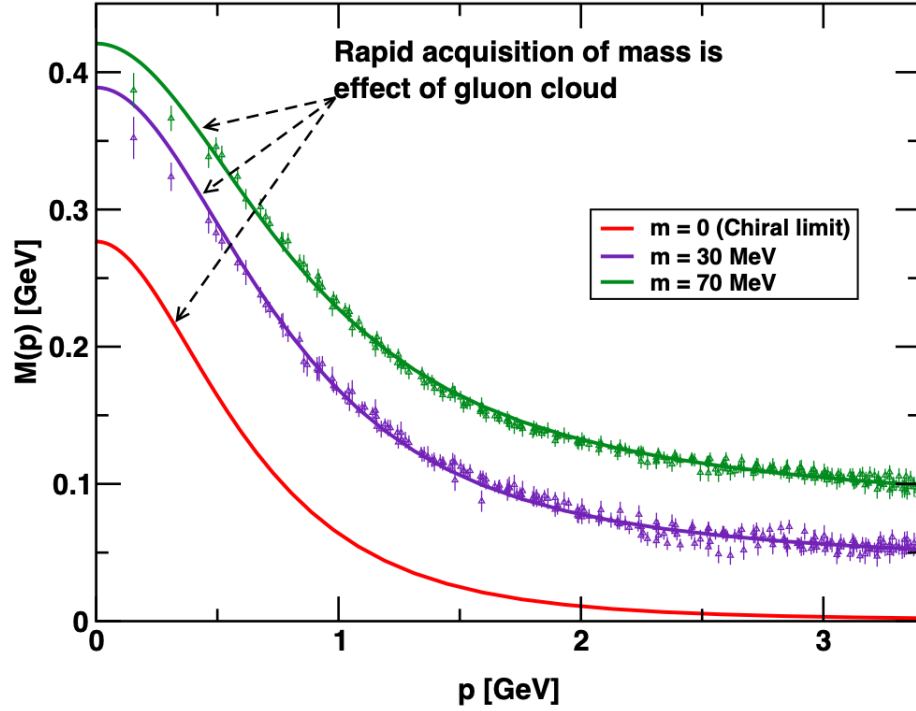


Figure 1.1: The dressed quark mass function, $M(p)$, and its dependence on momentum, p . [2]. The solid curves are theoretical predictions for bare quark masses of 0 MeV, 30 MeV and 70 MeV. The points are results from lattice QCD calculations.

In the type of experiment described in this thesis, the stable hadrons (the protons and neutrons) are “excited” by striking them with high energy particles. In this way, new particles are formed for a brief time before decaying back to their stable forms. The new particles can be organised and labelled by their properties which arise from the flavour of quark they contain. The energies we work at in hadron physics mean that we are in the “light quark” sector, i.e. particles are formed from a combination of up, down and strange quarks and their antiquarks. In Figures 1.2 and 1.3 we can see the variety of particles which are possible. The figures are organised by charge on the horizontal axis and by the property of “strangeness” on the vertical axis. The organisation of particles in this way by Gell-Mann and Ne’eman in fact led to the realisation that the baryons and mesons were made up of smaller building blocks, the constituent quarks.

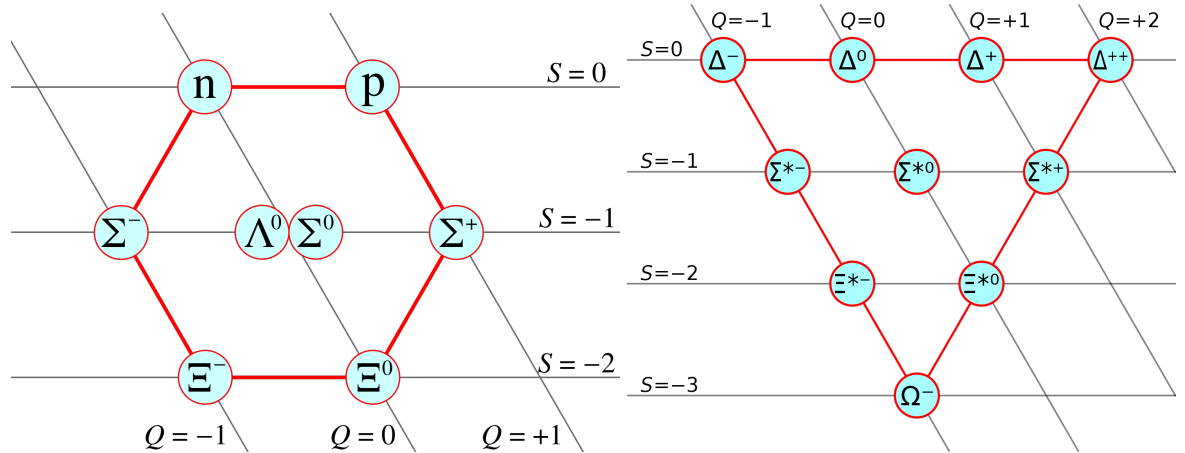


Figure 1.2: The baryon octet (spin 1/2) and decuplet (spin = 3/2). Images from [3].

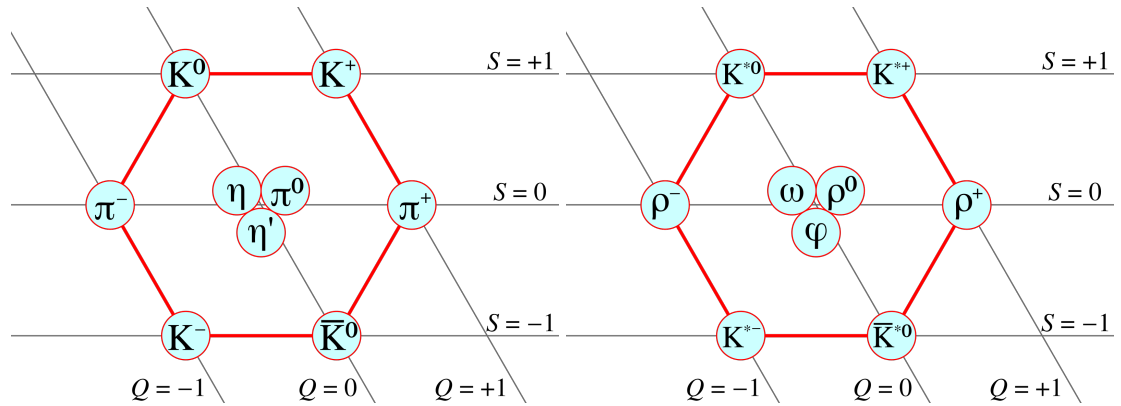


Figure 1.3: Pseudoscalar (spin 0) and vector (spin 1) meson nonets. Images from [3].

1.2 QCD in the Low-energy Regime

We might now wonder if the field theory of the strong force, Quantum Chromodynamics (QCD), may be used to make predictions from first principles for the quarks and gluons within hadrons. Quantum Chromodynamics is governed by the behaviour of the so-called running coupling constant, the non-constant factor which describes the strength of the interaction between the colour-charge carrying particles, the quarks and gluons. Fig. 1.4 shows the variation with momentum of the coupling constant, α_s . At high momentum and energy the coupling strength is relatively weak, whereas as we move to low energy the coupling strength increases and in fact approaches unity. Two of the defining properties of QCD, confinement and asymptotic freedom, can be understood by considering the behaviour of the coupling constant at either end of the momentum scale. At low momentum and energy, corresponding to conditions within a nucleon, the coupling is strong. We may also think of the momentum scale as a distance scale. At low momentum the typical distance between quarks and gluons is relatively large. If this distance scale increases, the force between particles increases further, and we observe the emergent property of

confinement. In fact, as we supply increasing energy to excite a nucleon we instead produce new particles in a process known as “hadronization” rather than increase the quark separation further. Although not forbidden by the theory of QCD, isolated quarks are not observed. At the other end of the scale, at high momentum and energy, the coupling is weaker. At this scale, quarks and gluons are asymptotically free. At such high energies, the typical separation is relatively small and interaction between particles is minimal.

Entwined with these concepts is the gluonic self-interaction. In QCD, the force carrying particles, the gluons, are colour-charge carrying themselves meaning gluon-gluon interactions are possible, contrasting with the charge free photon in Quantum Electrodynamics (QED). The incredibly accurate predictions of QED arise from the (Dyson expansion) method where each possible interaction, represented by a Feynman diagram, is considered. Theoretically, to obtain a completely accurate prediction an infinite number of possible diagrams should be included. However, as the possible interactions become more complex (i.e. more vertices are involved), the relative contribution is dependent on the coupling strength. So, for QED where the coupling strength is $1/137$, very accurate predictions can be made by considering the first few simplest possibilities for the interaction. In a similar vein, for strong interactions at higher energies, the coupling strength is well below 1 and predictions can become very accurate. The inclusion of higher order terms can be increased until the desired accuracy is achieved. Higher order terms are insignificant in comparison and can be ignored. The same does not apply to the situation at hadronic energies (i.e. of the order of 1 GeV). With the coupling constant close to unity each possible interaction makes a similar contribution to the overall and we cannot simplify the picture in this way. As a result, theoretical understanding of hadrons is very difficult. Theoretical methods such as lattice QCD require huge computation resources and time and only partially achieve a description of the reality. We therefore rely on phenomenological models informed by measurable quantities from fields such as hadron spectroscopy.

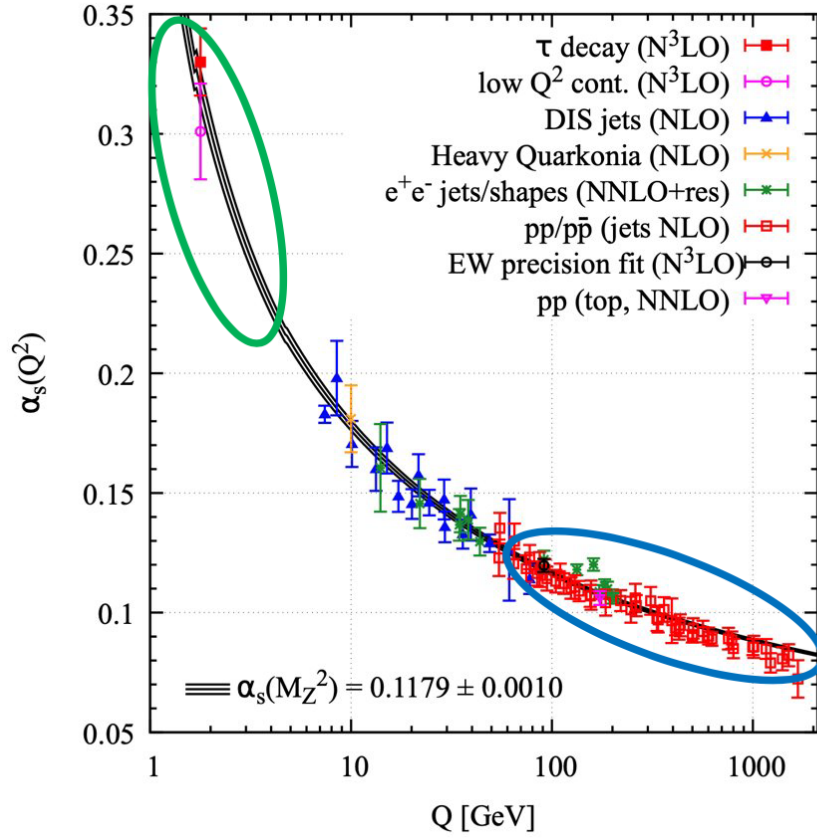


Figure 1.4: QCD running coupling constant, α_s , and its dependence on momentum transfer, Q . The areas highlighted represent the kinematic regions where we observe confinement (green), and asymptotic freedom (blue). Adapted from [1]

1.3 Hadron Spectroscopy

One method of obtaining information about the behaviour of the quarks and gluons within nucleons is through hadron spectroscopy. In a similar way to how the study of atomic spectra led to conclusions about the nature of the atom, we look at the spectra of hadrons to infer the dynamics of the quarks and gluons inside. We wish to know what are the relevant degrees of freedom? Are the degrees of freedom arising from three valence quarks (known as the Constituent Quark Model) sufficient to describe what we observe? Figure 1.5 shows the cross-section obtained from many experiments involving photoproduction on a proton target (similar experiments to the one analysed in this thesis). From this figure, one of the issues facing the field is clearly evident, that is, how do we identify features in the spectrum? The peaks are wide and overlapping, particularly the total cross-section shown in black, and cannot be identified from cross-sections alone. The situation improves slightly when we separate the contributions from different channels (in colour), but the problem remains. Figure 1.5 is typical of equivalent plots for other types of experiment, for example using pion or electron beams.

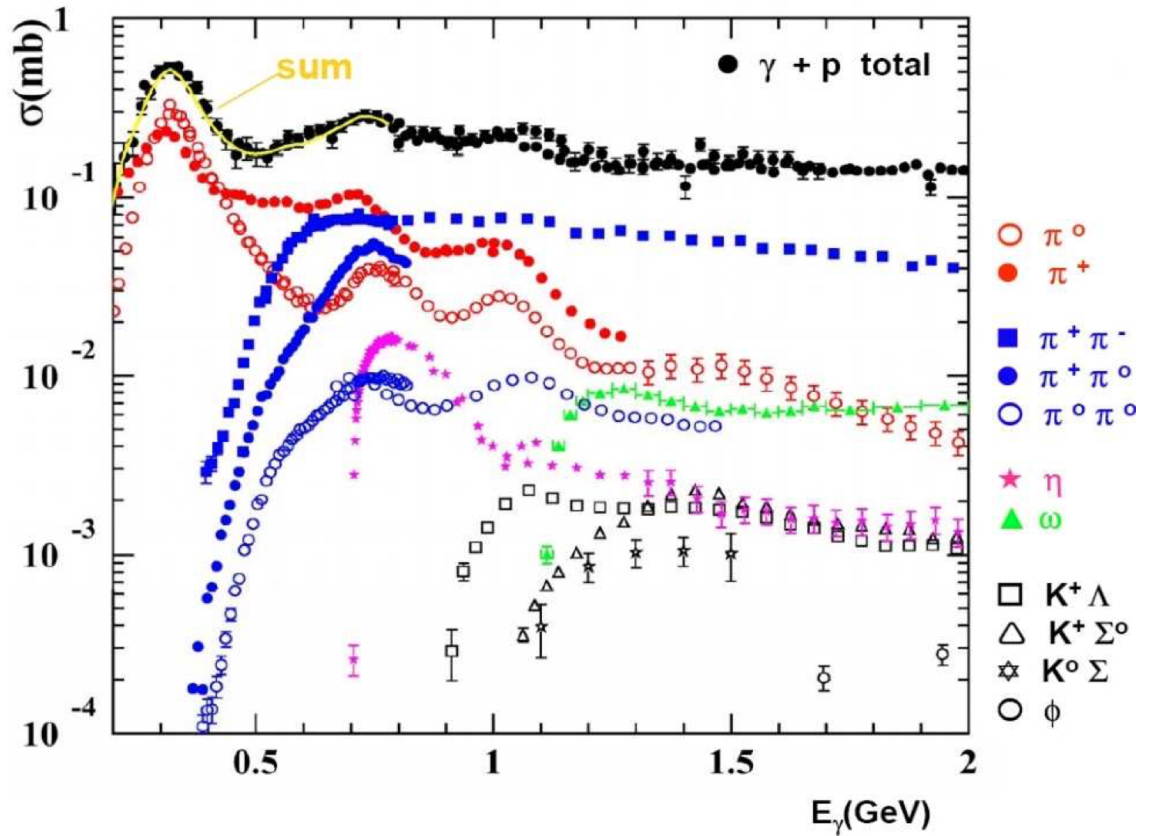


Figure 1.5: Cross-section obtained from photoproduction on the proton. The total cross-section is shown in black, and contributions from different channels in colour. [1]

The contributions to the cross section are the combination of different production mechanisms. The type of reaction can be broadly classified into s -channel, t -channel, and u -channel, for the Mandelstam variables s , t , and u . In an s -channel process, (Figure 1.6 (left)), the process is sensitive to \sqrt{s} , the total centre-of-mass energy. The nucleon reaches an intermediate excited state known as a resonance before decaying. In a t -channel process, (Figure 1.6 (right)), the process is sensitive to t , the four-momentum transfer squared. The reaction proceeds via a particle exchange. The u -channel differs from the t -channel in that the final state particles are interchanged. As such, s -channel processes contribute to the resonant contributions which we wish to understand. It is also important to understand the non-resonant processes as these will contribute to the background in any cross-section measurement. Each feature in the spectrum of the excited nucleon corresponds to a “resonance” (typically a short-lived intermediate hadronic state). We can look at the predictions for resonant states which arise from the constituent quark model and compare these to the evidence observed to confirm their existence. A substantial body of work has been done across decades to calculate these predictions, initially by Koniuk and Isgur in 1980 [4] and more recently in work by Capstick and Roberts [5, 6, 7]. What we find is that many of the states predicted are not observed - the so-called “missing resonances” problem. The situation is characterised in Figure 1.7 which shows the “ N^* ” resonances ($I = 1/2$)

and the corresponding evidence rating as assigned by the Particle Data Group. We can see that evidence is poor for many of the states and the standard of the evidence varies depending on the decay channel (the particles produced by the reaction). The fundamental question is: why do we not observe these states? Is it because they are difficult to observe due to the broad and overlapping nature of the spectrum? Or have we not yet done the right experiments to see them? Resonances which are not apparent when using a pion beam may be seen with a photon beam for example. Or do they simply not exist and we must revise the theory? These questions have led to a worldwide program of work to make measurements of the properties of these resonant states in each of the decay channels.

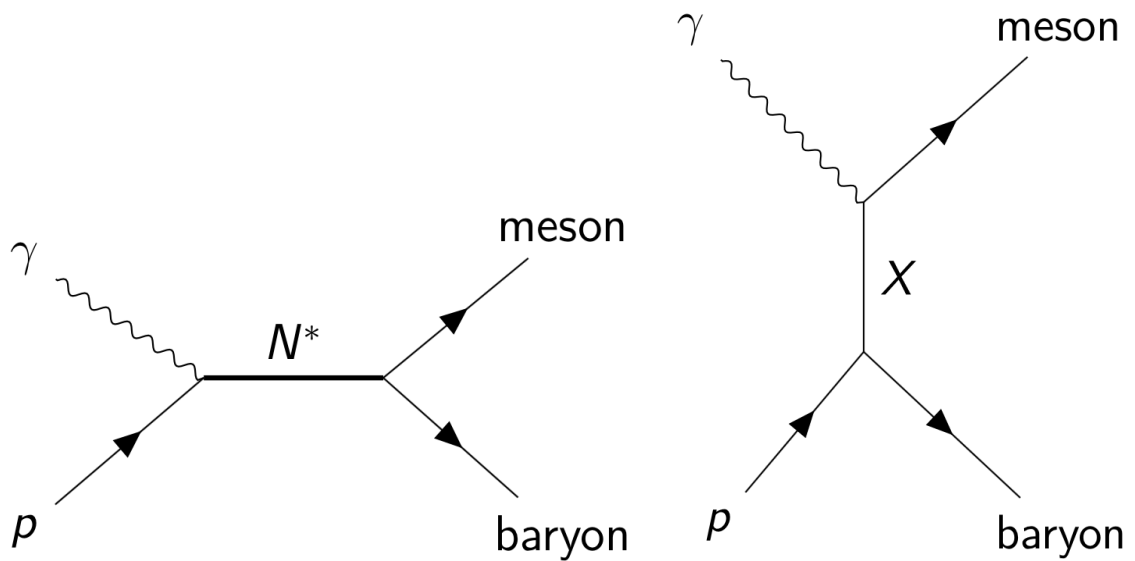


Figure 1.6: Production mechanisms for photoproduction from the proton. The resonant contributions are from the s-channel process (left) and background contributions are from the t-channel process (right).

Particle	J^P	overall	Status as seen in																		
			$N\gamma$	$N\pi$	$\Delta\pi$	$N\sigma$	$N\eta$	ΛK	ΣK	$N\rho$	$N\omega$	$N\eta'$									
N	$1/2^+$	****																			
$N(1440)$	$1/2^+$	****	****	****	****	***															
$N(1520)$	$3/2^-$	****	****	****	****	**	****														
$N(1535)$	$1/2^-$	****	****	****	***	*	****														
$N(1650)$	$1/2^-$	****	****	****	***	*	****	*													
$N(1675)$	$5/2^-$	****	****	****	****	***	*	*	*												
$N(1680)$	$5/2^+$	****	****	****	****	***	*	*	*												
$N(1700)$	$3/2^-$	***	**	***	***	*	*						*								
$N(1710)$	$1/2^+$	****	****	****	*		***	**	*	*	*	*	*								*
$N(1720)$	$3/2^+$	****	****	****	***	*	*	*	****	*	*	*	*								*
$N(1860)$	$5/2^+$	**	*	**		*	*														
$N(1875)$	$3/2^-$	***	**	**	*	**	*	*	*	*	*	*	*								*
$N(1880)$	$1/2^+$	***	**	*	**	*	*	*	**	**										**	**
$N(1895)$	$1/2^-$	****	****	*	*	*	****	**	**	*	*	*	*								****
$N(1900)$	$3/2^+$	****	****	**	**	*	*	*	**	**										*	**
$N(1990)$	$7/2^+$	**	**	**			*	*	*												
$N(2000)$	$5/2^+$	**	**	*	**	*	*													*	
$N(2040)$	$3/2^+$	*		*																	
$N(2060)$	$5/2^-$	***	***	**	*	*	*	*	*	*	*	*	*								*
$N(2100)$	$1/2^+$	***	**	***	**	**	*	*	*	*	*	*	*							*	**
$N(2120)$	$3/2^-$	***	***	**	**	**	**		**	*	*	*	*						*	*	*
$N(2190)$	$7/2^-$	****	****	****	****	**	*	**	*	*	*	*	*							*	*
$N(2220)$	$9/2^+$	****	**	****			*	*	*												
$N(2250)$	$9/2^-$	****	**	****			*	*	*												
$N(2300)$	$1/2^+$	**		**																	
$N(2570)$	$5/2^-$	**		**																	
$N(2600)$	$11/2^-$	***		***																	
$N(2700)$	$13/2^+$	**		**																	

**** Existence is certain.
*** Existence is very likely.
** Evidence of existence is fair.
* Evidence of existence is poor.

Figure 1.7: The predicted N^* resonances, their overall status, and status by channel. [1]. Note the scarcity of measurements for the ΣK channel which this work will supplement. The other channel studied in this work, $N\phi$, has so few measurements that is not featured in this table.

In this work, two reaction channels are studied. Both are reactions produced by a photon beam which can complement the world dataset which is currently predominantly from pion-induced reactions. The reaction channels studied are $\gamma p \rightarrow K_S^0 \Sigma^+$ and $\gamma p \rightarrow p \phi$. The properties of the particles involved are shown in Table 1.2. From another look at Figure 1.7 we can see that evidence for resonances from studies of the $K_S^0 \Sigma^+$ channel (as shown in the ΣK column) is poor. This is at least in part due to the scarcity of measurements of this channel, and the same can be said for the $p \phi$ channel, which is not featured in the table. The theoretical predictions also suggest that some resonances may couple more strongly to channels where strangeness is produced. Therefore, the study of the channels covered in this work will be a valuable addition

to the world dataset. The first reaction channel, $\gamma p \rightarrow K_S^0 \Sigma^+$, is the photoproduction of a pseudoscalar meson and a hyperon, for which we measure what are known as “polarisation observables”. The second reaction channel, $\gamma p \rightarrow p \phi$, is the photoproduction of a vector meson. The spin of the vector meson introduces an additional degree of freedom requiring a different approach to describing the reaction. For this we measure “spin density matrix elements”.

Particle	$I(J^P)$	Mass (MeV/c ²)	Mean lifetime (s)	Charge (e)	Valence quark content
p	$\frac{1}{2}(\frac{1}{2}^+)$	938.27		1	uud
K_S^0	$\frac{1}{2}(0^-)$	497.61	0.896×10^{-10}	0	$d\bar{s}$
Σ^+	$1(\frac{1}{2}^+)$	1189.37	0.802×10^{-10}	1	uus
ϕ	$0(1^-)$	1019.46	1.55×10^{-22}	0	$s\bar{s}$

Table 1.2: Properties of the particles involved in the reactions studied in this work as listed in the Particle Data Group [1].

1.3.1 Pseudoscalar Meson Photoproduction and Polarisation Observables

The photoproduction of pseudoscalar mesons can be described by four complex amplitudes comprising the scattering matrix (S -matrix) for the reaction. By measuring the cross-section of a reaction, the magnitudes of the amplitudes can be determined. However, to determine the phase and provide a description of the interference between overlapping processes, experimentalists aim to somehow access the eight real numbers which define the four complex amplitudes. These cannot be measured directly as there is no unique set of values which describe the reaction. Instead, the angular distribution of decay particles from the reaction can be described by bilinear combinations of the eight real amplitudes known as “polarisation observables”. In order to describe the angular distributions, there must be a reference direction from which to work. This can be introduced to the experiment by polarising the photon beam, either linearly or circularly, or by polarising the target. In some reactions, including the $\gamma p \rightarrow K_S^0 \Sigma^+$ reaction studied in this work, the recoil polarisation, that is, the polarisation of the recoiling baryon, can be determined without any explicit measurement. The baryons, such as Σ and Λ , are said to be “self-analysing” and we can determine the polarisation from the angular distributions of their decay products. A total of 16 polarisation observables can be accessed. These are shown in Figure 1.8. They are categorised by the experimental conditions which are required to access them. The analysis in this work of the $\gamma p \rightarrow K_S^0 \Sigma^+$ reaction uses a linearly polarised photon beam and an unpolarised target. Together with the self-analyzing property of the Σ^+ hyperon, we can therefore access five polarisation observables: Σ , P , T , O_x and O_z .

Photon		Target			Recoil			Target+Recoil			
		-	-	-	x'	y'	z'	x'	x'	z'	z'
		x	y	z	-	-	-	x	z	x	z
unpolarized	σ	-	T	-	-	P	-	$T_{x'}$	$-L_{x'}$	$T_{z'}$	$L_{z'}$
linearly pol.	Σ	H	(-P)	-G	$O_{x'}$	(-T)	$O_{z'}$	-	-	-	-
circularly pol.	-	F	-	-E	$-C_{x'}$	-	$-C_{z'}$	-	-	-	-

Figure 1.8: The polarisation observables categorised by their accessibility via polarised photon beam, polarised target or measuring the recoil polarisation. [8]

1.3.2 Vector Meson Photoproduction and Spin Density Matrix Elements

Contrasting to the study of pseudoscalar meson photoproduction, the production of vector mesons brings in an additional spin component from the spin-1 vector meson. This means that the number of amplitudes describing the reaction is large and, while an experimental analysis is not fundamentally impossible, the number of amplitudes is too large for it to be practical or viable. Instead, the quantum system can be regarded as an ensemble of states described by a density matrix. This can be applied to the spin polarisation states and the resulting complex amplitudes are referred to as “spin density matrix elements” (SDMEs). A full description of the use of this construct in the analysis of vector meson photoproduction is given in Schilling [9], and of the density matrix in more general terms in [10]. In a statistical mixture of n states, the density matrix is given by

$$\rho = \sum_{i,j} a_{ij} |\psi_j\rangle \langle \psi_i| \quad (1.1)$$

The probability that the system occupies a state i is given by the diagonal elements a_{ii} . The spin-state of a vector meson is a 3x3 matrix with complex elements, therefore the spin density matrix is described by 18 real values. The matrix is constrained to be Hermitian, with the result that the diagonal elements are real, and the off-diagonal elements, $i, j, j \neq i$, are the complex conjugate of element j, i . This reduces the independent, real variables to nine. These nine values provide the most complete description of the system available. The matrix elements describe the angular distributions of vector meson decay products and the secondary analysis described in this work (covered in Chapter 5) studies these distributions to extract the spin density matrix elements for the photoproduction of ϕ -mesons using linearly polarised photons.

1.4 Theoretical Models

Baryon spectroscopy models

Of particular relevance to photo- and electro-production experiments on the proton or neutron (of which the experiment analysed in this work is one) are the theoretical models of the N^* and Δ resonances. That is, excited states of the nucleon arising from radial excitation in the case of the N^* resonances, and excitation due to a spin flip in the case of the Δ resonances. For photoproduction reactions, the end goal is to determine the energy and width of the resonance, and the photon decay amplitudes, $A_{1/2}$ and $A_{3/2}$. The resonance energy corresponds to the pole position of the S -matrix for the reaction and is independent of the production mechanism. The photon decay amplitudes describe the contributions from electric and magnetic multipoles to the expansion of the amplitudes in the scattering matrix. A worldwide effort is underway to analyse the experimental data using partial wave analysis, where the scattering potential is broken down into contributions from angular momentum terms. Models such as the Mainz unitary isobar model, known as MAID, analyse pion photo- and electro-production[11] and kaon photo- and electro-production[12], adding each resonance as a sum of Breit-Wigner amplitudes. Other models, such as the Bonn-Gatchina multichannel partial wave analysis[13] use a multi-channel approach. Of particular interest to this work, the Juelich-Bonn dynamical coupled channel model performs a simultaneous analysis of pion and photon induced reactions taking into account intermediate states and background. The most recent published iteration of the model extends the model to include $K^+\Lambda$ photoproduction[14]. The conclusion of this thesis describes the effect of the measurements extracted by the primary analysis in this work on the Juelich-Bonn model. A comprehensive review of the models in current use for the field of light baryon spectroscopy is given in [15].

Phenomenological Models for vector meson photoproduction

A prevalent theory in vector meson photoproduction is the vector meson dominance model (VMD), a theory developed by Sakurai [16] in the 1960's pre-dating QCD. The incoming photon, having the same quantum numbers as a vector meson ($J^{PC} = 1^{--}$), can fluctuate into a vector meson and scatter off the proton in a diffractive manner by exchange of a Pomeron [17] as illustrated in Fig. 1.9. Perhaps an esoteric concept, the Pomeron is a type of Regge trajectory, a family of particles with increasing mass and spin. In models such as VMD the entire family of particles mediates the reaction.

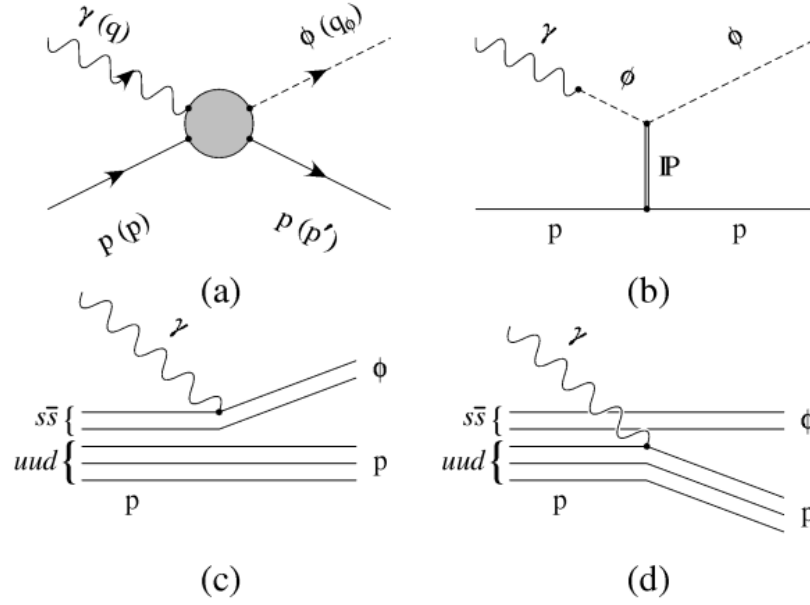


Figure 1.9: ϕ -meson photoproduction methods. a) The general case. b) In the vector meson dominance model. c,d) Direct knockout mechanism. [18]

VMD and other models based on diffractive Pomeron exchange are successful at higher energies and low momentum transfer. However, in this study the centre-of-mass energy is very near threshold where other production mechanisms may take part. Several authors, for example [18, 19], suggest that a direct knockout of the inherent $s\bar{s}$ content of the proton is involved, as shown in Figure 1.9 c) and d). A similar contribution may come from pseudo-scalar meson exchange[20, 21, 22] rather than the Pomeron exchange of VMD. Indeed, these suggestions motivated the original CLAS experiment proposal to extract the SDMEs[23]. The ϕ -meson, with its quark content $s\bar{s}$, means that OZI suppression plays a part. Since we have strangeness production from the proton which, in the familiar constituent quark model, is composed only of up and down quarks, the process is OZI suppressed. The OZI rule is named for the three scientists who independently proposed the rule, Okubo, Zweig, and Iizuka, and states that processes where particles in the final state may only be reached by disconnected quark lines are suppressed. This is equivalent to the Feynman diagram for the process having its final state reached by gluon lines only, i.e. the diagram can be cut in two passing through gluon lines only. Qualitatively, this can be understood in terms of asymptotic freedom: the gluons require to be high energy in order to form hadrons. High energy corresponds to short range, and therefore gluon coupling is weak and the process is suppressed [24]. OZI suppression affects the ϕ -meson decay as well as its production. Illustrated in Fig. 1.10, the dominant decay is to strange kaons and the pion decay mode is suppressed.

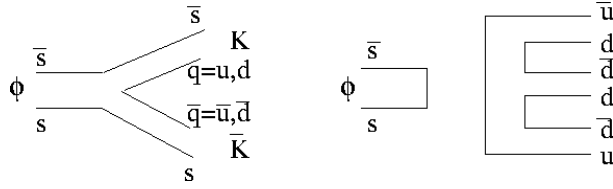


Figure 1.10: ϕ -meson decays showing the dominant kaon decay mode and OZI suppressed pion decay mode (right). From [25]

The theory of vector meson dominance [16] makes the following predictions for the values of the SDMEs:

- Only two SDMEs are non-zero: ρ_{1-1}^1 and $\text{Im}\rho_{1-1}^2$
- The two non-zero SDMEs are related: $\rho_{1-1}^1 = -\text{Im}\rho_{1-1}^2$
- For natural parity exchange via Pomeron (positive parity) exchange, $\rho_{1-1}^1 = -\text{Im}\rho_{1-1}^2 = +0.5$
- For unnatural parity exchange via pseudoscalar meson (negative parity) exchange, $\rho_{1-1}^1 = -\text{Im}\rho_{1-1}^2 = -0.5$

In fact the matrix element ρ_{1-1}^1 represents the asymmetry between contributions from natural and unnatural parity exchange:

$$\rho_{1-1}^1 = \frac{1}{2} \frac{\sigma^N - \sigma^U}{\sigma^N + \sigma^U} \quad (1.2)$$

The SDMEs also provide a useful way of studying helicity conservation. Further, by choice of reference system, we can separately study the helicity conservation during s-channel and t-channel processes. In the so-called “helicity” system, where the z quantization axis is chosen to align with the recoiling baryon in the vector meson rest frame, the SDMEs are sensitive to helicity conservation in the s-channel. To study helicity conservation in the t-channel, we use the “Gottfried-Jackson” system, where the z axis is aligned with the direction of the photon in the vector meson rest frame. Non-zero values for the ρ^0 are indicative of non-conservation of helicity[26]. That is, for helicity conservation $\rho_{00}^0 = \rho_{10}^0 = \rho_{1-1}^0 = 0$. A useful description of the helicity and Gottfried-Jackson frames and their relationship to s-channel and t-channel production is given in Appendix A of [27].

1.5 Current Status of Experimental Measurements

In the twentieth century, as experimentalists began to explore the field of baryon spectroscopy, activity was dominated by pion-nucleon scattering experiments studying the reactions $\pi^\pm p \rightarrow$

$\pi^\pm p$ and $\pi^- p \rightarrow \pi^0 n$. From the mid-nineties to the current day, the focus has turned to photoproduction experiments in order to understand nucleon excited states which may be accessed by an electromagnetic probe. With the development of facilities with a (polarised) photon beam, the number of measurements of cross-sections and polarisation observables from meson photoproduction began to outnumber those from pion scattering. This can be seen in Figure 1.11, where the sharp increase in photoproduction measurements (right) since the late nineties is in contrast to the relative plateauing of pion scattering measurements (left). The sharp rise in photoproduction measurements has been enabled by the development of facilities such as the GRe noble Anneau Accélérateur Laser[28] (GRAAL), the Mainz Microtron (MAMI) accelerator facility[29], the CBELSA/TAPS experiment[30] in Bonn, the CEBAF large acceptance spectrometer[31] (CLAS) in Virginia and the LEPS/Spring8 facility[32] in Japan.

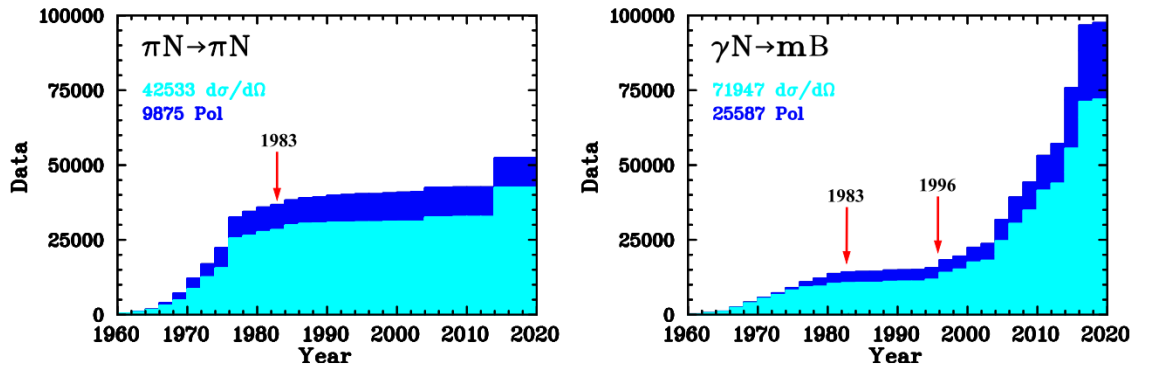


Figure 1.11: The number of measurements by year showing the split between cross-section measurements (light blue) and polarisation observable measurements (dark blue) for pion scattering (left) and single meson photoproduction (right). The figure was produced using data from SAID[33] in the review by Ireland et al.[34].

We can look further into the meson photoproduction measurement numbers by breaking them down by final state as shown in Figure 1.12 taken from the recent review of Light Baryon Spectroscopy by A. Thiel, F. Afzal and Y. Wunderlich[15]. Pion production dominates and there are relatively few measurements of kaon-hyperon final states. Since some nucleon resonances are expected to couple more strongly to final states involving strangeness[6], this is an interesting area of study. The primary analysis in this work concerns the $K^0\Sigma^+$ final state and will supplement the world data for one of the least studied final states. Further details can be found in several topical reviews which have been compiled over the years and thus provide an overview of the field as it has developed [35, 36, 37, 38, 34, 15].

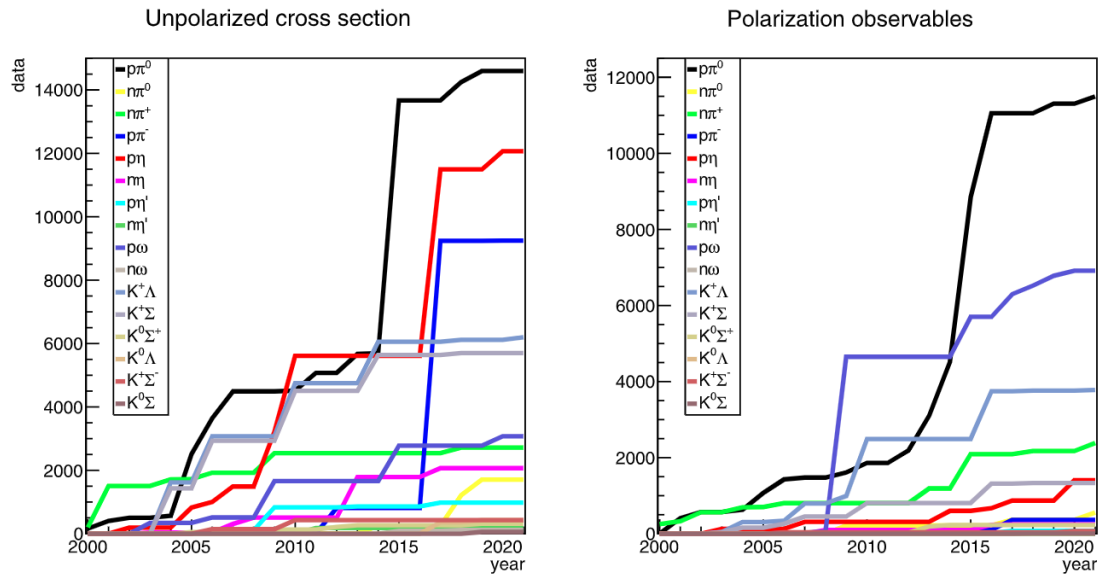


Figure 1.12: The increase in the number of measurements since 2000 of the unpolarised cross-section (left) and polarisation observables (right)[15]

1.6 Summary

The field of hadron spectroscopy has grown in the past few decades and a worldwide effort to measure observable quantities for as wide a range of reactions as possible is ongoing to inform the development of models which explain the interactions of quarks and gluons inside the nucleon. The following chapters describe the experiment at Jefferson Laboratory and two data analyses which extract quantities to add to this worldwide dataset.

Chapter 2

Thomas Jefferson National Accelerator Facility and CLAS

The data analyses described in this work are based on datasets obtained at the Thomas Jefferson National Accelerator Facility in Newport News, Virginia. The facility consists of the Continuous Electron Beam Accelerator Facility (CEBAF) and four experimental halls housing the experimental areas. The CEBAF Large Acceptance Spectrometer (CLAS) [31] was housed in one of these halls (designated “Hall B”). The accelerator was recently upgraded to increase the maximum electron energy from 6 GeV to 12 GeV and the CLAS detector system was upgraded to the CLAS12 detector system [39]. This chapter gives an overview of the facility and a description of the components of CLAS during the 6 GeV era when the data for the analyses within this work were taken. The final sections of this chapter describe the upgrade and give a summary of the work undertaken to develop calibration software for the time-of-flight detectors within CLAS12.

2.1 Continuous Electron Beam Accelerator Facility

The Continuous Electron Beam Accelerator Facility (CEBAF) [40] has the capability to accelerate electrons up to an energy of 6 GeV (12 GeV after the recent upgrade) and deliver a continuous electron beam to four experimental areas simultaneously. Electrons are produced by illuminating a GaAs photocathode with a pulsed laser driven at 499 MHz resulting in delivery of electron bunches (“beam buckets”) to the experimental areas every 2 ns. The acceleration is provided by applying a radio frequency wave in phase with the electron bunches inside superconducting niobium cavities kept in liquid helium in order to maintain their superconductivity. The superconductivity (i.e. zero resistance) of the cavities means that they do not heat up during running allowing the experiment to run at 100% duty cycle. An initial acceleration is applied to the electrons before injecting them into the main racetrack configuration of the accelerator, shown schematically in Figure 2.1. Each LINAC, consisting of 21 cryomodules each contain-

ing 8 cavities, increases the electron energy by approximately 500 MeV. The electrons are bent around the recirculation arcs by a system of magnetic optics and re-enter the LINAC for a maximum of 5.5 passes (therefore maximum energy of 5.5 GeV), before being directed to the CLAS experimental area.

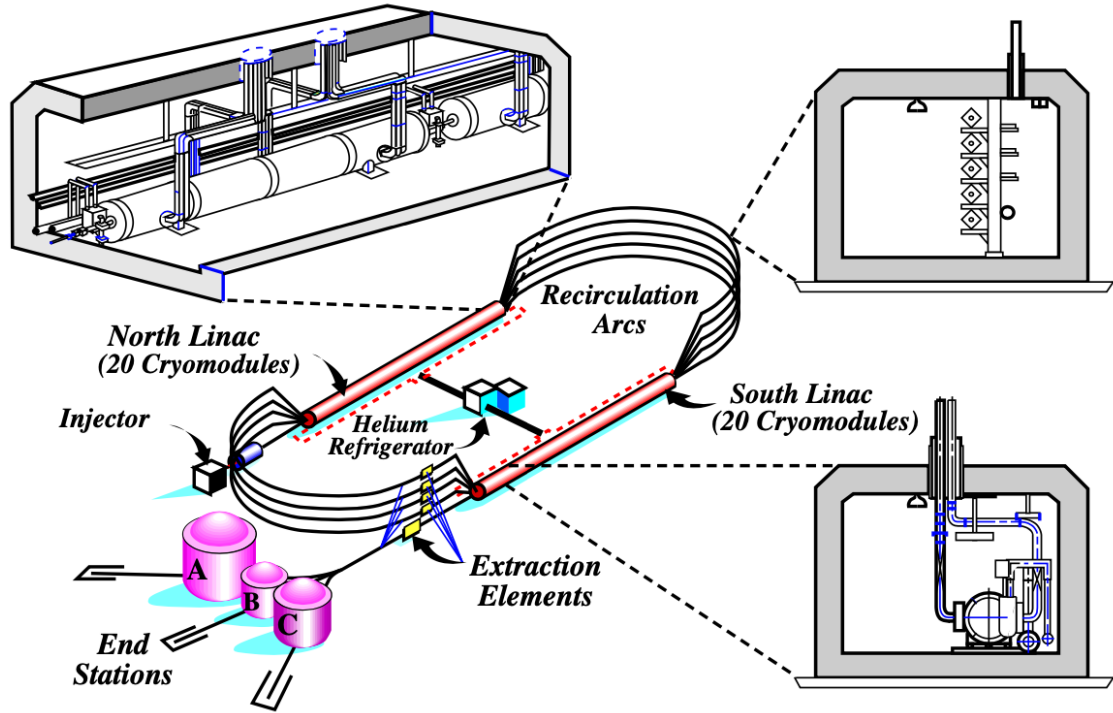


Figure 2.1: Schematic diagram of the Continuous Electron Beam Accelerator Facility[31]

2.2 Coherent Bremsstrahlung Facility and Photon Tagger

The coherent bremsstrahlung facility in Hall B [41] transforms the incoming beam of electrons into a beam of linearly polarised photons through the coherent bremsstrahlung technique [42, 43]. In bremsstrahlung radiation (“braking radiation”), electrons passing through a radiator emit photons as they decelerate within the material. When the radiator has a lattice structure such as the diamond radiator used for this experiment, the photons can interact with the lattice planes in such a way that they are linearly polarised and produced with a characteristic energy distribution. Figure 2.2, top panel, shows an example of a coherent bremsstrahlung distribution. This plot shows what is known as the “enhancement”, which is the photon energy spectrum obtained with the crystal divided by the same spectrum obtained with an amorphous radiator. The top panel shows the data in black and the enhancement distribution as calculated from theory in red. The bottom panel shows the corresponding calculated polarisation. The peak between 1200 MeV and 1400 MeV is termed the “coherent peak” and photons within this energy range will be highly polarised as shown in the bottom panel of this Figure. Precise rotation of the diamond wafer using the goniometer to align selected crystal planes controls the photon energy at the

coherent peak, and is also used to align the polarisation plane either parallel or perpendicular to the laboratory frame of reference. A description of how the linearly polarised photon beam is operated during experiments such as this is given in a CLAS collaboration note [44].

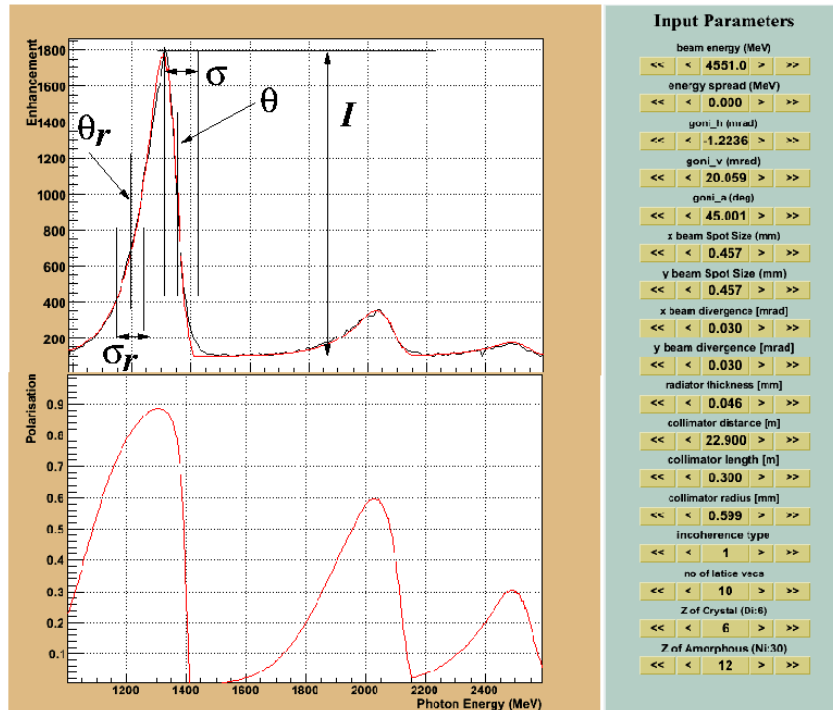


Figure 2.2: Example of coherent bremsstrahlung spectrum from g8b run period at CLAS. Top: the enhancement (photon energy spectrum obtained with the crystal divided by the spectrum obtained from an amorphous radiator). Data is in black and the enhancement distribution calculated from theory is in red. Bottom: The calculated polarisation.

In order to calculate the photon polarisation, and of course to determine the kinematics of the reaction being studied, the photon energy must be precisely measured. This is done using the Hall B photon tagging system [45]. The layout of the set up is shown in Figure 2.3. Electrons are incident on the diamond radiator positioned with the goniometer. Radiated photons pass through the tagger unaffected and are incident upon the experimental target. The energy degraded electrons are deflected by a magnetic field within the tagger on to an arrangement of scintillator detectors which measure the energy of the electron from its trajectory, and timing information which is used to associate the measurement with the photon. Since the energy of the electron in the beam is well known from the accelerator operations, the photon energy can be calculated as the energy loss from electron beam energy to tagged electron energy. Figure 2.4 shows the layout of the tagger. The uncharged photons pass straight through while any full energy electrons (i.e. beam electrons which have not lost energy in the radiator) are focussed

on to the tagger beam dump. Energy degraded electrons will follow a trajectory through the first layer of 384 E-counters for energy measurement and then through a second layer of 61 T-counters for timing measurement. The system can tag photons in a wide ranger of energy, from 20% to 95% of the beam energy, with a precision of approximately 0.1% of the beam energy.

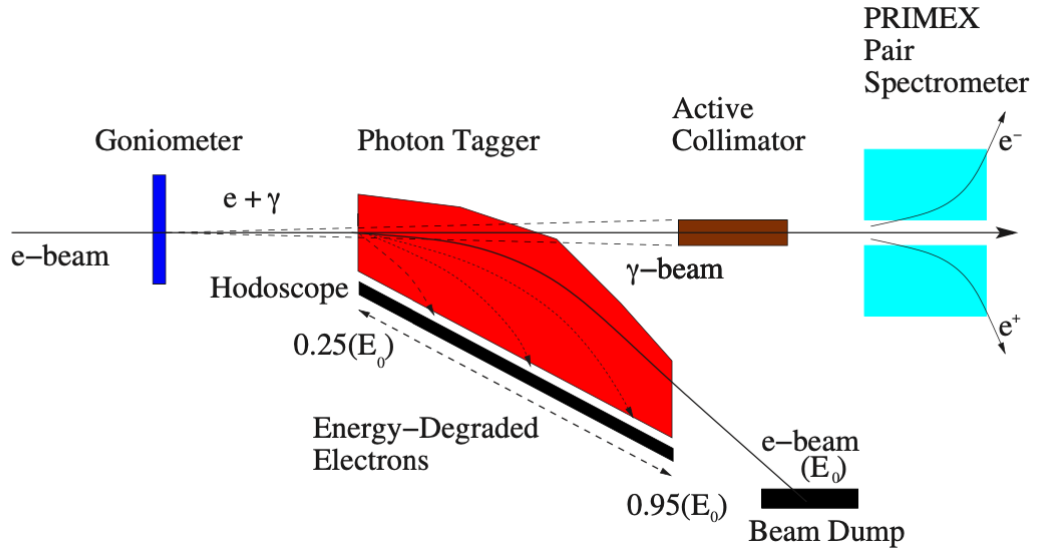


Figure 2.3: The layout of the coherent bremsstrahlung facility and photon tagger within Hall B [46]. As a scale reference, the length of the hodoscope focal plan is over 9m. The set up is situated approximately 15m upstream of the CLAS target.

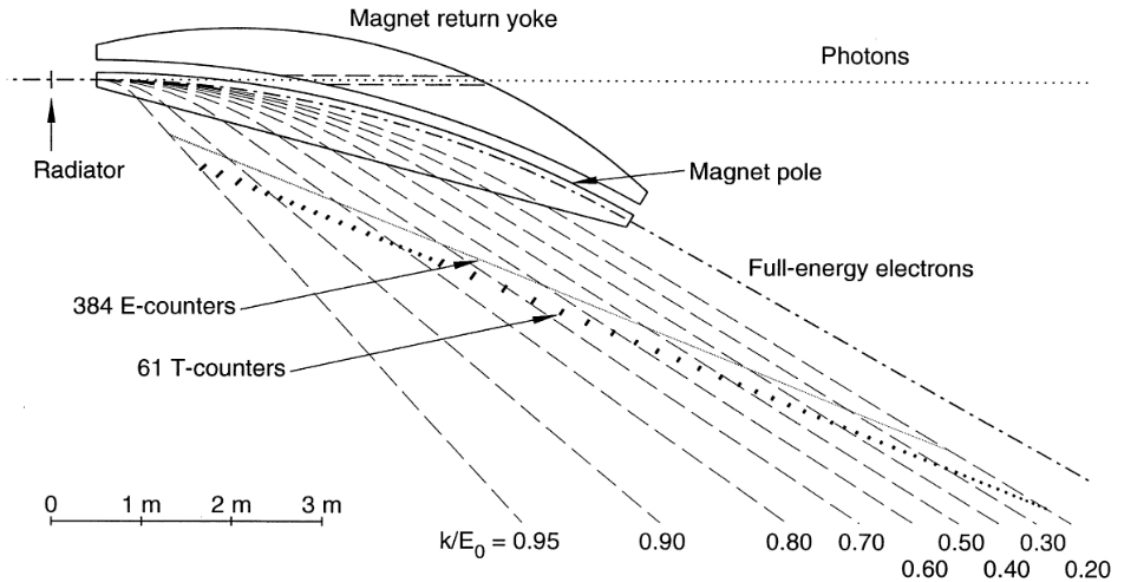


Figure 2.4: Geometry of the photon tagging system in Hall B. [45]

2.3 Target for g8 Experiment

The photon beam produced by the coherent bremsstrahlung facility is incident upon the CLAS g8 target: a cylinder of length 40.0 cm and radius 2.00 cm filled with liquid hydrogen. The target was positioned with its centre 20.0 cm downstream from the centre of CLAS.

2.4 Beamline Devices

The experimental data analysed in this work benefitted throughout the run period from several beamline devices for monitoring the beam quality. Beam position monitors (BPMs) measure the x and y co-ordinates of the beam by measuring the induced current in wires close to the beam. The measurements are used to keep the beam centred on the CLAS target and parallel with the z -axis of the CLAS co-ordinate system. The BPMs were placed 36.0 and 24.6 m upstream of the CLAS target. An additional BPM is situated 8.2 m upstream of the target but, since this monitor is downstream of the photon tagger, is only used for electron beam runs. The beam profile in the x - and y -directions is monitored by beam profile monitors (known as harp scanners) positioned 36.7, 22.1, and 15.5 m upstream of the target. The harp scan operates by passing a wire through the beam and detecting the scattered electrons with PMTs. Since the wire passes through the beam the monitoring is done outside of data taking, usually before the start of a run following a change in beam conditions.

To monitor the photon beam flux, two devices are installed: the pair spectrometer downstream of the photon tagger (shown in Figure 2.3) and the total absorption shower counter (TASC). The TASC is a lead glass scintillator array with essentially 100% efficiency which can be inserted into the beam line at low current. This allows two essential functions to be performed. First, the tagging efficiency of the photon tagger can be determined using the TASC measurement of the total flux. And second, the pair spectrometer can be calibrated against the TASC. The pair spectrometer operates by inserting an aluminium foil into the photon beam (removing only 1% of photons) and detecting the electron positron pairs which are produced. Since the pair spectrometer can operate during normal running conditions, the total flux can be inferred during data taking.

Full details of all beamline devices are given in [31].

2.5 CEBAF Large Acceptance Spectrometer

The CEBAF Large Acceptance Spectrometer (CLAS) [31] was the main detector situated in Hall B during the 6 GeV era. The detector components are arranged in a six-fold azimuthal symmetry

following the geometry of the superconducting toroidal magnet which divides the system into six sectors. Shown schematically in Figure 2.5, the spectrometer consists of drift chambers to track the paths of charged particles within the magnetic field provided by the toroidal magnet, scintillation counters to measure time of flight, calorimeters to measure energy deposition of electrons and neutral particles, and Čerenkov detectors for electron and pion identification. The system is designed to provide good momentum resolution over a large acceptance, close to 4π angular acceptance. Figure 2.6 represents a typical reaction and detection of resulting charged particles in CLAS. A photon or electron beam entering from the left interacts with the target and start counter at the centre. Charged reaction products are bent through the toroidal magnetic field and their trajectory and path length through the drift chambers is measured. The time-of-flight system measures the hit time allowing the velocity and mass to be determined. The Čerenkov counters and electromagnetic calorimeters are primarily used for electron beam running and are not utilised in this work. The remainder of this section provides more details on each of the detector components.

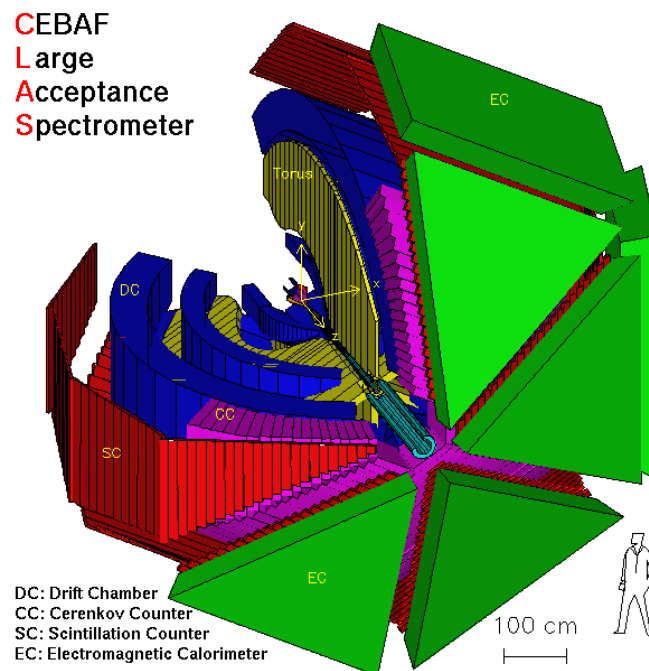


Figure 2.5: Schematic diagram of CLAS. Two of the sectors are cut away in the diagram showing the layout of the detectors within. [47]

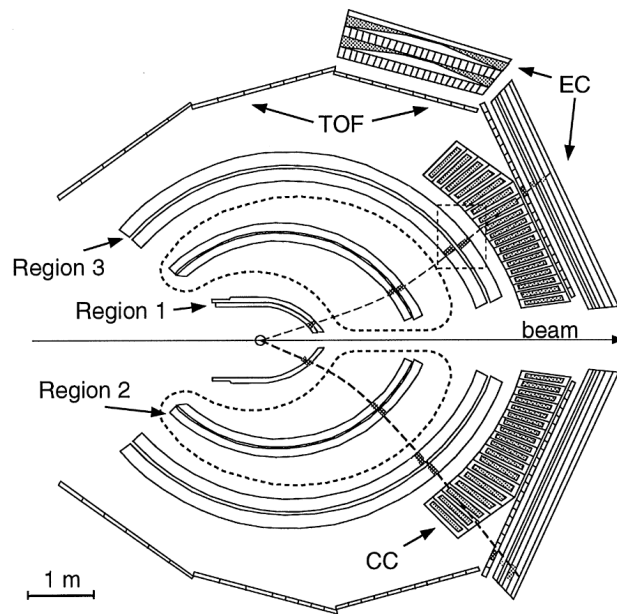


Figure 2.6: Cross-section of CLAS showing the layout of the detector components: Regions 1, 2 and 3 of the Drift Chamber, Time-of-flight (TOF), Electromagnetic Calorimeters (EC), and Cherenkov Counters (CC). The dotted lines around Region 2 of the drift chamber represent the projection of the torus coils. [48]

2.5.1 Start Counter

The start counter [49] consists of 24 scintillator paddles surrounding the target cell in a hexagonal formation aligned with the sectors of CLAS. The components of the start counter and the arrangement with respect to the target and photon beam are shown in Figure 2.7. The scintillator paddles are attached to photomultiplier tubes with acrylic light guides for readout. The purpose of this detector component is to determine the time of the photon-induced reaction within the target by detecting the outgoing particles. The time resolution is approximately 350 ps enabling the identification of the 2 ns beam bucket to which the incident photon belongs. The timing measurement and sector identification is used, together with coincident measurements in the time-of-flight detectors, for trigger configuration.

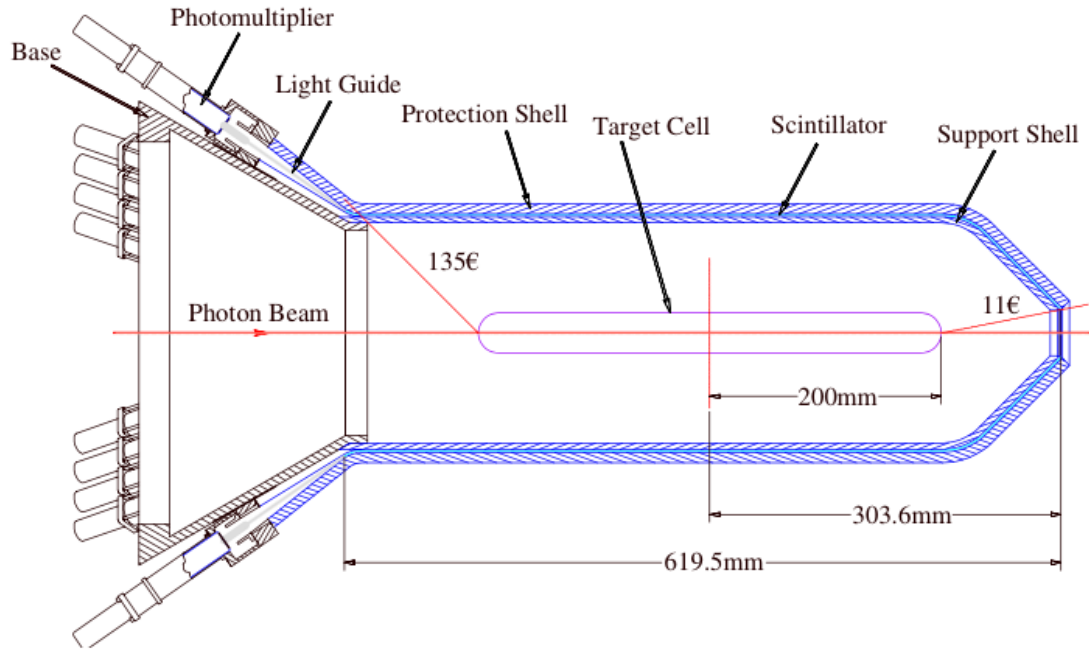


Figure 2.7: Diagram of the start counter showing the target cell within. [49]

2.5.2 Superconducting Toroidal Magnet

The magnetic field within CLAS is provided by the CLAS torus, a toroidal magnet [31, 50, 51] approximately 5 m in diameter and 5 m in length cooled with liquid helium. Six superconducting coils are arranged in a torus configuration around the beamline thus defining the split of CLAS into six 60° sectors. Figure 2.8 shows the toroidal magnet coils before installation. The torus generates a magnetic field of maximum strength 20 kG in the azimuthal directions as shown in Figure 2.9. The effect of the magnetic field on charged particles moving through the detector, together with the tracking systems, provides the necessary information for momentum analysis. The azimuthal field is transverse to particle momenta thus bending the particle tracks inward towards the low acceptance beamline region or outward toward the fiducial region of CLAS for oppositely charged particles. The polarity of the magnet can be switched between runs controlling whether negatively or positively charged particles are bent inward or outward. For this experiment the torus polarity was set such that negative particles were inbending, therefore the acceptance for negatively charged particles is lower than for positively charged particles in the experiment analysed in this work.



Figure 2.8: The CLAS torus prior to installation. Image source [52]

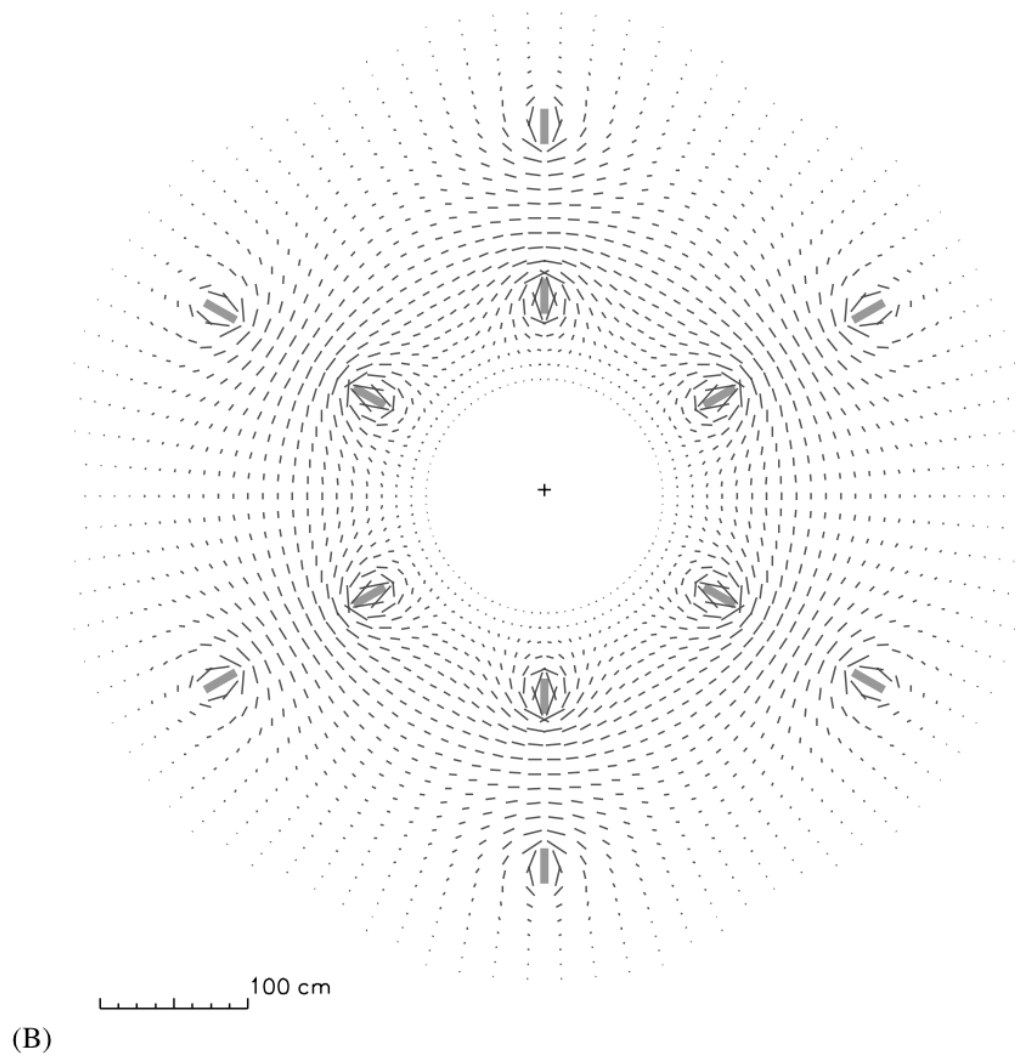
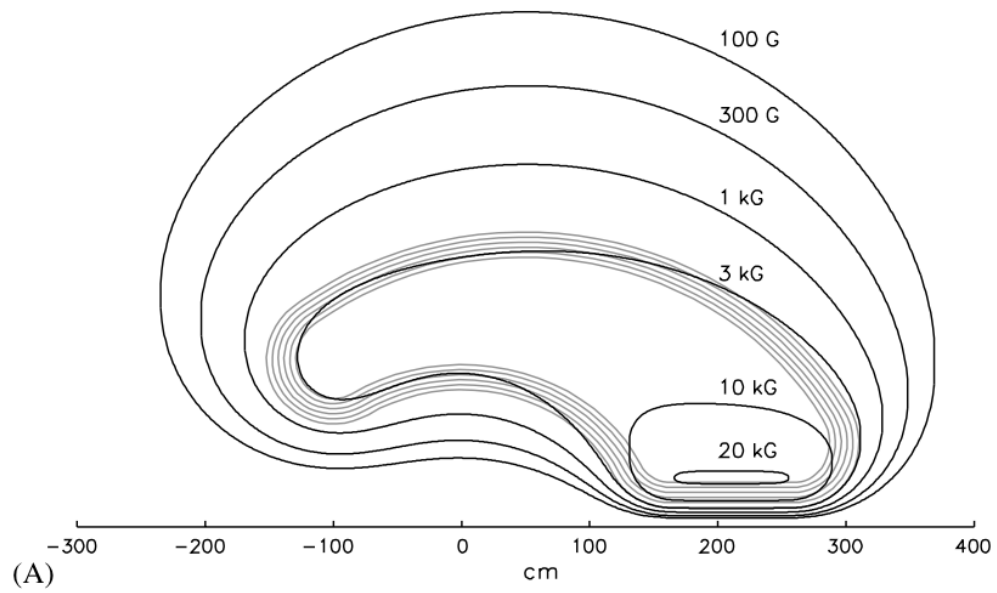


Figure 2.9: (A) Contours of magnetic field strength for a coil of the CLAS torus. (B) Magnetic field vectors for the CLAS torus. [31]

2.5.3 Drift Chambers

The CLAS Drift Chambers [48] are a system of multi-wire chambers designed to track the passage of charged particles as they travel through the magnetic field supplied by the toroidal magnet. The chambers are arranged in three “regions”. Region 1 surrounds the target and is enclosed within the centre of the torus. Region 2 is located between the torus coils and Region 3 lies radially outward of the torus. Figure 2.6 illustrates the relative position of the three drift chamber regions relative to the torus. In Figure 2.10 (left) the placing of Region 2 between the torus coils, and Region 3 outside the torus is shown. Region 2 lies in the area of the highest magnetic field and is therefore the region where the maximum curvature of particle tracks occurs. Each region is split into six chambers for each sector of CLAS, a total of 18 separate drift chambers. The chambers are filled with a gas mixture of 90% argon, 10% carbon dioxide. Within each chamber, the wires are arranged in hexagonal cells within 2 “superlayers” as illustrated in Figure 2.10 (right). Charged particles ionize the gas and the resulting freed electrons are collected by 20 micron gold-plated tungsten “sense” wires at the centre of each hexagon held at a positive voltage. 140 micron gold-plated aluminium alloy “Field” wires at the vertices of the hexagons are held at a negative voltage providing the potential difference needed to collect the pulse on the sense wires. As a “hit” registers in each cell, the particle tracks can be detected. The highlighted cells in Figure 2.10 show an example of a particle track through the two superlayers of Region 3. The curvature of the track and the known magnetic field strength from the torus enables the particle momentum to be measured. The CLAS drift chambers achieve momentum resolution of $\Delta p/p = 0.5\%$.

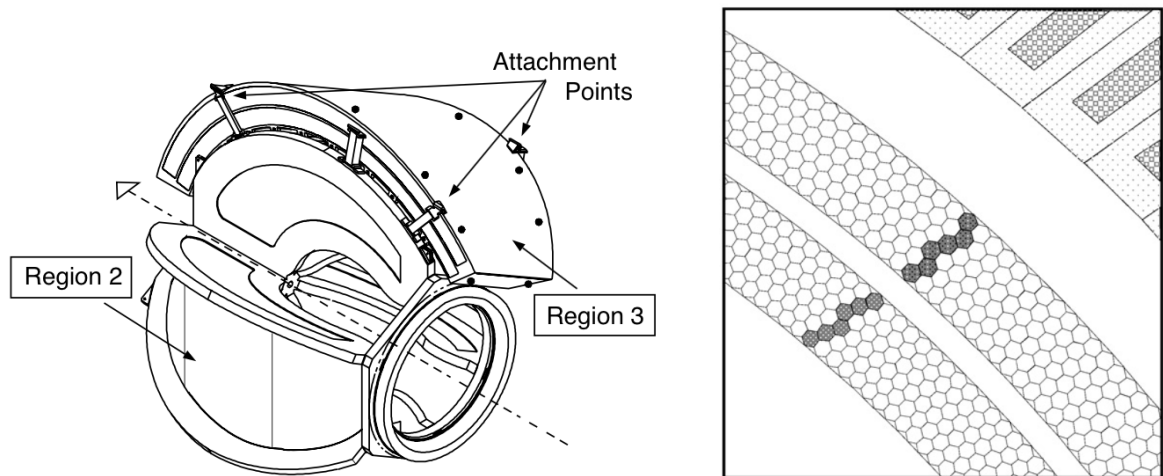


Figure 2.10: Left: the position of Region 2 of the Drift Chamber between the torus coils, and Region 3 radially outward of the torus coils. Region 1 is not shown. Right: Representation of the two superlayers of Region 3 of the Drift Chamber. Highlighted cells represent a particle track. Image source [31, 48]

2.5.4 Time-of-flight Scintillators

Beyond the drift chambers and covering the fiducial region of CLAS (lab polar angles from 8° to 142°), the time-of-flight system [53] is an arrangement of scintillator paddles providing high resolution timing information for the experiment. The plastic scintillator paddles are arranged in six groups of 57 paddles aligned with the sectors of CLAS (see Figure 2.6 for their position relative to other detector components). The scintillator paddles are 5.08 cm thick and vary in length and width depending on their position (see Figure 2.11). The paddles vary in length from 32 cm to 445 cm providing the full angular coverage of the CLAS geometry. At forward angles, the paddle width is 15 cm and at larger angles the paddle width is 22 cm. The timing resolution achieved is approximately 80 ps for the shorter paddles and 150 ps for the longer paddles. The timing measurement is used together with the path length and momentum measurements from the drift chamber to calculate the particle mass which is used for the initial particle identification in both analyses in this work. With the given timing resolution, pions can be distinguished from kaons up to momentum of 2.0 GeV/c, and pions from protons up to a momentum of 3.5 GeV/c [31].

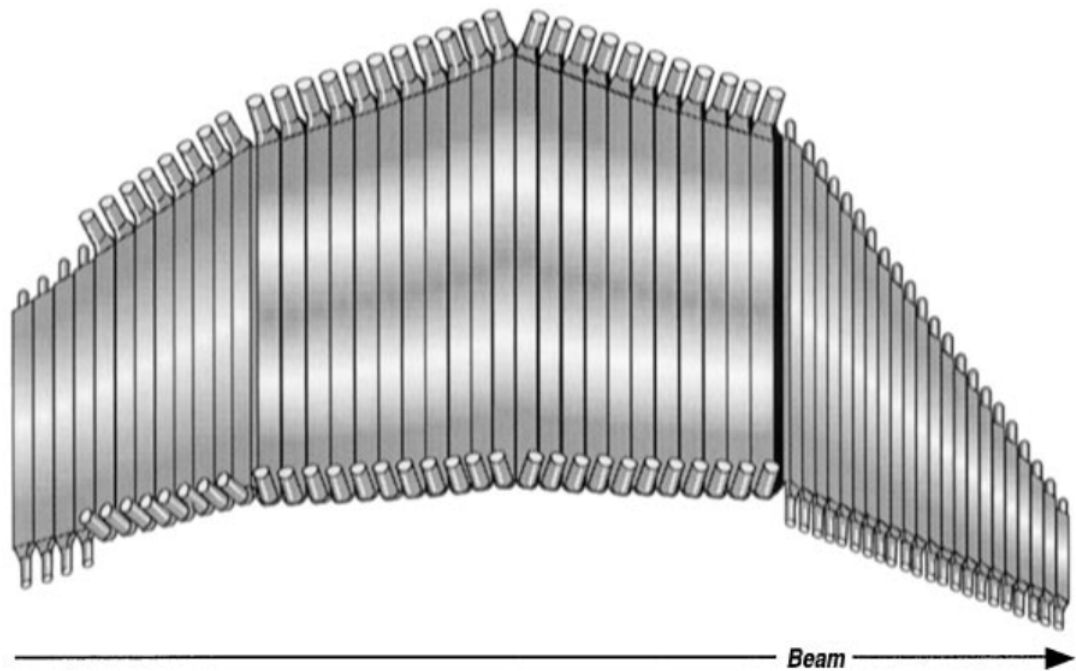


Figure 2.11: Time-of-flight scintillator paddles for one sector of CLAS. Each paddles is connected to a photomultiplier tube at each end. Image source [53]

2.5.5 Čerenkov Counters

Used exclusively for electron beam running, the Čerenkov Counters [54] identify and differentiate between electrons and pions using the characteristic opening angle of the cone of Čerenkov

light emitted when an energetic particle passes through the gas at a speed greater than the speed of light in the gas. The device operates by reflecting the emitted light through a system of mirrors on to a light collecting cone connected to a PMT. Since this work concerns a photon beam experiment, the data from this detector is not used.

2.5.6 Electromagnetic Calorimeters

The CLAS forward electromagnetic calorimeter [55] is located at forward angles ($8^\circ < \theta < 45^\circ$) at the outer shell of CLAS as shown in Figure 2.6. Its purpose is to detect electrons and neutral particles during their passage through an assembly of three layers of lead sheets sandwiched between scintillator bars (see Figure 2.12). They play an important role in defining triggering conditions for electroproduction experiments and in the reconstruction of π^0 and η mesons from their photon decays. In order to extend the detection capabilities to more backward angles, the large angle electromagnetic calorimeter covers polar angles up to 70° in two of the sectors of CLAS. The analyses in this work are for a photoproduction experiment relying on the detection of charged particles, therefore the data from these detectors are not used.

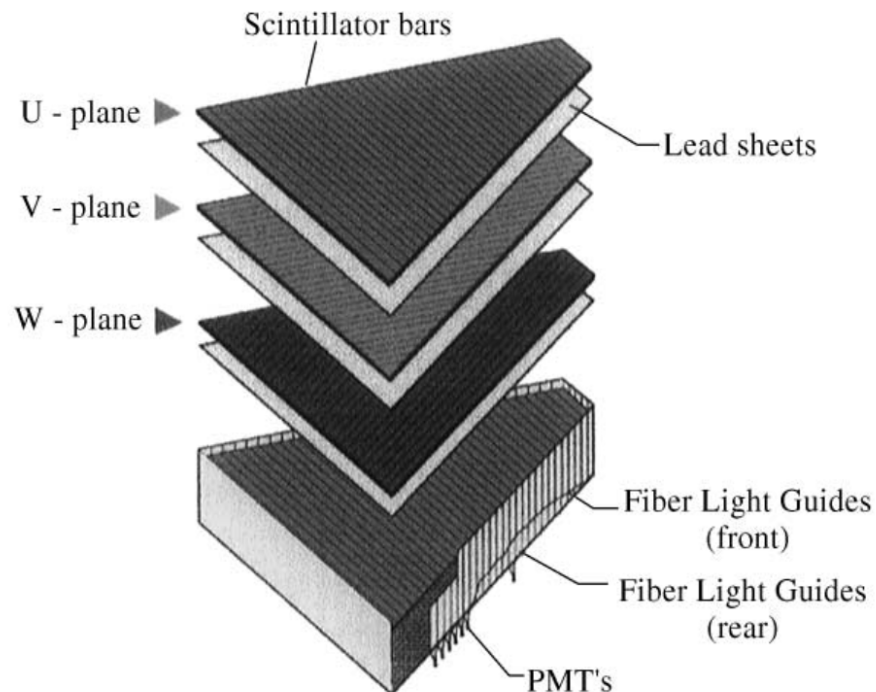


Figure 2.12: Exploded view of a section of the Electromagnetic Calorimeter. Image source [55]

2.6 Trigger, Data Acquisition and Reconstruction

The CLAS trigger system aims to maximise the data acquisition relating to physics events while minimising the deadtime. The trigger logic happens in two stages. The Level 1 trigger fires

when there is a coincidence of hits in key detectors. For this experiment, it was required that a hit was detected in the photon tagger, as well as the start counter and time-of-flight scintillators in the same sector. The data acquisition system (DAQ) is capable of writing out the digitized data from all detectors within 90 ns of the signal from the Level 1 trigger. In order to ensure that the event in question is likely of physics interest, i.e. arising from a reaction in the target, rather than from accidental coincidences caused by cosmic rays or electronic noise, the Level 2 trigger checks for likely tracks in the drift chamber by searching for track segments in overlapping regions of wires and layers. Should none be found, the data is cleared and reset to await the next Level 1 trigger. If a potential match is found, the data is written to a read out queue for asynchronous readout to tape.

2.7 The CLAS12 upgrade

The preceding sections have provided a full description of the the experimental set-up during the 6 GeV era. Alongside the analysis of the experimental data collected during this time, work was also done on the preparations for the 12 GeV era following the accelerator upgrade and the installation of the new CLAS12 detector. This section gives a brief overview of the upgraded experimental set up and a description of work undertaken as part of this PhD to develop calibration software for the time-of-flight detector systems.

2.7.1 Overview

The Continuous Electron Beam Accelerator Facility (CEBAF) at Jefferson Lab was upgraded to provide an electron beam of up to 12 GeV to all four experimental halls. The corresponding upgrade to CLAS (CLAS12) in Hall B [56, 39] required upgraded detector components, shown schematically in Fig. 2.13, to have capabilities to match the increased beam energy. Particular requirements were to be capable of running at increased luminosity (an order of magnitude greater than CLAS), and provide detection and separation of high momentum particles at forward angles. In particular, the existing time-of-flight detector [53] was refurbished and extended [57] to provide improved timing resolution, particularly at forward angles. Additionally, a new Central Time-of-Flight detector [58] was commissioned providing timing information which can be correlated with momentum measurements from the central detector system. The calibration software for both of these detectors was developed as part of this PhD and therefore more details of these detectors are given in the following sections. A full description of the calibration process and the software developed is given in Appendix A.

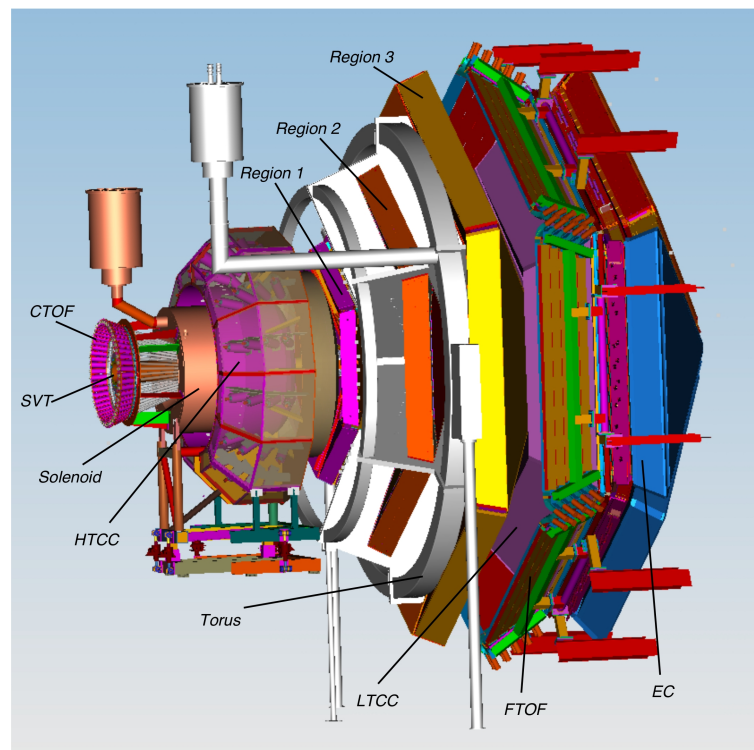
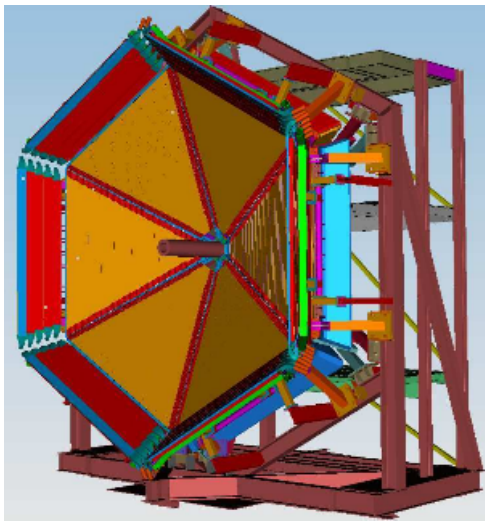


Figure 2.13: The CLAS12 detector showing the relative positions of the Central Time-of-flight detector (CTOF), Silicon Vertex Tracker (SVT), solenoid magnet, High-threshold Čerenkov Counters (HTCC), toroidal magnet (torus), low-threshold Čerenkov Counters (LTCC), Forward Time-of-flight detector (FTOF), Electromagnetic Calorimeters (EC) and Regions 1, 2 and 3 of the Drift Chambers. Image source [56]

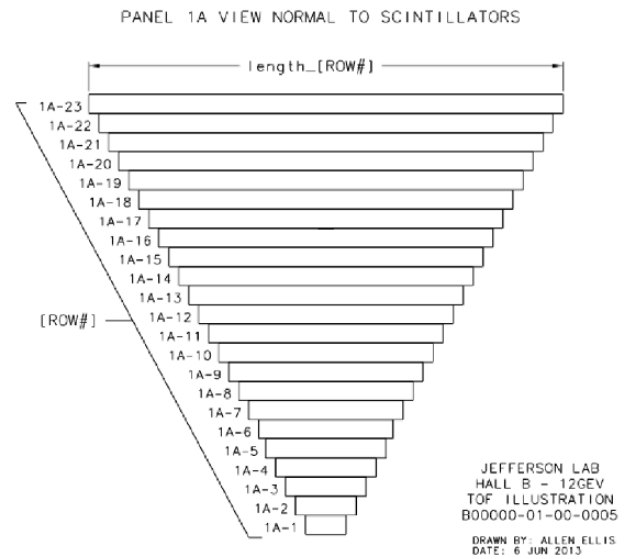
2.7.2 Time-of-flight Detectors

The Forward Time-of-flight detector (FTOF) consists of plastic scintillator paddles coupled to photomultiplier tubes (PMTs) at each end. The paddles are configured in triangular arrays in line with the six sectors of CLAS12. These are arranged in three panels, Panel 1-b consisting of 62 paddles per sector provides highly segmented coverage over an angular range of 5° to 35° in θ . Panel 1-a is situated downstream of panel 1-b with 23 paddles per sector providing the same angular coverage. Panel 2 extends the coverage to larger θ , up to 45° . The detector is approximately 10m in diameter and is situated 7m downstream from the target. A schematic diagram of the detector is shown in Fig. 2.14a with an illustration of the arrangement of the paddles in each sector shown in Fig. 2.14b.

The Central Time-of-flight detector (CTOF) is a barrel shaped arrangement of 48 plastic scintillator paddles at a radial distance of 25cm from the target. Each paddle is 92cm long and provides angular coverage of 35° to 125° in θ . The paddles are coupled to PMTs via light guides in order to place the PMTs at a lower magnetic field strength. The set up is shown in Fig. 2.15.



(a) The FTOF detector showing the panel-1b paddles in orange and the panel-2 paddles in red. The panel-1a paddles are downstream behind panel-1b.



(b) Example of the layout of paddles in each sector.

Figure 2.14: The CLAS12 Forward Time-of-Flight detector. Images from [59].

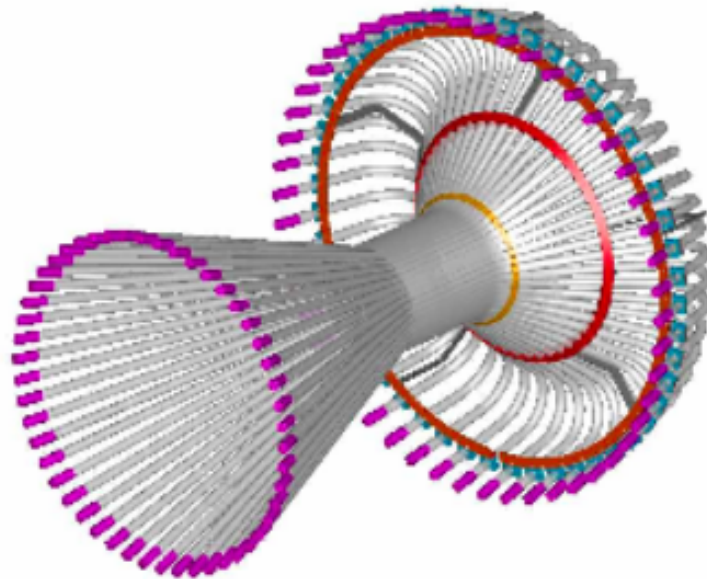


Figure 2.15: The CLAS12 Central Time-of-Flight detector. The central cylinder contains the scintillator paddles and the spokes extending from each side are light guides. From [60].

Chapter 3

Analysis methods

Before moving on to the details of the analyses in this thesis, this section provides an overview of the steps involved and gives some explanation of the techniques used which are common to both of the reactions presented.

3.1 Overview

The remainder of this thesis describes in detail how observable quantities were extracted from CLAS experimental data for two photoproduction reaction channels. A similar process and set of analysis methods and techniques were used in both analyses. An overview of the process is shown in Figure 3.1. The CLAS data acquisition system (DAQ) provided raw data containing detector readouts which were run through a process of calibration and reconstruction known as “cooking”. In this process, the raw detector readouts were used to create a set of events, each event containing several particles with mass, momentum, charge and timing information assigned to each particle. The data were then reduced to select events containing at least two charged particles (skimming). The first step in each individual analysis was to identify events which contained the required particles for the reaction by examining their measured charge and mass (“Final state particle ID and channel ID cuts”). At this stage, the objective was to reduce the set of events in preparation for the extraction of the signal.

The signal distributions were extracted using the sPlots technique: discriminatory variables were used to generate weights for subtracting off the background distributions.

Before extracting the observable values which describe the distribution, detector acceptance corrections were applied. Events are generated for each channel and passed through the detector simulation to create a set of simulated events. Finally, the observable values are extracted using likelihood sampling using the simulated data to calculate the normalisation integral. For any given set of observable values, it was determined how likely it was that they described the

signal-weighted measured distribution. By performing this calculation in a series of steps known as Markov Chain Monte Carlo (MCMC), probability density functions (PDFs) were derived for each observable. A comparison of the steps for the two reaction channels being studied is given in Table 3.1: this summarises the detailed description of the analyses given in Chapters 4 and 5. More details of the common analysis techniques are given in the following sections, describing the separation of signal and background using the sPlots technique and the MCMC likelihood sampling used to obtain the probability distributions for the observable quantities being measured.

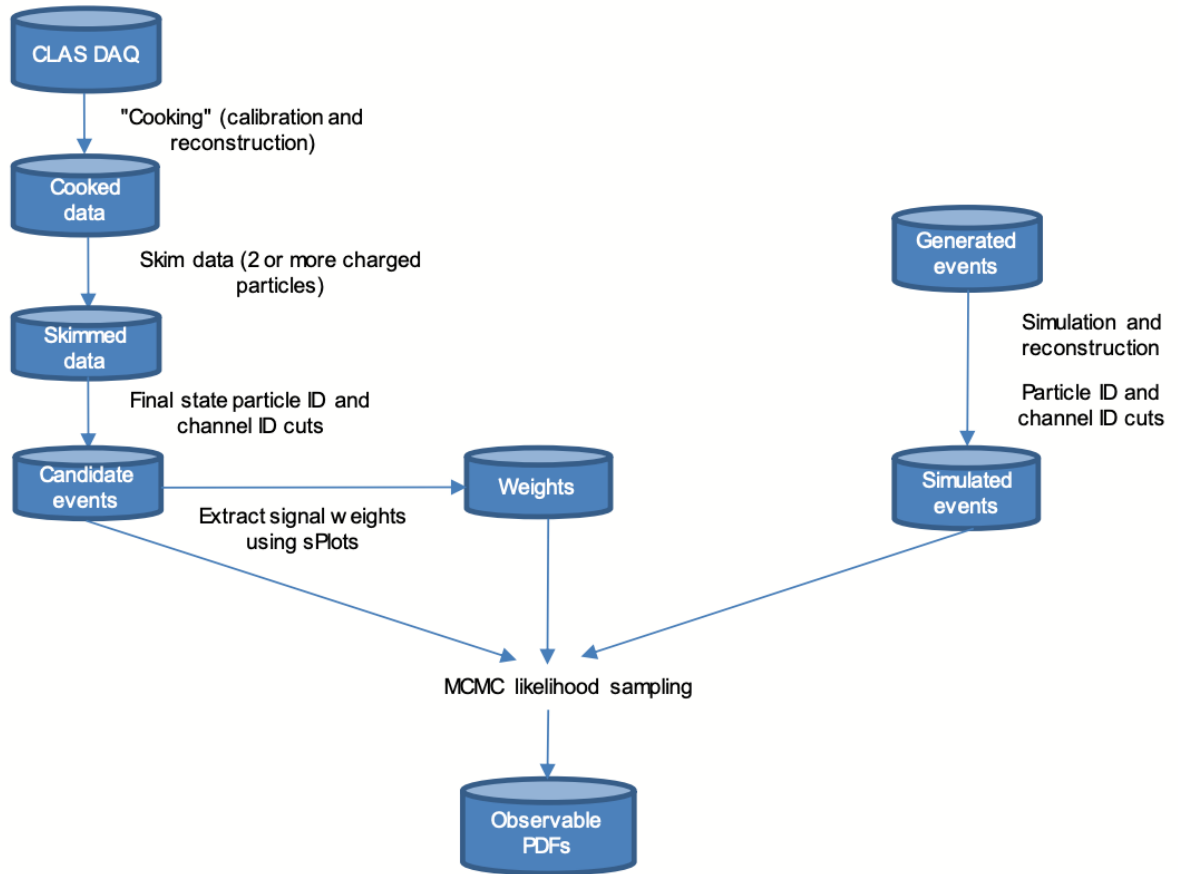


Figure 3.1: Overview of the analysis steps used in both analyses.

3.1.1 The sPlots technique

In order to study the angular distributions which are described by the observables of interest, the distributions must be separated into signal and background contributions. In this work the technique used to achieve this was the sPlots technique, “a statistical tool to unfold data distributions” developed by Pivk and Diberder and described in their 2005 paper [61]. Given a set of events which have arisen from several sources (typically signal and background), the tool allows for the extraction of yields and the assignment of weights to each event by the use of

Analysis step	Σ^+ analysis	ϕ analysis
“Cooking” (calibration and re-construction)	Raw detector readouts are used to create a set of events, each event containing several particles with mass, momentum, charge and timing information assigned to each particle. This step is common for both analyses.	
Skim data	The output from cooking is read and only events with two or more charged particles are retained. This step is common for both analyses.	
Reaction	Pseudo-scalar meson photoproduction $\vec{\gamma} p \rightarrow K_S^0 \Sigma^+$ then $\Sigma^+ \rightarrow p \pi^0$ and $K_S^0 \rightarrow \pi^+ \pi^-$	Vector meson photoproduction $\vec{\gamma} p \rightarrow p \phi$ then $\phi \rightarrow K^+ K^-$
Final state particle ID	$p \pi^+ \pi^-$ and optional neutral particles	$p K^+ K^-$
Channel ID	$\pi^+ \pi^-$ reconstruct to K^0 ; Missing mass ($\pi^+ \pi^-$) reconstruct to Σ^+	$K^+ K^-$ reconstruct to ϕ
Extract signal weights	Taken from fits to the peaks of π^0 mass (missing mass of $p \pi^+ \pi^-$) and kaon mass (mass of $\pi^+ \pi^-$)	Taken from fit to the peak of ϕ mass (mass of $K^+ K^-$)
Phase space event generation, simulation and reconstruction	Events are generated in the phase space for the reaction and passed through the CLAS detector simulation and reconstruction.	
Likelihood sampling	Extract polarisation observables $\{\Sigma, P, T, O_x, O_z\}$	Extract 9 spin density matrix elements

Table 3.1: Comparison of analysis steps for the Σ^+ and ϕ analyses.

a discriminatory variable. Based on the signal and background shapes and relative yields of the discriminatory variable, signal distributions of any uncorrelated variable can be obtained via weights.

To illustrate the technique, we step through a simple example (taken from [62]). Consider a mass distribution composed of signal and background as shown in Figure 3.2, which is chosen as the “discriminatory variable”. As the first step, the signal and background yields are fitted with appropriate shapes, in this case a gaussian signal on an exponential background (Figure 3.2 (top)). Using these fits the probability that each event is either signal or background can be computed as a function of the mass variable as shown in Figure 3.2 (middle). The sWeights are then calculated from the probabilities and covariance matrix from the fit of the signal and background yields following the method in [61] (Figure 3.2 (bottom)). A key thing to notice here is that the sWeights take negative values for some values of the discriminatory variable. This effectively subtracts background when making the weighted distributions: events with positive and negative weights combine together to give the true number of signal events.

In order to calculate the weights, we have assumed that, for a discriminatory variable, m , the distribution is described by

$$f(m) = N_0 d_0(m) + N_1 d_1(m) \quad (3.1)$$

for signal and background yields N_0 and N_1 , and probability distributions d_0 and d_1 . From the fit of distributions, to determine the yields, we obtain the covariance elements C_{00} and C_{01} . The signal weight for an event with discriminatory variable m_i is

$$w_s(m_i) = \frac{C_{00}d_0(m_i) + C_{01}d_1(m_i)}{N_0d_0(m_i) + N_1d_1(m_i)} \quad (3.2)$$

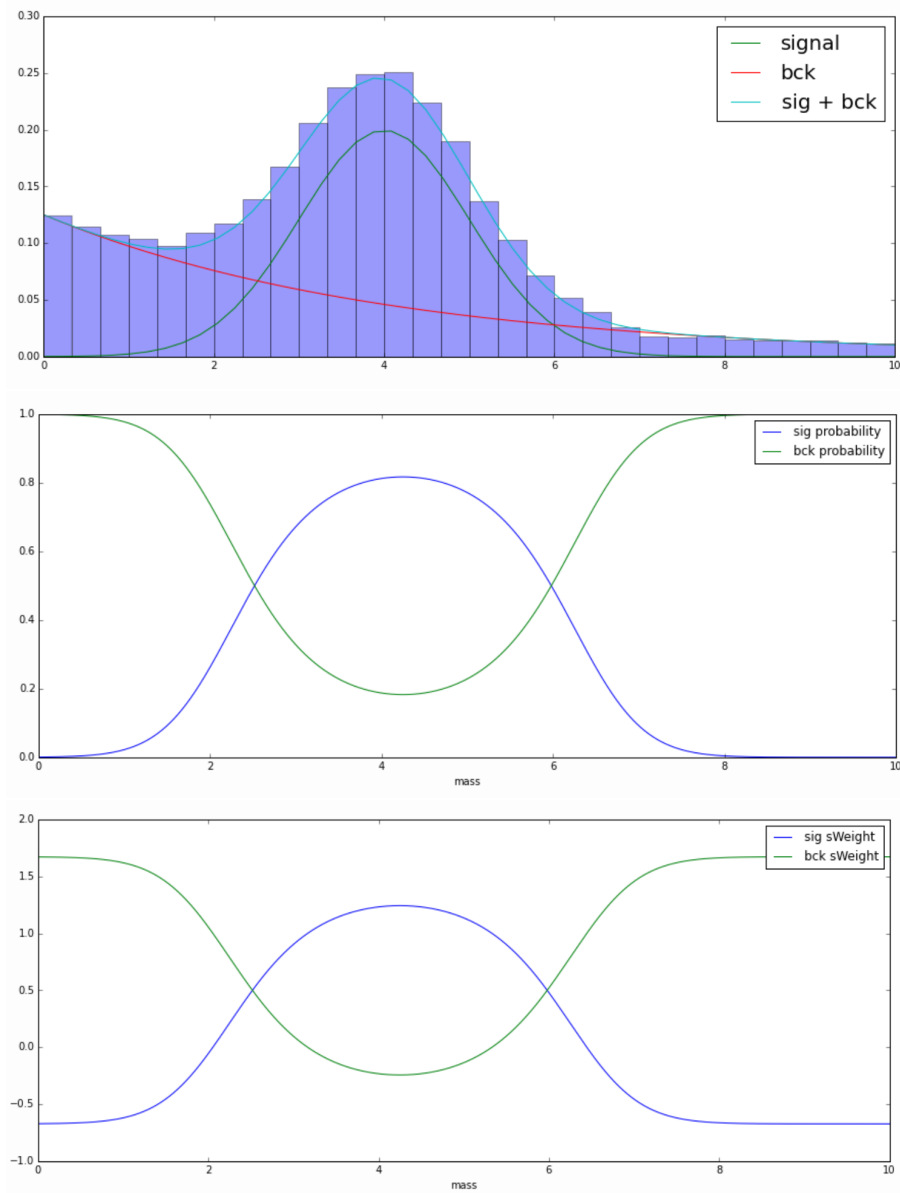


Figure 3.2: Illustration of the calculation of sWeights. A typical signal and background distribution (top) with calculated signal and background probabilities (middle) and the resulting sWeights (bottom). From [62].

3.1.2 Likelihood sampling with Markov Chain Monte Carlo

Calculation of likelihood

At each step in the MCMC sampling, a set of parameter values was randomly selected and the likelihood calculated summing over measured events, together with the signal weights. The simulated events accounted for the effect of detector acceptance. The following describes in detail how the likelihood was calculated.

For a distribution, \mathcal{I} , depending on measured variables τ , described by a parameter set p

and with acceptance given by $\eta(\tau)$, the likelihood that the distribution of N events is described by the specific set of parameters is given by

$$\mathcal{L}(p) = \prod_i^N \frac{\mathcal{J}(\tau_i : p) \eta(\tau_i)}{A(p)} \quad (3.3)$$

$A(p)$ is the probability normalisation integral given by

$$A(p) = \int \mathcal{J}(\tau_i : p) \eta(\tau_i) d\tau \quad (3.4)$$

For likelihood sampling using MCMC, the log likelihood was calculated for each step in the chain. Each event was assigned a signal weight, w_i , as described in Section 3.1.1 so that the background was subtracted off in the likelihood summation and the expression for the log likelihood including the weight term becomes

$$\ln \mathcal{L}(p) = \sum_i^N w_i \ln \mathcal{J}(\tau_i : p) \eta(\tau_i) - \ln A(p) \quad (3.5)$$

The inclusion of weights in the likelihood means that an additional factor was required to account for the effect of the weights on the parameter uncertainties. Specifically, the uncertainty will scale with the quantity $\frac{\sum_i w_i^2}{\sum_i w_i}$ as described in [63] and the expression for the log likelihood becomes

$$\ln \mathcal{L}(p) = \frac{\sum_i w_i^2}{\sum_i w_i} \left[\sum_i^N w_i \ln \mathcal{J}(\tau_i : p) \eta(\tau_i) - \ln A(p) \right] \quad (3.6)$$

Markov Chain Monte Carlo

The Markov Chain Monte Carlo method (MCMC) was used to obtain the probability distributions for the observable quantities which are being measured. It combines two approaches: ‘‘Monte Carlo’’ and ‘‘Markov Chain’’. The Monte Carlo aspect of the method refers to the practice of inferring the properties of a distribution by randomly sampling that distribution. In this work, the sampling is applied to the ‘‘parameter space’’ of the observable values, i.e. all possible combinations of values of the observables. This is combined with the Markov Chain method which defines how each set of parameter values is chosen, thereby creating the ‘‘chain’’ of values. The key feature of the Markov Chain is that each new set of values in the chain is dependent on the previous set only. The population of the chain proceeds as follows.

1. Begin with a starting set of parameter values, and calculate the likelihood that those values describe the data
2. Generate a new set of parameters based on the previous set of parameters using a defined method (the “proposal”)
 - In this analysis, the new set of parameters was generated by making a step alteration to a single randomly selected parameter at a time.
3. Decide whether to accept the new set of parameters into the chain. The method used to do this is known as the Metropolis Hastings algorithm, the details of which are as follows.
 - Calculate the likelihood that the new set of parameters describe the data
 - If the likelihood is greater than the likelihood for the previous set of values, accept the new set of values into the chain
 - If the likelihood is less than the likelihood for the previous set of values, the new set of values may or may not be accepted into the chain. The new set of values will be accepted with a probability equal to the ratio of the likelihoods for the current and previous step. So, for example, if the new set of parameters is only half as likely to describe the data, then there is a 50% likelihood that they will be accepted into the chain.
4. Repeat the process from Step 2 using the most recently accepted set of parameters.

In this way, distributions of parameter values are created, known as the posterior distributions. This is visualised in Figure 3.3. The posterior distributions obtained in this way are the probability density functions for the observable quantities being investigated and are used to report the results of the analyses.

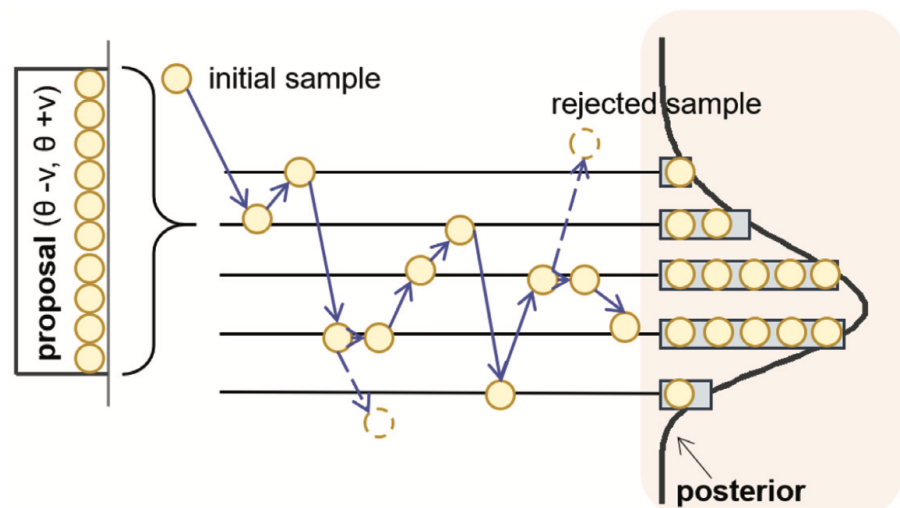


Figure 3.3: Illustration of Markov Chain Monte Carlo sampling. From [64]

In performing the MCMC sampling, there were several parameters relating to the execution of the sampling which were varied to tune the sampling process. First, the number of steps in the chain was considered. The number of steps was chosen to be high enough that increasing the number of steps beyond this did not significantly affect the results obtained, and low enough that practical considerations of computing time were within a manageable range. Following studies which varied the number of steps in the chain, the number of steps in the chain was set at 2000 for both analyses in this work. During the initial steps in the chain, there is likely to be a period of what is known as “burn in”. This is a period during which the initial steps in the chain contain parameters sets of relatively low likelihood. The parameter values are likely to move across the parameter space until values with high likelihood are reached and the chain is said to have converged. By studying the time evolution of the parameters an appropriate burn in period was identified. These initial burn in steps were omitted from the posterior distributions used for the results.

Finally, it is important also to be confident that the parameter space is being sampled widely enough so that minima are not missed. In our method, this was controlled by the step size used in the step proposal function to generate the next set of parameters. A larger step size will ensure that greater coverage of the available parameter space is achieved. However, again there is a compromise as a larger step will make acceptance of the new set of parameter values less likely. The proposal acceptance rate gives a measure of this, i.e. the percentage of parameter sets proposed which are subsequently accepted into the chain. If the proposal acceptance is too high, this may be an indication that the parameter space is not being sampled widely. However, if the proposal acceptance is very low, this introduces issues with computing time. In both analyses, the step size was chosen so that the proposal acceptance rate was approximately 25%. This is within manageable computing time, but since 75% of proposed parameter sets are rejected, we can be comfortable that adequate sampling of the parameter space was achieved.

3.2 Summary

The analyses in this work share some common steps and methods. An overview of the steps and techniques has been given in this section. The remainder of the document will describe in detail the analyses carried out and the results obtained.

Chapter 4

Extracting Polarisation Observables for

$$\vec{\gamma} p \rightarrow K_S^0 \Sigma^+$$

The following chapters describe in detail the analysis of the reaction $\vec{\gamma} p \rightarrow K_S^0 \Sigma^+$ in CLAS for data taken during the g8b run period, in which a linearly polarised photon beam (denoted $\vec{\gamma}$) is incident upon a proton target. The hyperon and kaon are reconstructed from their decay to $p \pi^0$ and $\pi^+ \pi^-$ respectively. A schematic view of the reaction and final state is shown in Figure 4.1. The methods used to correctly identify the particles of interest in CLAS, and the procedures used to extract the various polarisation observables are described. Results will then be presented for the polarisation observables $\{\Sigma, P, T, O_x, O_z\}$ as angular distributions ($\cos \theta_K$) for bins in photon energy E_γ .

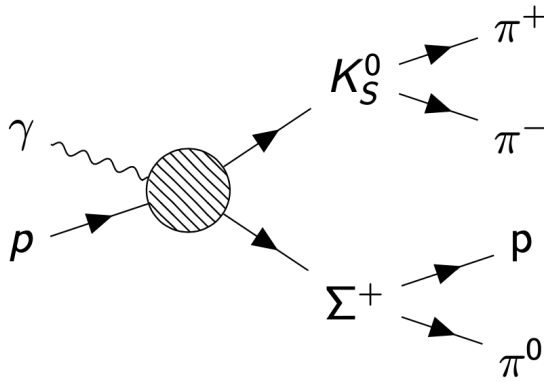


Figure 4.1: Schematic view of the $\gamma p \rightarrow K_S^0 \Sigma^+$ reaction and subsequent decay.

4.1 Formalism

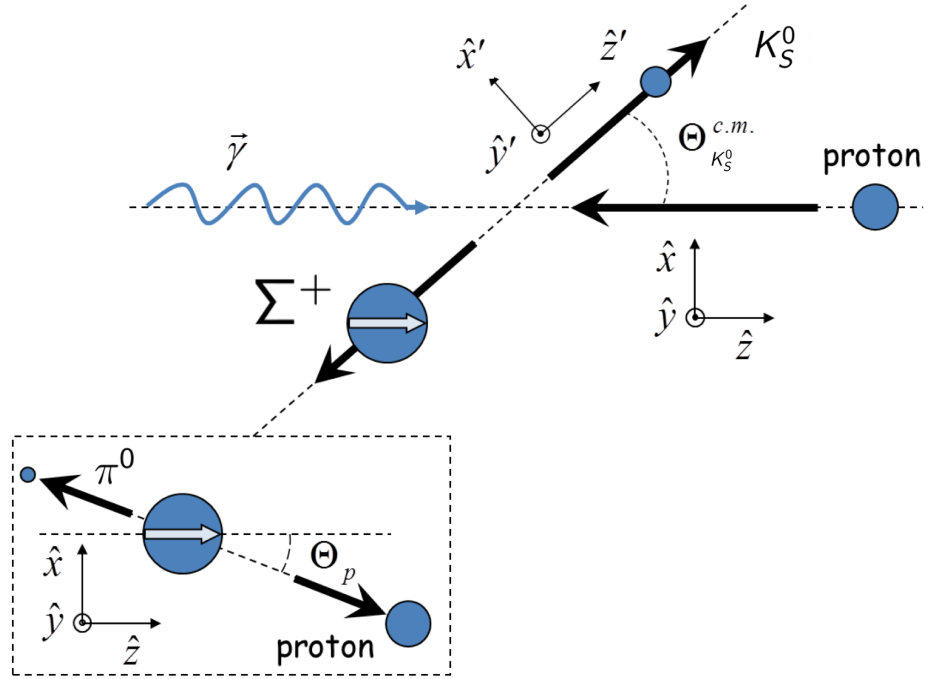


Figure 4.2: Kinematics of the $\gamma p \rightarrow K^0 \Sigma^+$ reaction. Adapted from [46].

The coordinate system and kinematical variables used in the description of kaon photoproduction are shown for the centre-of-mass reference frame in Figure 4.2. Several coordinate systems are commonly used in the literature. The unprimed coordinate system is chosen where the z-axis is orientated along the momentum axis of the incoming photon; the primed system is where the z-axis is orientated along the direction of the outgoing K^0 meson. In terms of unit vectors, and for photon momentum, k , and kaon momentum, q :

$$\hat{z} = \frac{\vec{k}}{|\vec{k}|}; \quad \hat{y} = \frac{\vec{k} \times \vec{q}}{|\vec{k} \times \vec{q}|}; \quad \hat{x} = \hat{y} \times \hat{z} \quad (4.1)$$

$$\hat{z}' = \frac{\vec{q}}{|\vec{q}|}; \quad \hat{y}' = \hat{y}; \quad \hat{x}' = \hat{y}' \times \hat{z}' \quad (4.2)$$

Note that one frame can transform into another by a simple rotation of θ_K^{CM} about the y-axis. For this analysis the unprimed coordinate system was used to enable more straightforward comparisons with models.

The differential cross section for the reaction, assuming that photon and recoil polarisation

can be determined, reads

$$\begin{aligned}
 \frac{d\sigma}{d\Omega} \equiv \sigma(\phi, \cos\theta_x, \cos\theta_y, \cos\theta_z) = & \sigma_0 \{ 1 - P^\gamma \Sigma \cos 2\phi \\
 & - \alpha \cos\theta_x P^\gamma O_x \sin 2\phi \\
 & + \alpha \cos\theta_y P - \alpha \cos\theta_y P^\gamma T \cos 2\phi \\
 & - \alpha \cos\theta_z P^\gamma O_z \sin 2\phi \},
 \end{aligned} \tag{4.3}$$

where σ_0 represents the unpolarised cross-section, P^γ is the photon polarisation, ϕ is the azimuthal angle between the scattering plane and the photon polarisation direction, $\cos\theta_x$, $\cos\theta_y$, $\cos\theta_z$ are the direction cosines of the decay proton in the Σ^+ rest frame, α is the Σ^+ weak decay asymmetry and everything else is a polarisation observable.

The variation of the cross-section as a function of the variables $\phi, \cos\theta_x, \cos\theta_y, \cos\theta_z$ allows us to extract photon beam asymmetry (Σ), the double polarisation observables (O_x and O_z), the target asymmetry (T) and the recoil asymmetry (P).

4.2 Event Selection

This section describes in detail the event selection process used to identify the following reaction in CLAS:

$$\vec{\gamma}p \rightarrow K_S^0 \Sigma^+ \rightarrow p \pi^+ \pi^- \pi^0$$

In this reaction the final state particles are from the decay of the Σ^+ into a p and π^0 and the decay of the K_S^0 into $\pi^+ \pi^-$.

The overall objective of this step is to identify candidate events which may correspond to this reaction, and retain these events to be used in the next step of the analysis (Signal/Background separation). Events which are not of interest are removed from the dataset thereby providing a much reduced set of events to be used in the signal extraction. The procedure starts with a set of cuts, first to identify the charged final state particles from their charge and mass. Then, a further cut is applied to ensure that the $p\pi^+\pi^-$ missing mass is consistent with a π^0 in the final state, thus ensuring the event contains the four particles in the final state. The procedure continues by applying cuts to ensure that the combined masses of the final state particles are consistent with them decaying from the channel of interest. In order to fully describe the reaction we must also identify the beam photon which has caused the reaction. The method of doing this by comparing to the vertex time is described. There are a few more improvements to the dataset done at this stage: events are restricted to those where the reaction vertex occurs within the target, and the energy and momenta of the detected particles are corrected for energy losses within the detector. Finally, the events carried forward to the next step are restricted to those where the photon polarisation is in the region of relatively high polarisation, within 200 MeV below the coherent peak setting. All of these procedures are described in detail in the remainder of this section.

4.2.1 Initial Event Filter

After the data were calibrated and cooked, a selection of runs based on quality control criteria was produced. These “golden” runs are those which the g8b group have flagged as being of sufficient quality (such as stable run conditions during data taking and the effectiveness of applied calibrations). The full list is given in Appendix B. For the g8b run a fairly loose trigger condition was used during data acquisition, which accepted a variety of particle events that could be used in multiple proposed analyses. The trigger was configured so that an event was recorded when there was coincidence of a signal in the start counter and a TOF counter in the same sector. The end result of this was a data set of 11,475 files totalling ~ 25 TBytes of disk space, of which $K_S^0 \Sigma^+$ events contribute only a small percentage. This data was stored on the JLab tape silo and simply retrieving it in its original form for analysis would not only use up a large amount of disk space but would also be very time consuming. Instead the dataset was skimmed using

the ROOTBEER software package [65], into Data Summary Tapes (DSTs) that contained two or more charged particles. Since the final state of interest contains three charged particles, this initial skim removes many events which are not relevant to the analysis.

4.2.2 Coherent Peak Selection

During data taking at CLAS, the diamond radiator is positioned to create a photon beam in one of five “coherent peak” positions, with peak positions ranging from 1.3 to 2.1 GeV. This analysis was carried out using all five coherent peak positions, with a cut applied to restrict the data to the photon energy ranges corresponding to each of these settings. The most highly polarised photons for each setting are found in a 200 MeV wide bin with an upper limit at the coherent edge position and therefore events are restricted to those with photon energy in those ranges. The 200 MeV band is the optimum region for consistency of the polarisation value, as demonstrated by the study described in [46]. The nominal bins are defined in Table 4.1. More information on the photon beam polarisation is given in Section 2.2.

Detailed studies of the relationship between polarisation degree and photon energy for each of the coherent peak settings has been performed in [66]. The study produced “polarisation tables” which provided the facility for future analyses (this work included) to simply look up the polarisation degree for a given photon energy and coherent peak setting. A further study [67] found that a small correction to the polarisation values was required. Using high statistics from the reaction $\gamma p \rightarrow p \pi^0$ the photon asymmetry Σ was measured for each tagger energy bin. It was shown that a small systematic correction should be applied to the photon polarisation value obtained from the lookup tables based on the difference between the photon energy and the coherent edge energy. A function to modify the polarisation has been included in this analysis. In order to estimate the systematic uncertainty introduced by this method, the application of the method to the measurement of Σ for $\gamma p \rightarrow p \pi^0$ and $\gamma n \rightarrow \pi^+ n$ is discussed in a CLAS Analysis note [68]. From this study the estimated systematic error on the beam polarisation is 4% for the 1.3, 1.5, 1.7, 1.9 GeV coherent peak settings, and this is borne out by the good agreement between the measured photon asymmetries and previously published data. At 2.1 GeV where the fits to the data were less consistent the systematic error is estimated to be 6%. The results were further validated for $\gamma p \rightarrow K^+ \Lambda$ and $\gamma p \rightarrow K^+ \Sigma^0$ by comparing photon asymmetries in the overlap regions between adjacent coherent peak settings. This study is described in detail in [46].

Setting Label	Photon Energy Range (GeV)	
	Lower Limit	Upper Limit
1300	1.1	1.3
1500	1.3	1.5
1700	1.5	1.7
1900	1.7	1.9
2100	1.9	2.1

Table 4.1: The definition of the nominal coherent peak settings.

4.2.3 Particle Identification

Hit Multiplicity and TOF Mass Cuts

The filtering process initially required a loose determination of the reaction products that identify the $K_S^0 \Sigma^+$ final state particles. The efficiency of CLAS for detecting photons from the decay of the π^0 is low, so although the possibility of one or two photons being in the data was retained it was not explicitly required for the identification of the reaction channel.

The first step in the filtering was to select only events where 3 or 4 particles were recorded in CLAS along with a valid tagger hit. Once an event had satisfied these criteria an initial identification of the particles was made using the mass calculated from the drift chambers and time-of-flight system (TOF mass). The following criteria were used to make the initial identification taking the mass and charge from the EVNT bank in the cooked data:

- All particles of non-zero charge must have a valid track in the drift chamber (consisting of hits in 5 out of the 6 superlayers) and a valid hit in the time-of-flight detector
- Particles with positive charge and $0.49 < M^2 < 1.44 \text{ GeV}^2/c^4$ were identified as protons
- Particles with positive charge and $0.0 < M^2 < 0.09 \text{ GeV}^2/c^4$ were identified as π^+
- Particles with negative charge and $0.0 < M^2 < 0.09 \text{ GeV}^2/c^4$ were identified as π^-

Events were then retained which contained exactly 1 proton, 1 π^+ , 1 π^- , and 0 or 1 neutral particles.

In addition, the events were limited to ones where the reaction has taken place within the target. The centre of the CLAS detector is at $z = 0.0 \text{ cm}$ and for this experiment the target cell was 40.0 cm long, situated slightly upstream from the detector centre. The vertex z coordinate was therefore limited to $-40.0 \text{ cm} < v_z < 0.0 \text{ cm}$.

Figure 4.3 shows (relativistic) β ($=v/c$) versus momentum for positively and negatively charged particles, along with the hit multiplicity for events which satisfy the initial selection criteria. The plots shown are for events where the coherent edge was 1.5 GeV. Similar results have been obtained using different coherent edges. It can be seen from the β - momentum plots that the mass cuts are wide enough to ensure that no good protons or pions are discarded. The vast majority of events have multiplicity 3, that is, no neutral particle detected.

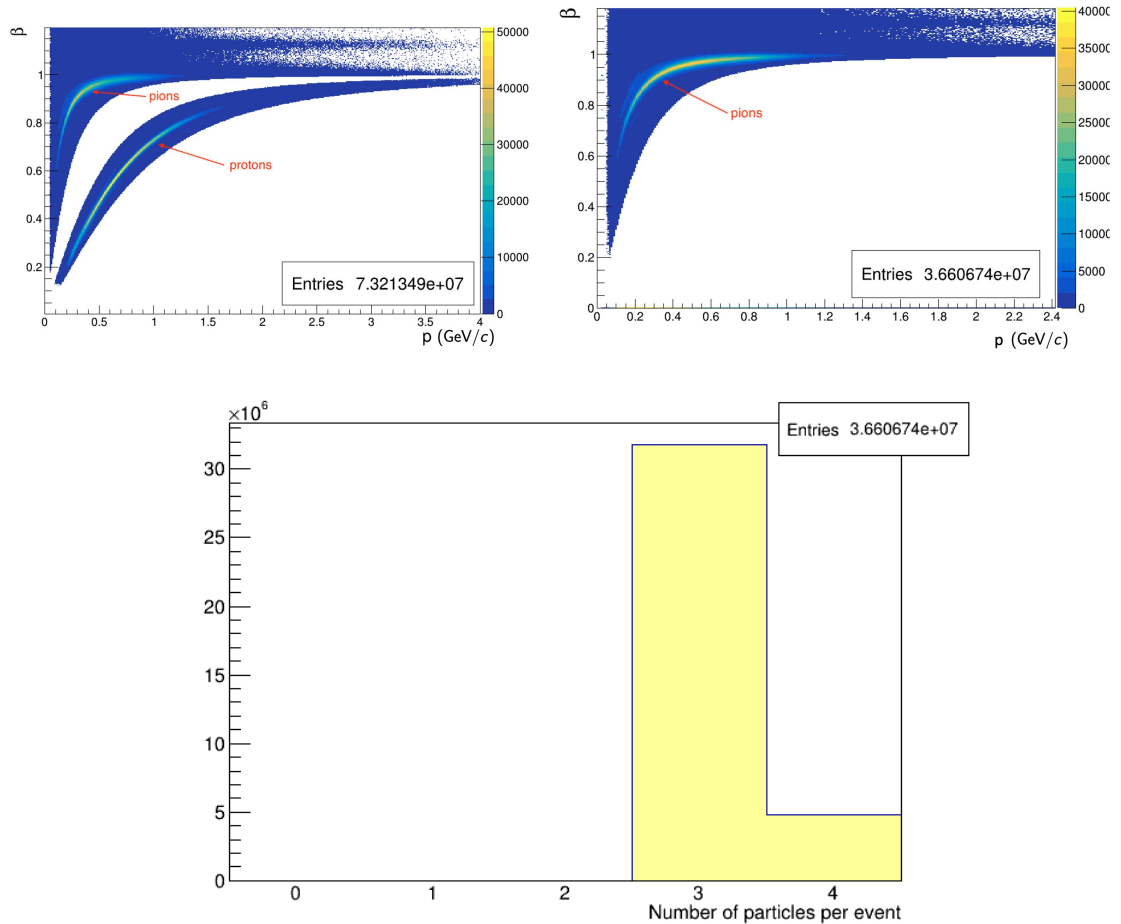


Figure 4.3: β vs momentum for positive particles (top left) and negative particles (top right) after event selection based on number of particles and the mass calculated from the time-of-flight system. The hard lines correspond to the invariant mass cuts and have sufficient breadth around the proton and pion events to ensure minimal good events are discarded. The multiplicity of hits (bottom) shows that only 3 or 4 particle events are retained at this stage. The plots shown are for events where the coherent edge was 1.5 GeV.

Z-Vertex Cut

A necessary step in the event selection is to cut on the z-vertex distribution of each particle to be within the target geometry. The z-vertex is provided by the experiment reconstruction procedure by reconstructing the drift chamber track back to the target, and taking the z-coordinate of the point of closest approach to the beamline. For g8b the target z position was in the range $(-40, 0)$ cm. Events with z-vertex outside this range were therefore excluded. Figure 4.4 shows the z-vertex distributions for all positive particles following the initial skim, and the distribution for particles identified as protons following the mass cut described in the previous section and the z-vertex cut.

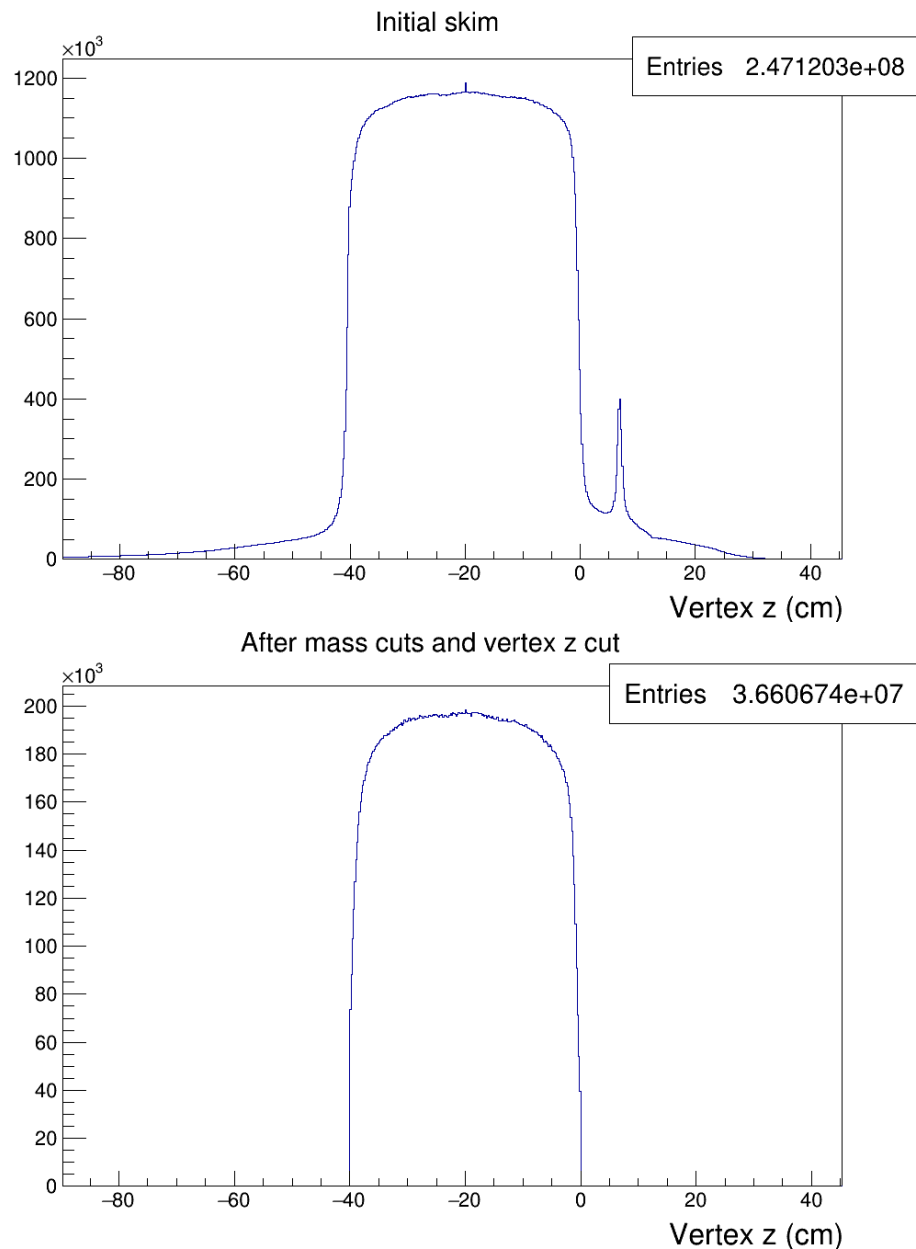


Figure 4.4: z -vertex distributions of the positive particles following initial skim (top) and with the applied cuts (bottom). The peak at 7cm in the top plot comes from events occurring in the foil downstream of the target window. The plots shown are for events where the coherent edge was 1.5 GeV.

Photon Selection

The next stage in the selection process was to determine the time at which a physics event took place by matching photons to the hadronic tracks within CLAS. To achieve this, information on the hadronic vertex time provided by the TOF was used. The timing information from charged particles detected by the TOF was extrapolated backwards to provide information on when the

event occurred. If the TOF and tagger timing calibrations are well defined then the tagger and TOF vertex times are expected to be identical. This is shown to be the case in Figure 4.5 (top) where the majority of events have the vertex timing difference between tagger and TOF centered on zero. The 2 ns beam bucket structure corresponds to hadrons that have been miscorrelated with random photons. A major area of ambiguity in the selection of the real interaction photons is that for many physics events there are multiple photons recorded. In order to select the actual photon corresponding to the event, the photon whose time is closest to the hadronic vertex time is chosen. The identification of this “best” photon is obtained by minimizing the difference between the proton vertex time and the photon vertex time. The proton vertex time is calculated by adjusting the time of the proton hitting the TOF detector by the time to travel the path from the vertex position to the hit position on the TOF detector:

$$vt_{proton} = t_{TOF} - \frac{d_{TOF}}{c \times \beta} \quad (4.4)$$

The proton β is calculated using the PDG mass for the proton and the measured momentum (taken from the EVNT bank in the cooked data):

$$\beta = \frac{P_p}{\sqrt{P_p^2 + m_{pdg}^2}} \quad (4.5)$$

The photon vertex time is calculated from the event photon time at the centre of the target adjusted by the time to the reaction vertex:

$$vt_{\gamma} = t_{\gamma} + \frac{z}{c} \quad (4.6)$$

The quantities used in the above calculations are defined as:

- t_{TOF} = proton TOF hit time
- d_{TOF} = proton path length from event vertex to the TOF detector
- t_{γ} = event photon vertex time to center of target
- z = z -vertex position of the proton
- c = speed of light

Figure 4.5 (middle) shows the timing difference after the selection of the best photons using the process outlined above. The plots show a slight asymmetry in the distribution which is due to the proton vertex time having a momentum dependence.

Once the “best photon” of the event has been identified a cut is applied to restrict the timing difference to be no more than ± 1 ns. There may be events where more than one photon meets the 1 ns timing difference criteria. Should the best photon be wrongly identified in this case, the

event will be removed during signal background separation. The resulting vertex time difference distribution is shown in Figure 4.5 (bottom).

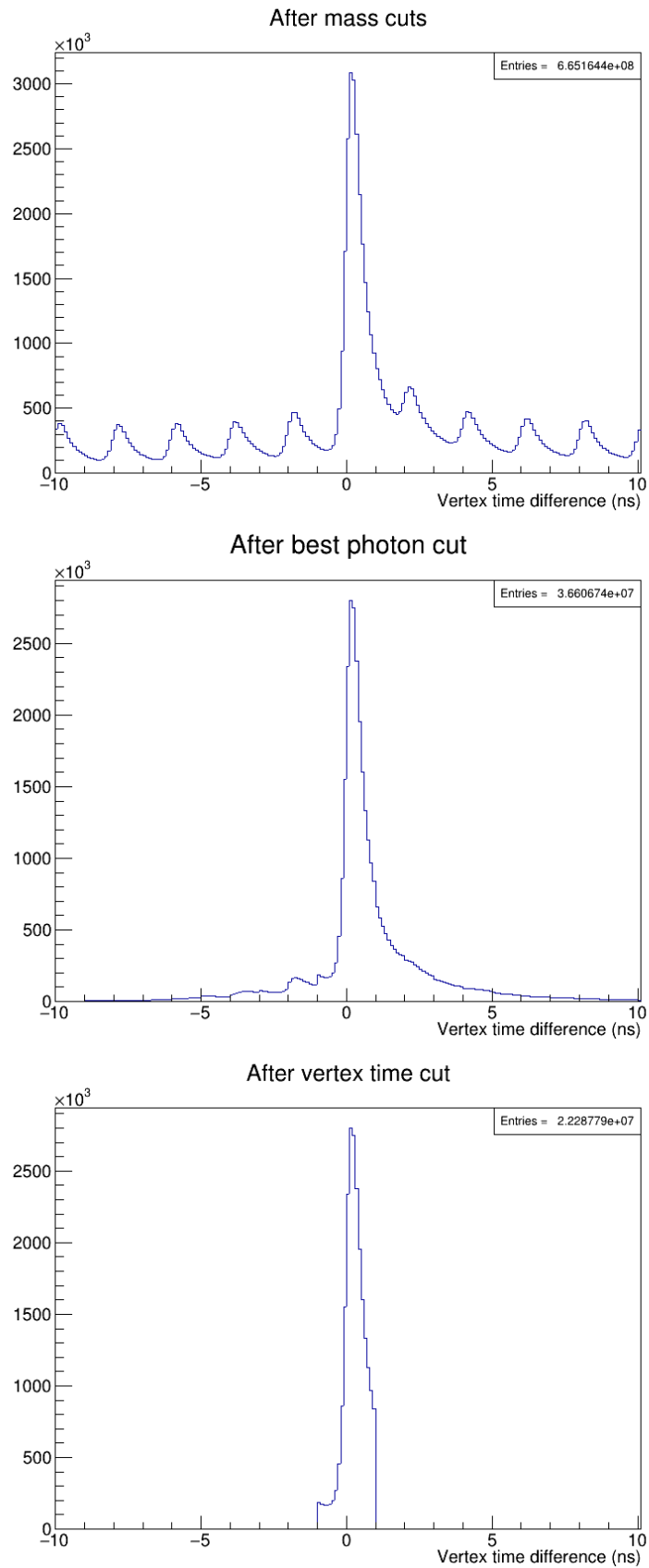


Figure 4.5: Tagger vertex time subtracted from the time-of-flight vertex time before best photon selection with the 2 ns beam bucket structure clearly evident (top) and after photon selection (middle). The bottom plot shows the effect of the ± 1 ns cut on the time difference. The plots shown are for events where the coherent edge was 1.5 GeV

Polarisation

Only events where the photon identified as “best” photon has a valid entry in the polarisation tables are retained. This means that there is a measurement of the polarisation degree of a photon of that energy. As mentioned previously, only events with photon energies within 200 MeV below the coherent peak setting are retained. More details on the polarised photon beam are given in Section 4.2.2 and specifically the method for generating the polarisation tables is described in [66].

Energy Loss Corrections

The reconstruction algorithms for the g8b experiment calculate the energy and momenta at the position where the particle is detected. However, as the particles move through the material of the detector they will lose energy. In order to use values for energy and momentum which are as close as possible to the values at the reaction vertex, energy losses in the target and surrounding material were calculated using the ELOSS package [69]. The ELOSS package was developed as an add-on to the g8b reconstruction algorithms and takes the 4-vector of the particle of interest, derives the path length in each section of the detector and thus determines the energy loss. The energy and momentum can then be corrected to match the corresponding values at the reaction vertex.

The energy loss dependence on momentum for each of the detected particles is shown in Figure 4.6. As can be seen, the energy losses are larger for higher mass particles, resulting in the greatest correction required. The trajectories away from the bulk of the data represent a small number of misidentified particles. These will be removed during signal background separation.

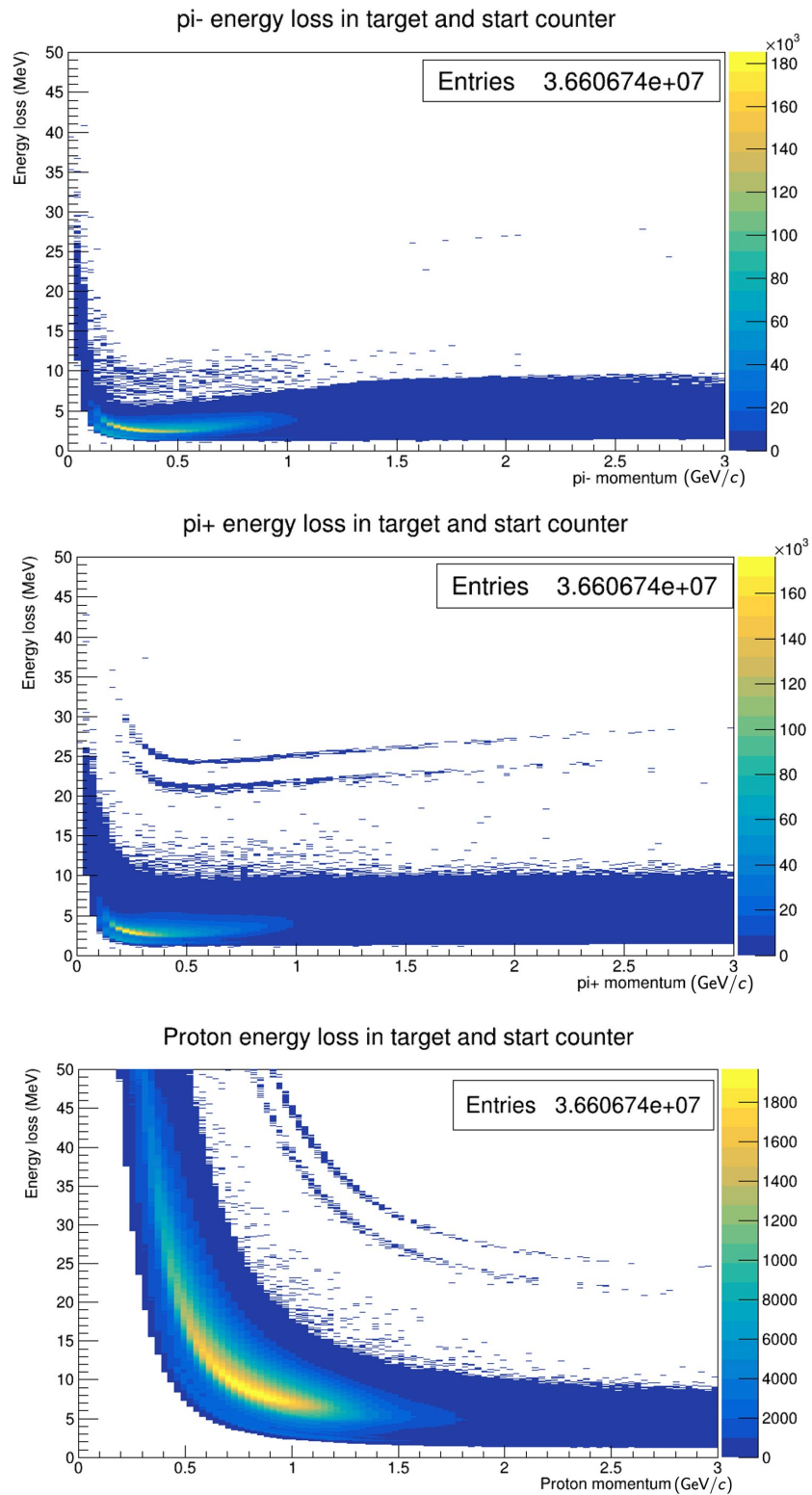


Figure 4.6: Total energy loss in target and start counter vs. momentum for the π^- (top), π^+ (middle) and proton (bottom). The trajectories away from the bulk of the data represent a small number of misidentified particles.

4.2.4 Channel ID

After the application of the particle identification procedure described, we must now ensure that the invariant masses reconstruct the intermediate particles in the channel of interest, $\vec{\gamma}p \rightarrow K_S^0 \Sigma^+ \rightarrow p \pi^+ \pi^- \pi^0$. In the case of the π^0 and Σ^+ particles, the missing mass 4-vector corresponding to each particle is constructed using knowledge of the total reaction 4-vector (photon and proton) and the measured 4-vectors for the other final state particles. The following invariant mass restrictions are placed on the reconstructed particles:

- π^0 mass: $0.05 \text{ GeV}/c^2 < \text{Missing mass } (p \pi^+ \pi^-) < 0.22 \text{ GeV}/c^2$
- K^0 mass: $0.450 \text{ GeV}/c^2 < \text{Mass } (\pi^+ \pi^-) < 0.550 \text{ GeV}/c^2$
- Σ^+ mass: $1.150 \text{ GeV}/c^2 < \text{Missing mass } (\pi^+ \pi^-) < 1.250 \text{ GeV}/c^2$

We can then place these loose cuts around the invariant masses or missing masses and proceed with the signal and background separation using sPlots as described in Section 4.3.

Figure 4.7 shows Missing mass $(\pi^+ \pi^-)$ versus Mass $(\pi^+ \pi^-)$ at each stage of the invariant mass cuts. In the top plot, the π^0 mass cut is not yet made, and events where there is no π^0 dominate. For these events Missing mass $(p \pi^+ \pi^-)$ is zero, and Missing mass $(\pi^+ \pi^-)$ is therefore at the proton mass. After cutting these events (bottom), the events of interest are evident at Mass $(\pi^+ \pi^-)$ around the kaon mass and Missing mass $(\pi^+ \pi^-)$ around the Σ^+ mass. The white rectangle shows the extent of the cut around the kaon mass and the hyperon mass, the final cut for this stage. Only the events within the white rectangle are retained and used for the next steps of the analysis.

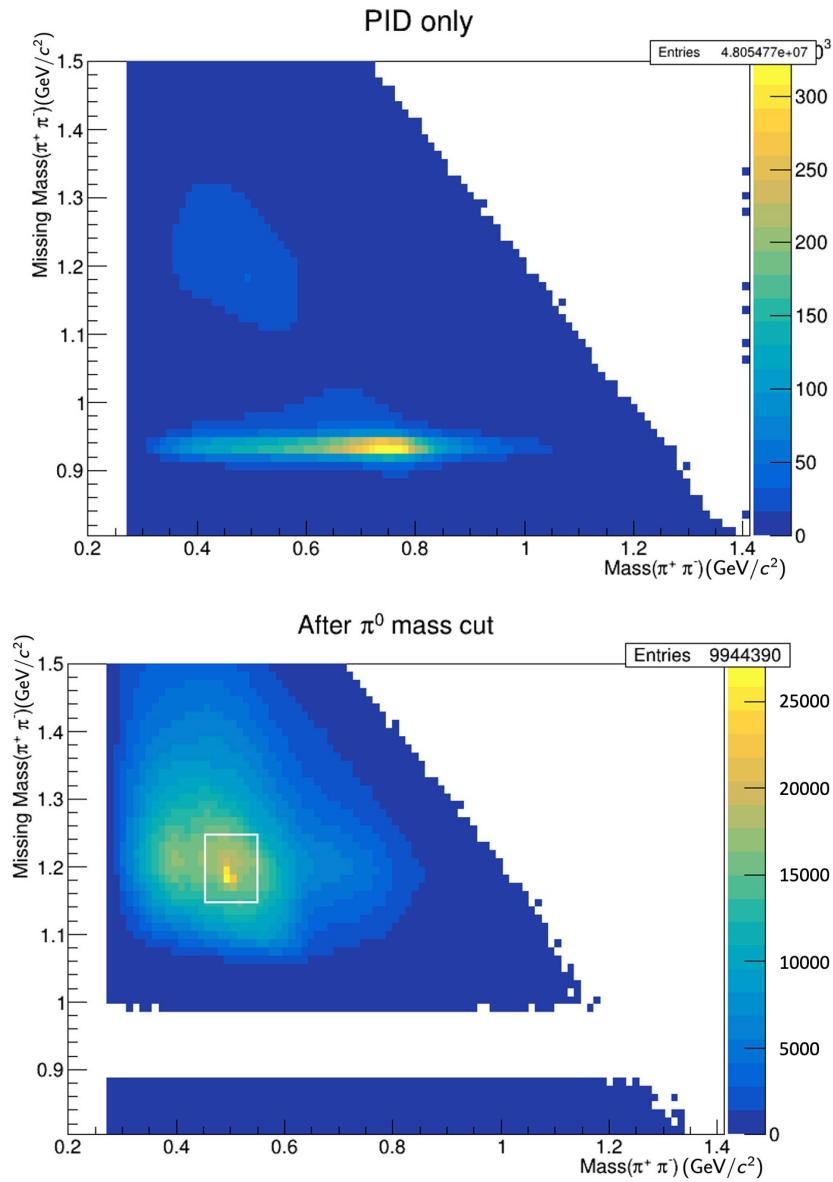


Figure 4.7: Missing mass ($\pi^+ \pi^-$) versus Mass ($\pi^+ \pi^-$) at each stage of the invariant mass cuts. Top: after particle ID only. Bottom: after cut around π^0 mass, white rectangle shows extent of cut around kaon and hyperon masses. Only the events within the white rectangle are retained and used for the next steps of the analysis.

4.2.5 Summary

Applied Cut	Details	# of Events
Initial skim	3 charged particles, optional neutral particle in final state	6.04×10^8
z-vertex cut, proton and pion mass cuts	$-40 < z < 0$ cm $0.49 < M^2(p) < 1.44 \text{ GeV}^2/c^4$ $M^2(\pi^{+/-}) < 0.09 \text{ GeV}^2/c^4$	2.44×10^8
γp vertex timing	$ \text{Vertex time}(\text{best photon}) - \text{Vertex time}(\text{proton}) < 1.0$ ns	1.48×10^8
Polarisation	Entry exists in polarisation tables	5.06×10^7
Mass cuts	π^0 mass (GeV/c^2) $\in (0.05, 0.22)$ K^0 mass (GeV/c^2) $\in (0.45, 0.55)$ Σ^+ mass (GeV/c^2) $\in (1.15, 1.25)$	1.15×10^6

Table 4.2: Analysis cuts applied and resulting number of events for all coherent peak settings.

An analysis algorithm was developed to allow for the identification of the particles of interest and the extraction of final yields for $\vec{\gamma}p \rightarrow K^0 \Sigma^+$. Initial filters based on simple TOF mass cuts were used to skim the dataset down to a manageable size for full analysis. A minimal set of cuts were then implemented to reduce the background and correctly identify the detected final state particles, without discarding too many good events.

4.3 Signal/Background Separation with sPlots

This section describes the process to separate the distributions into contributions from the signal (i.e. events arising from the reaction of interest) and the background. The sPlots technique described in Section 3.1.1 is used to assign weights to each event. In order to use the technique, one or more discriminatory variable must be chosen which differentiates signal events from background events. In this analysis, two discriminatory variables are chosen: the π^0 mass (reconstructed from the missing mass of $p \pi^+ \pi^-$) and the K^0 mass (reconstructed from the mass of $\pi^+ \pi^-$). Weights are first obtained from the π^0 fit and used to plot a weighted K^0 mass distribution. The weights obtained from this second fit are used to weight events in the later stages of the analysis. The resulting total number of signal weighted events is approximately 24,000.

4.3.1 Binning

In choosing the binning system, there are two aims that must be borne in mind. First, we wish to maximise the number of bins so that the number of data points we may provide to theoretical models is as large as possible. However, we must also ensure that there are enough events per bin to allow successful fitting of the data. Following studies where the bin size was varied, we concluded that the fit could consistently succeed with approximately 1000 signal weighted events. Therefore, the bins in E_γ and $\cos \theta$ of the kaon in the centre-of-mass system were chosen such that the integrated signal weight in each bin was approximately 1000 weighted events, allowing for some variation in E_γ without comprising the number of $\cos \theta$ bins to show the angular dependence. With 4 uniform bins in E_γ and variable bins in $\cos \theta$, we can obtain 21 bins as shown in Figure 4.8.

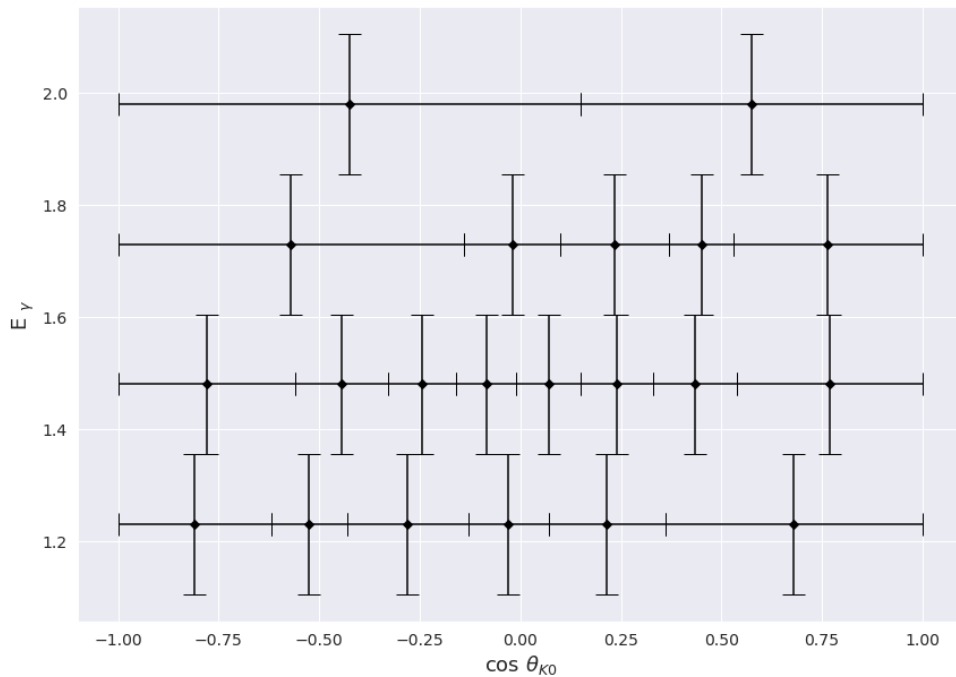


Figure 4.8: Binning system used throughout this analysis.

4.3.2 Signal and Background Shapes

In each bin, the distribution is modelled as a Gaussian peak on a Chebyshev polynomial background. The Chebyshev polynomials are chosen to give a simple polynomial background shape whilst improving the performance of the fit convergence. Since a Chebyshev polynomial is limited to the interval $[-1,1]$, the coefficients cannot vary greatly and are more easily handled by the fit.

The Chebyshev polynomials used for the background fit are defined as

$$1 + \sum_{i=1}^n a_i T_i(x) \quad (4.7)$$

Up to order 2, the $T_i(x)$ are defined as

$$T_0(x) = 1; T_1(x) = x; T_2(x) = 2x^2 - 1 \quad (4.8)$$

More details can be found in [70].

4.3.3 Extraction of Weights

Weights were obtained from fits to the π^0 mass (reconstructed from the missing mass of $p \pi^+ \pi^-$) modelled as a Gaussian peak on a quadratic Chebyshev polynomial background. A representative selection of the fits for 6 $\cos \theta_{K_0}$ bins for $E_\gamma = 1.23$ GeV are shown in Figures 4.9 and 4.10.

Using the weights obtained from the π^0 mass, the weighted K^0 mass (reconstructed from the mass of $\pi^+ \pi^-$) is modelled as a Gaussian peak on a linear Chebyshev polynomial background. The fits obtained are shown in Figures 4.11 and 4.12 for the 6 $\cos \theta_{K_0}$ bins for $E_\gamma = 1.23$ GeV.

In each of these subplots, the left plot shows data points in black, combined signal and background model in solid red, signal in dotted black, and background in dotted red. Top right and bottom right are the residual and the pull respectively.

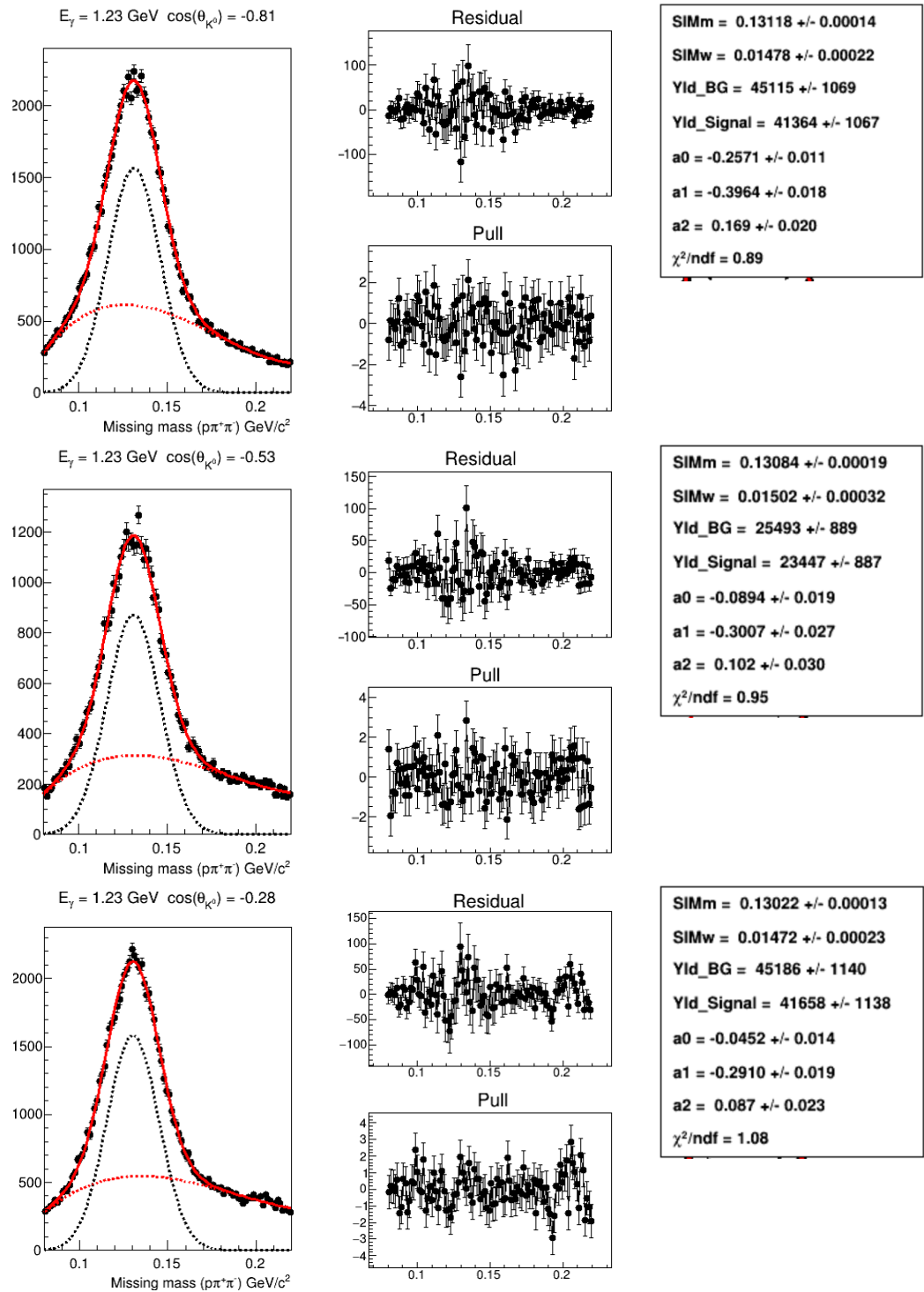


Figure 4.9: π^0 mass fits for E_γ bin 1.23 GeV, $\cos \theta_{K^0}$ bins -0.81, -0.53 and -0.28. The fit parameters are the signal gaussian mean and width (SIMm and SIMw), the signal and background yield (Yld_Signal and Yld_BG), and the background function parameters.

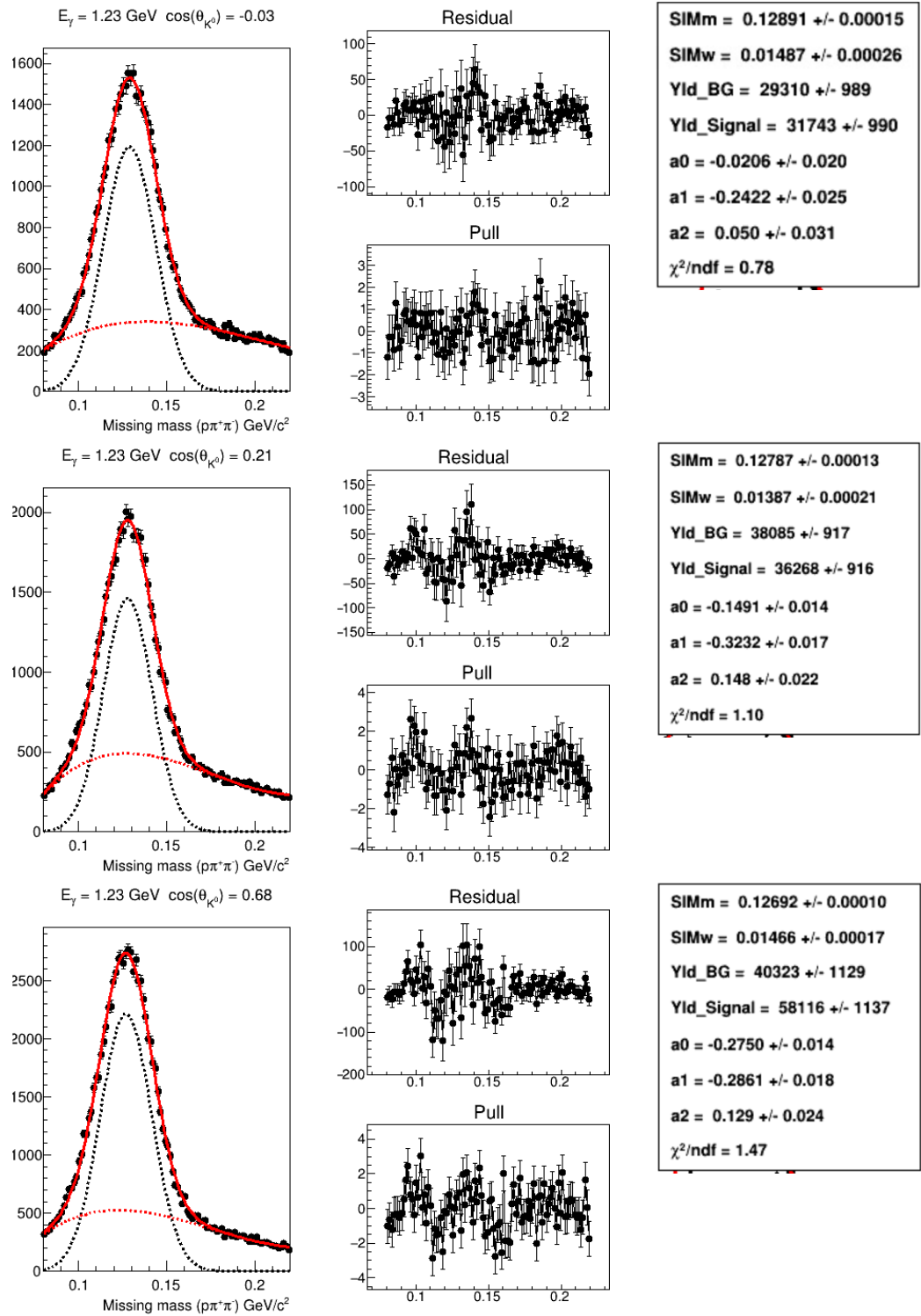


Figure 4.10: π^0 mass fits for E_γ bin 1.23 GeV, $\cos \theta_{K^0}$ bins -0.03, 0.21 and 0.68. The fit parameters are the signal gaussian mean and width (SIMm and SIMw), the signal and background yield (Yld_Signal and Yld_BG), and the background function parameters.

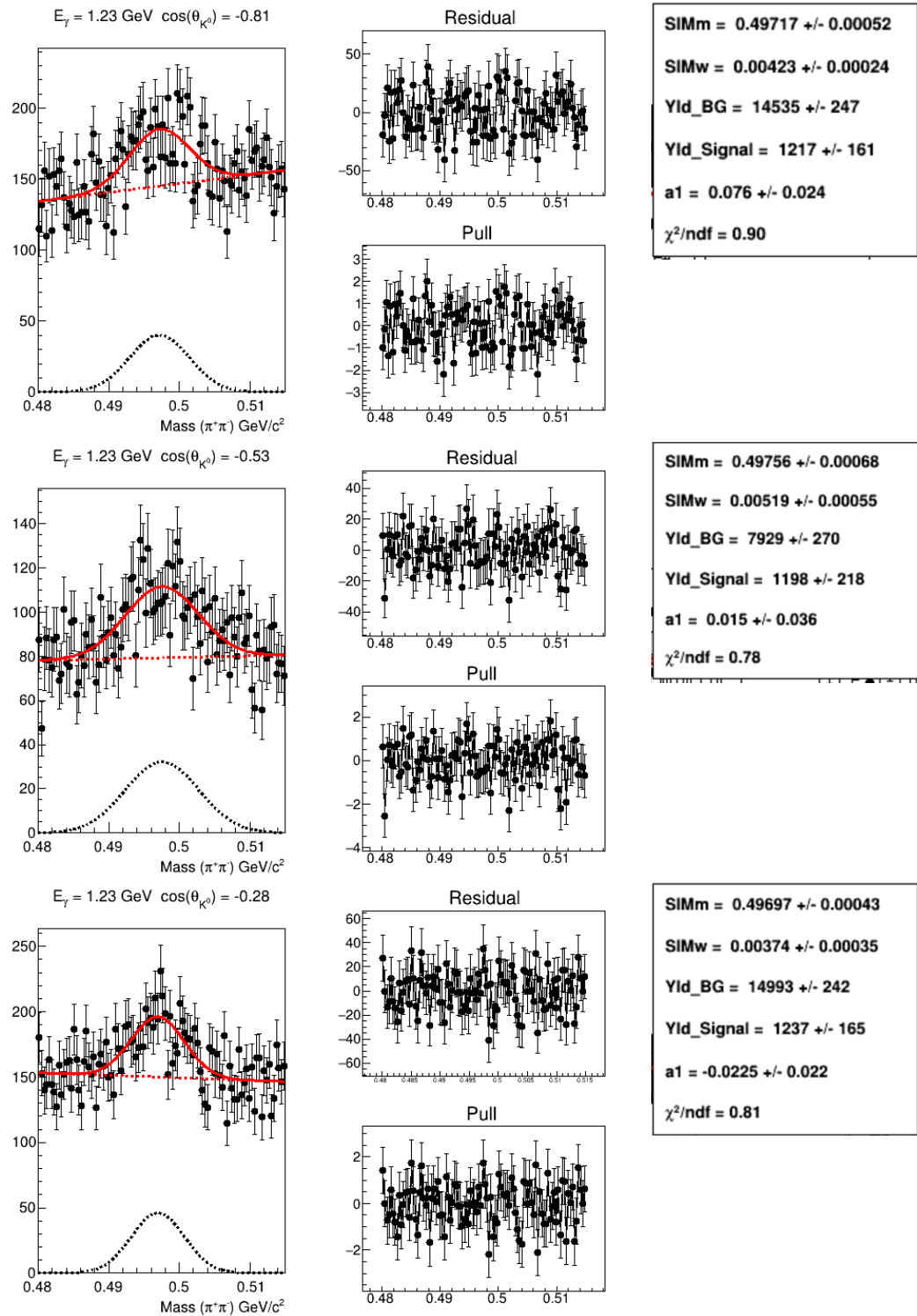


Figure 4.11: K^0 mass fits for E_γ bin 1.23 GeV, $\cos\theta_{K^0}$ bins -0.81, -0.53 and -0.28. The fit parameters are the signal gaussian mean and width (SIMm and SIMw), the signal and background yield (Yld_Signal and Yld_BG), and the background function parameter.

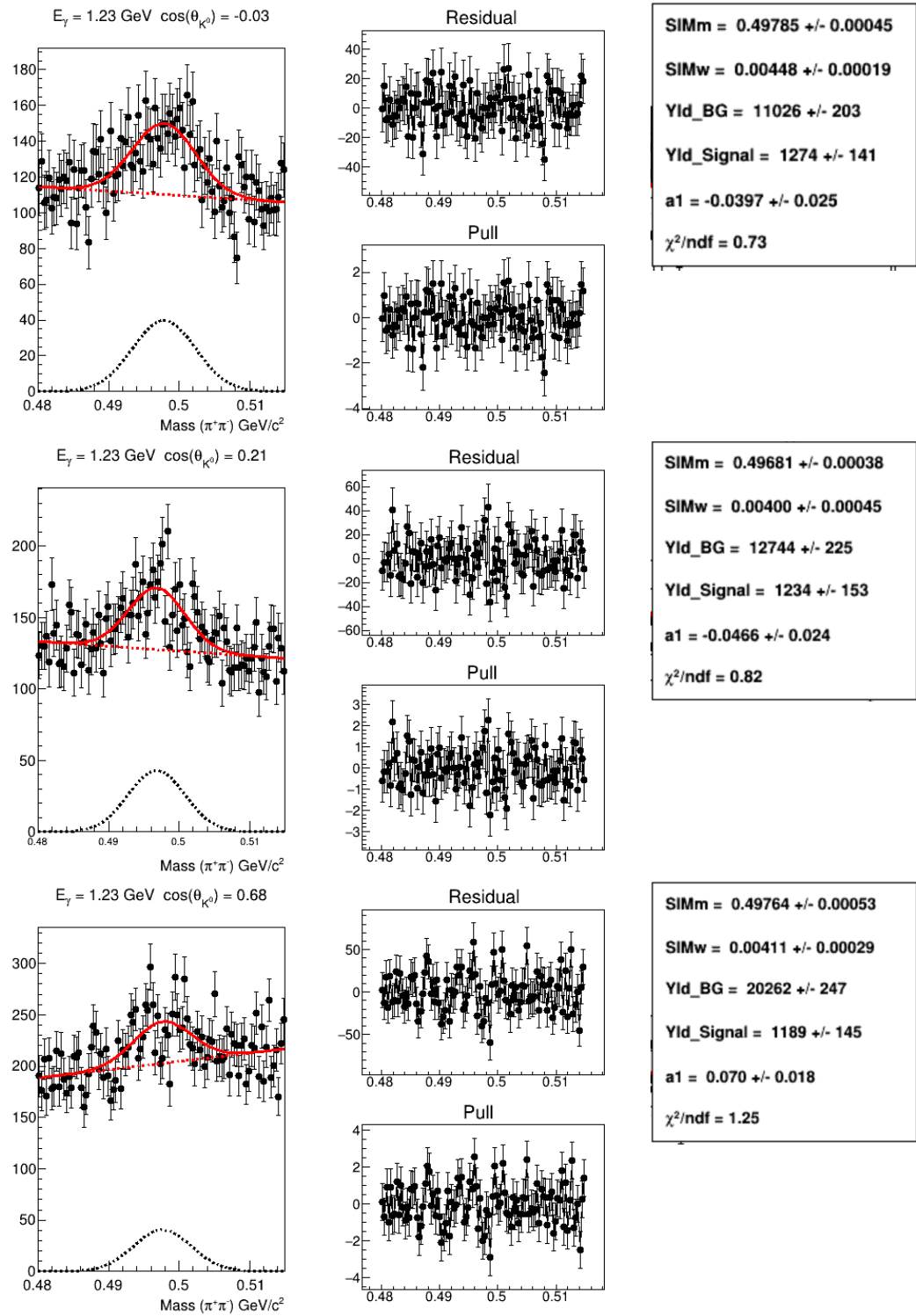
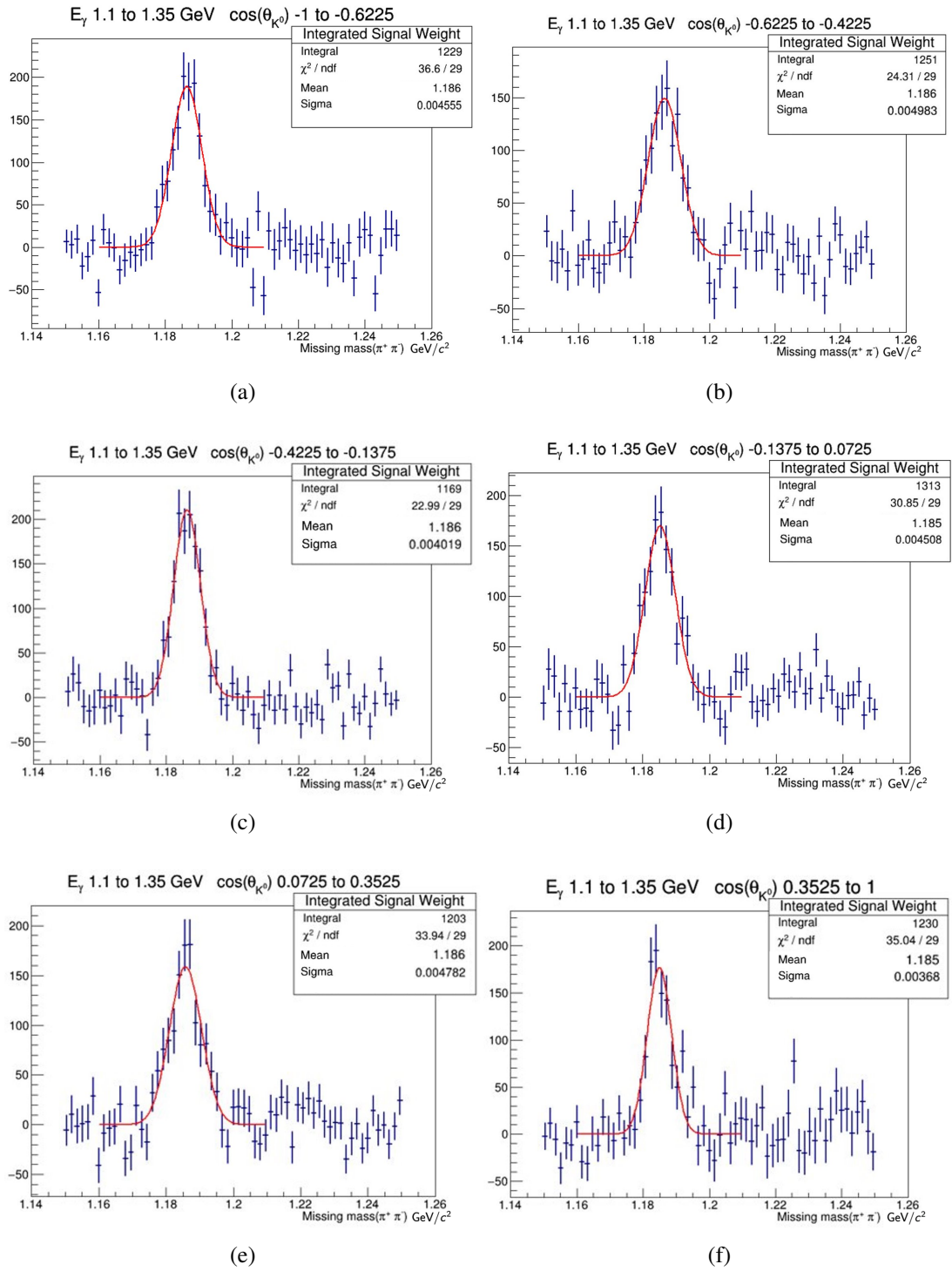


Figure 4.12: K^0 mass fits for E_γ bin 1.23 GeV, $\cos\theta_{K^0}$ bins -0.03, 0.22 and 0.68. The fit parameters are the signal gaussian mean and width (SIMm and SIMw), the signal and background yield (Yld_Signal and Yld_BG), and the background function parameter.

4.3.4 Weighted Mass Distributions

The missing mass of $(\pi^+\pi^-)$, i.e. the reconstructed Σ^+ mass, for signal weighted events peaks around the expected mass of the Σ^+ , 1189 MeV/ c^2 . Figure 4.13 shows the missing mass distributions for the 6 bins at $E_\gamma = 1.23$ GeV. The mass distributions have been fitted with a gaussian to estimate the peak of the distribution. The value for this peak across all bins varies from 1185 to 1188 MeV, within 0.3% of the PDG value.

Also of interest, from the background weighted distribution for the 3 pion mass, shown in Figure 4.14 it is evident that events resulting from ω decay form a significant part of the background.


 Figure 4.13: Missing mass ($\pi^+\pi^-$) for E_γ bin 1.23 GeV.

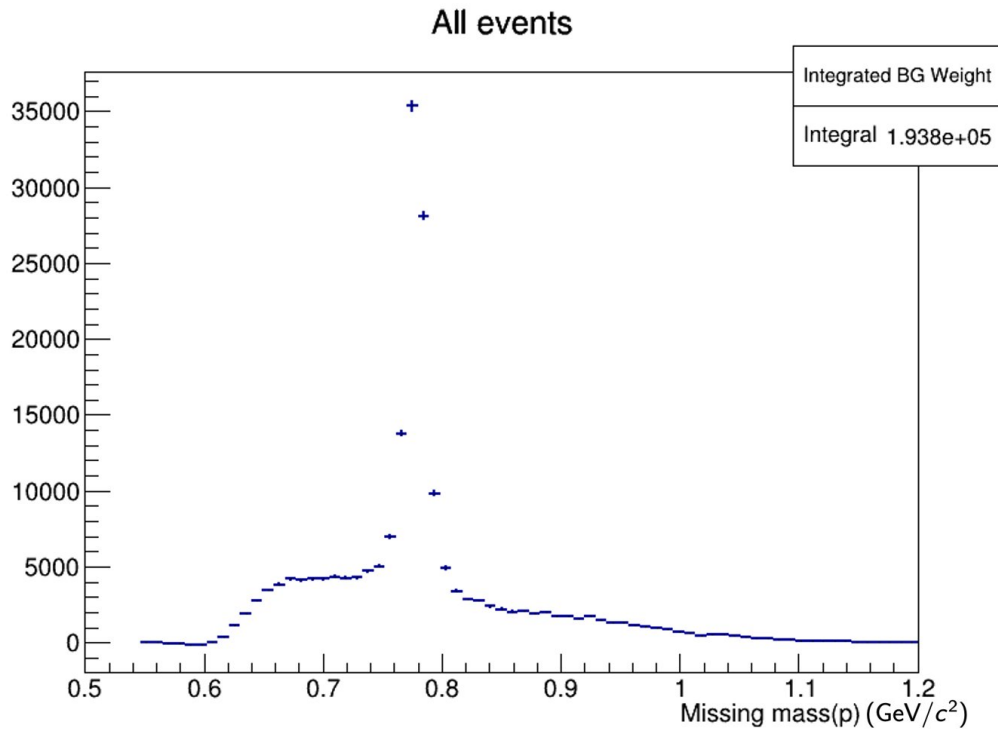


Figure 4.14: Mass ($\pi^+ \pi^- \pi^0$) for all events, background weights applied. The ω peak is visible at $782 \text{ MeV}/c^2$.

4.3.5 Summary

Weights have been extracted using the sPlots technique using the particle masses as discriminatory variables. The weights obtained will be used to create the angular distributions used in the next steps to extract the polarisation observables.

4.4 Simulation

The previous sections have described a method to identify the signal events with a view to examining the dependence of the angular distribution of these events on the polarisation observables. However, the detector acceptance will also affect the angular distributions. In order to account for this, events were generated for the signal reaction and passed through the detector simulation to create a set of simulated events to use in the next step of the analysis. Events were generated in “phase space” for the reaction, creating random events which could arise from the proton target and the given photon energy range.

4.4.1 Event Generation

The “EdGen” software [71] is an event generator which utilises the ROOT (root.cern.ch) phase space generator to generate events for a specified reaction or series of reactions. This was used to generate 4×10^6 events for a uniform distribution of $E_\gamma \in (1.1, 2.1)$ GeV. It is important to have more simulated data than measured data so that the dominant cause of statistical uncertainty comes from the measured data. The mean lifetime of the K^0 and the Σ^+ were supplied to the generator so that detached vertices were created by the generator. The reactions and mean lifetimes were defined as shown in Table 4.3.

Vertex	Mean Lifetime, τ	$c\tau$	Decay products
γp	n/a	n/a	$\Sigma^+ K_S^0$
Σ^+	8.018×10^{-11} s	2.404 cm	$p \pi^0$
K_S^0	8.954×10^{-11} s	2.684 cm	$\pi^+ \pi^-$

Table 4.3: Reaction vertices for event generation.

The simulation was weighted so that the random events generated in phase space were accepted or rejected based on a probability derived from the real distributions of E_γ and the transferred momentum, t , so that the simulated distributions in E_γ and t resembled those in the data. These are shown in Figure 4.15.

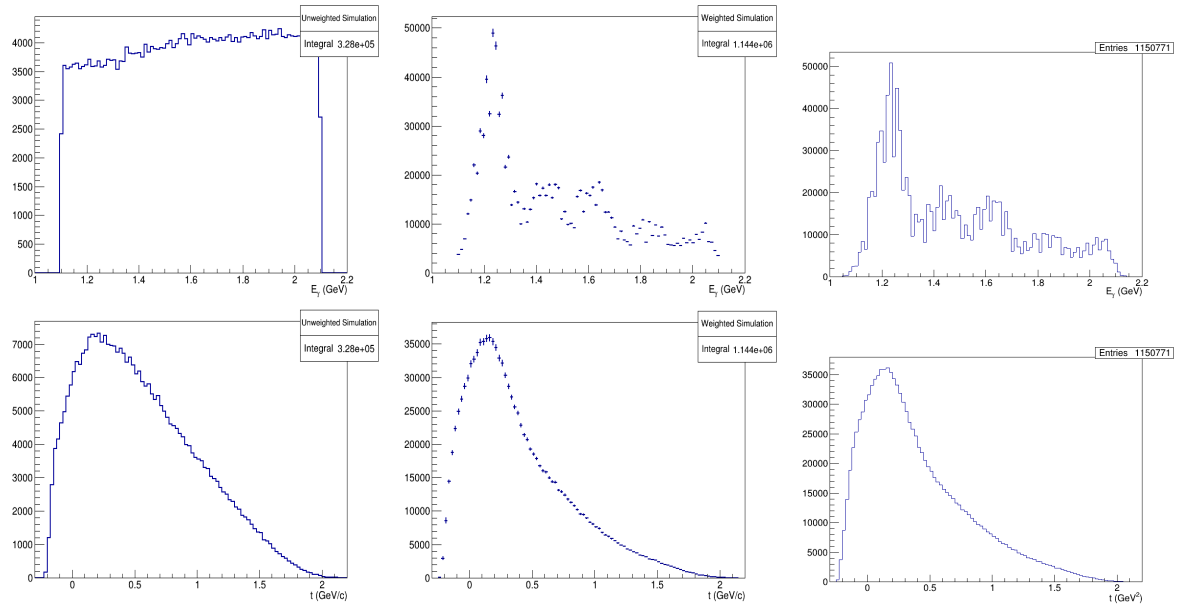


Figure 4.15: Distributions in E_γ (top row) and momentum transfer, t , (bottom row) showing from left to right, unweighted simulation, weighted simulation and data.

4.4.2 g8 Simulation and Reconstruction

The simulation and reconstruction developed for the g8 experimental run period was used to create files in the same format as the data files for the experimental data. The simulated data were run through the same final state particle ID and channel ID analysis process as was done for the real events, creating a set of simulated events for use in the extraction of observables.

4.5 Extracting Observables

This final step in the analysis process brings together the set of measured events identified as being the correct channel (described in Section 4.2), the derived signal weights (described in Section 4.3) and the set of simulated events (described in Section 4.4). The steps to derive the probability density functions for the polarisation observables using Markov-Chain Monte Carlo likelihood sampling are described and the results are presented.

4.5.1 Data Model

The coordinate system employed in this analysis is the so-called ‘‘unprimed’’ frame (the same as described in Section 4.1), where for a photon momentum \vec{k} and a kaon momentum \vec{q} , axes are defined such that

$$\hat{z}_{evt} = \frac{\vec{k}}{|\vec{k}|}; \quad \hat{y}_{evt} = \frac{\vec{k} \times \vec{q}}{|\vec{k} \times \vec{q}|}; \quad \hat{x}_{evt} = \hat{y}_{evt} \times \hat{z}_{evt}$$

In order to construct a likelihood function, one must provide a probabilistic model for what the data would be, given the model with its parameters set to specific values. The differential cross section for the reaction, assuming linear photon polarisation only and that recoil polarisation can be determined, reads

$$\begin{aligned} \frac{d\sigma}{d\Omega} \equiv \sigma(\phi, \cos \theta_x, \cos \theta_y, \cos \theta_z) = & \sigma_0 \{ 1 - P^\gamma \Sigma \cos 2\phi \\ & + \alpha \cos \theta_x P^\gamma O_x \sin 2\phi \\ & + \alpha \cos \theta_y P - \alpha \cos \theta_y P^\gamma T \cos 2\phi \\ & + \alpha \cos \theta_z P^\gamma O_z \sin 2\phi \}, \end{aligned} \quad (4.9)$$

where σ_0 represents the unpolarised cross-section, P^γ is the degree of linear photon polarisation, ϕ is the azimuthal angle between the scattering plane and the photon polarisation direction, α is the Σ^+ weak decay asymmetry and everything else is a polarisation observable. The variables $\cos \theta_x, \cos \theta_y, \cos \theta_z$ are the direction cosines of the decay proton in the Σ^+ rest frame.

4.5.2 Likelihood Sampling Using MCMC - Method

Likelihood sampling using Markov Chain Monte Carlo (MCMC) was performed in order to estimate the five parameters, that is, the five polarisation observables. A description of the general method is given in Section 3.1.2.

Construction of Observable Space

In order to study the complex scattering amplitudes describing the reaction, we must first choose a basis. Similar analyses to this work, and relevant theoretical models, commonly use the ‘‘he-

licity” basis or the “transversity” basis. A description of these can be found in [72]. In this work, in order to be consistent with other studies and models, the transversity basis is used. In the normalized transversity representation as defined in Vrancx [72], there are four complex amplitudes from which we can calculate the polarisation observables. We can therefore use an 8-dimensional parameter space (comprising the real and imaginary parts of the four complex amplitudes) for the MCMC chain, thereby ensuring we obtain physical values for the polarisation observables at each step in the chain.

For transversity amplitudes, a_i , with magnitudes, r_i , the polarisation observables are calculated as follows.

$$\Sigma = r_1^2 + r_2^2 - r_3^2 - r_4^2 \quad (4.10)$$

$$P = r_1^2 - r_2^2 - r_3^2 + r_4^2 \quad (4.11)$$

$$T = r_1^2 - r_2^2 + r_3^2 - r_4^2 \quad (4.12)$$

$$O_x = 2\text{Re}(a_1 a_4^* + a_2 a_3^*) \quad (4.13)$$

$$O_z = 2\text{Im}(a_1 a_4^* - a_2 a_3^*) \quad (4.14)$$

Before proposing the set of amplitudes for the chain, they are converted to normalized amplitudes so that the parameters represent values on an eight-dimensional unit hypersphere. That is,

$$\sum_i r_i^2 = \sum_i \left((\text{Re } a_i)^2 + (\text{Im } a_i)^2 \right) = 1 \quad (4.15)$$

Calculation of Likelihood

The likelihood that a given parameter set describes the data was calculated as described in Section 3.1.2. In the case of this analysis, the distribution is dependent on the measured values τ ($= \{P^\gamma, \phi, \theta_x, \theta_y, \theta_z\}$) and is described by the parameter set p ($= \{\Sigma, O_x, O_z, T, P\}$).

MCMC Time Series and Posterior Distributions

The MCMC sampling was performed until 2000 steps had been accepted in the chain. After a certain number of steps, no further improvement in precision is obtained and, following studies with higher numbers of steps included, 2000 steps was judged to be high enough to obtain the best possible precision. This number includes 50 burn-in steps which are excluded from the

posterior distributions. The time evolution of the MCMC steps is shown in Figure 4.16 for a typical bin, where we see that the distribution has settled around the mean value well before the 50 burn in steps have been generated. Figure 4.17 shows the time evolution of a typical bin with the burn-in steps excluded. The proposal acceptance fraction varied from 20% to 54% with most bins around 30 – 35%. The resulting probability density functions are shown in Figures 4.18 to 4.22 for each of the observables. In addition to this we can examine the correlation between observables in the corner plots shown in Figure 4.23. We observe that correlations arise due to certain physical constraints on the observables known as Fierz identities (see, for example, [72]). For example, in Figure 4.23c, the value for the recoil polarisation, P , is close to one, resulting in the correlation between the beam asymmetry, Σ , and the target polarisation, T . All three observables cannot be close to one, hence for higher values of Σ we must have correspondingly lower values of T and vice versa. The figures show the results for the $6 \cos \theta_{K^0}$ bins for E_γ bin 1.23 GeV.

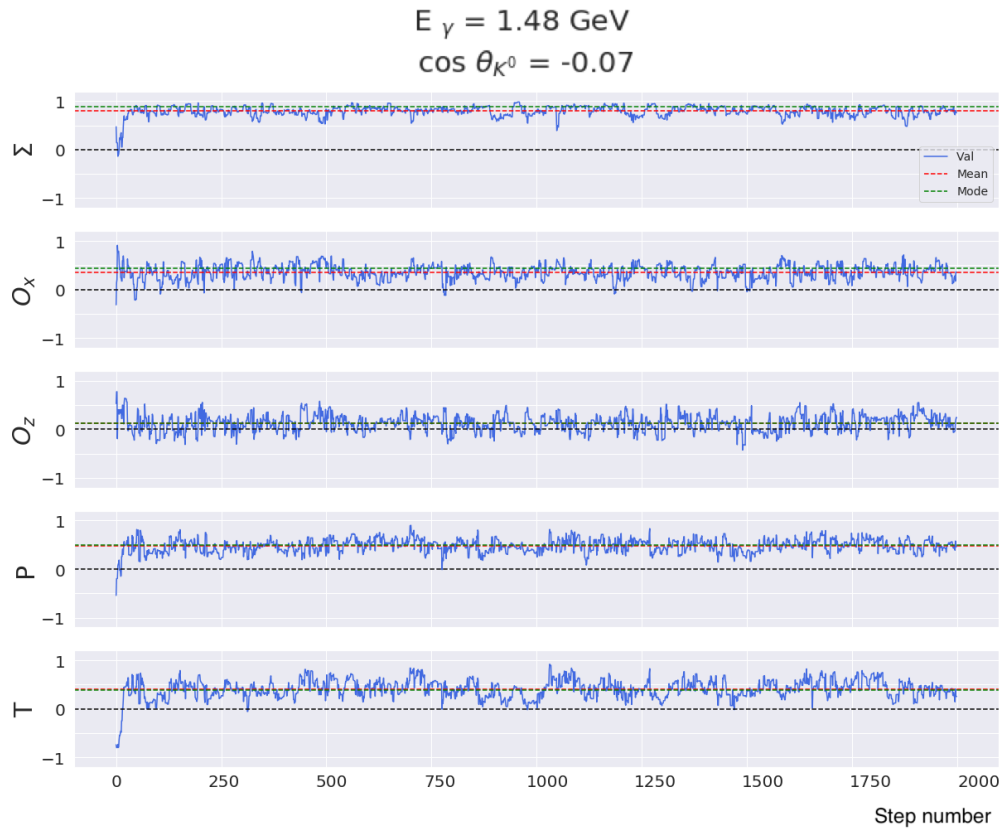


Figure 4.16: MCMC time series including the 50 burn-in steps

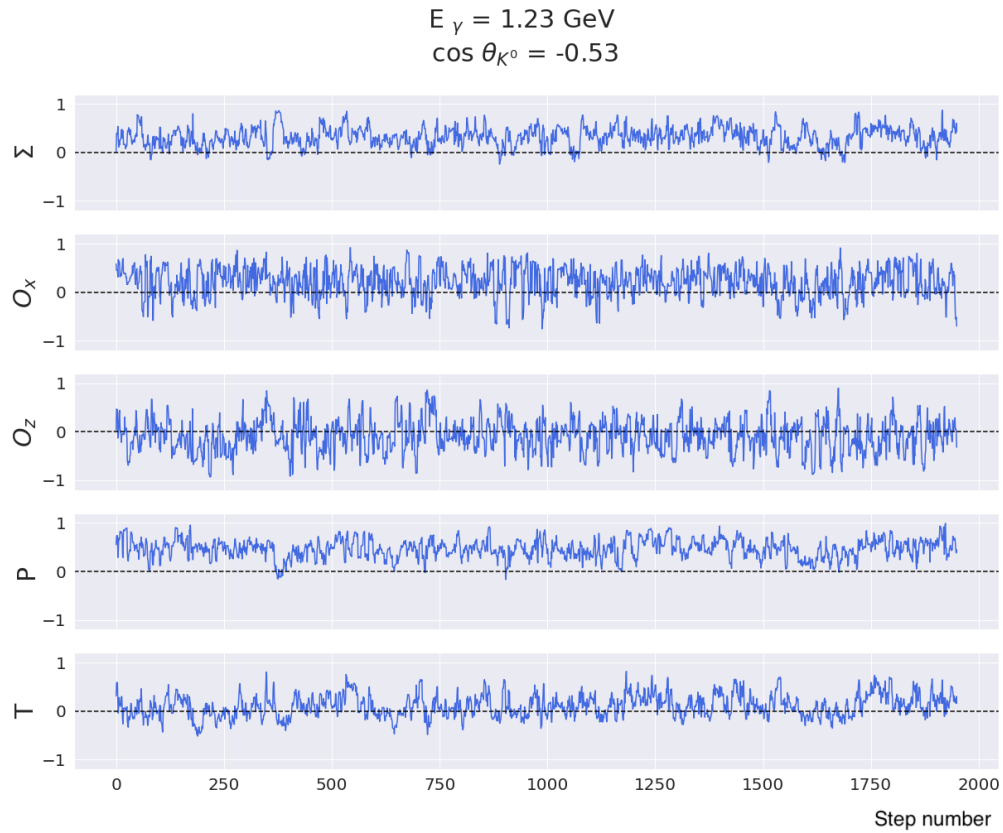


Figure 4.17: MCMC time series for a typical $\cos \theta_{K^0}$ bin within E_γ bin 1.23 GeV

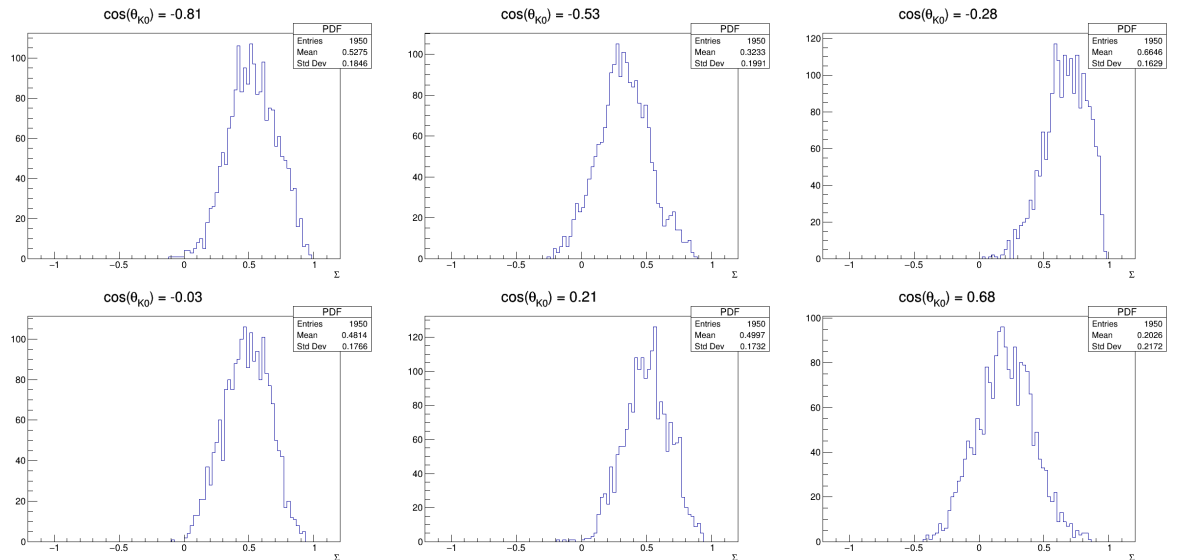


Figure 4.18: Beam asymmetry, Σ , posterior probability density function for all $\cos \theta_{K^0}$ bins within E_γ bin 1.23 GeV

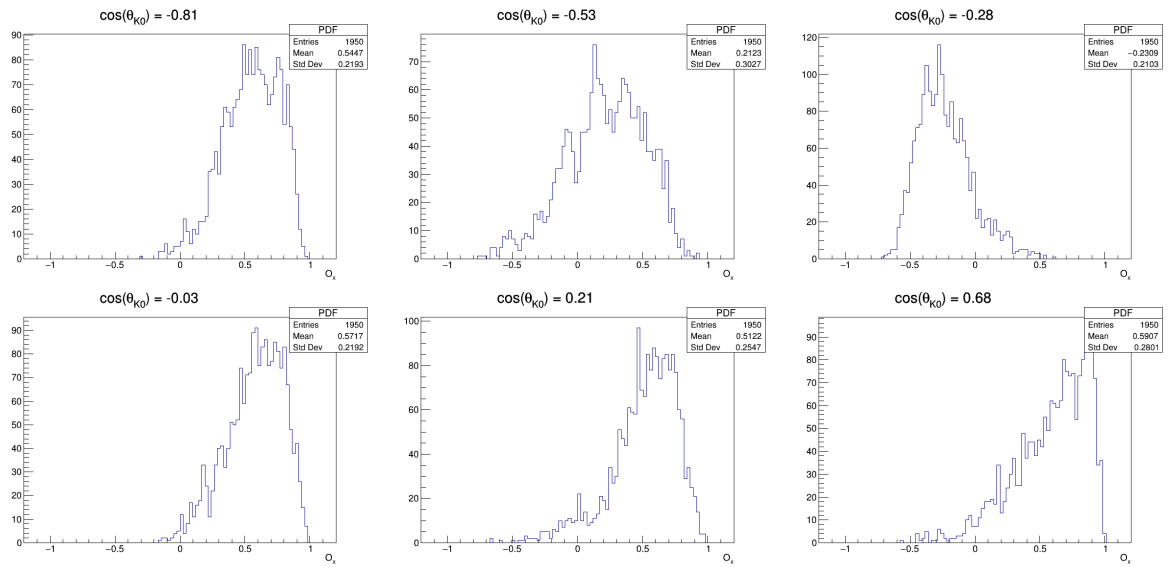


Figure 4.19: O_x posterior probability density function for all $\cos\theta_{K0}$ bins within E_γ bin 1.23 GeV

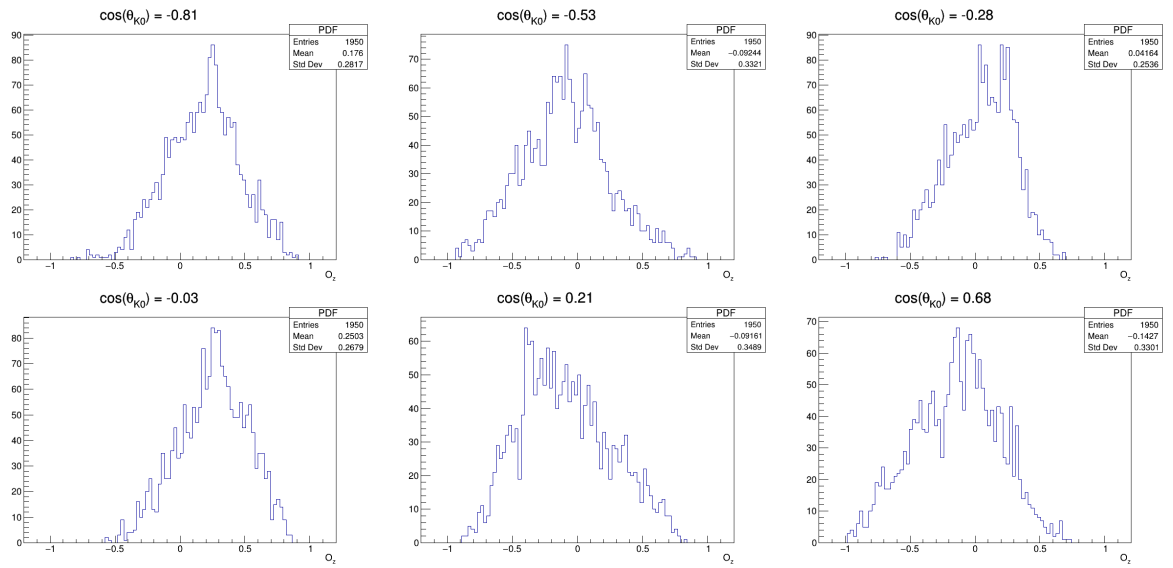


Figure 4.20: O_z posterior probability density function for all $\cos\theta_{K0}$ bins within E_γ bin 1.23 GeV

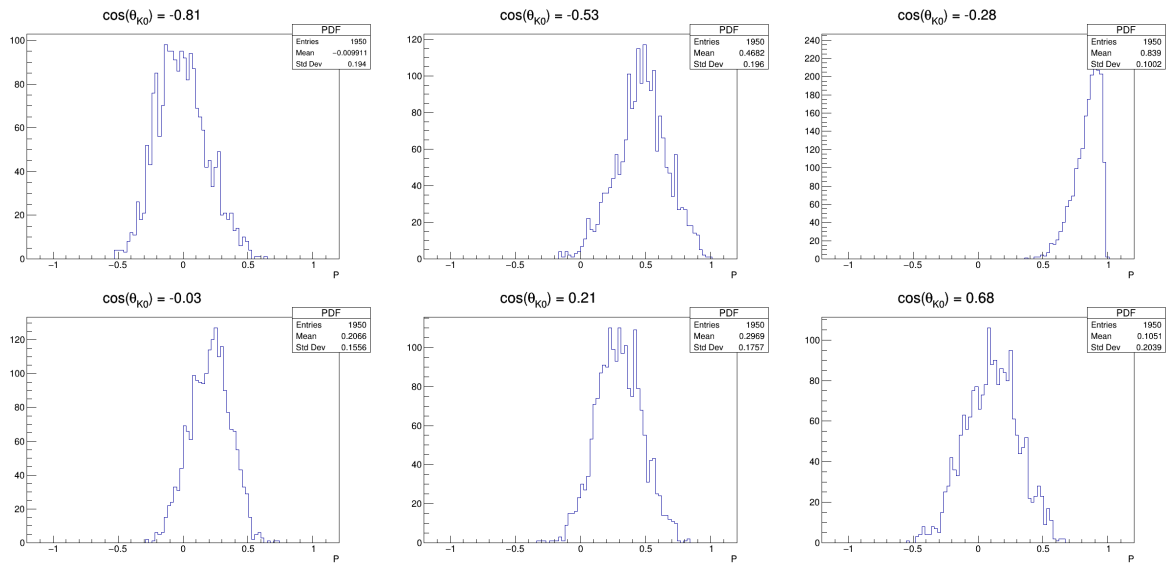


Figure 4.21: Recoil asymmetry, P , posterior probability density function for all $\cos \theta_{K0}$ bins within E_γ bin 1.23 GeV

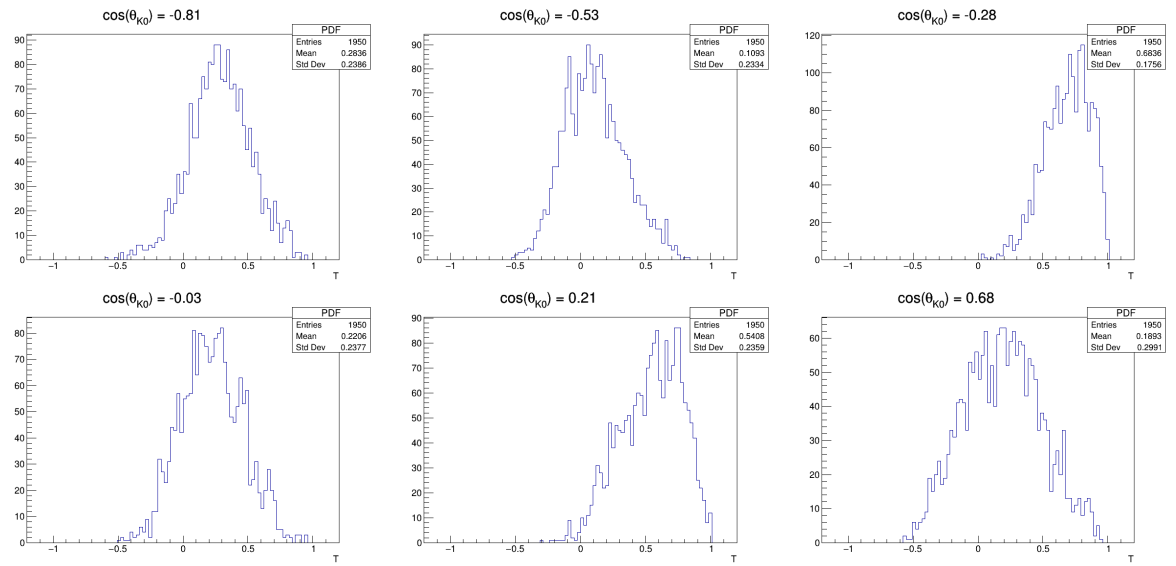


Figure 4.22: Target asymmetry, T , posterior probability density function for all $\cos \theta_{K0}$ bins within E_γ bin 1.23 GeV

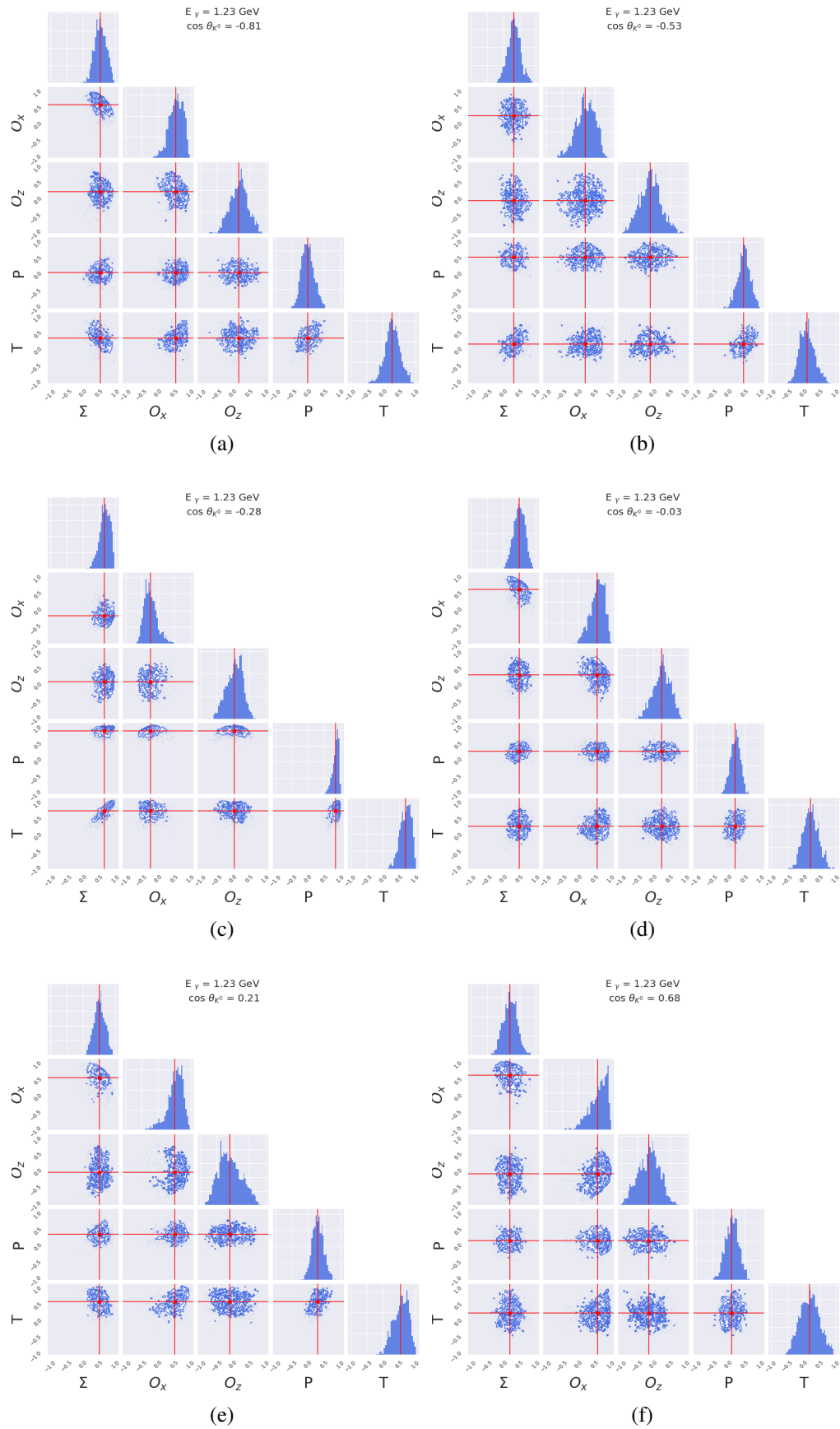


Figure 4.23: PDFs and correlations for all $\cos \theta_{K^0}$ bins within E_γ bin 1.23 GeV. The red lines indicate the mean of the distributions.

4.5.3 Results

The posterior PDFs obtained using the MCMC likelihood analysis provide all the information which has been extracted by the study. In order to characterise the distributions with a discrete set of values, we extract: mode, mean, standard deviation, 16th, 25th, 50th (median), 75th, and 84th quantiles. These are tabulated in Appendix C. In Figures 4.24 to 4.28, the measurements are plotted for each observable. The mode, as the likeliest value, is reported as the result and is the value which will be later passed to theorists. The points plotted are the mode of the posterior PDF and the error bars extend from the 16th to the 84th quantile. Specifically, 68% of the MCMC sample lies within the error bars, equivalent to an uncertainty of 1σ .

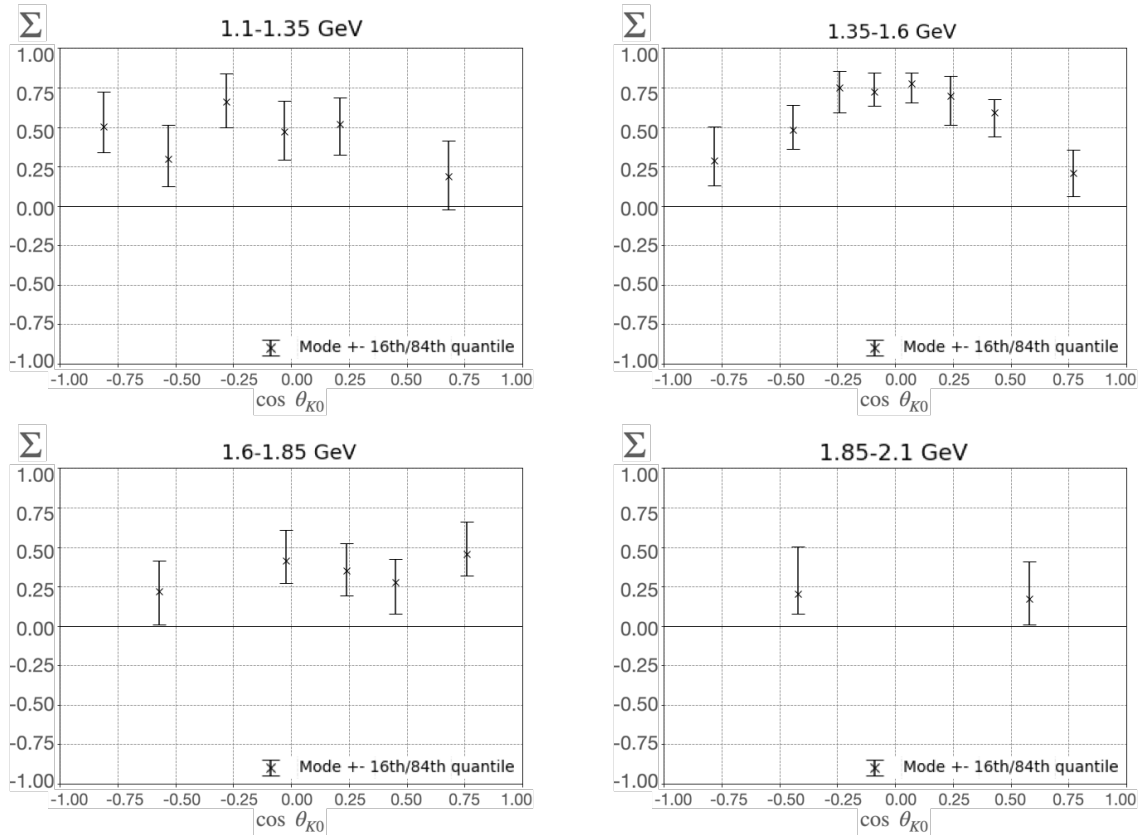


Figure 4.24: Measurements obtained for beam asymmetry, Σ . The points plotted are the mode of the posterior PDF and the error bars extend from the 16th to the 84th quantile.

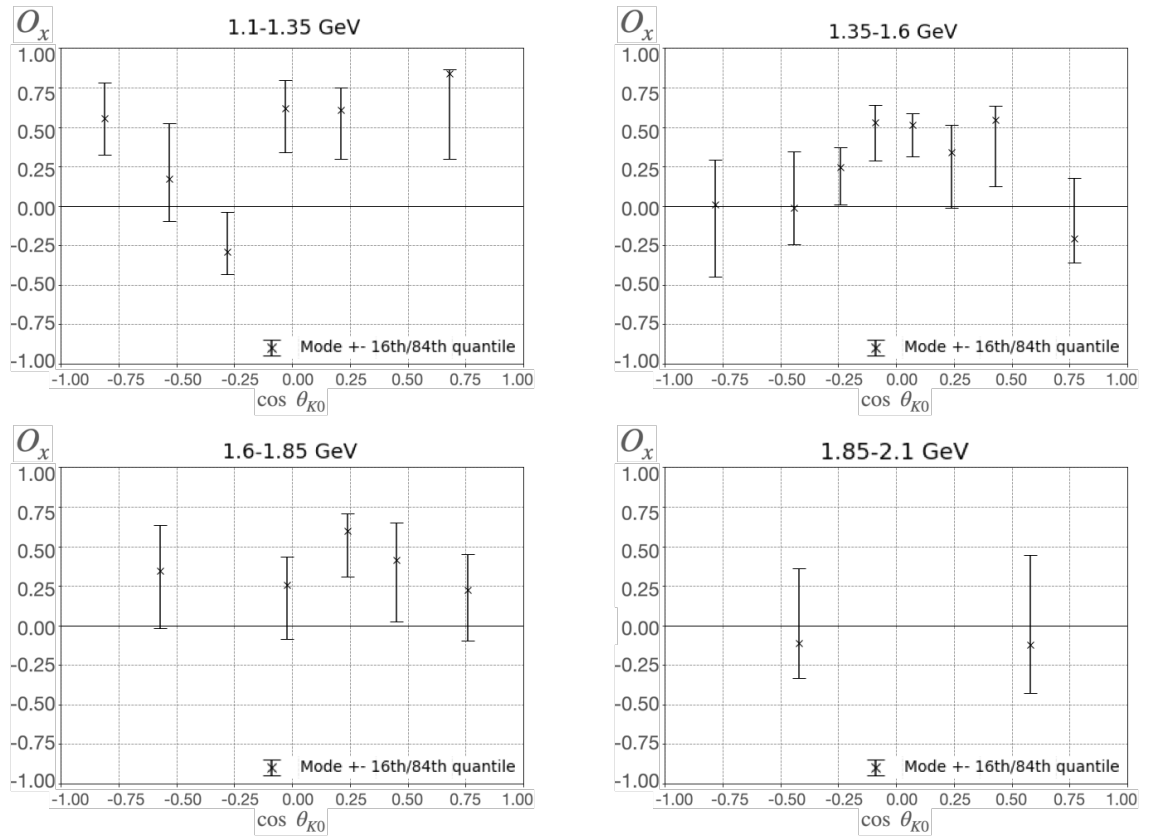


Figure 4.25: Measurements obtained for O_x . The points plotted are the mode of the posterior PDF and the error bars extend from the 16th to the 84th quantile.

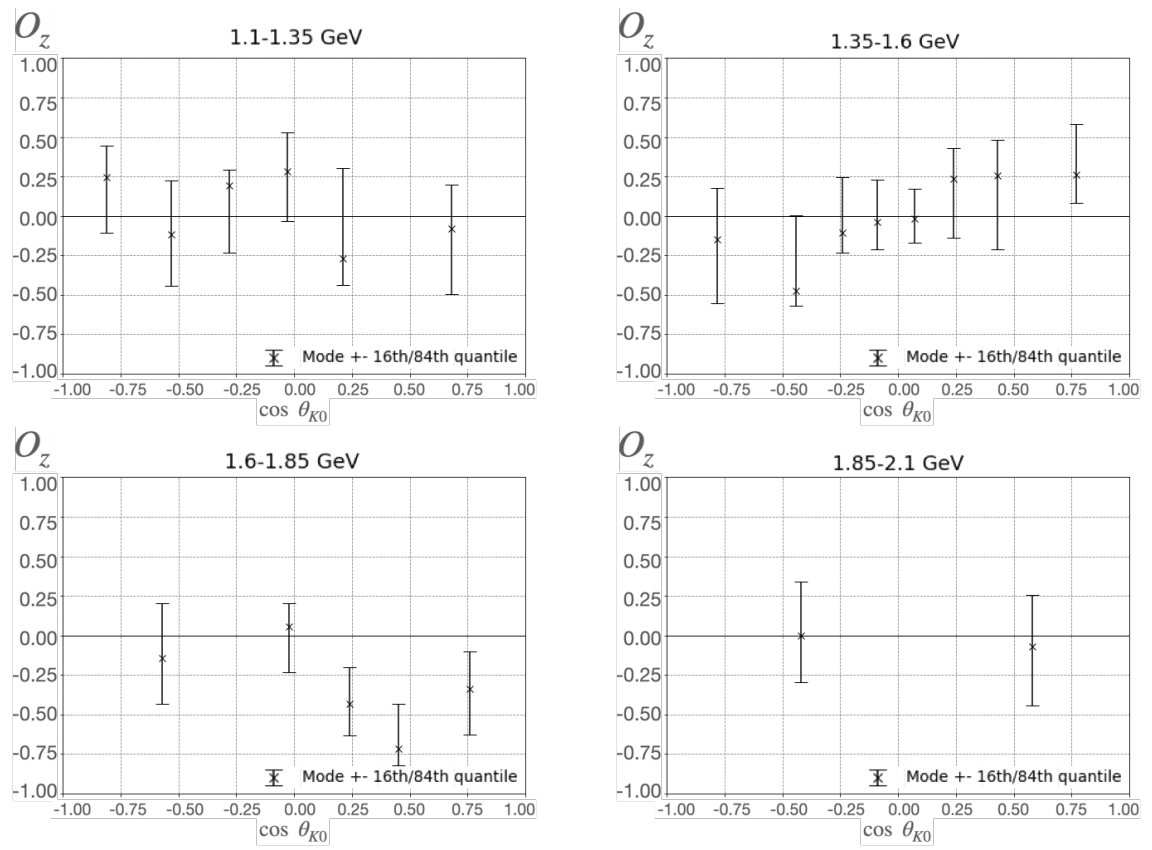


Figure 4.26: Measurements obtained for O_z . The points plotted are the mode of the posterior PDF and the error bars extend from the 16th to the 84th quantile.

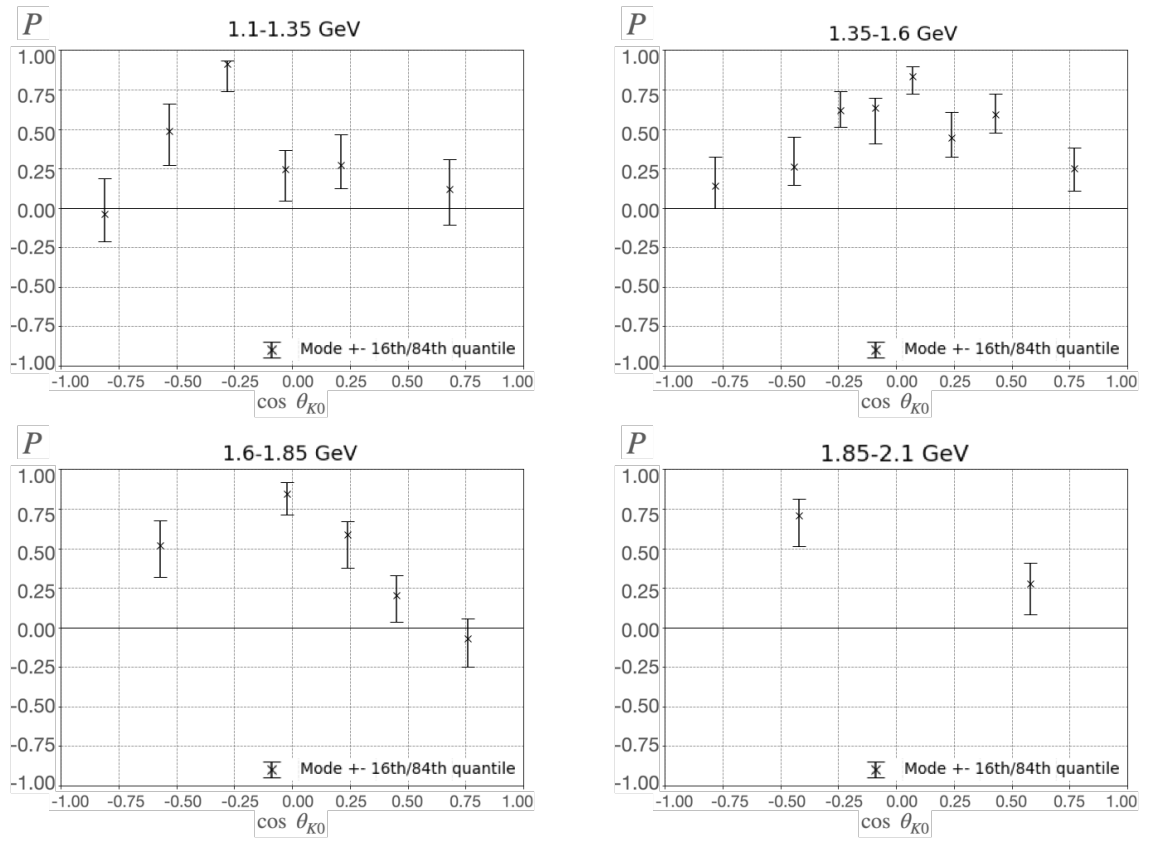


Figure 4.27: Measurements obtained for recoil asymmetry, P . The points plotted are the mode of the posterior PDF and the error bars extend from the 16th to the 84th quantile.

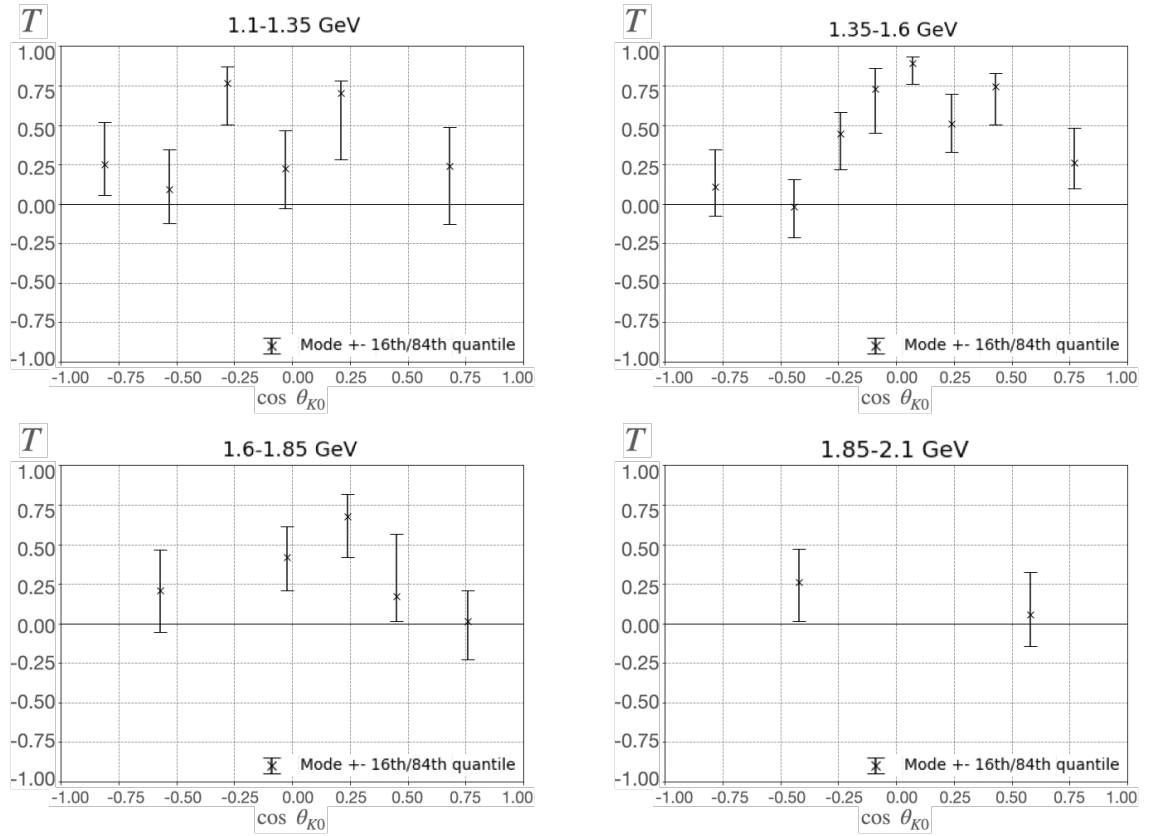


Figure 4.28: Measurements obtained for target asymmetry, T . The points plotted are the mode of the posterior PDF and the error bars extend from the 16th to the 84th quantile.

Calculation of mode using KDE smoothing

The mean, standard deviation and positions of quantiles can all be extracted directly from the PDF distribution. In order to extract the mode (as plotted previously in Figures 4.24 to 4.28), the distribution is binned and smoothed using a gaussian kernel density estimation. In this process, histogram bins are replaced with gaussian kernels (of width derived using the ‘‘Scott’’ method [73]) which are summed to produce a smoothed distribution. The peak of this distribution is reported as the mode in Appendix C. An example of the KDE curve overlaid on the PDF histogram is shown in Figure 4.29.

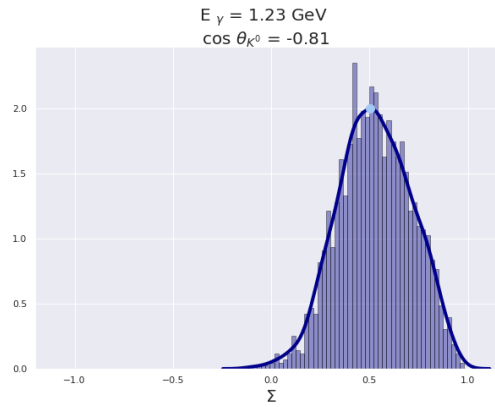


Figure 4.29: Example PDF with KDE smoothing (dark blue curve). The mode is reported as the peak of the KDE curve (light blue circle).

4.5.4 Summary

The polarisation observables Σ, O_x, O_z, T and P have been measured for the reaction $\vec{\gamma}p \rightarrow K^0 \Sigma^+$. The next section summarises the validation and systematic uncertainty studies which were carried out and presents the overall statistical and systematic uncertainties associated with the measurements.

4.6 Systematic and Validation Studies

Systematic studies were performed by varying the parameters used in the analysis method and rerunning the analysis. The following parameters were varied and the observables re-extracted.

- The width of the sWeights fit around the π^0 mass
- The width of the sWeights fit around the K^0 mass
- The background shape for the sWeights fit around the K^0 mass
- The MCMC step size

The parameter which was observed to have the dominant effect on the results obtained was the width of the K^0 sWeights fit. The details of this study follow in Section 4.6.1. Since we use the polarisation degree in our likelihood calculations, we must also recognise the effect of the known systematic uncertainty in this value as described in [68]. As an additional “sanity check”, the beam asymmetry, Σ , is extracted in isolation for comparison with the main results from the full extraction. This is described in Section 4.6.3. In order to quantify the additional systematic uncertainty introduced by the method, the observables were extracted from generated data and the spread of measurements obtained was used to extract a value for the systematic uncertainty (Section 4.6.4). This is combined with the known uncertainty in the polarisation degree to obtain an overall systematic uncertainty.

4.6.1 Systematic Uncertainty Due to K^0 Fit Width

Study of Correlations

In order for the sWeights to correctly subtract the background contributions, each variable studied with the distribution must be uncorrelated with the discriminatory variables used to obtain the weights. In many of the kinematic bins, it was found that there was indeed a correlation between the $\cos \theta_x$ variable (as defined in Section 4.1) and the reconstructed kaon mass which is used for the sWeights. Figure 4.30 shows the relationship between the two for signal weighted events (left), background weighted events (centre) and all events (right) for an example bin. It can be seen that the two are correlated, and the effect of this on the weighted $\cos \theta_x$ distribution is shown in Figure 4.31 (left), which shows the signal weighted $\cos \theta_x$ distribution integrated over all other variables. Since the control and discriminatory variable are correlated the weights are not correctly calculated. The effect of this is an artificial structure in the distribution of the weighted data (black points). In order to minimise this effect the weights are obtained with as narrow as possible interval for fitting the kaon mass. Figure 4.31 (right) shows the distribution when a narrower interval is used for the fit.

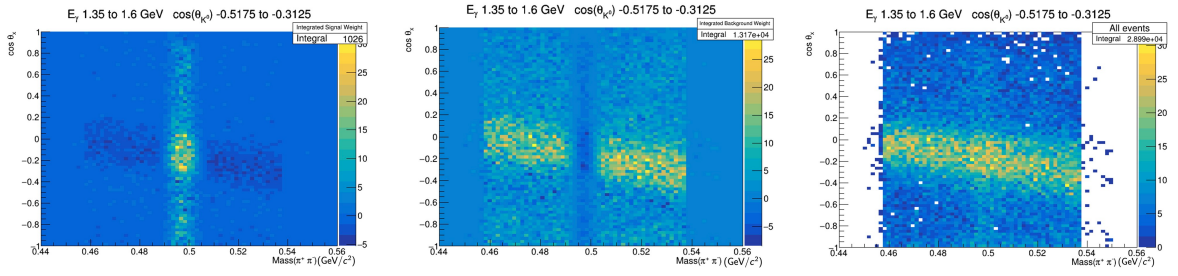


Figure 4.30: Correlations between $\cos \theta_x$ and Mass ($\pi^+ \pi^-$) for signal weighted events (left), background weighted events (centre) and all events (right).

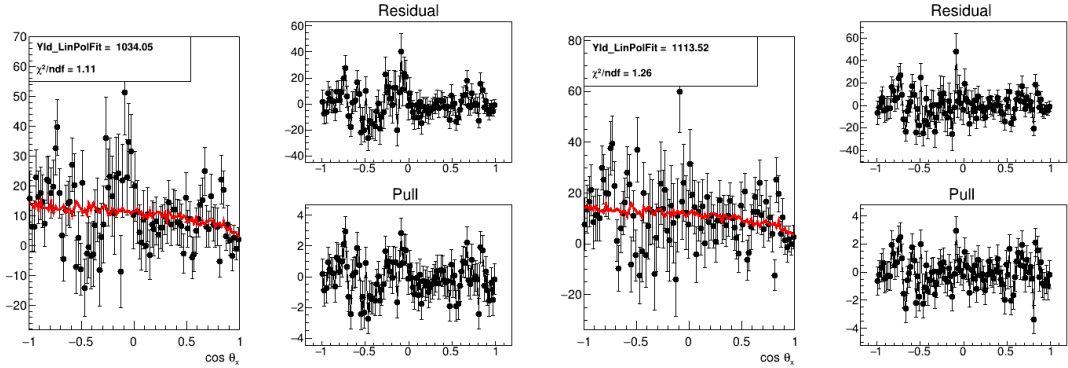


Figure 4.31: Signal weighted $\cos \theta_x$ distributions for fit interval of $80 \text{ MeV}/c^2$ (left) and $35 \text{ MeV}/c^2$ (right). The signal weighted data are the black points, and the red line shows the model, i.e. the simulated events with a distribution corresponding to the extracted observables.

Results of Systematic Study

The results described in Section 5.5.2 are based on weights obtained from fitting around the K^0 mass with the optimal interval of $35 \text{ MeV}/c^2$ (as determined in Section 4.6.1 ensuring the effect of correlations is minimised). To study the effect of varying this width, four iterations of the analysis were performed with the intervals of $35, 50, 65$ and $80 \text{ MeV}/c^2$. The sWeights fits obtained are shown for an example bin in Figure 4.32. For the narrowest interval, $35 \text{ MeV}/c^2$, a linear Chebyshev polynomial is used to model the background instead of the quadratic Chebyshev polynomial used for the others.

In order to study the effect, MCMC chains were obtained as described in Section 4.5 using each of the sets of weights. The chains were then merged to create a posterior distribution which includes the effect of the systematic variation. The chain created using the optimum method (i.e. sWeights fit range $35 \text{ MeV}/c^2$) was included with a weight of 3 times the others so that the resulting merged chain was 50% from the optimum method and 50% non-optimum.

The results of the study are shown in Figures 4.33 to 4.37. Each point is the median of the posterior PDF with error bars extending from 16th to 84th quantile. The points in blue are the

results from the optimum method, and the points in red are the results from the merged chain. Any effect due to the choice of fit interval is outweighed by the statistical uncertainty.

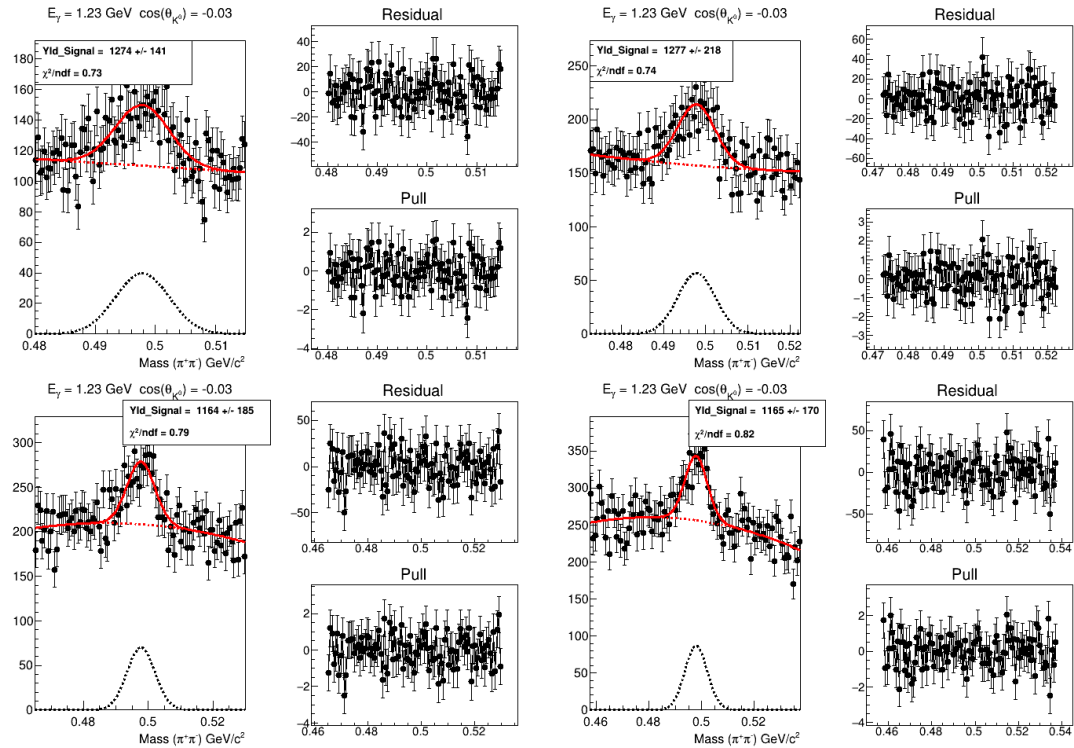
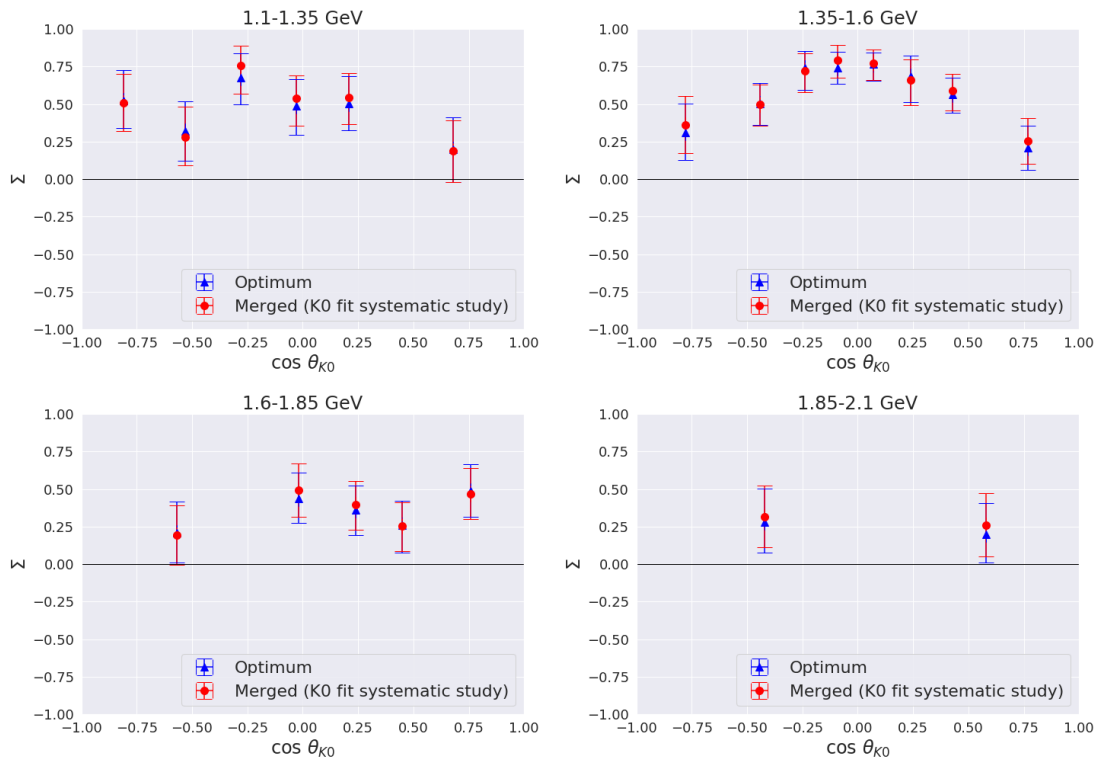
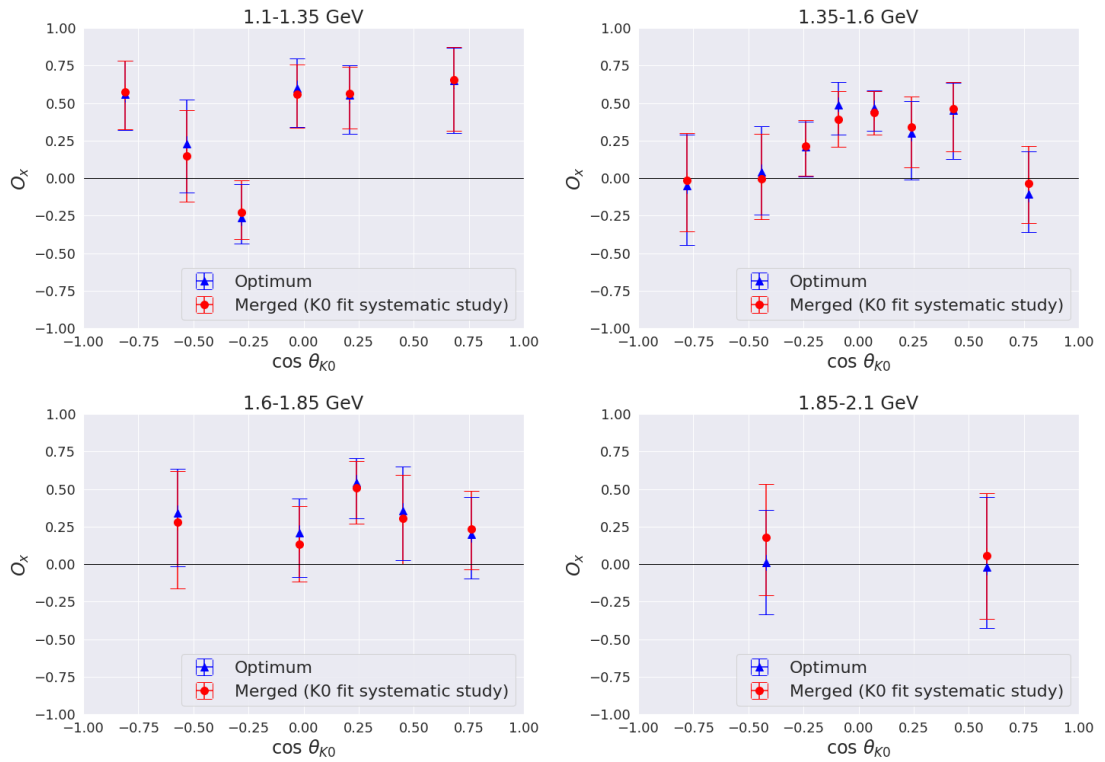
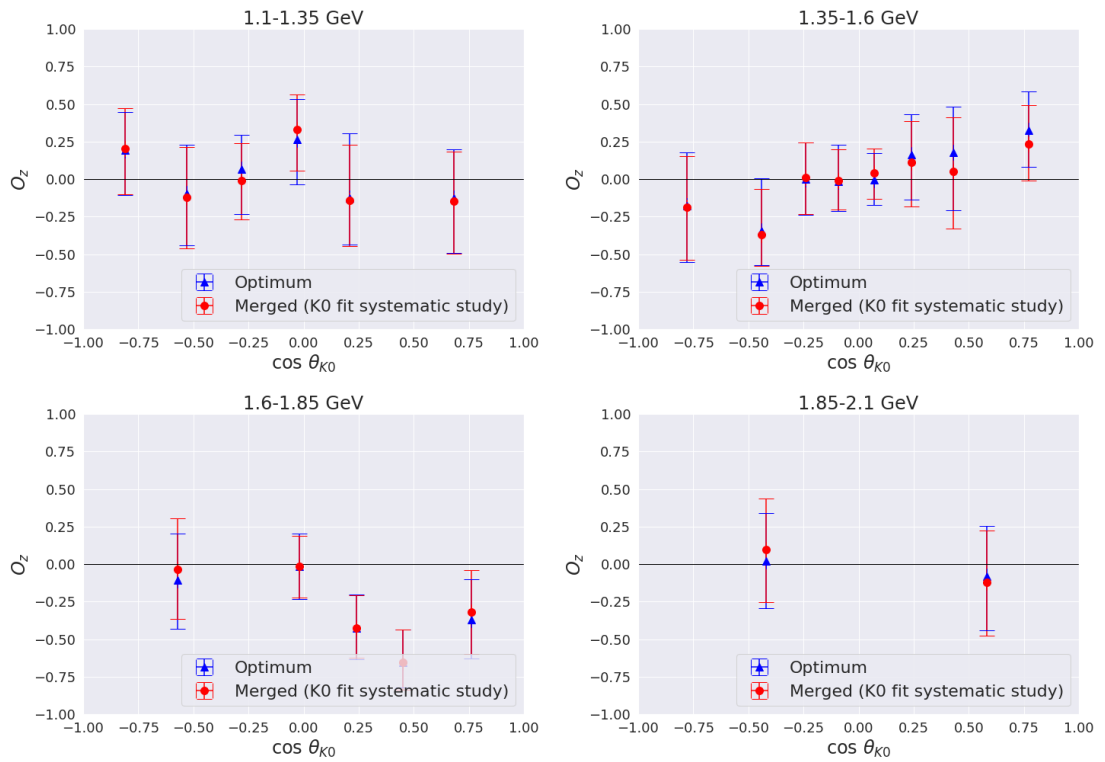
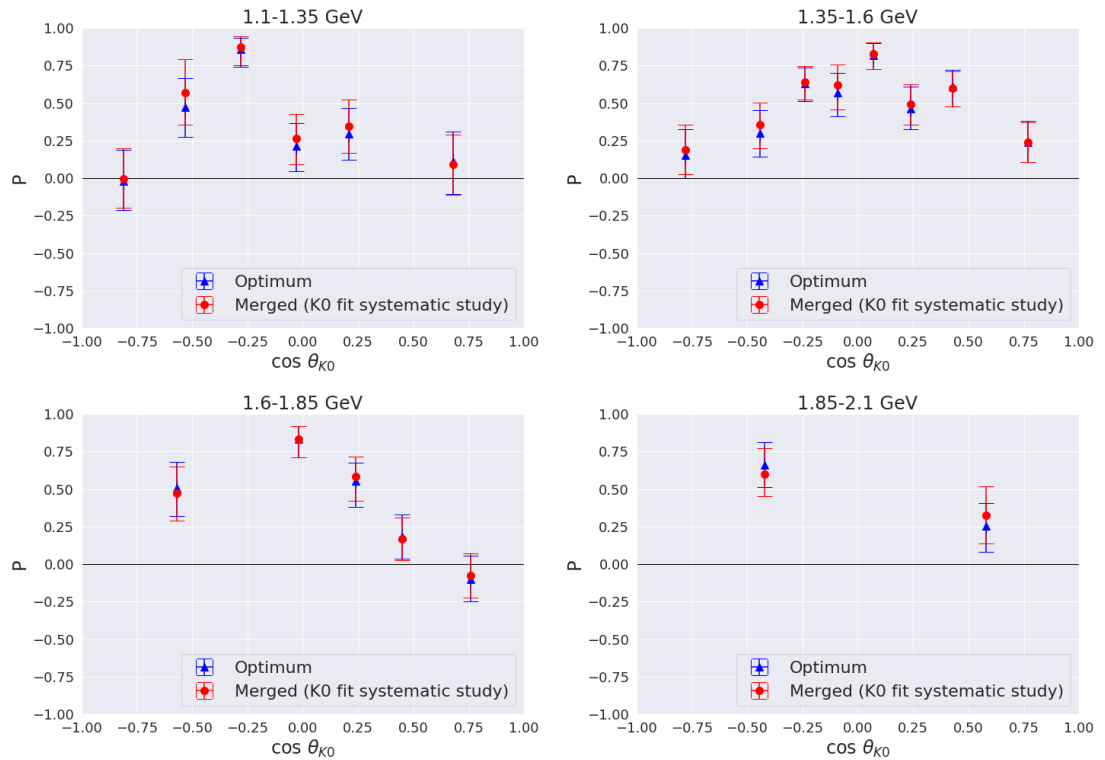


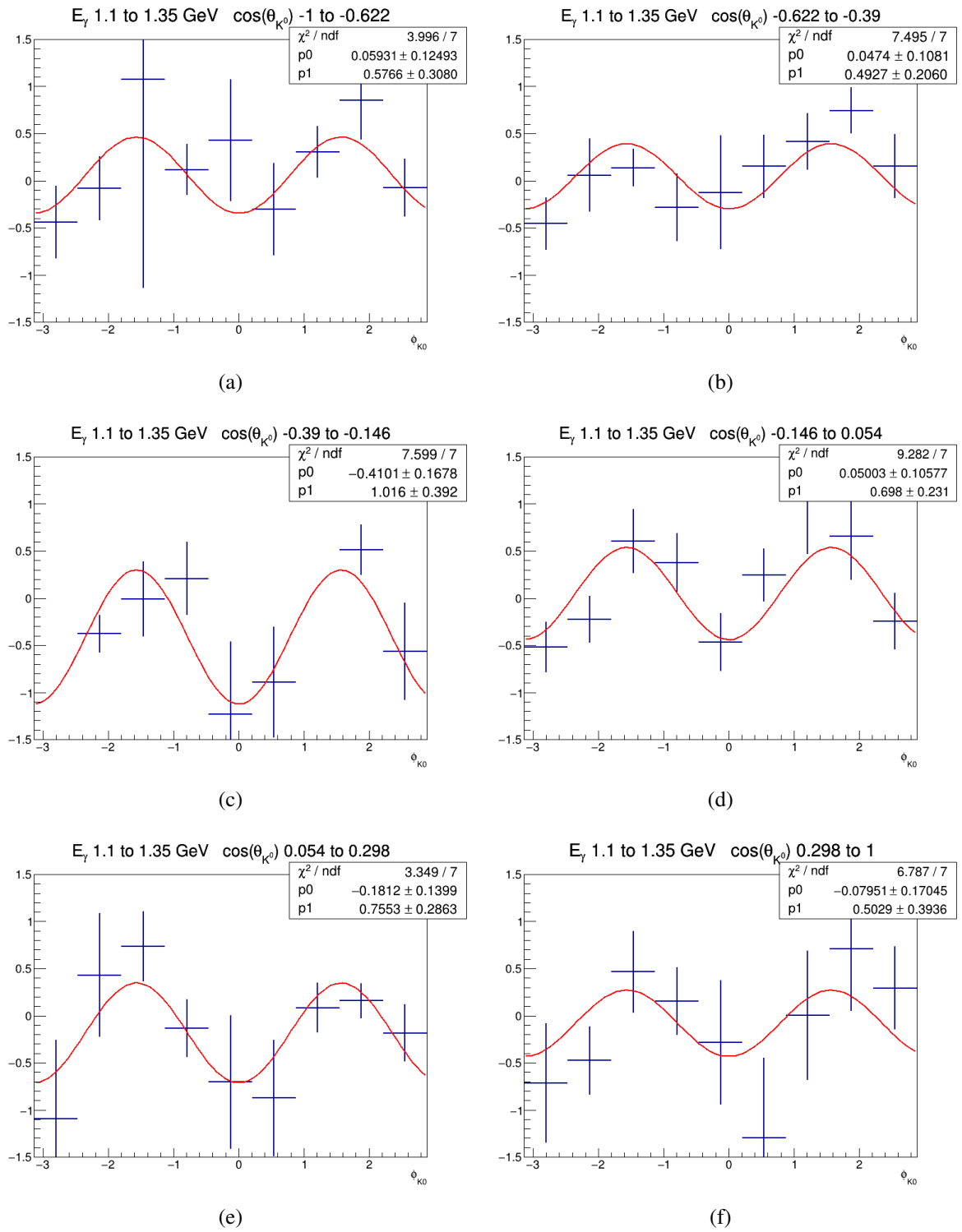
Figure 4.32: sWeights fits around K^0 using varied interval widths, 35 MeV/c^2 (top left), 50 MeV/c^2 (top right), 65 MeV/c^2 (bottom left) and 80 MeV/c^2 (bottom right).

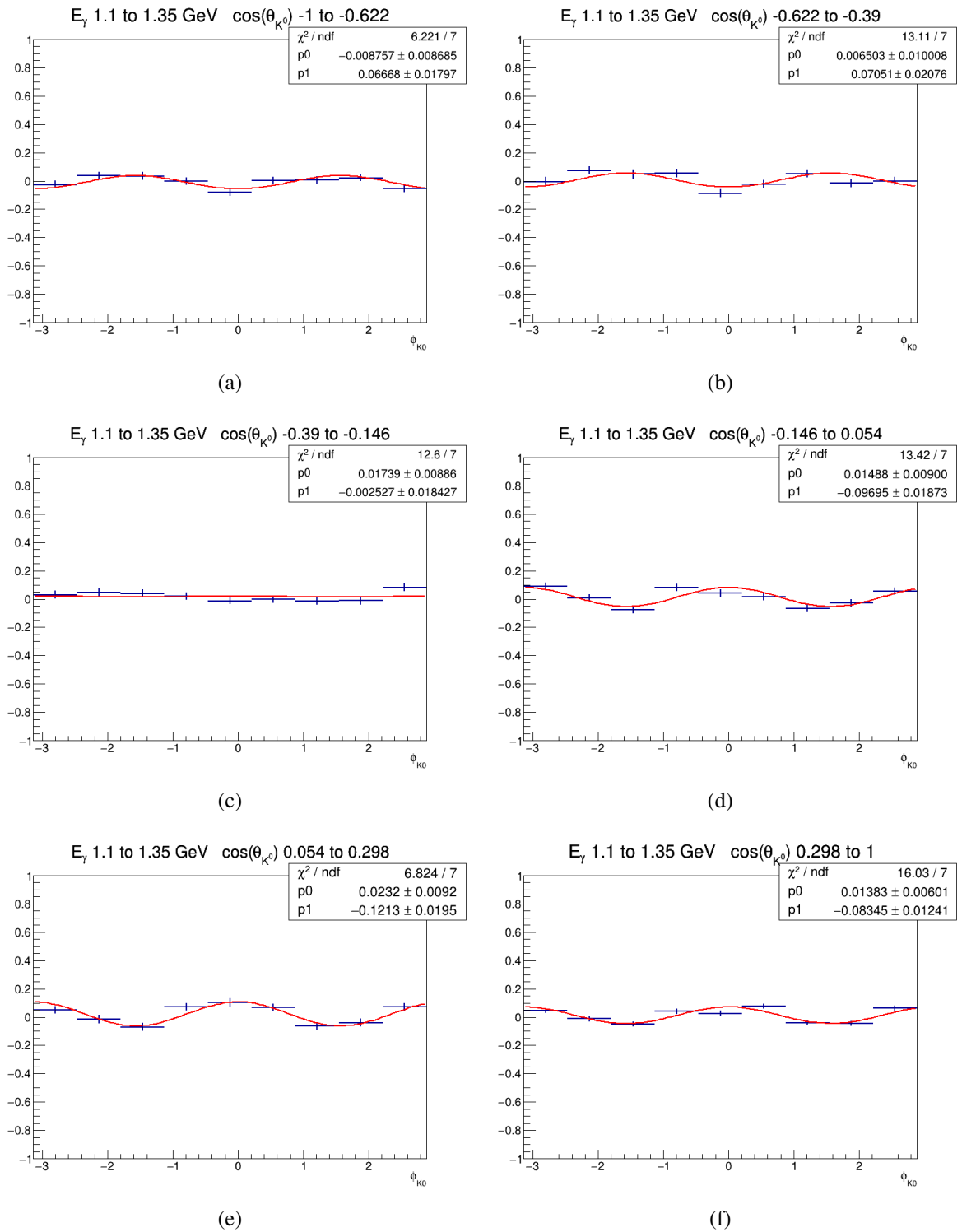

 Figure 4.33: Results of K^0 fitting systematic study for beam asymmetry, Σ

 Figure 4.34: Results of K^0 fitting systematic study for O_x


 Figure 4.35: Results of K^0 fitting systematic study for O_z

 Figure 4.36: Results of K^0 fitting systematic study for recoil asymmetry, P

$$\frac{N_{\perp} - N_{\parallel}}{N_{\perp} + N_{\parallel}} = 1 - P^{\gamma\Sigma} \cos 2\phi_{K^0} \quad (4.16)$$

The asymmetry distributions obtained for signal weighted events for E_{γ} bin 1.23 GeV are shown in Figure 4.38. The asymmetry distributions were also extracted for background weighted events to investigate whether any asymmetry in the background might affect the measurements. The background distributions for E_{γ} bin 1.23 GeV are shown in Figure 4.39. The background asymmetry is of smaller magnitude by a factor of approximately 4 for all bins, and is opposite in sign to the signal asymmetry for most. The results were consistent with the MCMC study, full details are given in the next section.

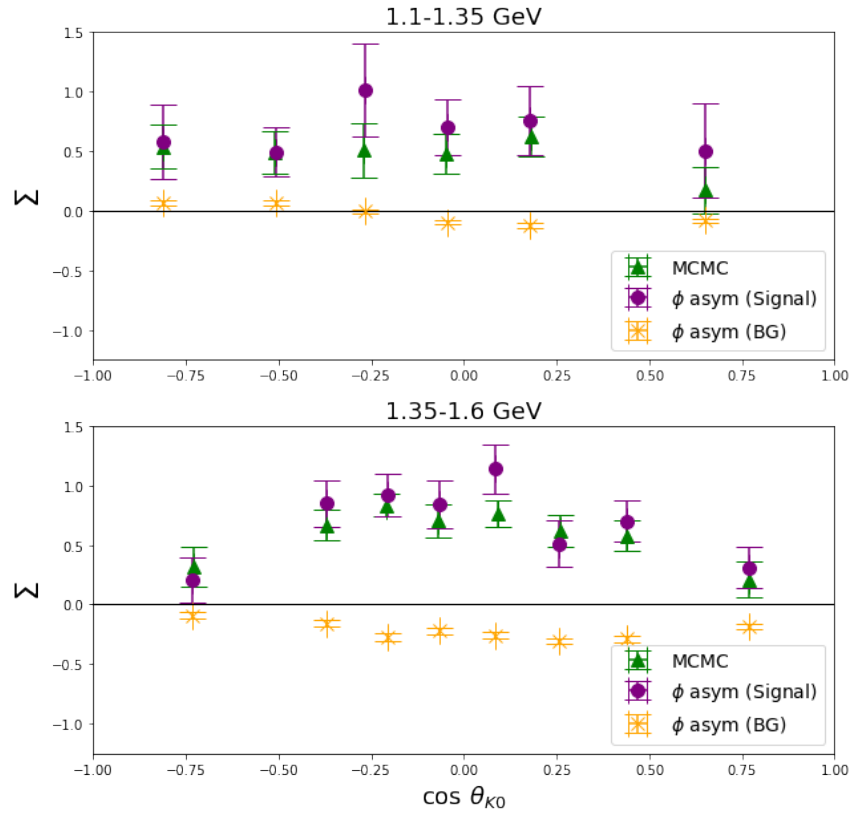

 Figure 4.38: Signal weighted $K_S^0 \phi$ asymmetry for E_γ bin 1.23 GeV


 Figure 4.39: Background weighted $K_S^0 \phi$ asymmetry for E_γ bin 1.23 GeV

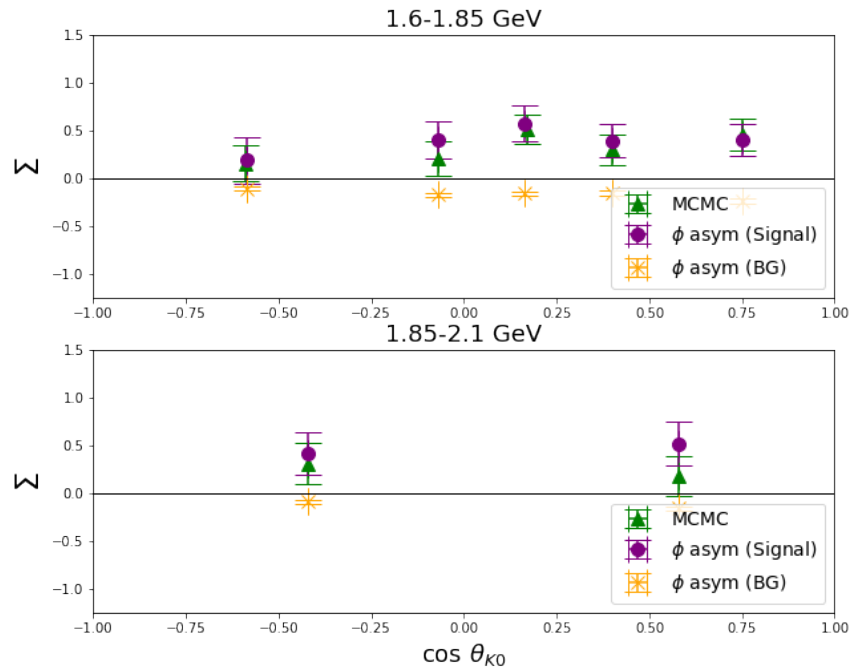
1-D Extraction of Σ - Results

Figure 4.40 plots the measurements of the beam asymmetry, Σ , using MCMC likelihood sampling (green triangles) and from the asymmetry measurements (purple circles). The two sets

of results are consistent within the uncertainties. The asymmetry measurement for background events is also shown for comparison (yellow crosses).



(a)



(b)

Figure 4.40: Comparison of measured $K_S^0 \phi$ asymmetry

4.6.4 Toy Data Study

In order to validate the method, and to quantify the systematic uncertainty introduced by the method, we test whether we can correctly extract observable values from toy data generated with set values of the observables. Toy events were created starting from phase space simulation data and the observable values set equal to those extracted for the real data. The phase space simulated events are then accepted or rejected based on the probability of them being included in a distribution with the given observable values. Five sets of toy data were generated for all bins, with number of events in each set approximately equal to the integrated signal for that bin. The results extracted for the toy data agree with the expected values within the uncertainties as shown in Figures 4.41 to 4.45. More sets of toy data were generated in order to plot the deviation (measured - true value) for each observable. The measured value is the value extracted by fitting the generated toy data. 30 sets of toy data were produced for each of the six $\cos \theta_{K^0}$ bins in the first energy bin and the distributions of (measured - true value) for each observable are shown in Figure 4.46. The mean of these distributions is of the order 0.01-0.03 which is an order of magnitude less than the standard deviations quoted in our results. We therefore conclude that any bias introduced by our fitting method is insignificant in comparison to the statistical uncertainties.

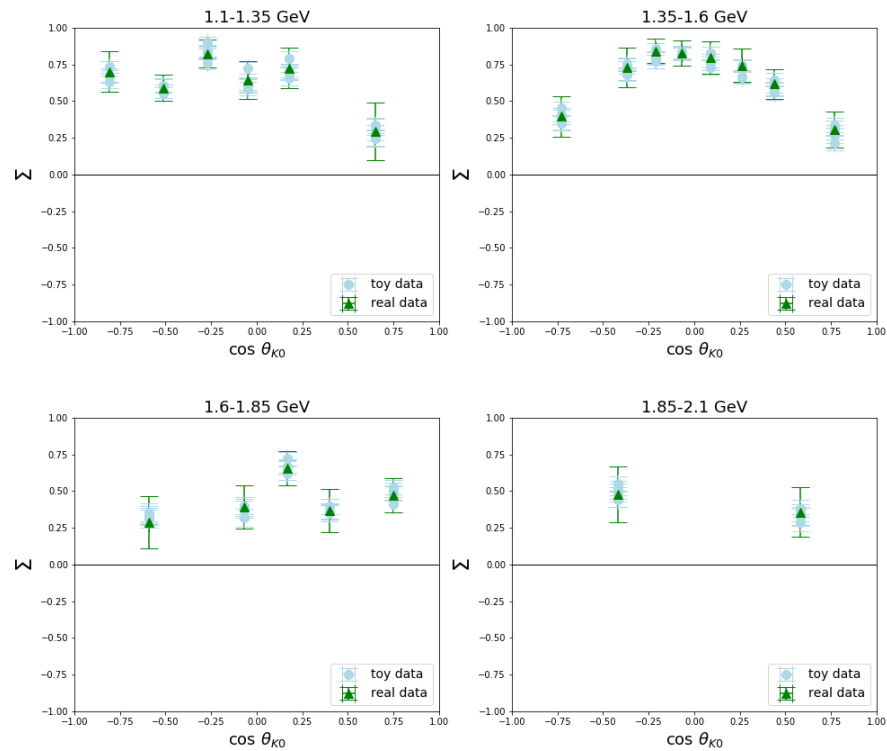


Figure 4.41: Comparison of results extracted for toy data (light blue circles) and real data (green triangles) for beam asymmetry, Σ

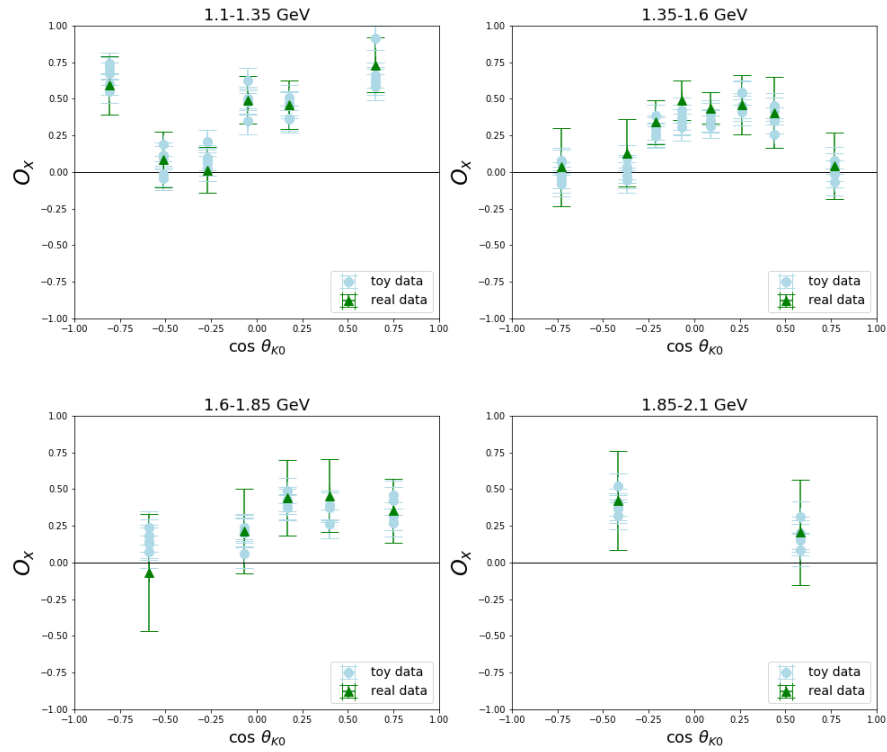


Figure 4.42: Comparison of results extracted for toy data (light blue circles) and real data (green triangles) for O_x

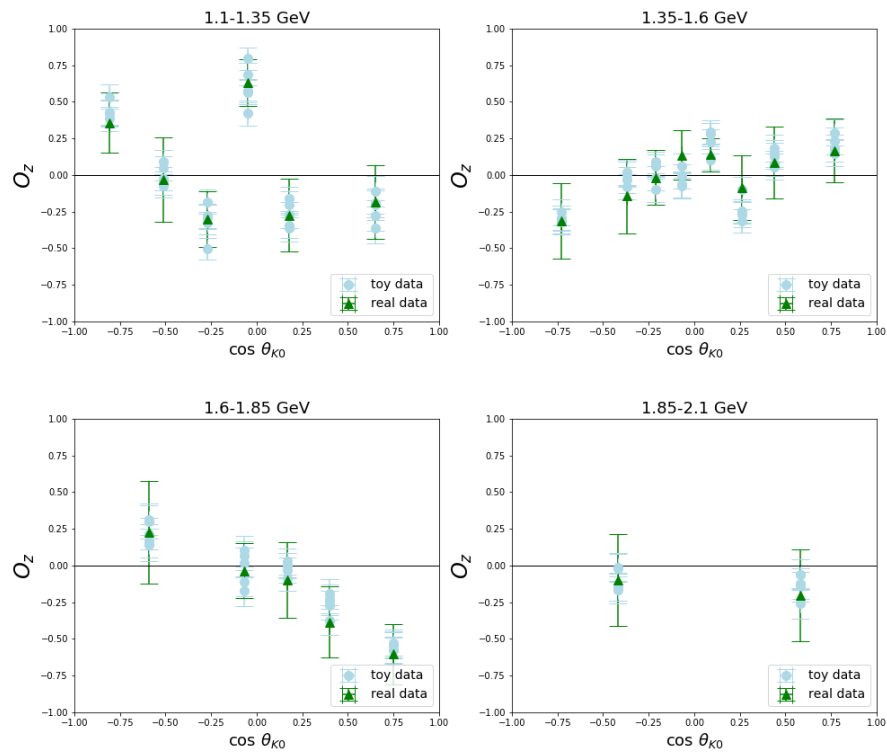


Figure 4.43: Comparison of results extracted for toy data (light blue circles) and real data (green triangles) for O_z

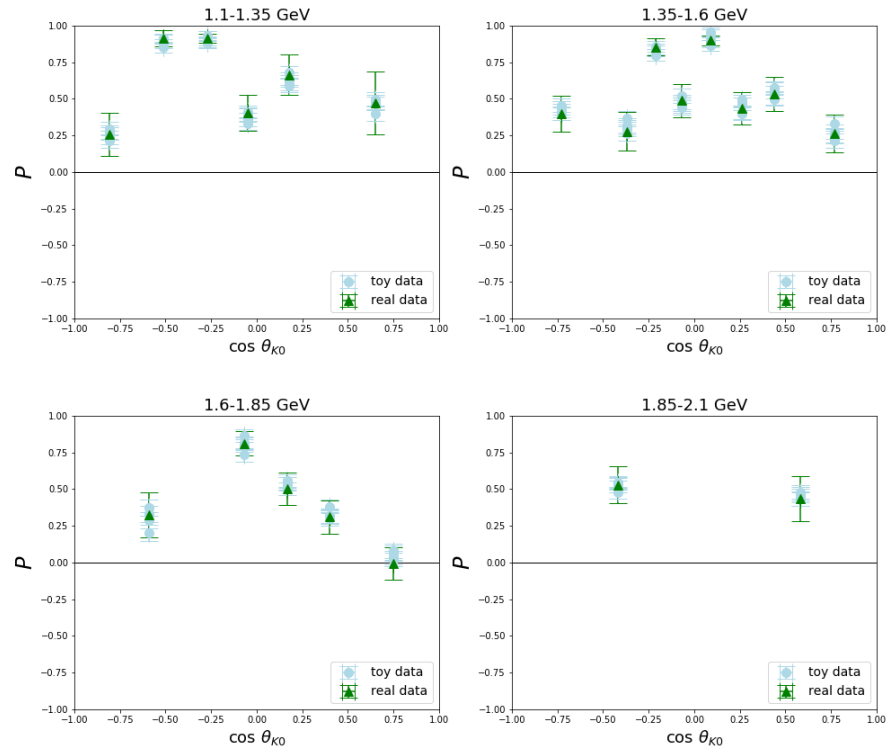


Figure 4.44: Comparison of results extracted for toy data (light blue circles) and real data (green triangles) for recoil asymmetry, P

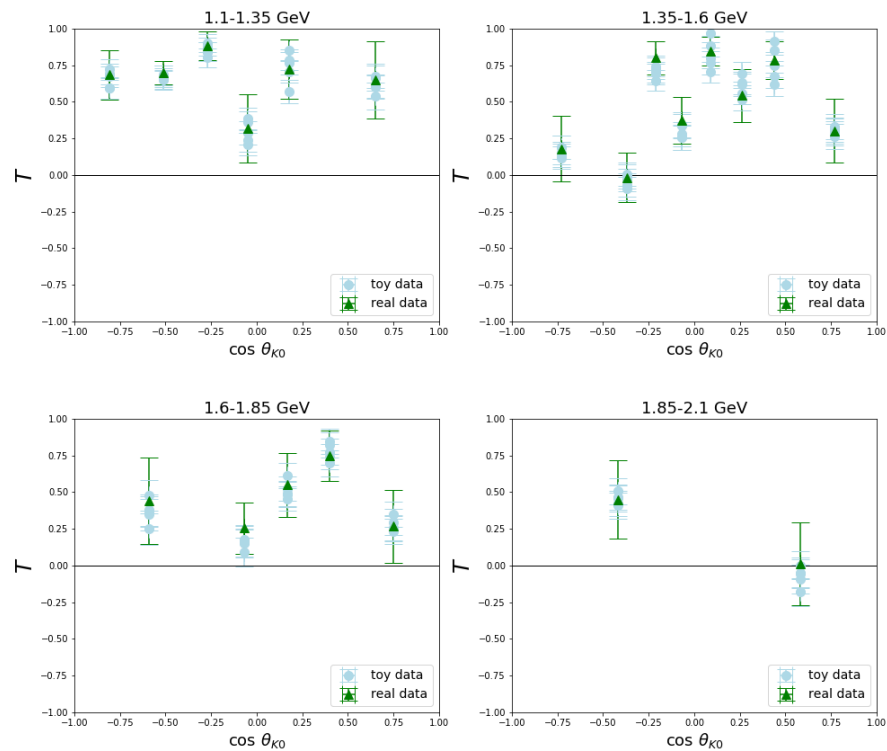


Figure 4.45: Comparison of results extracted for toy data (light blue circles) and real data (green triangles) for target asymmetry, T

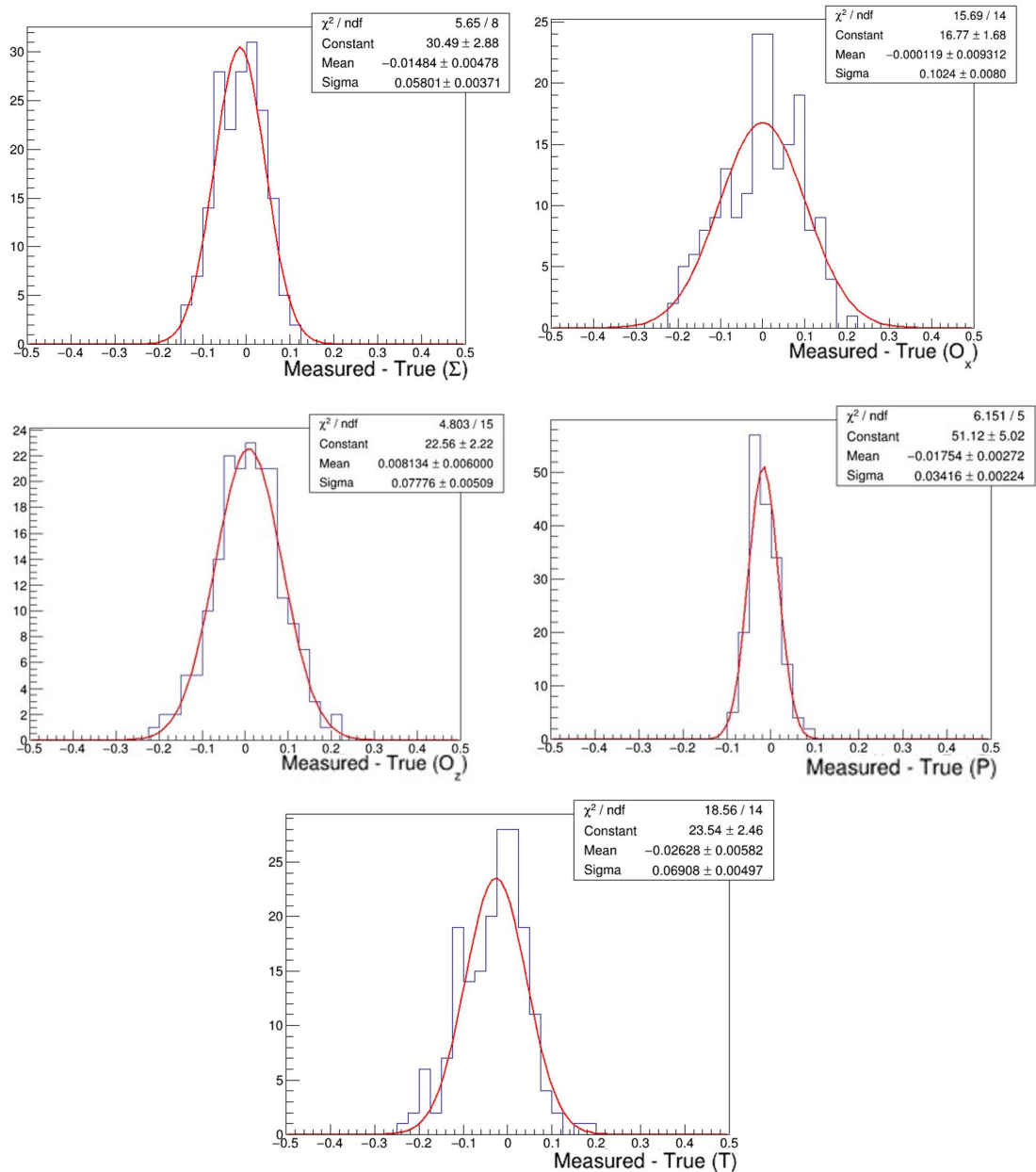


Figure 4.46: Distributions of (measured - true value) for each observable for toy data studies. Measured values are the values extracted by fitting the generated toy data. True values are the values passed to the toy data generator.

4.6.5 Conclusions from Systematic and Validation Studies

In Section 4.6.1 we examined the effect of changing the included background by varying the fit interval when extracting the signal weights, and in Section 4.6.4 we tested for any bias in our fitting method by fitting toy data. The systematic uncertainties introduced were found to be insignificant in comparison to the statistical uncertainties. From the toy data study we find that the measured values deviate from the true values by approximately 0.01 to 0.02 (whereas the statistical uncertainties are of the order 0.2).

We also consider the systematic uncertainty introduced by the uncertainty in the Σ^+ weak decay parameter, α , which is 1.7%. Adding this in quadrature to the systematic uncertainty due to the polarisation degree (4% for photon energy bins in the range 1.1-1.85 GeV and 6% for energy bin 1.85-2.1 GeV) we arrive at a contribution to the systematic uncertainty of 4.3% for photon energy bins in the range 1.1-1.85 GeV and 6.2% for energy bin 1.85-2.1 GeV. Including the absolute uncertainty derived in the toy data study, the systematic uncertainty can therefore be quoted as $\pm 4.3\% \pm 0.02$ for photon energy bins in the range 1.1-1.85 GeV and $\pm 6.2\% \pm 0.02$ for energy bin 1.85-2.1 GeV. In order to place an upper limit on the systematic uncertainty as a percentage, we can assume that the absolute error contributes a systematic uncertainty of approximately 4% (i.e. an uncertainty of 0.02 at a typical measurement of 0.5). Adding all three in quadrature we arrive at an upper limit on the systematic uncertainty of 6% for photon energy bins in the range 1.1-1.85 GeV and 7% for energy bin 1.85-2.1 GeV.

The implications of these measurements for theoretical models are discussed in Chapter 7. Before moving on to this discussion, the next chapter describes the second analysis: the extraction of spin density matrix elements for the reaction $\vec{\gamma}p \rightarrow p\phi$.

Chapter 5

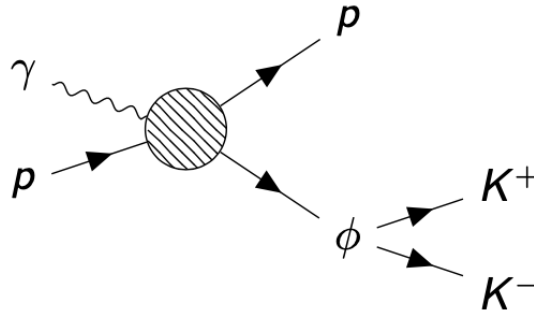
Extracting Spin Density Matrix Elements for $\vec{\gamma} p \rightarrow p \phi$

The preceding chapter has presented an analysis for data in CLAS taken in the run period known as g8b, using linearly polarised photons incident on a liquid hydrogen target. This chapter describes a second analysis, in this case to extract the spin density matrix elements (SDMEs) for the reaction $\gamma p \rightarrow p \phi$, using the same data and analysis methods. The details and results of the analysis are described, with reference to the common methods used for both analyses.

The three most common decay modes of the ϕ -meson constitute 98.4% of decays [1]. The associated contributions are shown in Table 5.1. The CLAS detector is well equipped to detect the first of these, where $\phi \rightarrow K^+ K^-$. This work will therefore consider the first decay mode amounting to 48.9% of decays. A schematic view of the reaction and final state is shown in Figure 5.1.

This analysis will include four possible topologies of the $p K^+ K^-$ final state allowing for detection of all 3 final state particles and for any one of the three to escape the detector undetected. In these cases the missing particle is reconstructed from the missing mass. The efficiency of the CLAS detector varies greatly for negatively and positively charged particles depending on the polarity of the toroidal magnetic field. For this experiment, the torus polarity was set such that negatively charged particles were inbending. Consequently the K^- particles are bent back towards the beamline where acceptance is low meaning that in the vast majority of events the K^- has not been detected, but instead is reconstructed from the missing mass.

ϕ decay mode	Fraction
K^+K^-	$(48.9 \pm 0.5)\%$
$K_L^0 K_S^0$	$(34.2 \pm 0.4)\%$
$\rho\pi + \pi^+\pi^-\pi^0$	$(15.32 \pm 0.32)\%$

Table 5.1: ϕ -meson decay modes from Particle Data Group [1].Figure 5.1: Schematic view of the $\gamma p \rightarrow p\phi$ reaction and subsequent decay.

5.1 Formalism

In the formalism described by Schilling [9], the intensity distribution for the photoproduction of vector mesons with linearly polarised photon depends on

1. the polar and azimuthal decay angles, θ and ϕ , of the daughter K^+ in the rest frame of the vector meson,
2. the angle between the beam polarisation vector and the production plane of the $\gamma p \rightarrow p\phi$ reaction, Φ
3. the degree of linear polarisation of the photon causing the reaction, P_γ
4. the spin density matrix elements, denoted $\hat{\rho}$ or ρ_{jk}^i

The dependency is shown in Equations 5.1 to 5.4 below.

$$\begin{aligned}
 W(\Omega, \Phi; \hat{\rho}) &= W(\cos\theta, \varphi, \Phi; \hat{\rho}) \\
 &= W^0(\cos\theta, \varphi; \hat{\rho}) - P_\gamma \cos 2\Phi W^1(\cos\theta, \varphi; \hat{\rho}) - P_\gamma \sin 2\Phi W^2(\cos\theta, \varphi; \hat{\rho})
 \end{aligned} \tag{5.1}$$

$$\begin{aligned}
 W^0 &= \frac{3}{4\pi} \left[\frac{1}{2} (1 - \rho_{00}^0) + \frac{1}{2} (3\rho_{00}^0 - 1) \cos^2\theta \right. \\
 &\quad \left. - \sqrt{2} \operatorname{Re} \rho_{10}^0 \sin 2\theta \cos\varphi - \rho_{1-1}^0 \sin^2\theta \cos 2\varphi \right]
 \end{aligned} \tag{5.2}$$

$$\begin{aligned}
 W^1 &= \frac{3}{4\pi} \left[\rho_{11}^1 \sin^2\theta + \rho_{00}^1 \cos^2\theta \right. \\
 &\quad \left. - \sqrt{2} \operatorname{Re} \rho_{10}^1 \sin 2\theta \cos\varphi - \rho_{1-1}^1 \sin^2\theta \cos 2\varphi \right]
 \end{aligned} \tag{5.3}$$

$$\begin{aligned}
 W^2 &= \frac{3}{4\pi} \left[\sqrt{2} \operatorname{Im} \rho_{10}^2 \sin 2\theta \sin\varphi \right. \\
 &\quad \left. + \operatorname{Im} \rho_{1-1}^2 \sin^2\theta \sin 2\varphi \right]
 \end{aligned} \tag{5.4}$$

Three reference systems can be used to extract the SDMEs: Helicity, Gottfried-Jackson and Adair. In all three cases, we define the axes in the vector meson rest frame. The y -axis in all three reference systems is normal to the production plane and the systems therefore differ only in the definition of the z -axis. In Schilling's notation, in the centre-of-mass frame, the beam three-momentum is denoted k and the ϕ -meson three-momentum q . The y -axis, normal to the production plane, can therefore be defined as:

$$\hat{y} = \frac{k \times q}{|k \times q|}$$

The z -axis is set for each reference system as shown in Table 5.2 and the x -axis definition follows from $x = y \times z$.

System	z -axis
Helicity	\hat{q}
Gottfried-Jackson	Direction of photon in ϕ -meson rest frame
Adair	Direction of photon in centre-of-mass frame (equivalent to lab z)

Table 5.2: z -axis orientations.

In the analysis that follows, the results are extracted in each of the frames. This is useful to do as measurements extracted in each of the frames are sensitive to different reaction mechanisms.

5.2 Event Selection

The overall objective of this step is to identify candidate events which may correspond to this reaction, and retain these events to be used in the next step of the analysis (Signal Background

separation). Events which are not of interest are removed from the dataset thereby providing a much reduced set of events to be used in the signal extraction. The procedure starts with a set of cuts, first to identify the charged final state particles from their charge and mass. There are no further cuts at this stage to identify the reaction channel (i.e. to verify that the K^+ , K^- have decayed from a ϕ -meson. This is taken care of in the signal/background separation process. In order to fully describe the reaction we must also identify the beam photon which has caused the reaction, this is done using the same method described in Section 4.2.3. There are a few more improvements to the dataset done at this stage: events are restricted to those where the reaction vertex occurs within the target, and the energy and momenta of the detected particles is corrected for energy losses within the detector. Finally, the events carried forward to the next step are restricted to those where the photon polarisation is in the region of relatively high polarisation, within 200 MeV below the coherent peak settings described in Section 2.3. All of these procedures are described in detail in the remainder of this chapter.

5.2.1 Photon Energy Bins (Coherent Peak Settings)

For ϕ -meson photoproduction, a threshold photon energy of 1.57 GeV is required to produce the ϕ -meson from a proton target. Therefore, the events produced from the three highest energy coherent peak settings are used for this analysis, that is, photon energy from 1.5 GeV to 2.1 GeV. Events were limited to those where the photon energy was within the optimum region for high polarisation, a 200 MeV wide bin with an upper limit at the coherent edge position.

5.2.2 Hit Multiplicity and TOF Mass Cuts

After an initial event filter as described for the Σ^+ analysis to obtain a set of events which contain two or more charged particles, a series of cuts were made in order to loosely determine the final state particles.

The first step in the filtering was to select only events where 3 or 4 particles were recorded in CLAS along with a valid tagger hit. Once an event had satisfied these criteria an initial identification of the particles was made using the mass calculated from the drift chambers and time-of-flight system (TOF mass). The following criteria were used to make the initial identification taking the mass and charge from the EVNT bank in the cooked data:

- All particles of non-zero charge must have a valid hit in the drift chamber and either TOF or EC
- Particles with positive charge and $0.49 < M^2 < 1.44 \text{ GeV}^2/c^4$ were identified as protons
- Particles with positive charge and $0.09 < M^2 < 0.49 \text{ GeV}^2/c^4$ were identified as K^+
- Particles with negative charge and $0.09 < M^2 < 0.49 \text{ GeV}^2/c^4$ were identified as K^-

Events were then retained where at least two out of the three final state particles were detected with the intention that the third particle will be reconstructed from the missing mass for the reaction. A further constraint was placed on the missing mass (MM) for each of the topologies as follows.

- p, K^+, K^- detected: $-0.1 < MM < 0.1 \text{ GeV}/c^2$
- K^+ or K^- not detected: $0.4 < MM < 0.6 \text{ GeV}/c^2$
- p not detected: $0.84 < MM < 1.04 \text{ GeV}/c^2$

After the implementation of these restrictions the data set comprises the numbers of events per topology as shown in Figure 5.2. With the CLAS torus magnet polarity such that negatively charged particles were inbending towards the low acceptance region close to the beamline, it is mainly K^- particles which have escaped detection. Events where the K^- particle has escaped detection constitute over 70% of all events.

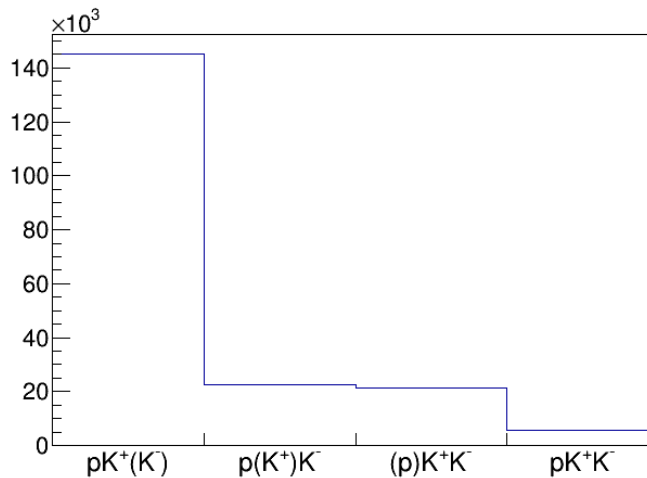


Figure 5.2: Number of events per topology.

Figure 5.3 shows β versus momentum for positively charged particles after the hit multiplicity and TOF mass cuts have been applied. The relationship between β and momentum depends on the mass of the particle resulting in characteristic trajectories for each particle. The trajectories for protons and kaons are evident in Figure 5.3. An additional check at this stage of the analysis is that the cuts around the mass are broad enough that no good protons or kaons are discarded. Since the bands around the particle trajectories on the β -momentum plots include background around the trajectories we can conclude that suitable mass cuts have been chosen. The plots shown are for events where the coherent edge was 2.1 GeV. Similar results have been obtained using different coherent edges.

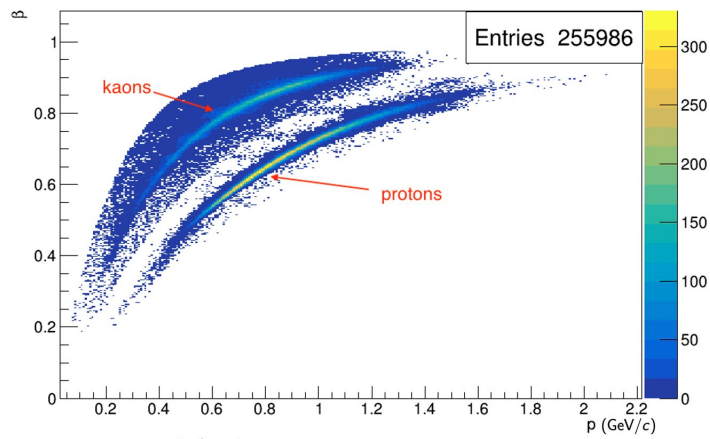


Figure 5.3: β vs momentum for positive particles after event selection based on number of particles and TOF mass. The plot shown is for events where the coherent edge was 2.1 GeV.

5.2.3 Z-Vertex Cut

Similar to the $K^0\Sigma^+$ analysis, events were restricted to those with z-vertex within the range of the g8b target position, $(-40, 0)$ cm. Figure 5.4 shows the effect of this cut.

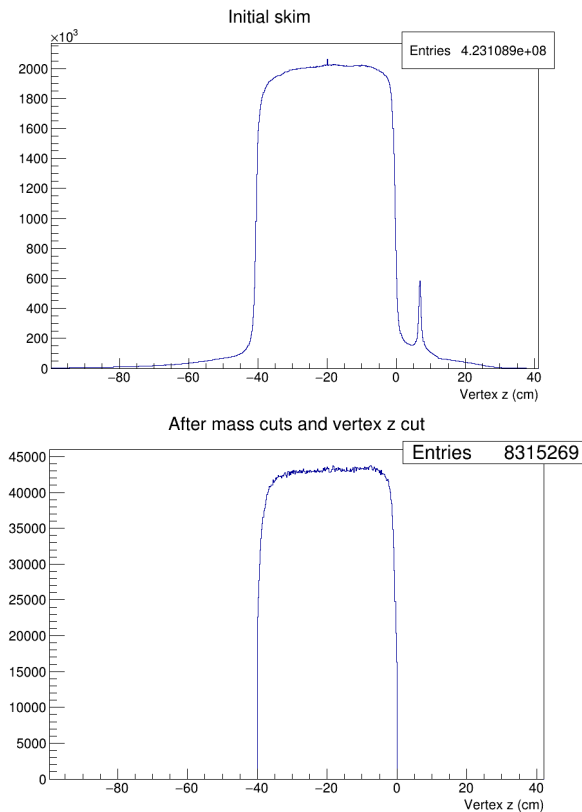


Figure 5.4: z-vertex distributions of the positive particles following initial skim (top) and with the applied cuts (bottom). The plots shown are for events where the coherent edge was 2.1 GeV.

5.2.4 Photon Selection

To identify the photon causing the reaction from the multiple photons recorded in the event, the proton vertex time is compared to the photon vertex time and the best photon is selected using the method described in Section 4.2.3. The vertex time difference distributions are shown in Figure 5.5.

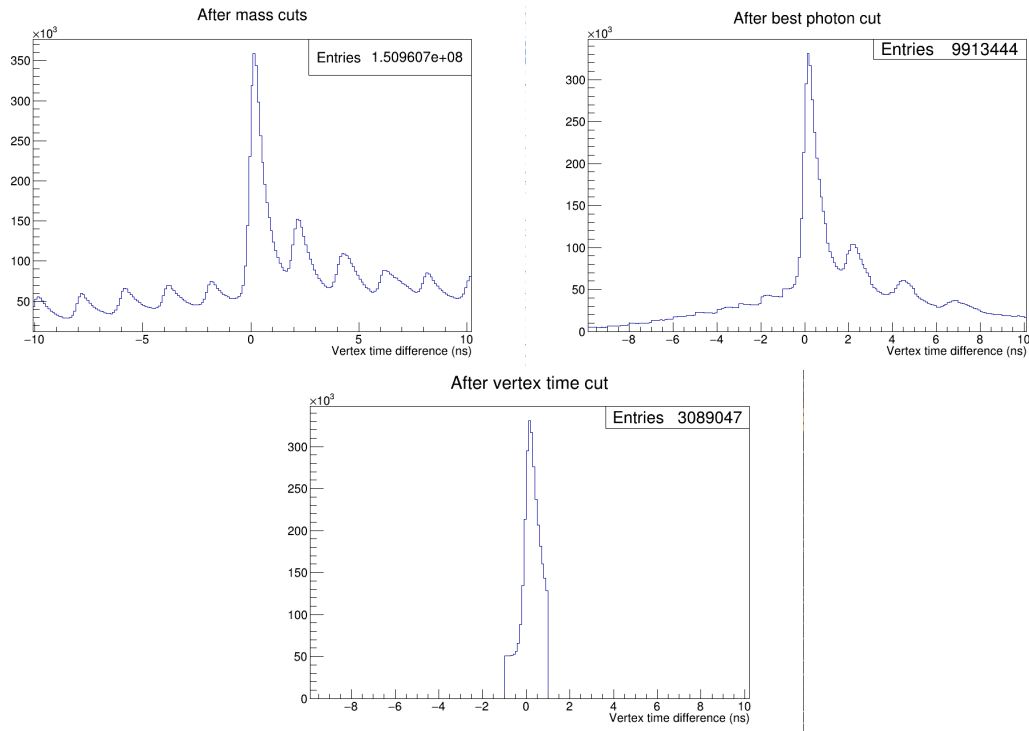


Figure 5.5: Tagger vertex time subtracted from the time-of-flight vertex time before best photon selection with the 2 ns beam bucket structure clearly evident (top left) and after photon selection (top right). The bottom plot shows the effect of the ± 1 ns cut on the time difference. The plots shown are for events where the coherent edge was 2.1 GeV

5.2.5 Energy Loss Corrections

Energy losses in the target and surrounding material were corrected by the ELOSS package [69]. The energy loss dependence on momentum for each of the detected particles is shown in Figure 5.6.

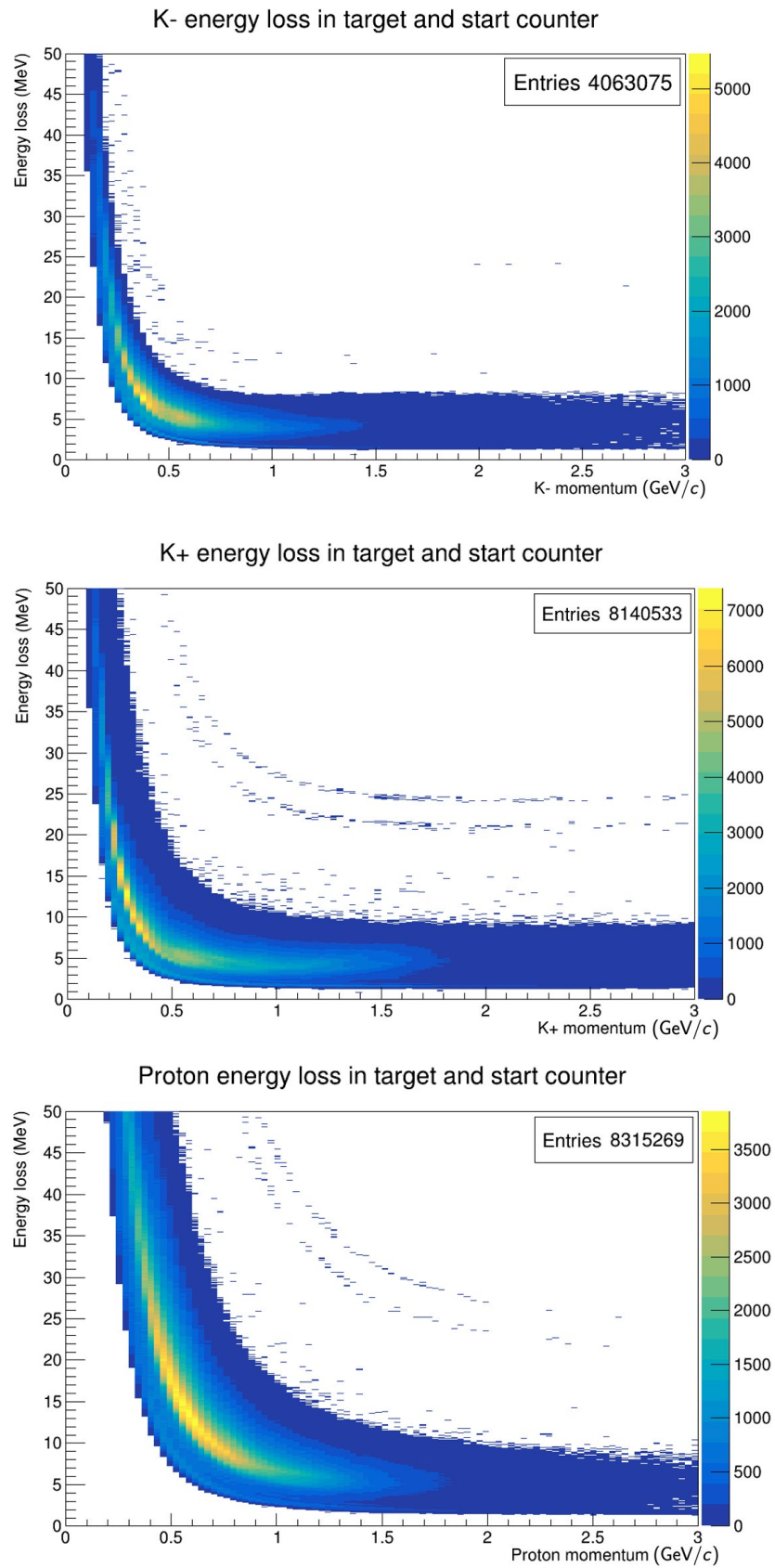


Figure 5.6: Energy loss vs. momentum for the K^- (top), K^+ (middle) and proton (bottom).

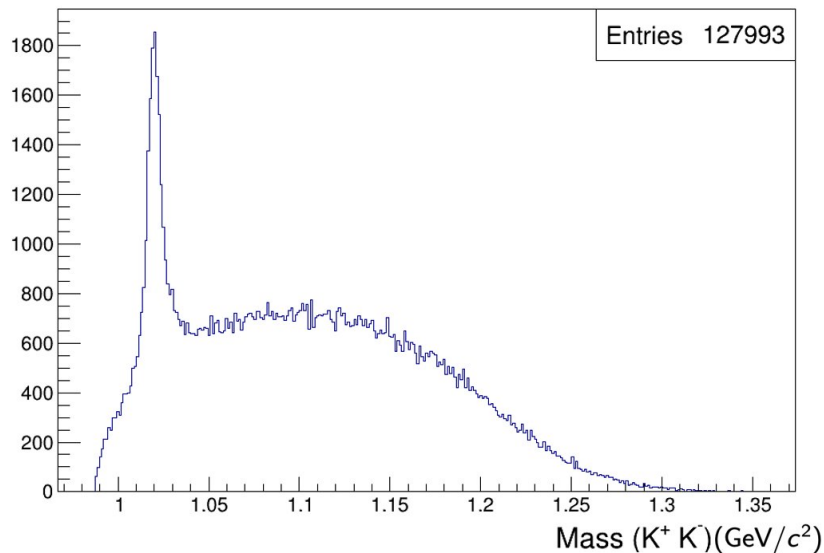


Figure 5.7: Invariant mass of (K^+K^-) . The ϕ peak is apparent at $1.019 \text{ GeV}/c^2$. The plot shown is for events where the coherent edge was 2.1 GeV .

5.2.6 Channel ID

With the final state particles identified we can examine the K^+K^- invariant mass distribution, shown in Figure 5.7 for events where the coherent peak was 2.1 GeV . The peak around the ϕ -meson mass of $1.019 \text{ GeV}/c^2$ where the two kaons reconstruct to the ϕ -meson are the signal events. However, we place no further cuts at this point as the signal-background separation procedure described in Section 5.3 will cut around this mass and fit the ϕ -meson peak to extract the signal events.

Contained within the background for the pK^+K^- final state, are events where the pK^- have been produced from the decay of a $\Lambda(1520)$ baryon. Specifically, we are seeing the reaction $\gamma p \rightarrow \Lambda K^+$, with the subsequent decay of the Λ to pK^- . The reaction is shown schematically in Figure 5.8. We can see these events as a peak at the Λ mass of $1.520 \text{ GeV}/c^2$ on the invariant mass distribution for pK^- as shown in Figure 5.9. The impact that these events will have on our extraction of ϕ -meson production events is apparent when we inspect the distribution of K^+K^- mass versus pK^- mass as shown in Figure 5.10. We can see that the vertical band of Λ events overlaps with the horizontal band of ϕ -meson events. Although we will cut around the ϕ -meson mass during signal extraction removing the majority of these, some Λ events will remain.

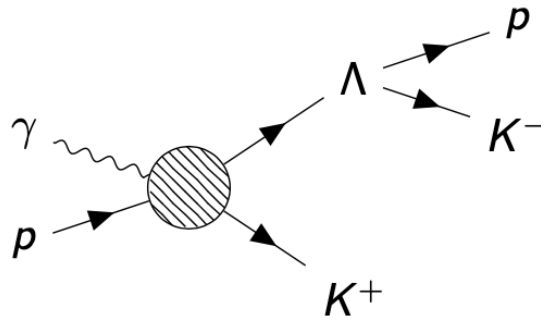


Figure 5.8: Schematic view of the $\gamma p \rightarrow \Lambda K^+$ reaction and subsequent decay.

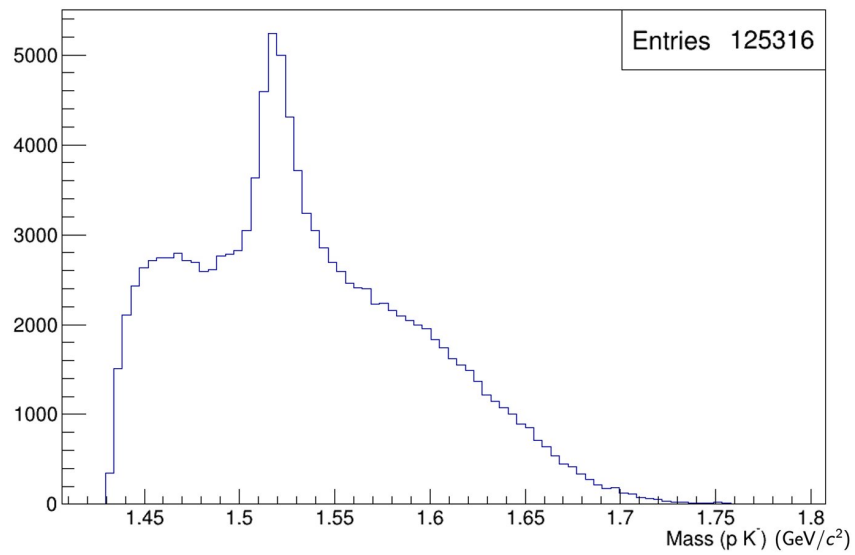


Figure 5.9: Invariant mass of $(p K^-)$. The Λ peak is apparent at $1.520 \text{ GeV}/c^2$. The plot shown is for events where the coherent edge was 2.1 GeV .

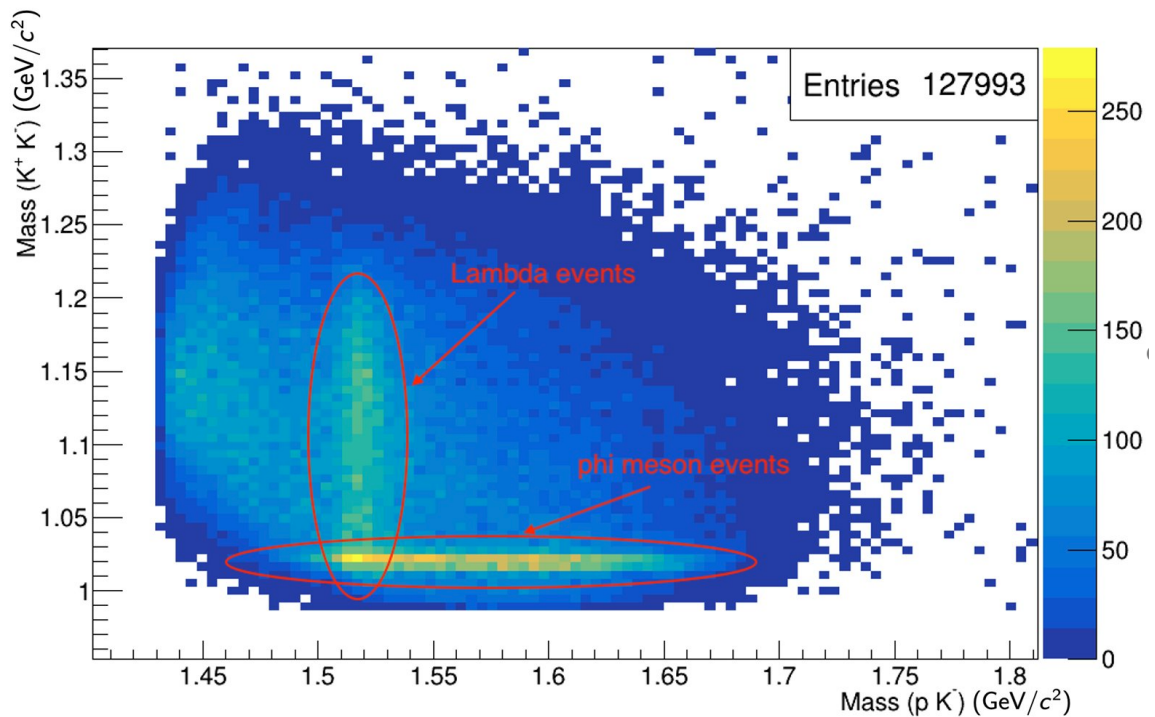


Figure 5.10: Invariant mass of (K^+K^-) versus invariant mass of $(p K^-)$ showing the overlap of Λ production with ϕ production. The plot shown is for events where the coherent edge was 2.1 GeV.

5.2.7 Summary

Applied Cut	Details	# of Events
Initial skim	2 to 3 charged particles in final state	approx. 7×10^8
z-vertex cut, proton and kaon mass cuts	$-40 < z < 0$ cm $0.49 < M^2(p) < 1.44 \text{ GeV}^2/c^4$ $0.09 < M^2(K^{+/-}) < 0.49 \text{ GeV}^2/c^4$	3.2×10^7
γp vertex timing	$ \text{Vertex time}(\text{best photon}) - \text{Vertex time}(\text{proton}) < 1.0$ ns	1.1×10^7
Missing Mass cuts	Missing Mass (GeV/c^2) $\in (-0.1, 0.1)$ $(p, K^+, K^- \text{ detected})$ Missing Mass (GeV/c^2) $\in (0.4, 0.6)$ (missing kaon) Missing Mass (GeV/c^2) $\in (0.84, 1.04)$ (missing proton)	2.1×10^5

Table 5.3: Analysis cuts applied and resulting number of events for all coherent peak settings.

An analysis algorithm was developed to allow for the identification of the particles of interest for $\vec{\gamma}p \rightarrow p\phi$. Initial filters based on simple TOF mass cuts were used to skim the dataset down to a manageable size for full analysis. Various cuts were then implemented to reduce the background and correctly identify the detected final state particles, without discarding too many good events.

5.3 Signal/Background Separation with sPlots

In order to separate signal from background, the sPlots technique is used once again. More details of the technique can be found in Section 3.1.1. Having identified the final state, we now wish to produce signal weights corresponding to the events where the K^+ and K^- arise from the decay of the ϕ -meson. We therefore choose the invariant mass of the 2 kaon system as our discriminatory variable and perform a fit in the region of the ϕ -meson mass ($1019 \text{ MeV}/c^2$).

5.3.1 Binning

The bins in E_γ and $\cos\theta$ of the ϕ -meson in the centre-of-mass system were chosen such that the integrated signal weight in each bin was approximately 1000 weighted events. With 3 uniform bins in E_γ and variable bins in $\cos\theta$, we can obtain 18 bins as shown in Figure 5.11.

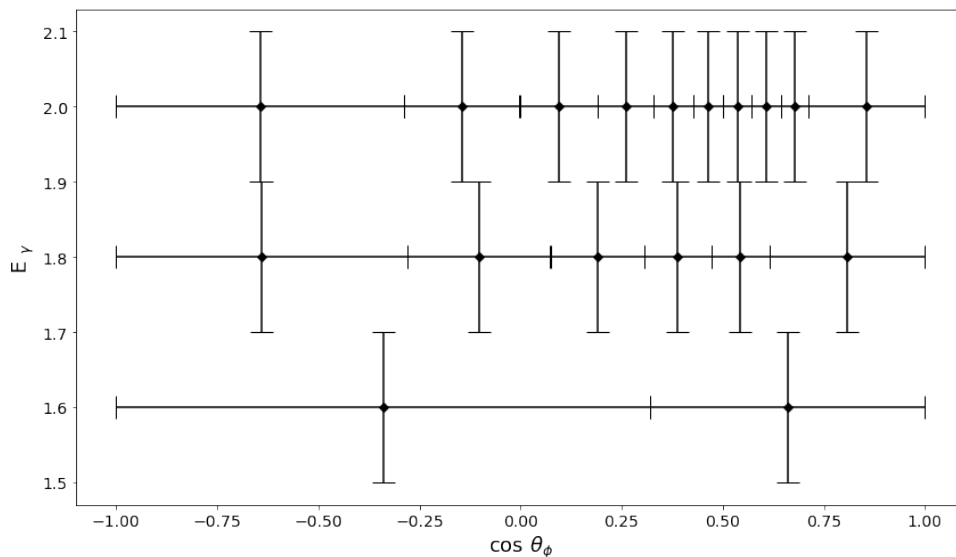


Figure 5.11: Binning system used throughout the ϕ -meson SDME analysis.

5.3.2 Extraction of Weights

In order to obtain the signal weights, we fit around the mass of the ϕ -meson (reconstructed from the mass of K^+K^-). We fit the peak as a Gaussian on a quadratic Chebyshev polynomial

background. A representative selection of the fits for 6 $\cos\theta_\phi$ bins for $E_\gamma = 1.80$ GeV are shown in Figures 5.12 and 5.13.

In each of these subplots, the left plot shows data points in black, combined signal and background model in solid red, signal in dotted black, and background in dotted red. Top right and bottom right are residual and pull respectively.

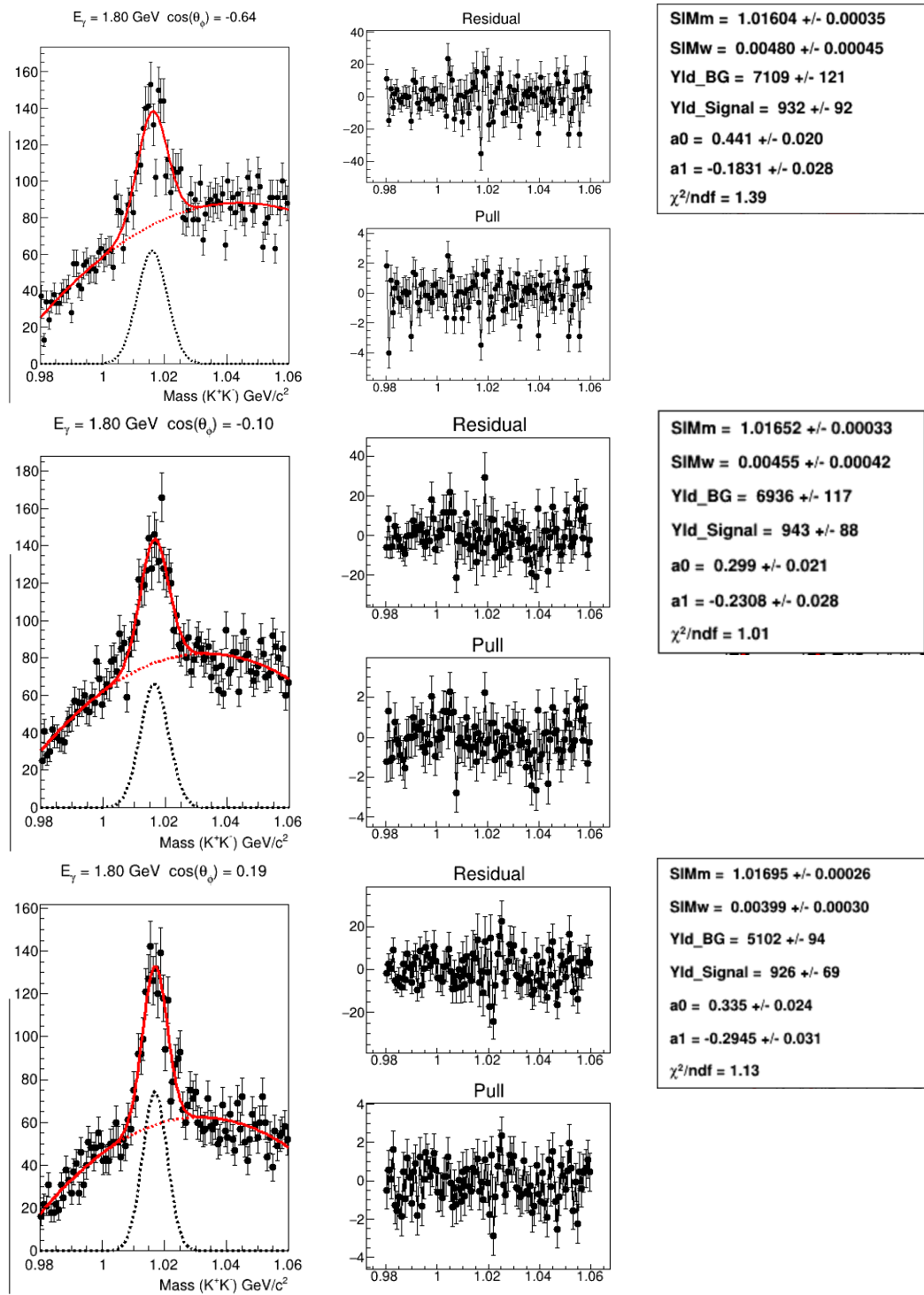


Figure 5.12: ϕ mass fits for E_γ bin 1.80 GeV, $\cos\theta_\phi$ bins -0.64, -0.10 and 0.19. The fit parameters are the signal gaussian mean and width (SIMm and SIMw), the signal and background yield (Yld_Signal and Yld_BG), and the background function parameters.

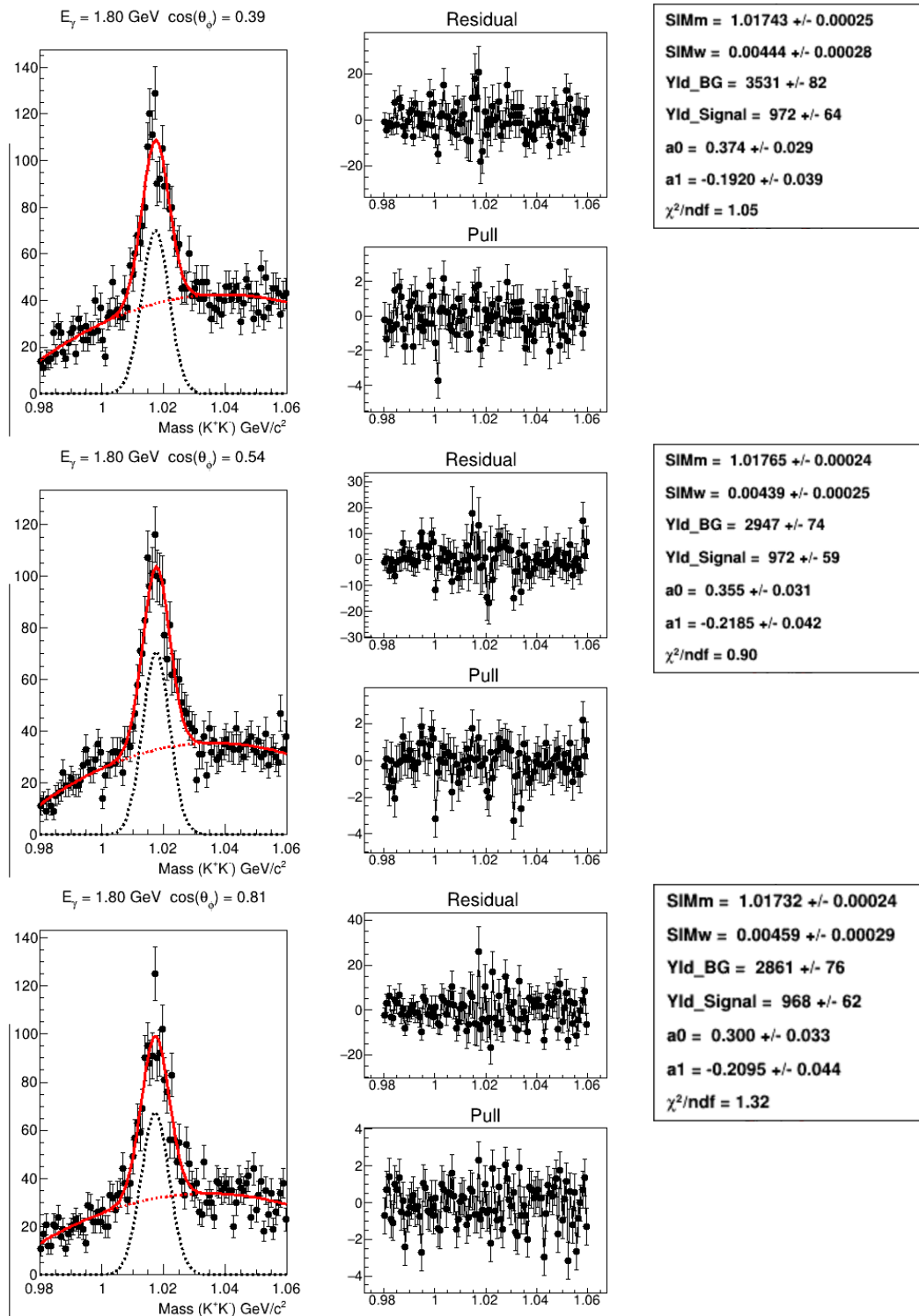


Figure 5.13: ϕ mass fits for E_γ bin 1.80 GeV, $\cos\theta_\phi$ bins 0.39, 0.54 and 0.81. The fit parameters are the signal gaussian mean and width (SIMm and SIMw), the signal and background yield (Yld_Signal and Yld_BG), and the background function parameters.

5.3.3 Weighted Mass Distributions

It can be seen from the sWeights fits shown in the previous section that the events corresponding to ϕ -meson production have been successfully assigned signal weights. Using these weights, we can also examine the background contributions, particularly the presence of events where a $\Lambda(1520)$ baryon has been produced as described in Section 5.2.6. Figure 5.14 shows the invariant mass of the $p K^-$ for signal weights in red, and background weights in blue. The peak at $1520 \text{ MeV}/c^2$ where the $p K^-$ have decayed from a $\Lambda(1520)$ is prominent in the background weighted distribution, however the peak is much reduced in the signal weighted distribution.

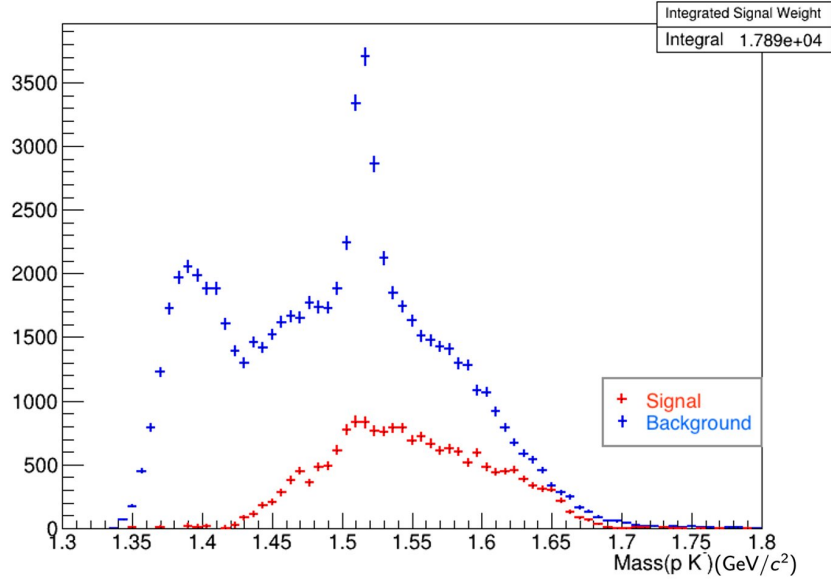


Figure 5.14: Signal and Background weighted distributions for the invariant mass of pK^- . Signal weighted events are shown in red, Background weighted events are shown in blue. The prominent peak in the background at $1520 \text{ MeV}/c^2$ are $\Lambda(1520)$ events.

5.4 Simulation

Simulated data were produced in a similar manner to the Σ^+ analysis (described in Section 4.4) using the “EdGen” [71] event generator and the g8 simulation and reconstruction. In this case, only two vertices are required, the beam target interaction and the decay of the ϕ -meson to K^+K^- . Since the mean lifetime of the ϕ -meson is 1.55×10^{-22} s, there is no need for a detached vertex. An initial 10^6 events were generated resulting in 7×10^5 events being detected. The ratio of simulated events to signal events in the data is therefore 30:1.

The distributions in E_γ and t for simulation and data are shown in Figure 5.15. Ideally, the simulation would be weighted so that the random events generated in phase space were accepted or rejected based on a probability derived from the real distributions of E_γ and the transferred momentum, t , so that the simulated distributions in E_γ and t resembled those in the data. This

may be done in a future improvement of the analysis.

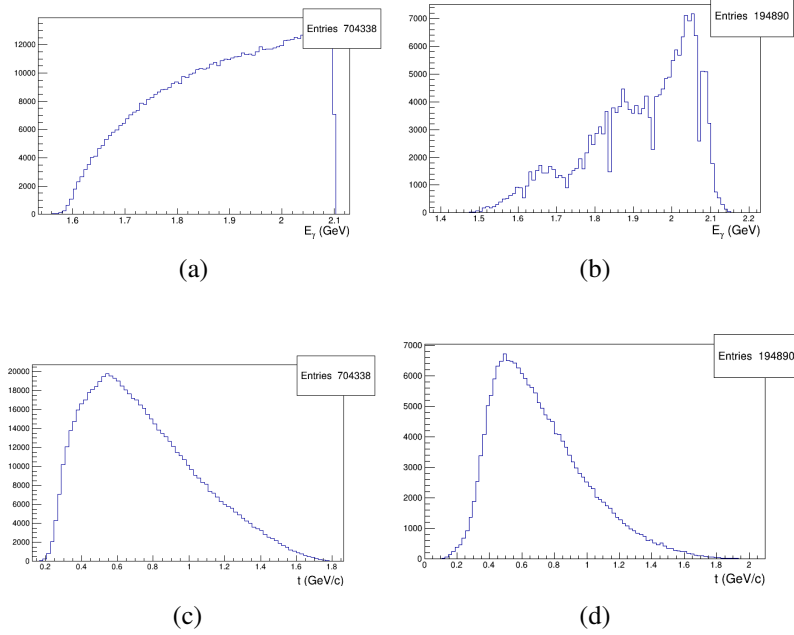


Figure 5.15: Distributions in E_γ (top row) and t (bottom row) showing simulation (left) and data (right).

5.5 Extracting Spin Density Matrix Elements

Likelihood sampling using Markov Chain Monte Carlo is performed in order to extract the spin density matrix elements (SDMEs). In the calculation of the likelihood, we use the intensity distribution as described in Section 5.1. The kinematic variables and reference frames are also described in this section. The SDMEs are extracted in each of the three commonly used reference frames: helicity, Gottfried-Jackson and Adair.

5.5.1 MCMC Time Series and Posterior Distributions

The MCMC sampling was performed until 2000 steps had been accepted in the chain. This number includes 50 burn in steps which are excluded from the posterior distributions. The proposal acceptance fraction varied from 18% to 38% with most bins around 30%. The resulting probability density functions for each of the nine SDMEs are shown for a typical bin in Figures 5.16 (Helicity system), 5.17 (Gottfried-Jackson system), and 5.18 (Adair system). In addition to this we can examine the correlation between observables in the corner plots shown in Figures 5.19 to 5.21. The plots show that no strong correlation between any of the variables has been detected. The time evolution of the MCMC steps is shown in Figures 5.19 to 5.21, where we see that the distribution has settled around the mean value well before the 50 burn in steps have

been generated. Further, the sampled values are immediately around the extracted value. This is possible as no steps are accepted in the chain until they are relatively likely compared to the starting values provided.

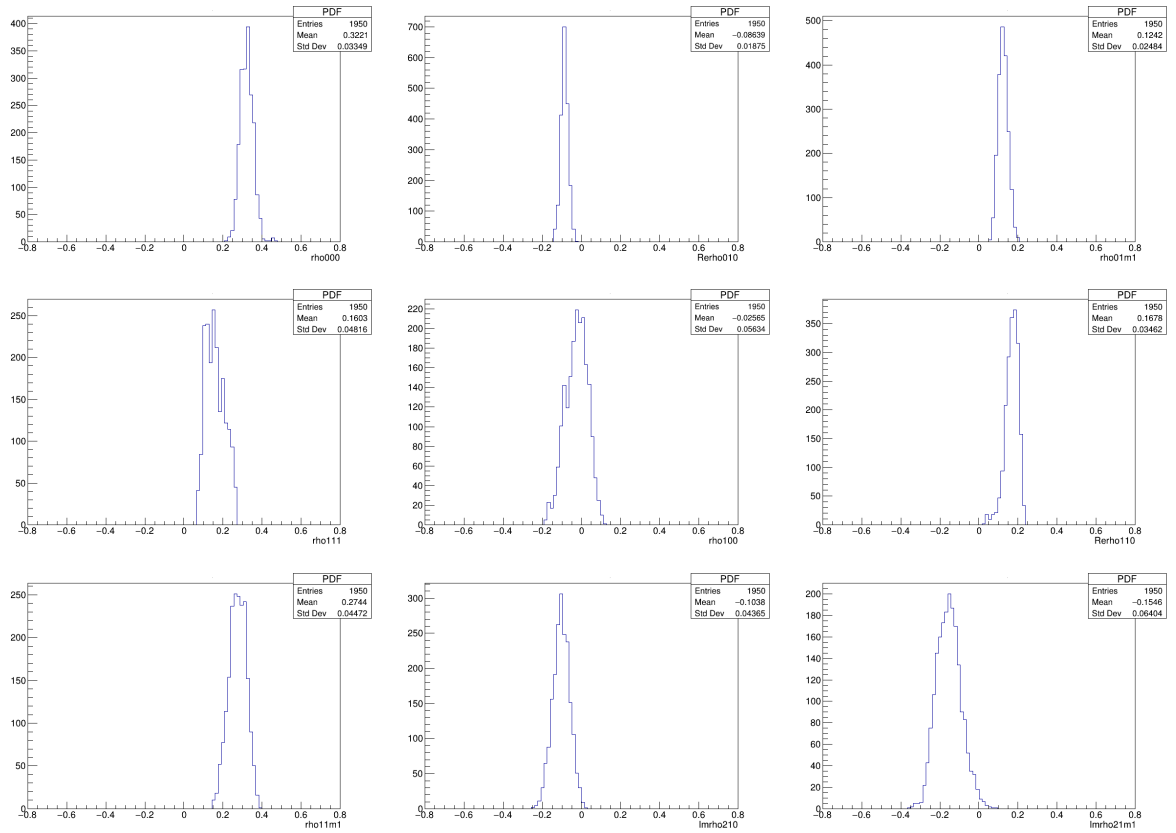


Figure 5.16: Posterior probability density functions for SDMEs extracted for a typical bin ($E_\gamma = 2.00$ GeV, $\cos(\theta_\phi) = 0.26$) in the helicity system

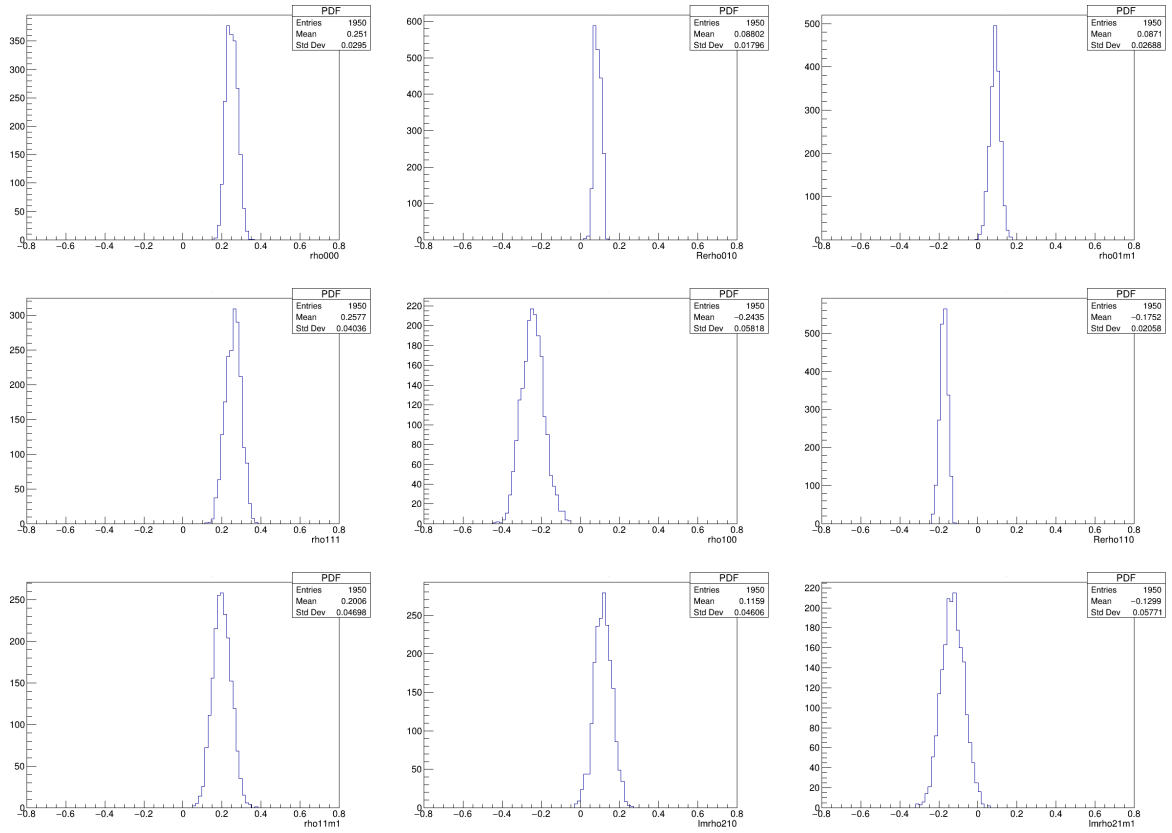


Figure 5.17: Posterior probability density functions for SDMEs extracted for a typical bin ($E_\gamma = 2.00$ GeV, $\cos(\theta_\phi) = 0.26$) in the Gottfried-Jackson system

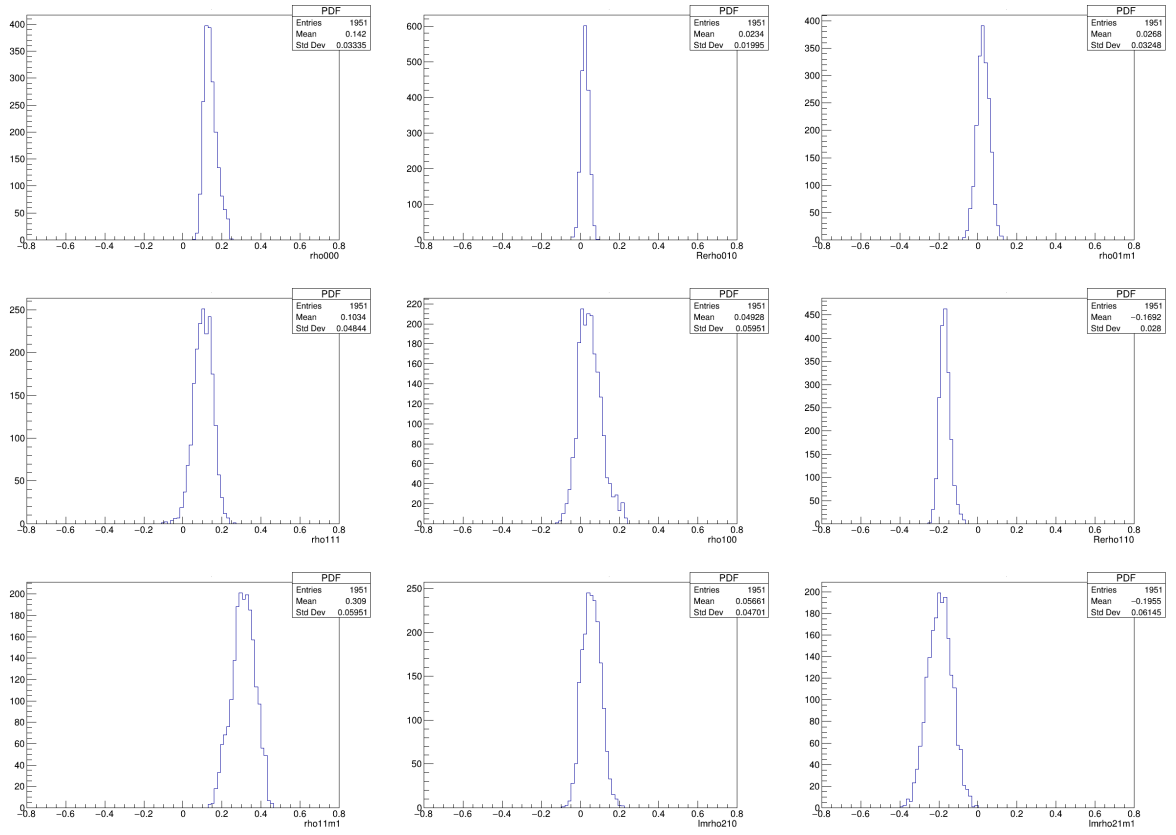


Figure 5.18: Posterior probability density functions for SDMEs extracted for a typical bin ($E_\gamma = 2.00$ GeV, $\cos(\theta_\phi) = 0.26$) in the Adair system

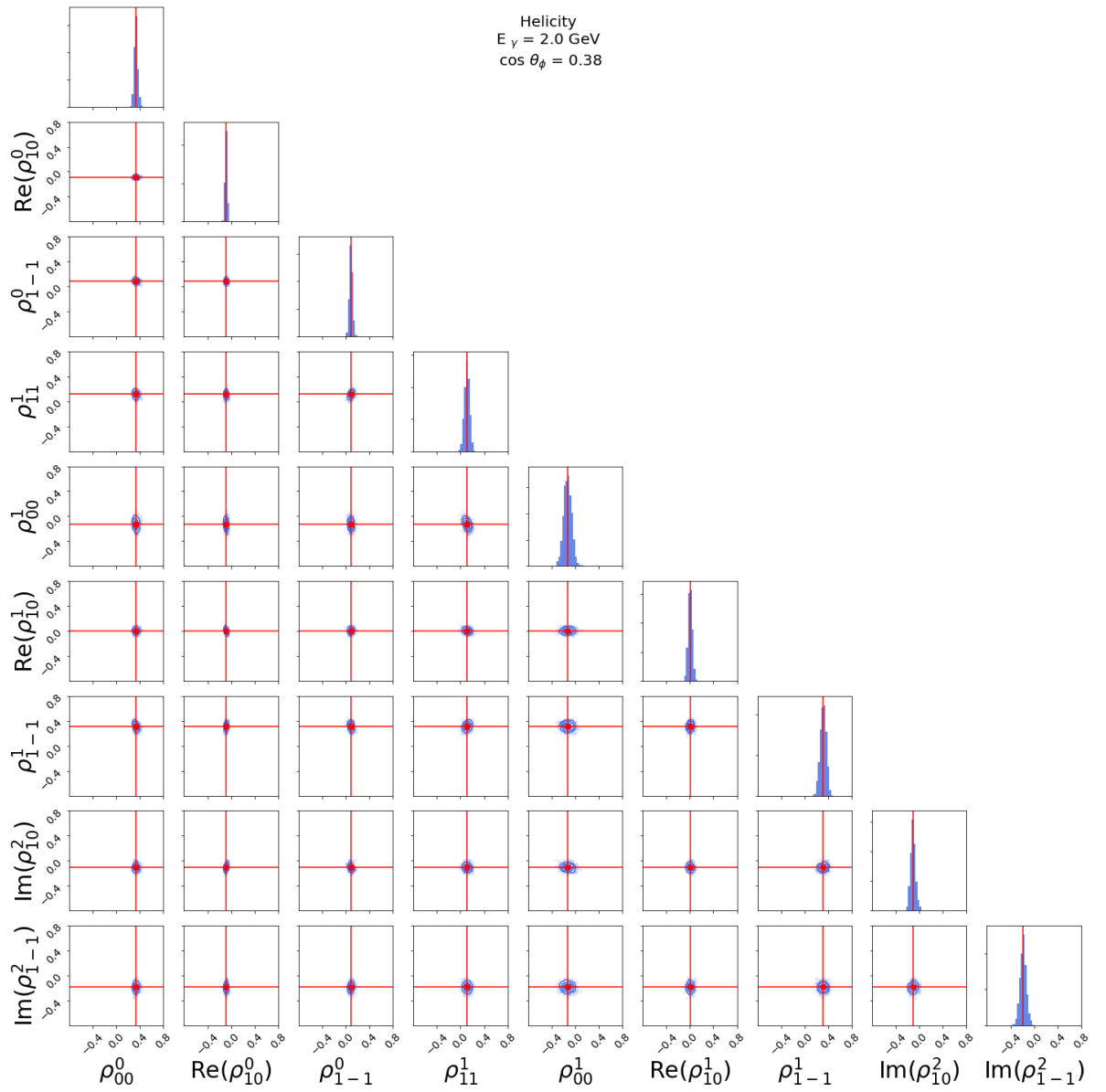


Figure 5.19: PDFs and correlations for a typical bin ($E_\gamma = 2.00 \text{ GeV}$, $\cos(\theta_\phi) = 0.26$) in the Helicity system

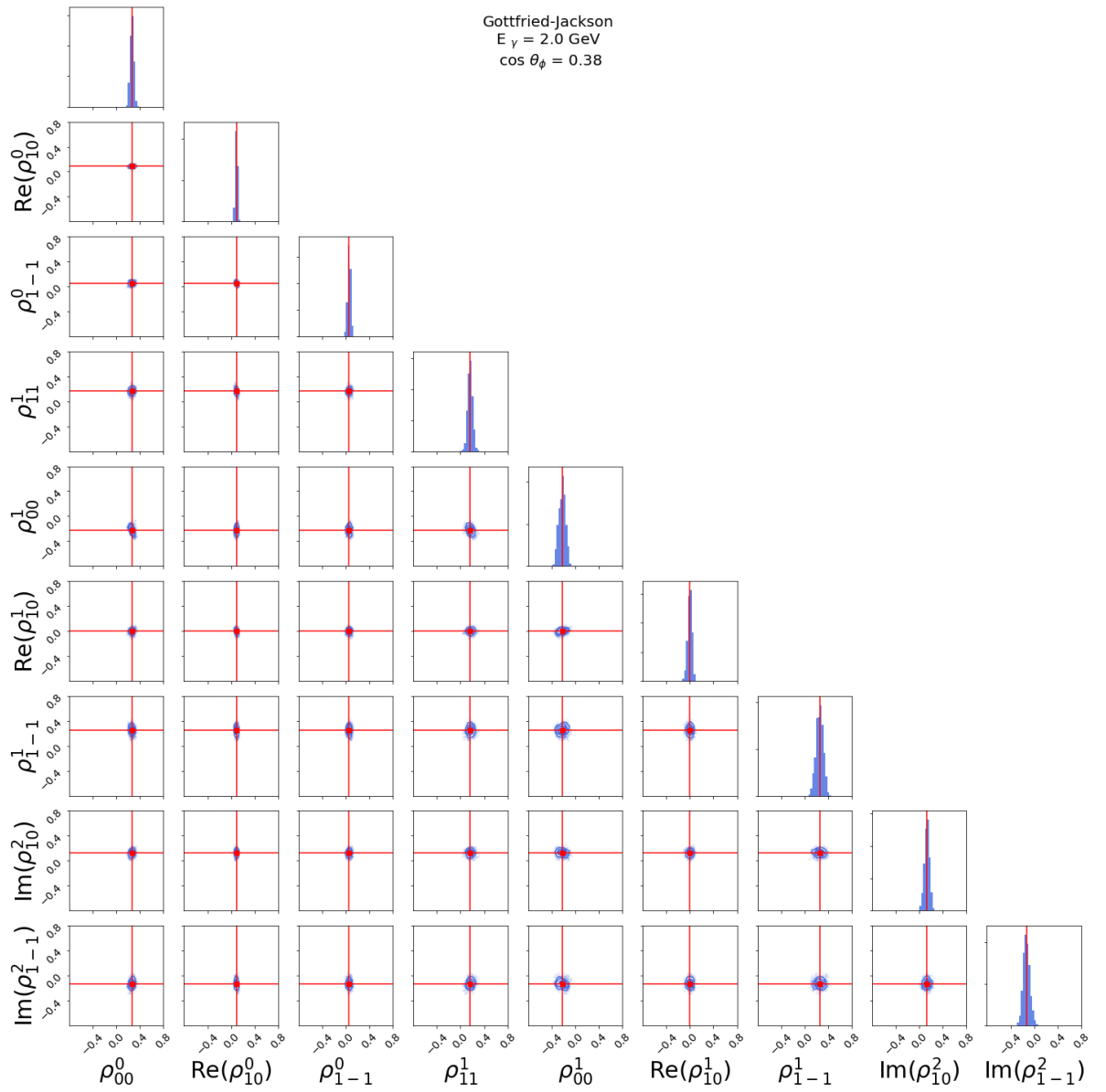


Figure 5.20: PDFs and correlations for a typical bin ($E_\gamma = 2.00$ GeV, $\cos(\theta_\phi) = 0.26$) in the Gottfried-Jackson system

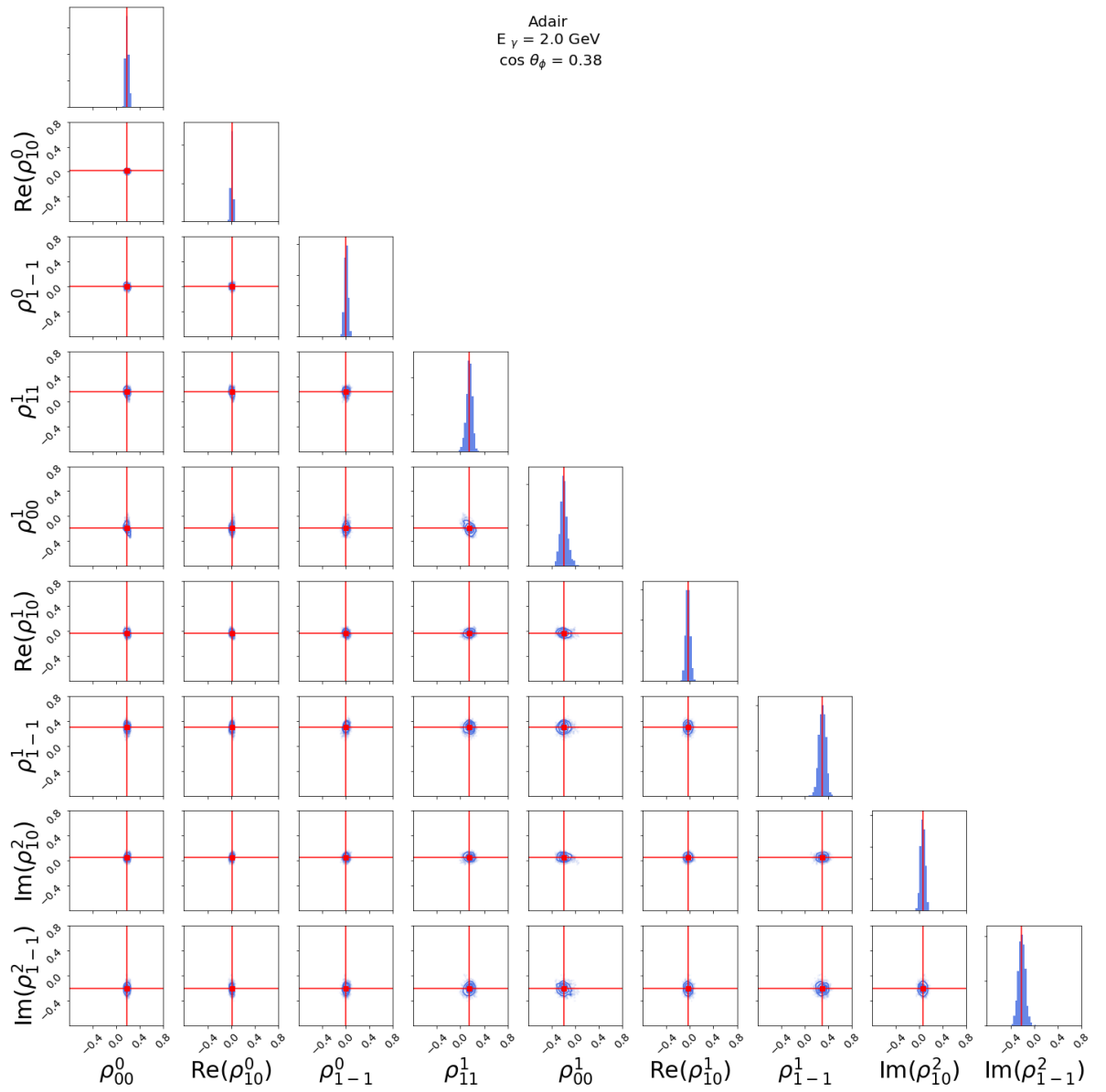


Figure 5.21: PDFs and correlations for a typical bin ($E_\gamma = 2.00$ GeV, $\cos(\theta_\phi) = 0.26$) in the Adair system

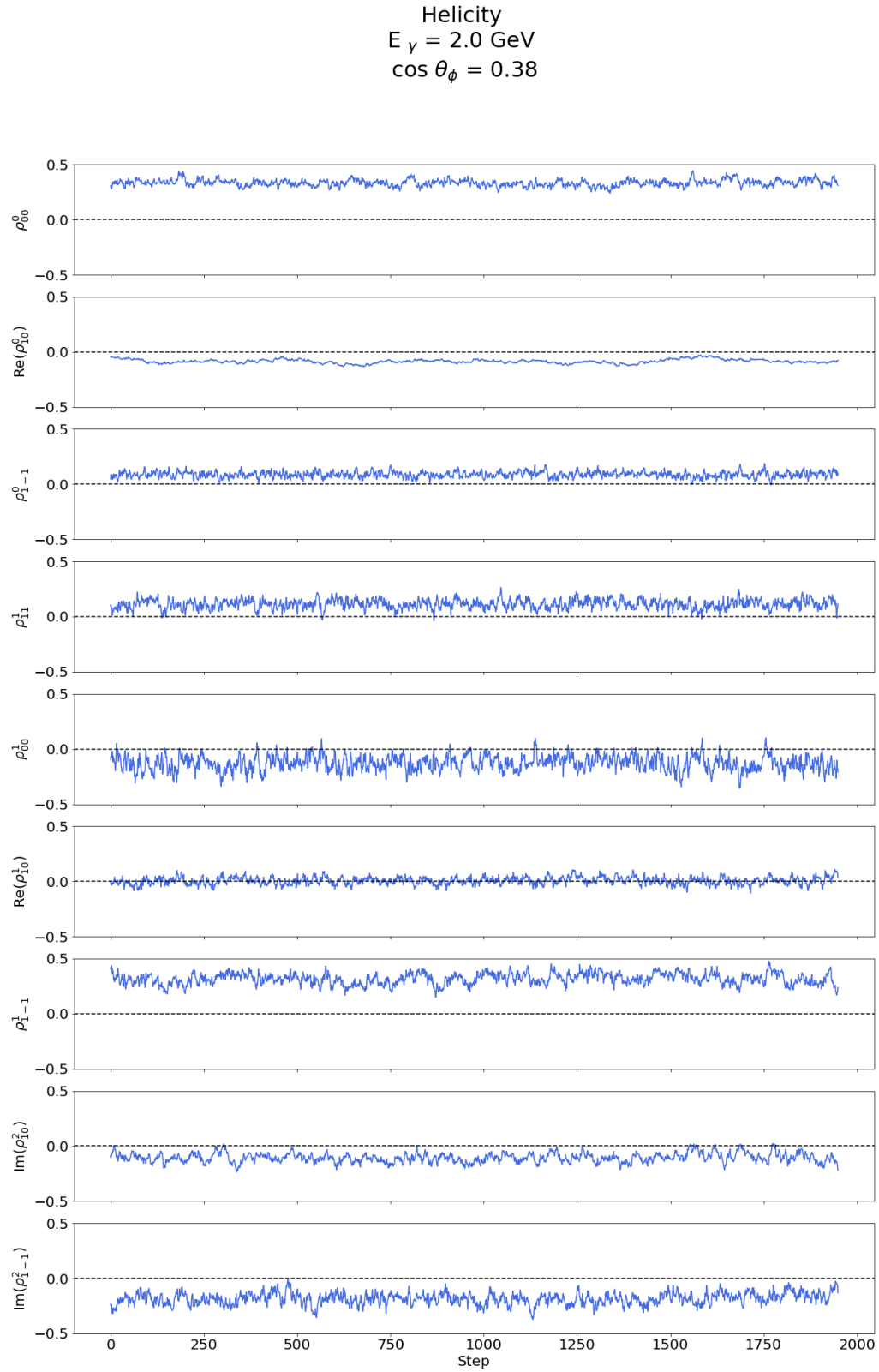


Figure 5.22: MCMC time series for a typical bin ($E_\gamma = 2.00$ GeV, $\cos(\theta_\phi) = 0.26$) in the Helicity system

Gottfried-Jackson
 $E_\gamma = 2.0$ GeV
 $\cos\theta_\phi = 0.38$

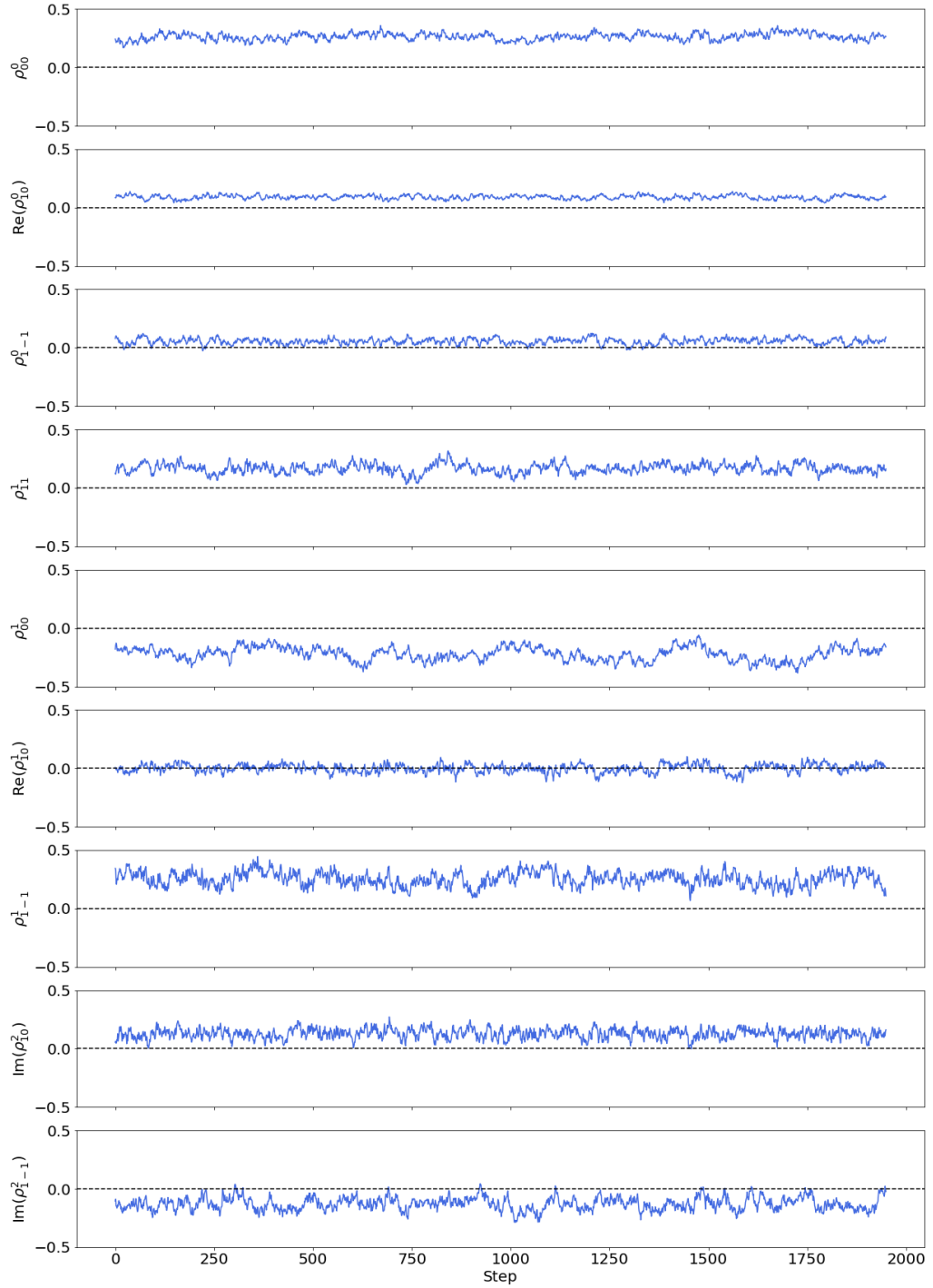


Figure 5.23: MCMC time series for a typical bin ($E_\gamma = 2.00$ GeV, $\cos(\theta_\phi) = 0.26$) in the Gottfried-Jackson system

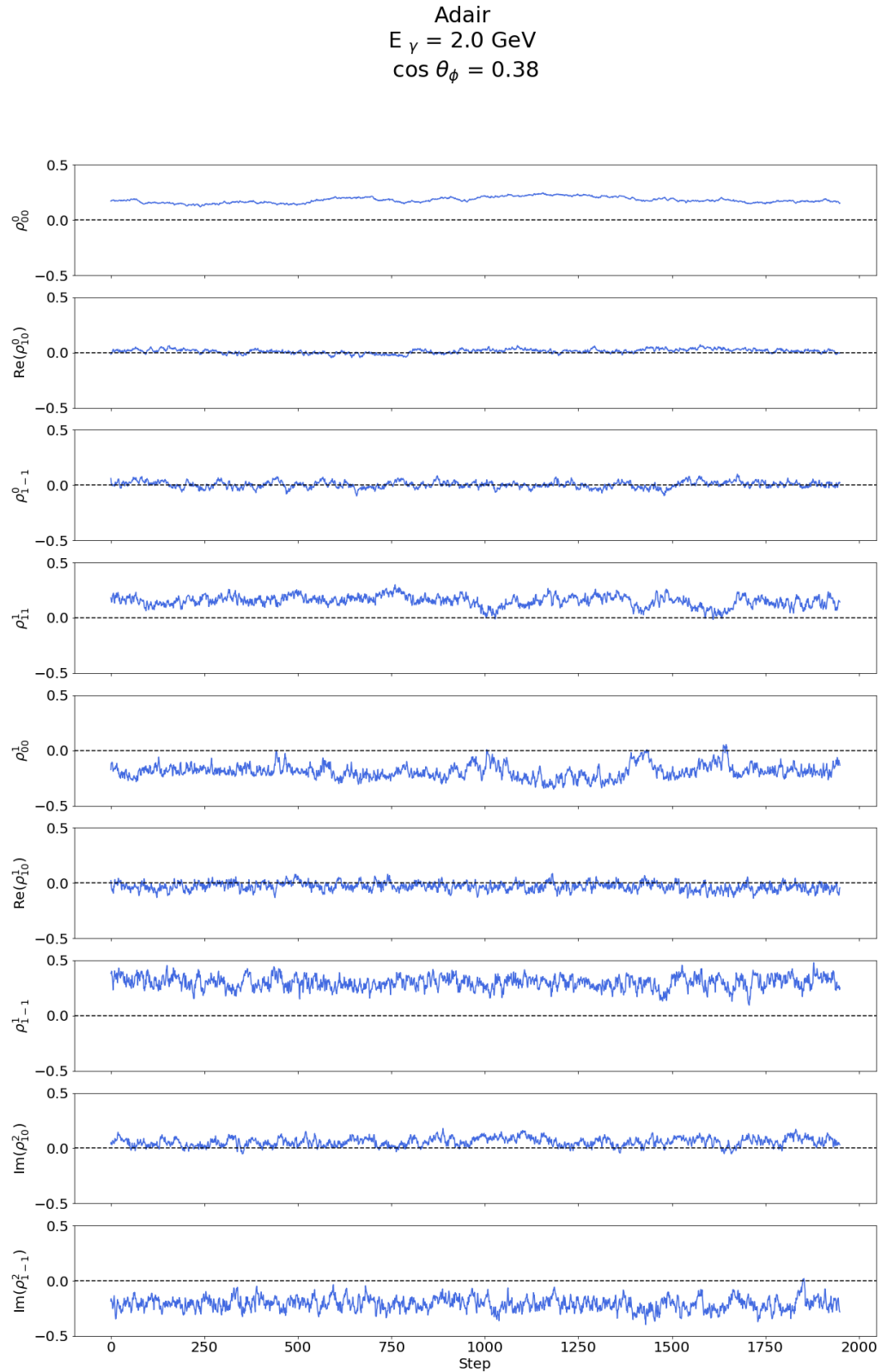


Figure 5.24: MCMC time series for a typical bin ($E_\gamma = 2.00$ GeV, $\cos(\theta_\phi) = 0.26$) in the Adair system

5.5.2 Results

The posterior PDFs obtained using the MCMC likelihood analysis provide all the information which has been extracted by the study. In order to characterise the distributions with a discrete set of values, we extract: mean, standard deviation, 16th, 25th, 50th (median), 75th, and 84th quantiles. These are tabulated in Appendix D. The results are plotted in Figures 5.25 to 5.27 (Helicity system), Figures 5.28 to 5.30 (Gottfried-Jackson system), and Figures 5.31 to 5.33 (Adair system). The points plotted are the median of the posterior PDF and the error bars extend from the 16th to the 84th quantile. Specifically, 68% of the MCMC sample lie within the error bars, equivalent to an uncertainty of 1σ .

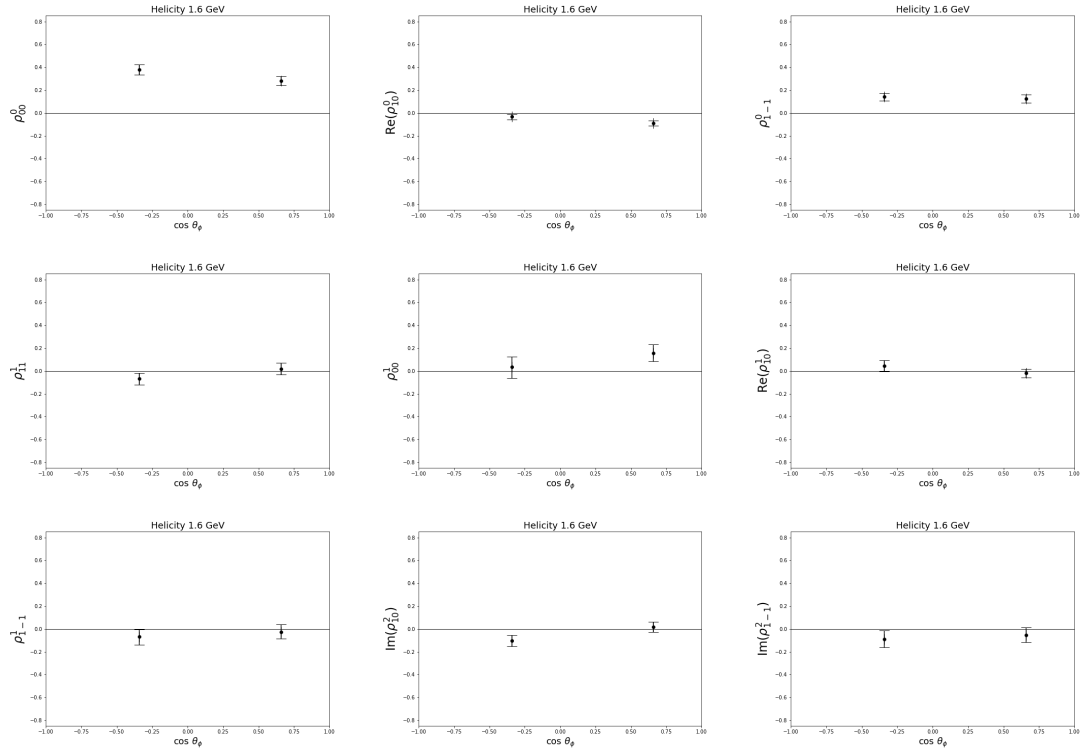


Figure 5.25: Measurements obtained for SDMEs in the 1.6 GeV energy bin in the Helicity system.

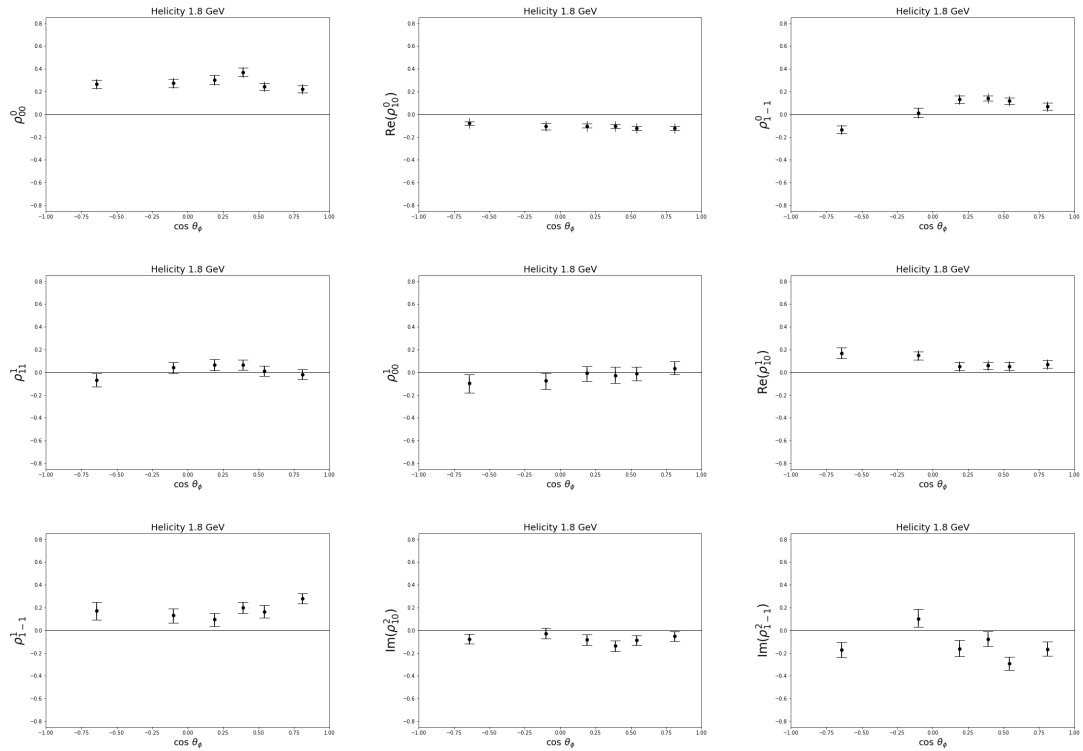


Figure 5.26: Measurements obtained for SDMEs in the 1.8 GeV energy bin in the Helicity system.

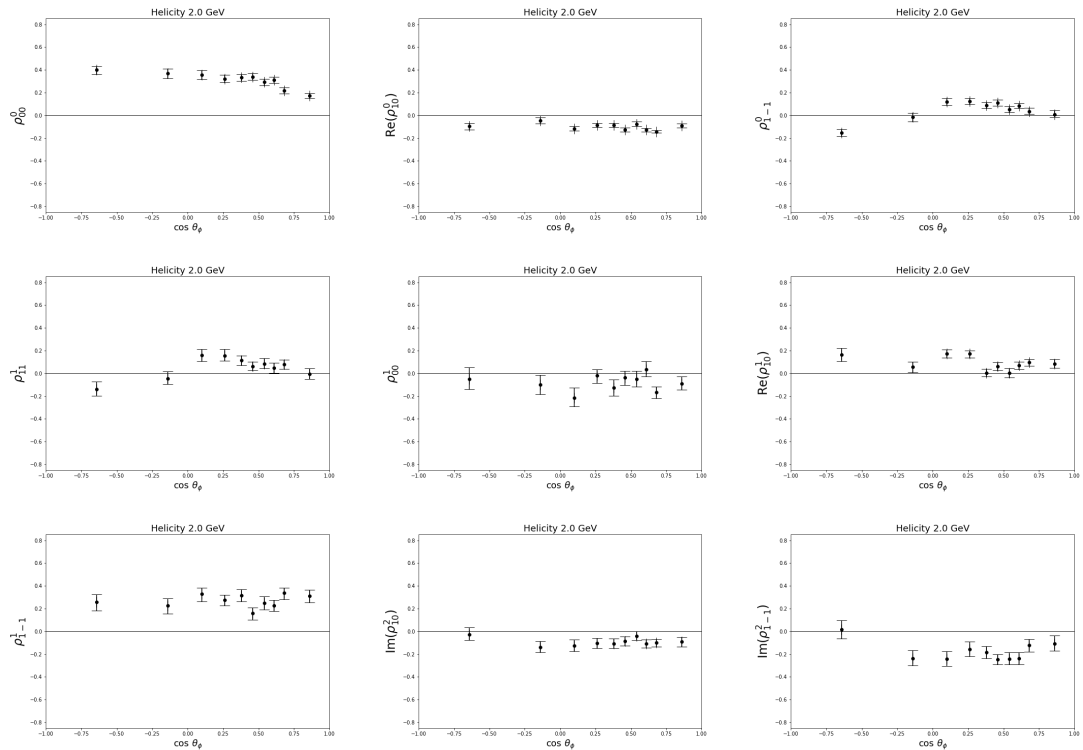


Figure 5.27: Measurements obtained for SDMEs in the 2.0 GeV energy bin in the Helicity system.

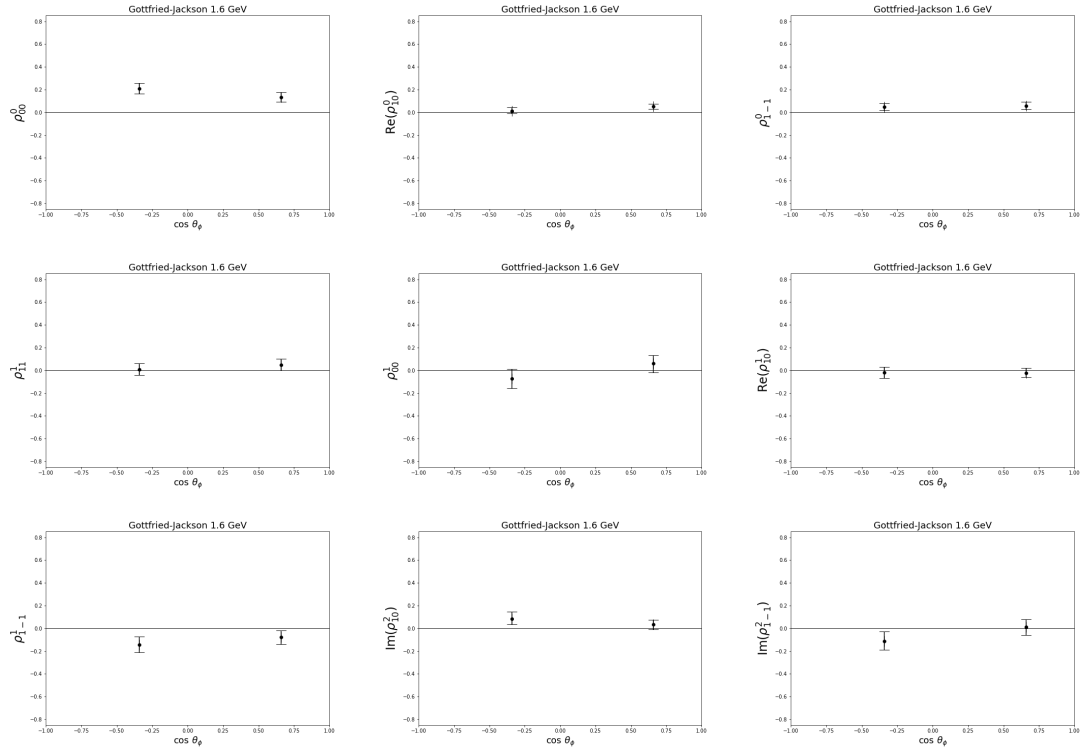


Figure 5.28: Measurements obtained for SDMEs in the 1.6 GeV energy bin in the Gottfried-Jackson system.

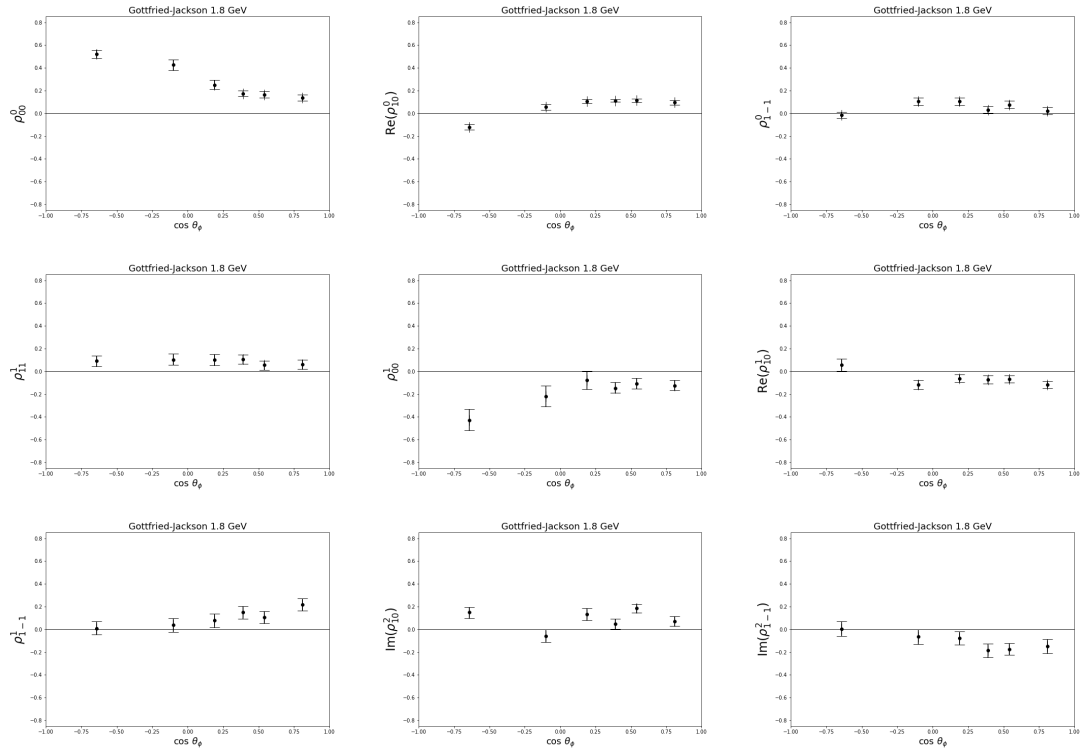


Figure 5.29: Measurements obtained for SDMEs in the 1.8 GeV energy bin in the Gottfried-Jackson system.

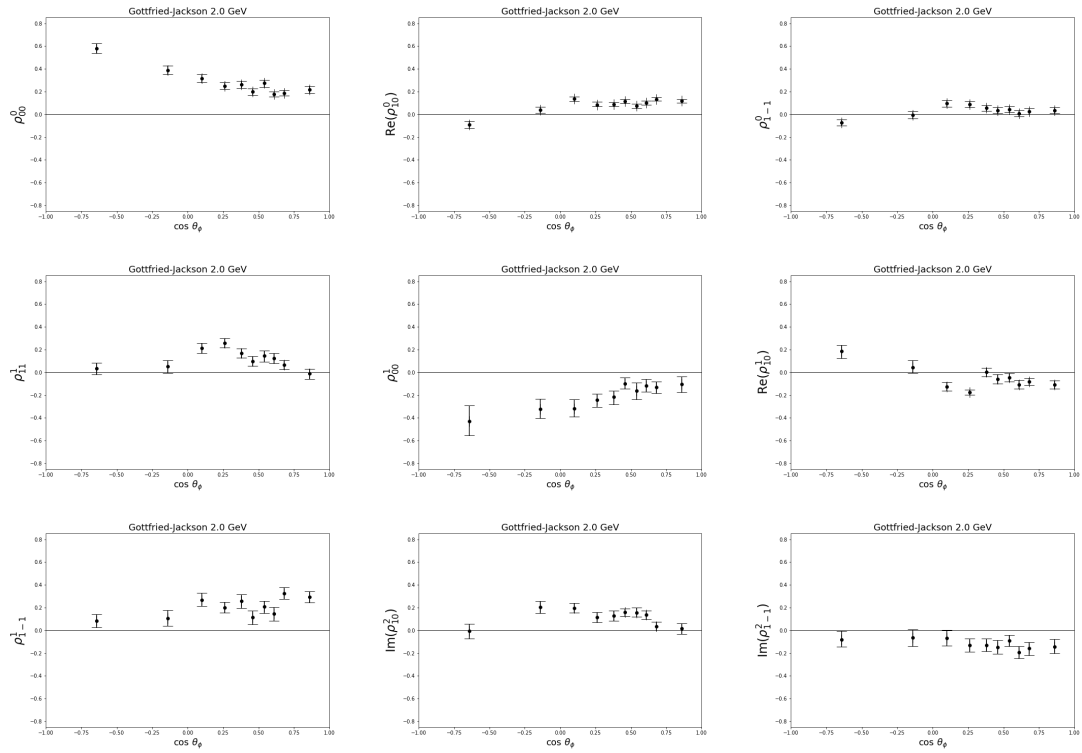


Figure 5.30: Measurements obtained for SDMEs in the 2.0 GeV energy bin in the Gottfried-Jackson system.

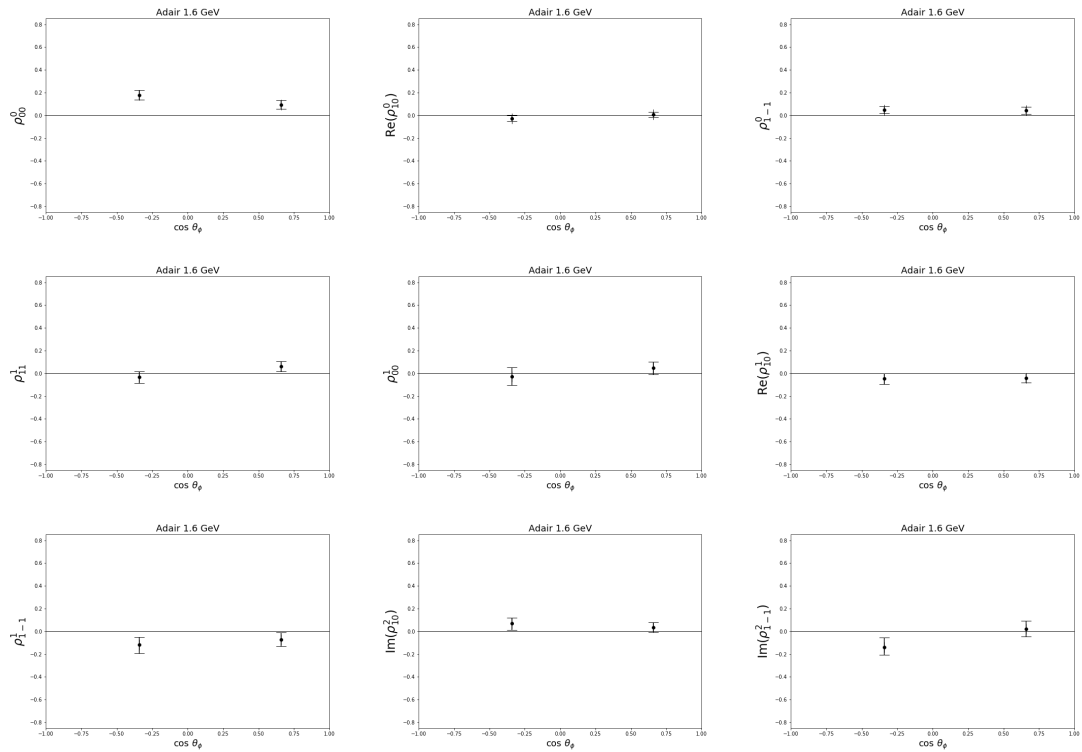


Figure 5.31: Measurements obtained for SDMEs in the 1.6 GeV energy bin in the Adair system.

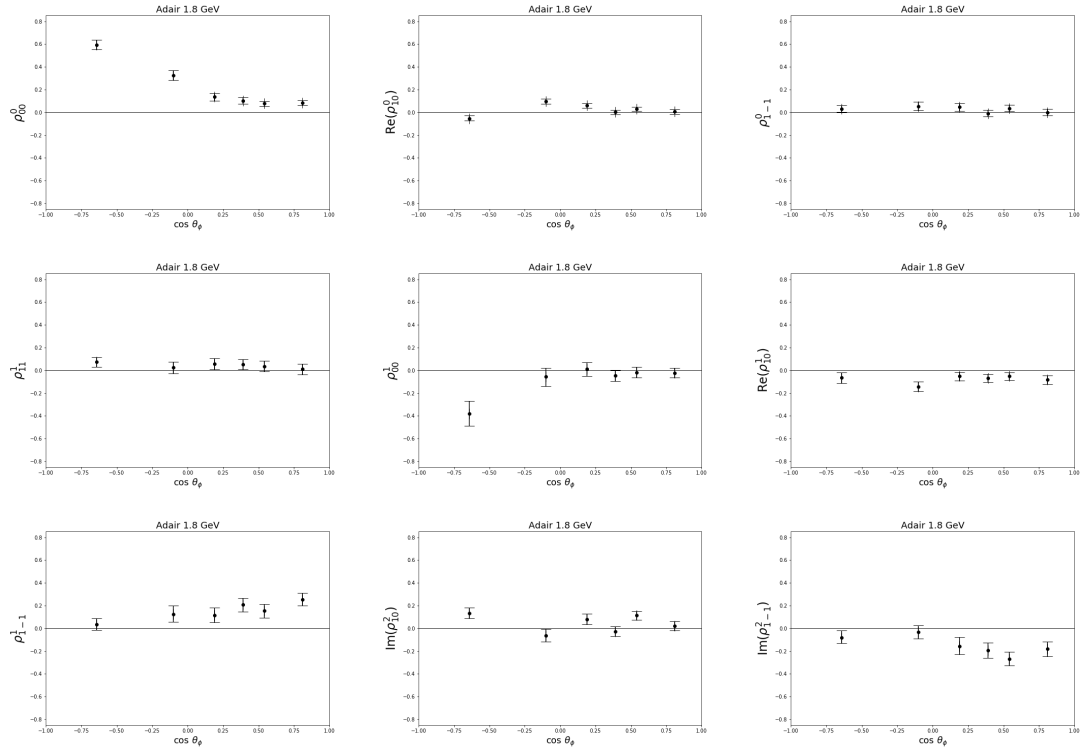


Figure 5.32: Measurements obtained for SDMEs in the 1.8 GeV energy bin in the Adair system.

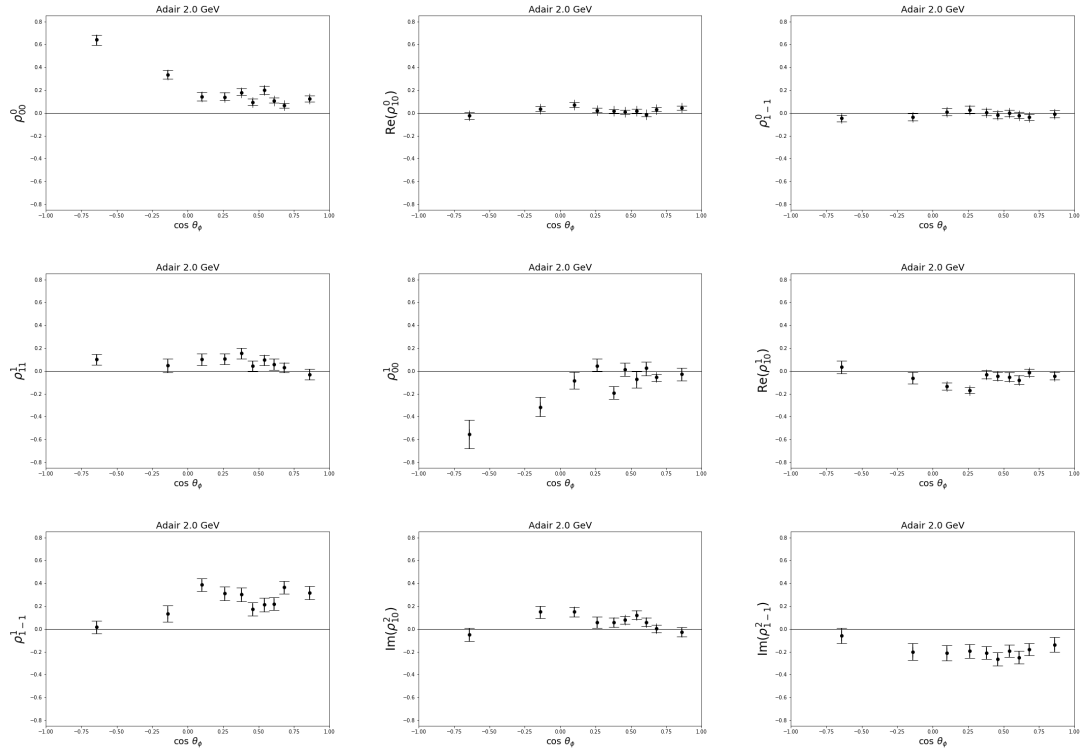


Figure 5.33: Measurements obtained for SDMEs in the 2.0 GeV energy bin in the Adair system.

5.6 Systematic and Validation Studies

At time of writing, no systematic and validation studies have been performed for this secondary analysis. In order to complete the work, systematic studies should be performed by varying the analysis method used and rerunning the analysis. For example, the following parameters may be varied and the SDMEs re-extracted.

- The width of the sWeights fit around the ϕ mass
- The background shape for the sWeights fit around the ϕ mass
- The MCMC step size and other parameters

The effect of these changes on the extracted values for the SDMEs should then be examined. Since we use the polarisation degree in our likelihood calculations, we must also recognise the effect of the known systematic uncertainty in this value as described in [68].

Toy data studies should be carried out in order to validate the method, and to quantify the systematic uncertainty introduced by the method. To generate the “toy” data, simulated events starting from phase space simulation data will be created which are then accepted or rejected based on the probability of them being included in a distribution with a given set of values for the SDMEs. The same analysis method can then be applied to the toy data and the SDMEs extracted. The distribution of these extracted values around the “true” value (used for the simulation) will give a measure of the systematic uncertainty introduced by the method.

A possible plan of work to complete the analysis is as follows.

- Ascertain the effect of sPlots method parameters on extracted observables.
 - Vary width of fit around ϕ mass
 - Vary background shape for sWeights fit around the ϕ mass.
 - Rerun the remaining analysis steps for each variation and compare results to the baseline.
 - Make conclusion about contribution to overall systematic uncertainty.
- Stress test the MCMC study. Certain of the MCMC time evolution plots show a very narrow range of values being accepted into the chain. In order to validate that this is a true representation and to ensure the parameter space is being sampled fully, some additional tests are desirable.
 - Vary the MCMC step size and monitor that the posterior distributions are consistent with the initial results reported here.

- Vary the starting values (far from the extracted values) and verify that this does not change the posterior distributions (after burn-in).
- Increase the length of the MCMC chain and study the effect of values and uncertainties extracted. Ascertain an optimum length for the chain if improvement in the uncertainties results in increasing the chain length.
- Toy data study.
 - Generate approximately 30 sets of toy data as described above.
 - Run analysis for each set of toy data
 - Quantify the systematic uncertainty from the distribution of the extracted values around the “true” values.

Chapter 6

Comparison to Previous Measurements

The measurements obtained in this work extend the world data for both of the reaction channels analysed, either by making a first measurement of an observable for the channel, or by extending the kinematic range over which the measurements are made. In both cases, however, there is overlap with measurements from other experiments. In this chapter, the results obtained in this work are compared to previous measurements of the same observables. A subset of the polarisation observables for $\vec{\gamma} p \rightarrow K_S^0 \Sigma^+$ have been measured by other experiments at CLAS, and by the CBELSA/TAPS experiment at the University of Bonn. More details are given in Section 6.1. Measurements of SDMEs for $\vec{\gamma} p \rightarrow p\phi$ have been made previously by CLAS and by the LEPS/Spring8 facility. The previous CLAS measurements used an unpolarised beam and therefore accessed only three of the nine SDMEs. At LEPS/Spring8, all nine SDMEs were measured, but over a narrow kinematical range. More details are given in Section 6.2.

6.1 Polarisation Observables for $\vec{\gamma} p \rightarrow K_S^0 \Sigma^+$

This work constitutes a first measurement of T , O_x and O_z for the reaction. The beam asymmetry, Σ , and the recoil asymmetry, P , are more easily accessible analytically as they can be extracted from one-dimensional angular asymmetries. Measurements of P have been made by previous CLAS analyses, in the paper by Nepali et al. [74], and in the recent Florida State University CLAS analysis by Volker Crede and Frank Gonzalez [75] which used a circularly polarised beam to measure P , and the double polarisation observables for circulation polarisation, C_x and C_z . Measurements of Σ and P were made in the CBELSA/TAPS experiment, published in a 2014 paper by Ewald et al. [76] with further details in the related thesis [77]. The previous measurements of P are largely consistent with this work, however, some discrepancies exist between this work and the Σ measurements made in [76], [77]. The status is summarised in Table 6.1.

Analysis	Measurements	$E\gamma$	Notes
CLAS g11 Nepali et al. [74]	P	1.0-3.5 GeV	Difference in frame means different sign is extracted Good agreement with this work
CBELSA/TAPS [76]	Σ P	1.15-1.65 GeV 1.05-2.25 GeV	Σ extracted using cross sections P results agree, but Σ do not
FSU analysis [75]	P C_x, C_z	1.15-3.05 GeV	P results agree
CLAS g8b	$\Sigma, P, T,$ O_x, O_z	1.1-2.1 GeV	This work

Table 6.1: Comparison of this work to previous measurements

6.1.1 Recoil Polarisation

Previous CLAS measurement

In order to compare results with the Nepali work it was necessary to change the sign of the measured values for P due to a difference in frames being used (see Figure 6.1). In this work, the z-axis is aligned with the direction of the photon momentum in the hyperon rest frame, whereas in the Nepali work, the z-axis is taken as normal to the reaction plane with the y-axis aligned with the Σ^+ resonant momentum. The end result is opposite signs for the extracted values of P .

$$\hat{z}_{\text{evt}} = \frac{\vec{k}}{|\vec{k}|}, \quad \hat{y}_{\text{evt}} = \frac{\vec{k} \times \vec{q}}{|\vec{k} \times \vec{q}|}, \quad \hat{x}_{\text{evt}} = \hat{y}_{\text{evt}} \times \hat{z}_{\text{evt}}.$$

(a)

$$\hat{n}_z = \frac{\hat{p}_\gamma \times \hat{p}_{\Sigma^+}}{|\hat{p}_\gamma \times \hat{p}_{\Sigma^+}|},$$

$$\hat{n}_y = \hat{p}_{\Sigma^+},$$

$$\hat{n}_x = \hat{n}_y \times \hat{n}_z.$$

(b)

Figure 6.1: Definition of axes a) this work, and b) from Nepali et al. CLAS measurements.[74]

It may also be helpful to highlight that the x-axis values of the angular distribution are also changed sign for comparison due to this work binning in $\cos \theta$ of the K^0 , whereas the Nepali paper bins in $\cos \theta$ of the Σ^+ . The K^0 and Σ^+ are back to back in the centre-of-mass frame and therefore $\cos \theta_{K^0} = -\cos \theta_{\Sigma^+}$.

With these requirements being taken into account, the results from this work have been superimposed on the published results by Nepali and are shown in Figure 6.2. There are differences in the binning in E_γ , therefore the closest match in E_γ bins are compared. The majority of the measurements are consistent within the uncertainties.

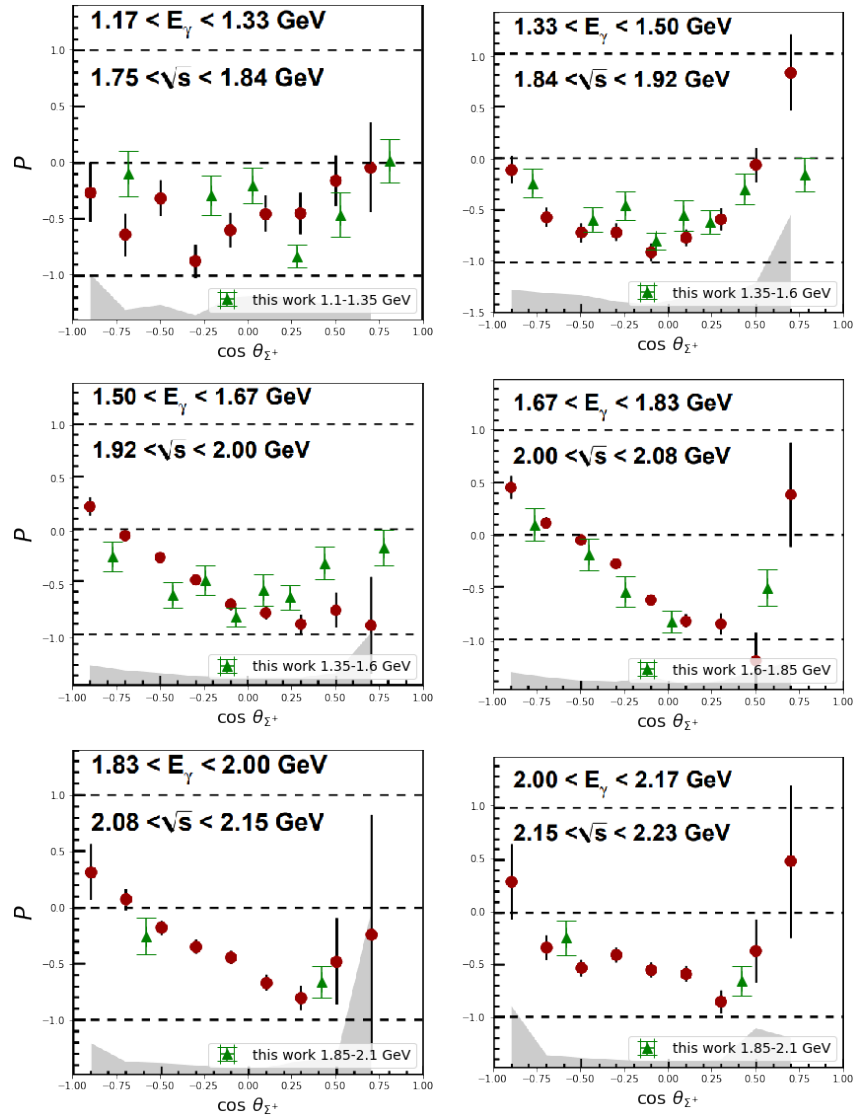


Figure 6.2: Recoil polarisation measurements from Nepali et al. [74] (red circles) and this work (green triangles). Figure adapted from [74].

Previous CBELSA/TAPS Measurement

In Figure 6.3, the measurements from this work are compared to the latest CBELSA/TAPS (black dots), the previous CBELSA/TAPS (red crosses) and SAPHIR (blue squares) data for the recoil polarisation, P . The curves (taken from [76]) represent the results of the Bonn-Gatchina PWA solutions, BG2011-02m (black dashed) and BG2011-02 (black solid), and the K-MAID parametrisations, standard (red solid) and modified to study the origin of a cross section anomaly at the K^* threshold (red dashed). The results plotted for this work are preliminary measurements

using the same energy binning as in [76] in order to compare. The majority of measurements are consistent within the uncertainties with the most recent CBELAS/TAPS measurements (black dots). It is also interesting to note that the measurements from this work would seem to support the Bonn-Gatchina BG2011-02m solution (black dashed) over the others, particularly for energy bins $E_\gamma = 1350$ to 1650 and 1650 to 1950 MeV. More details of the solutions can be found in [76].

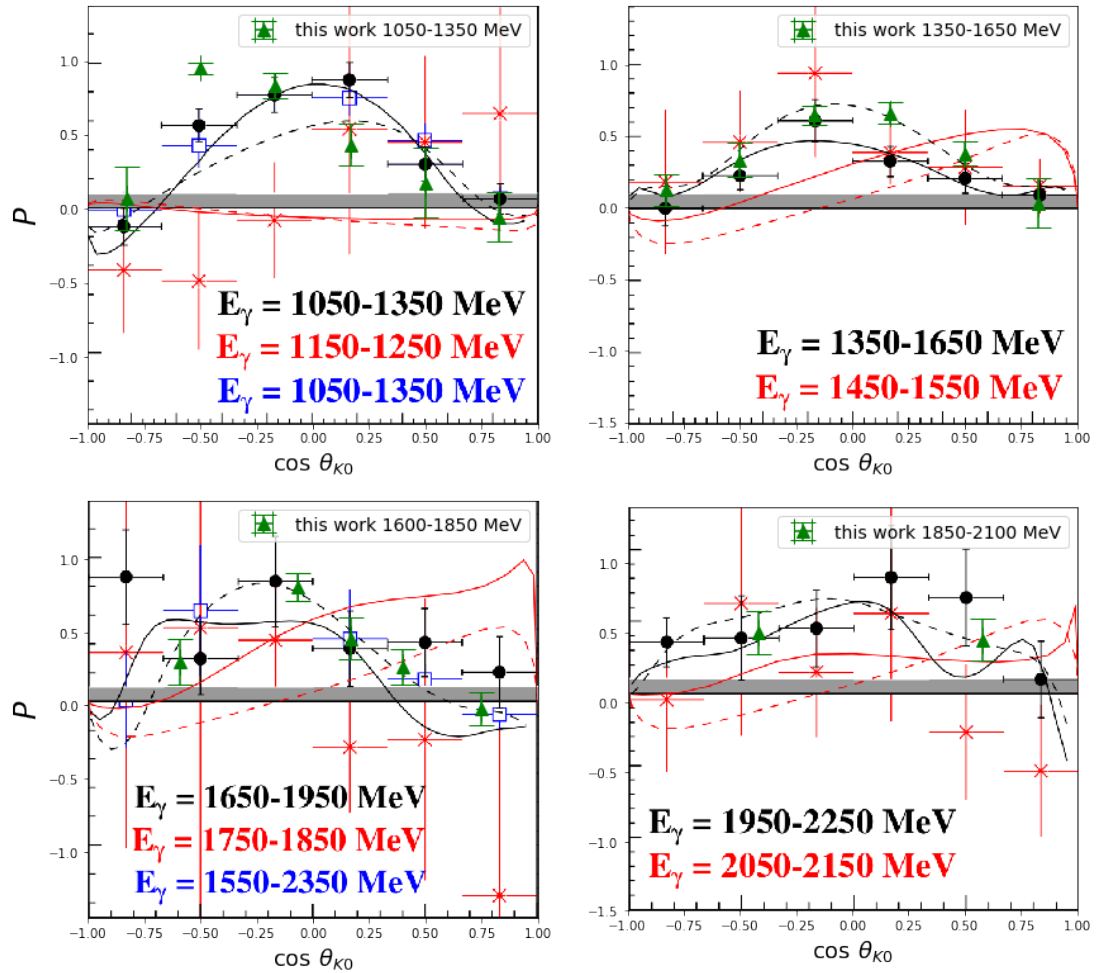


Figure 6.3: Recoil polarisation measurements from the most recent CBELSA/TAPS [76] (black circles), previous CBELSA/TAPS (red crosses), SAPHIR (blue squares) and this work (green triangles). Figure adapted from [76].

CLAS analysis in progress (Florida State University)

Figure 6.4 compares the measurements P from this analysis to the preliminary results shared by Volker Crede and Frank Gonzalez of Florida State University (FSU) [75]. The FSU analysis used a circularly polarised photon beam and therefore accessed the double polarisation observables C_x and C_z , equivalent to the linear polarisation observables O_x and O_z extracted in this work. Both studies however, accessed the recoil polarisation, P . The energy bins differ slightly therefore results are plotted together with the closest matching energy bin in the other study. The results

are consistent within the uncertainties for the majority of bins.

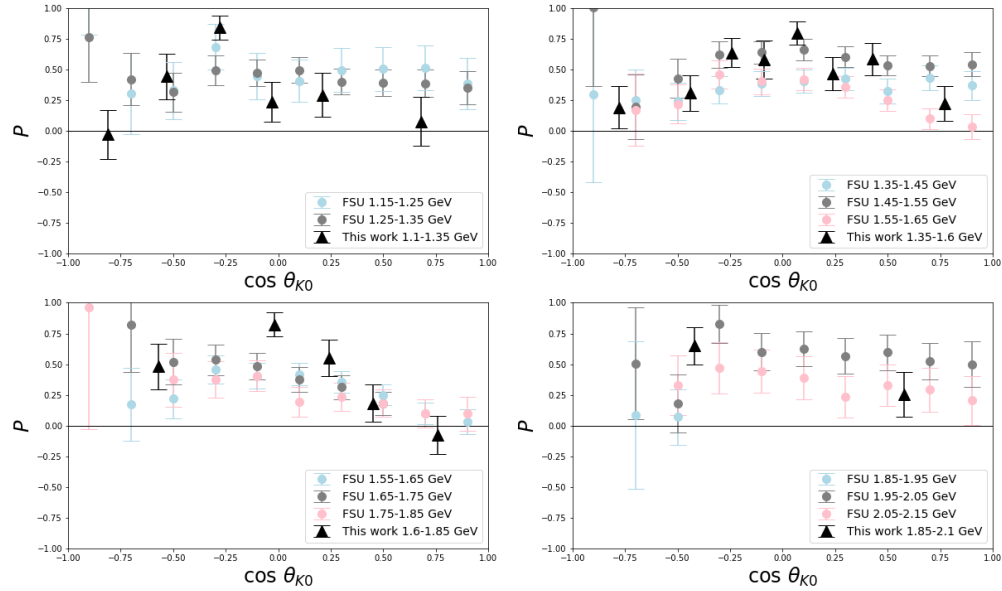


Figure 6.4: Recoil polarisation preliminary measurements from FSU (circles) and this work (black triangles).

6.1.2 Beam Asymmetry

Previous CBELSA/TAPS Measurement

While the recoil measurements agree to a good extent, there is little agreement between the beam asymmetry measured in this work compared to that measured in the CBELSA/TAPS measurement [76]. Figure 6.5 shows the differences. The discrepancy may arise from the different methods used. The method used by the CBELSA/TAPS paper is illustrated by the plot shown in Figure 6.6, taken from the associated thesis [77]. The fits were done to the modulation of the cross-section, done separately for $0-180^\circ$ and $180-360^\circ$ and the average amplitude taken.

The curves shown in Figure 6.5 are the same as described in Section 6.1.1 (further details in [76]). They represent the results of the Bonn-Gatchina-PWA solutions, BG2011-02 (black solid) which is modified in BG2011-02m (black dashed) to include the beam asymmetry data from [76], and the K-MAID parametrisations, standard (red solid) and modified to study the origin of a cross section anomaly at the K^* threshold (red dashed). Other than the inclusion of the beam asymmetry from [76] in the modified Bonn-Gatchina model, there is no beam asymmetry data included, therefore agreement with the model is not expected.

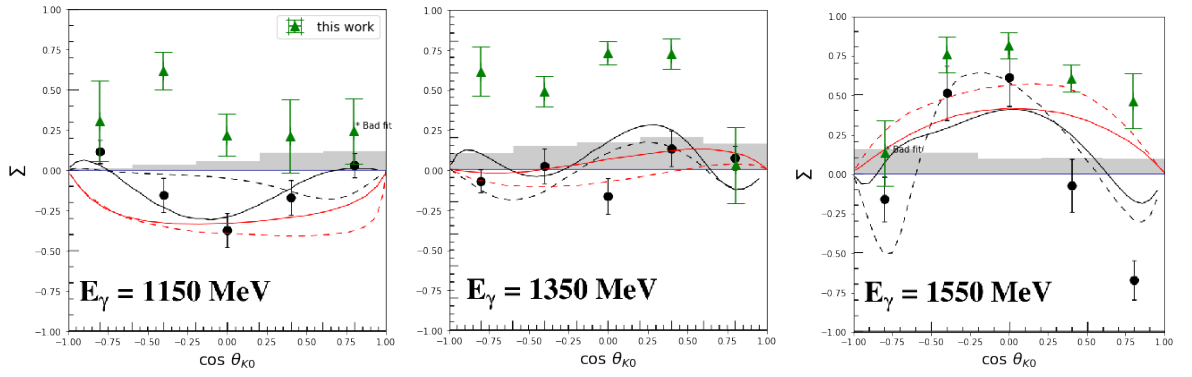


Figure 6.5: Beam asymmetry measurements from Ewald et al. [76] (black circles) and this work (green triangles).

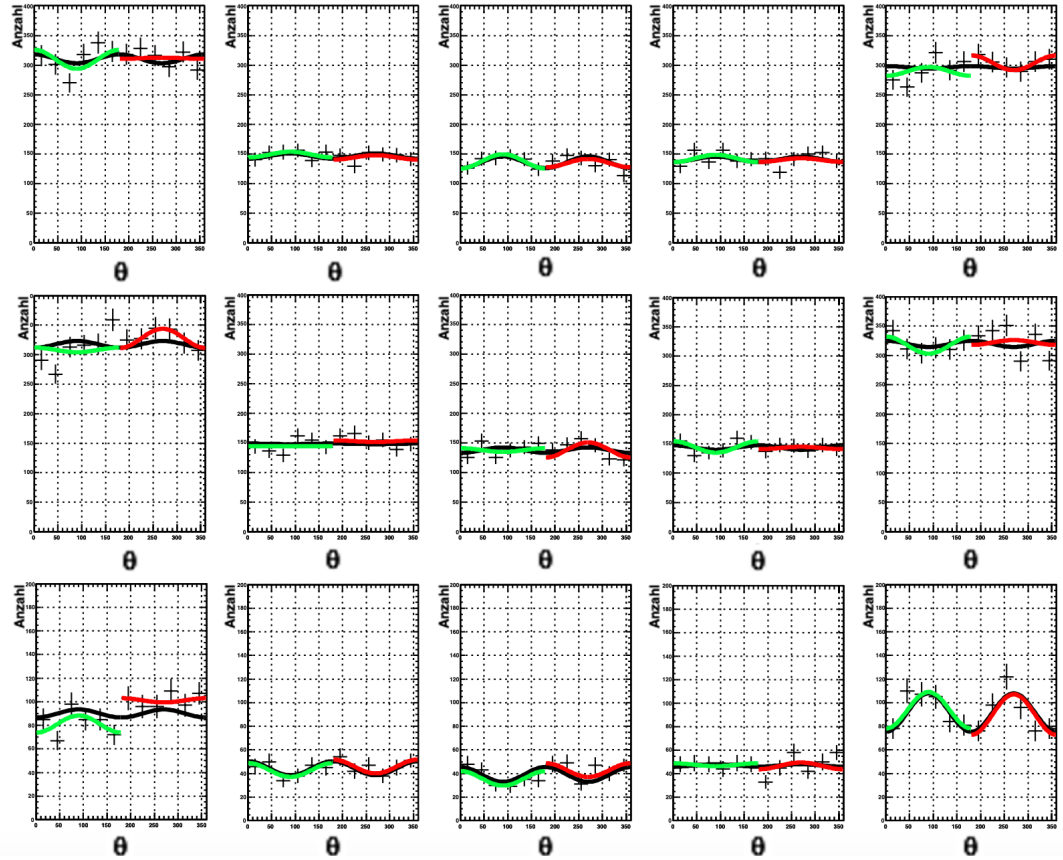


Figure 6.6: Beam asymmetry cross-section modulations from Ewald thesis [77] showing the cross-section angular distribution and the cross-section modulation fits for each bin.

6.2 Spin Density Matrix Elements for $\vec{\gamma} p \rightarrow p\phi$

Relatively few measurements of the spin density matrix elements for $\vec{\gamma} p \rightarrow p\phi$ have been made at time of writing. Those that do exist are limited either in the number of elements extracted or in the kinematical coverage of the ϕ -meson decay angle. A previous CLAS experiment [52, 78]

used an unpolarised beam to perform a high statistics extraction of the spin density matrix elements ρ_{00}^0 , $\text{Re}\rho_{10}^0$ and ρ_{1-1}^0 . The results are compared to this work in Figures 6.7 to 6.9. The energy bins in the previous work are far smaller than in this work, 10 MeV bins in centre-of-mass energy compared to the 200 MeV bins used in this work. The results are compared to those with centre of mass energy (\sqrt{s}) for the bin centre closest to the corresponding photon energy. In Figure 6.7, the two sets of results for ρ_{00}^0 follow a similar trend, but the results from this work are systematically higher in the Helicity system (top row), and systematically lower in the Gottfried-Jackson and Adair systems (middle and bottom row). The magnitude of the discrepancy increases for the higher energy bin in the Gottfried-Jackson system. For the $\text{Re}\rho_{10}^0$ SDME, shown in Figure 6.8, the two sets of results are consistent for the Helicity system (top) and the Gottfried-Jackson system (middle), but the results from this work are systematically lower in the Adair system (bottom), particularly in the higher energy bin. The comparison for ρ_{1-1}^0 is similar, shown in Figure 6.9, in this case the results for the Helicity system (top) are consistent, but the results in the other two systems exhibit systematic differences. As mentioned previously, the SDME measurements obtained in this work are preliminary measurements, and these comparisons should be reviewed again following systematic studies. It should also be emphasised here that the measurements in each system are not physically different quantities, but are related to one other by a rotation in reference frame, therefore inconsistencies between measurements should be reflected in each reference system, which is not the case here. An additional comparison is given in Figure 6.10 in which the results from this work are shown in black against the CLAS and LEPS results for the Gottfried-Jackson frame. The figures are adapted from [78] in which their data were rebinned to match the wider energy bins used in the LEPS paper. These plots again highlight the discrepancy between the results in this work (black), and the previous CLAS measurements (red) [78, 52]. It is interesting to note that the largest discrepancies between the measurements occur at points where the previous CLAS measurements have the smallest uncertainties. The plots also show the LEPS measurements [79] (blue), illustrating the narrow kinematic range of that experiment. Note that a subset of the SDMEs were measured for a slightly wider kinematic range by a later LEPS experiment[80]. Both sets of CLAS measurements appear to follow a trend which is consistent with the LEPS measurements. Finally, the full set of nine SDMEs can be compared to the LEPS measurements. These are shown in Figures 6.11 and 6.12 for the results obtained in the helicity system. Both studies used energy bins which are 200 MeV wide with a slight difference in bin centre, the LEPS energy bin centres being at 1.87 GeV and 2.07 GeV compared to 1.8 GeV and 2.0 GeV in this work. Although the overlap in kinematic range is narrow, the two sets of results are compatible within the uncertainties and exhibit similar trends.

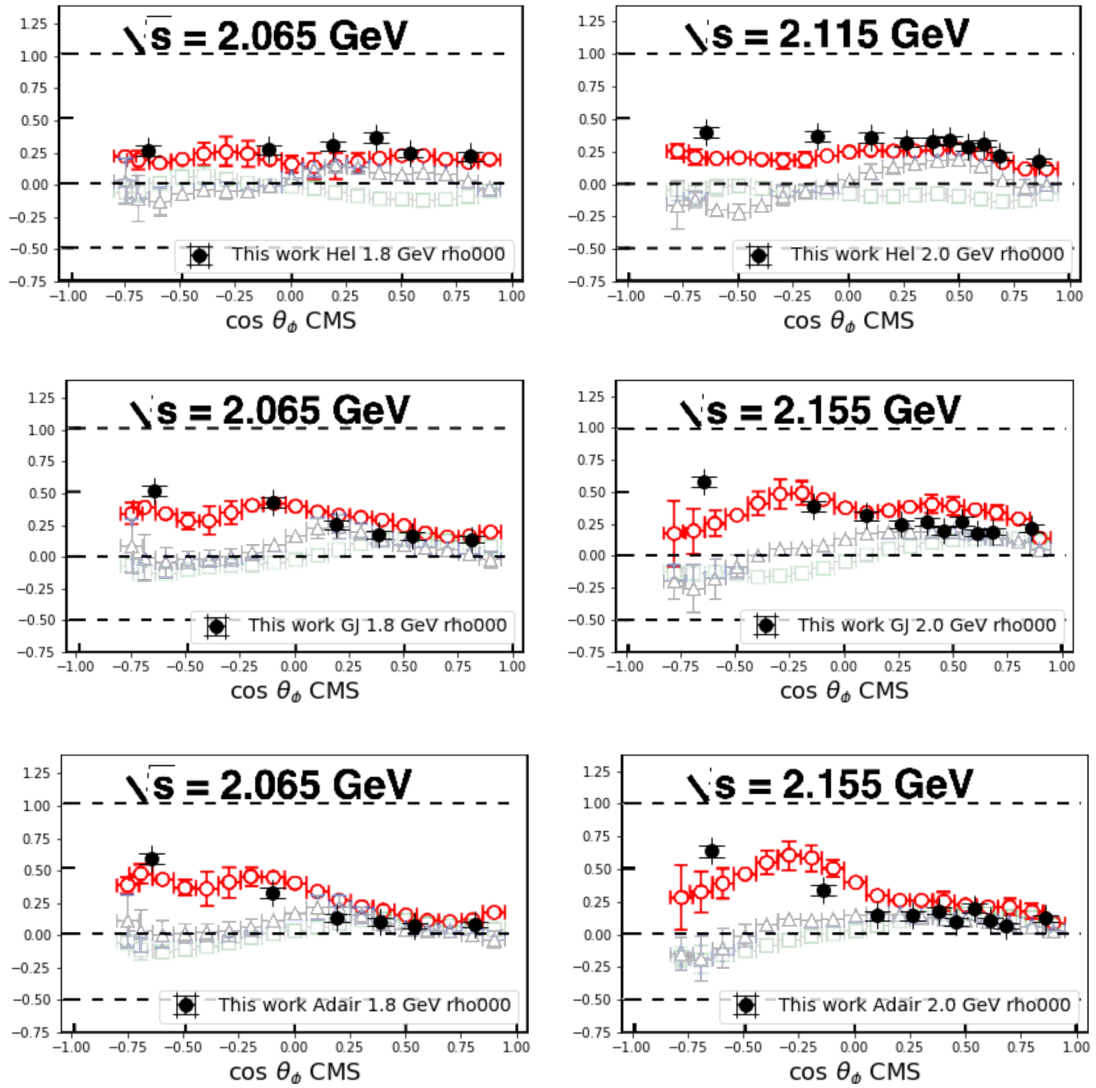


Figure 6.7: Comparison of the ρ_{00}^0 SDME from this work (black) and from previous CLAS results[52] (red) for Helicity system (top), Gottfried-Jackson system (middle) and Adair system (bottom). Image adapted from [52] with results from this work superimposed. The previous CLAS results for $\text{Re} \rho_{10}^0$ and ρ_{1-1}^0 are greyed out to aid comparison.

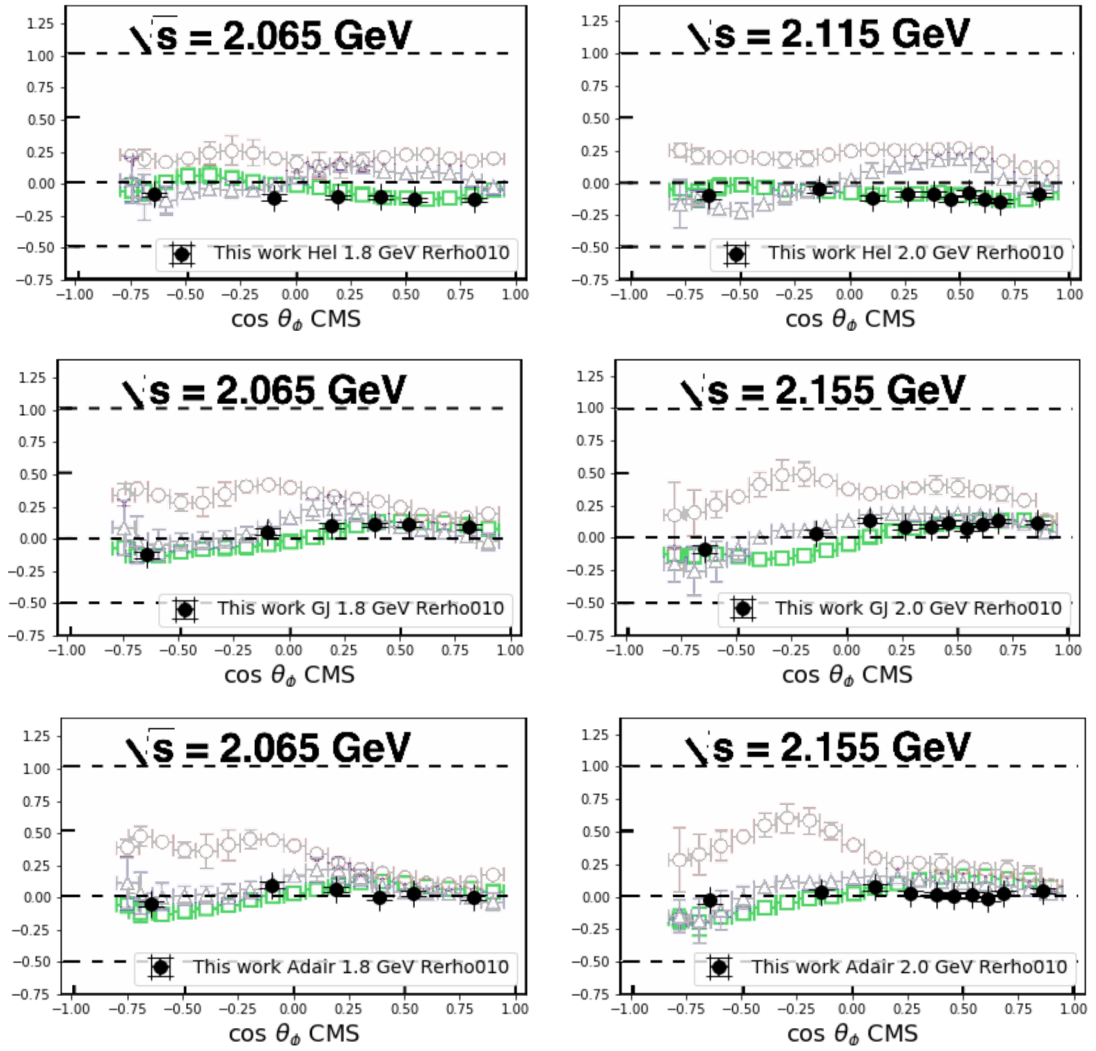


Figure 6.8: Comparison of the $\text{Re } \rho_{10}^0$ SDME from this work (black) and from previous CLAS results[52] (green) for Helicity system (top), Gottfried-Jackson system (middle) and Adair system (bottom). Image adapted from [52] with results from this work superimposed. The previous CLAS results for ρ_{00}^0 and ρ_{1-1}^0 are greyed out to aid comparison.

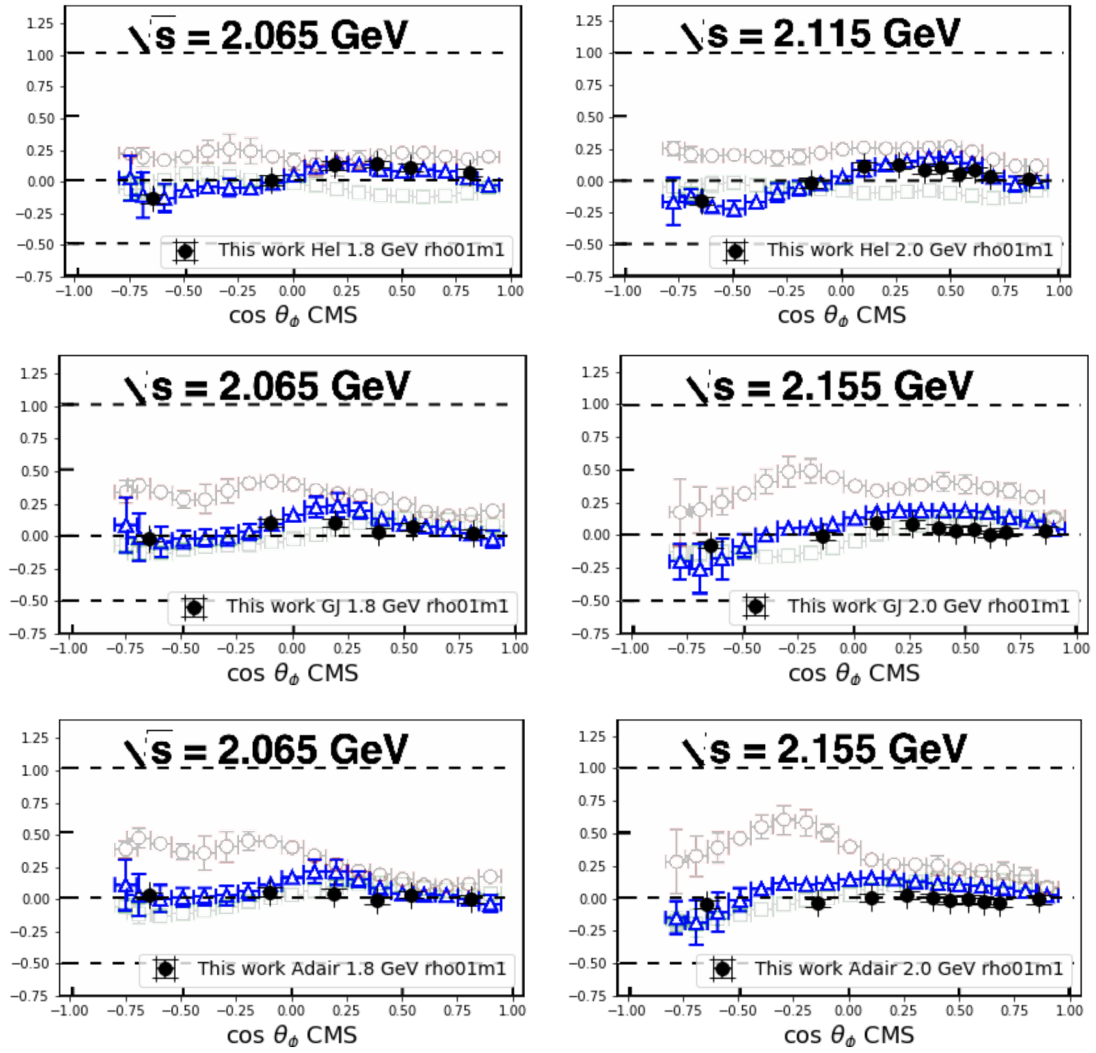


Figure 6.9: Comparison of the ρ_{1-1}^0 SDME from this work (black) and from previous CLAS results[52] (blue) for Helicity system (top), Gottfried-Jackson system (middle) and Adair system (bottom). Image adapted from [52] with results from this work superimposed. The previous CLAS results for ρ_{00}^0 and $\text{Re} \rho_{10}^0$ are greyed out to aid comparison.

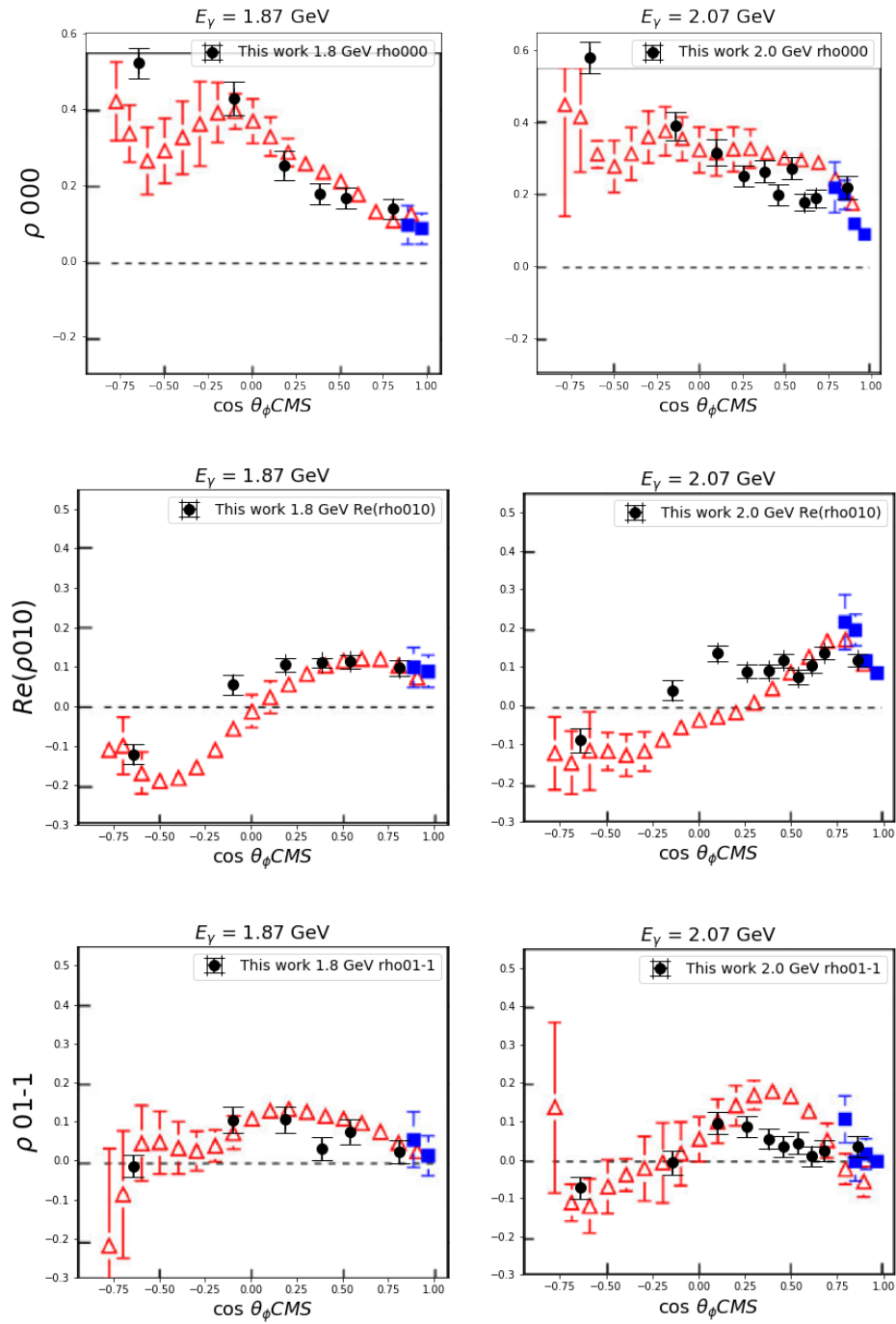


Figure 6.10: Comparison of the unpolarised SDMEs (ρ_{00}^0 , $\text{Re}(\rho_{10}^0$, and ρ_{1-1}^0) from this work (black) and from previous CLAS results[78] (red) and LEPS results[79] (blue) for the Gottfried-Jackson system. Image adapted from [78] with results from this work superimposed.

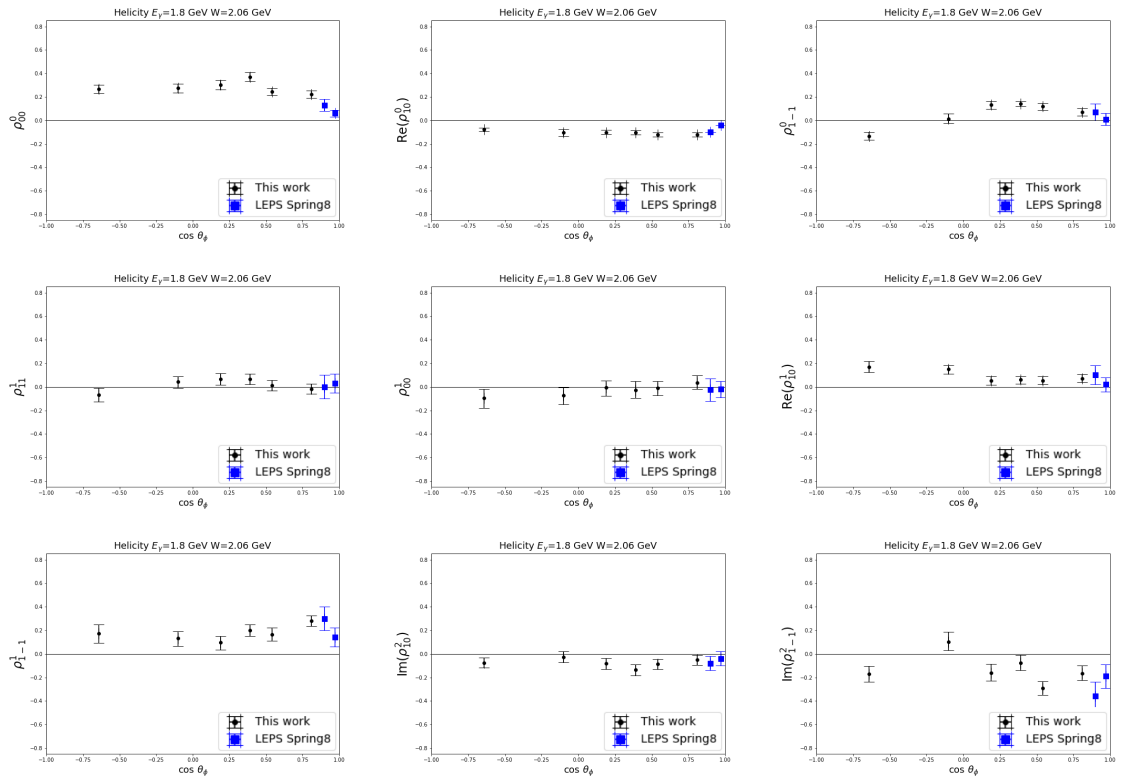


Figure 6.11: Comparison of this work ($E_\gamma = 1.8$ GeV to LEPS-Spring8 results[79] ($E_\gamma = 1.87$ GeV for the Helicity system.

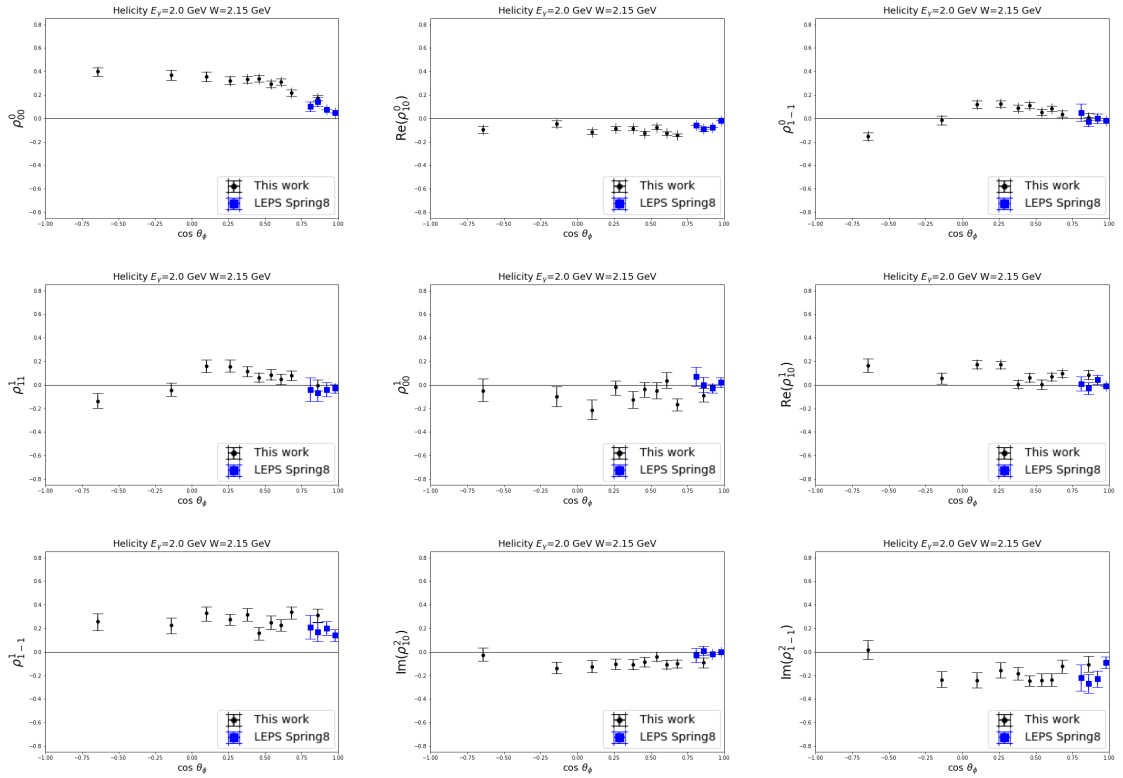


Figure 6.12: Comparison of this work ($E_\gamma = 2.0$ GeV to LEPS-Spring8 results[79] ($E_\gamma = 2.07$ GeV for the Helicity system).

6.3 Summary

Previous measurements (where they exist) have been compared to the results for both analyses in this work. For the $\vec{\gamma} p \rightarrow K_S^0 \Sigma^+$ analysis, there is good agreement with other experiments for the recoil polarisation, P . However, a previous measurement of the beam asymmetry at CBELSA/TAPS obtained different results from this work. Measurements of SDMEs for $\vec{\gamma} p \rightarrow p\phi$ show similar trends to previous measurements of unpolarised SDMEs at CLAS, with some systematic differences. The measurements for all nine SDMEs are consistent with the LEPS measurements, however the kinematic range over which we can compare is limited.

Chapter 7

Impact on Models and Conclusion

In this chapter, the implications of the measurements for theoretical models are considered, the possible next steps are summarised and concluding remarks are given.

7.1 Polarisation Observables for $\vec{\gamma} p \rightarrow K_S^0 \Sigma^+$

The Juelich-Bonn dynamical coupled channel model was recently extended to include $K^+ \Lambda$ photoproduction [14] and work is ongoing to include $K^0 \Sigma^+$ photoproduction. Before this work, for the $K^0 \Sigma^+$ channel, only measurements of the unpolarised cross-sections and the recoil polarisation, P , were available to include in the dataset, which includes over 40,000 data points obtained from pion induced and photoproduction reactions. The measurements made in this work have been passed to the group to be included in the fit and the effect of the new data on the fit and the physics parameters are described in this section. It is important to emphasise that these are early fit results from the group, but should in time become part of their next published fit and may subsequently be used in the Particle Data Group Tables.

In Figure 7.1, the data points from this work are shown in black, the red lines represent the model before the inclusion of the new data from this work, and the green lines represent the refitted model. Since the previous model (in red) only included measurements of P and had no measurements of the other four observables for the $K^0 \Sigma^+$ final state, it is no surprise that the previous model does not describe the data well for these observables. It is interesting to note that the P data are well described by the previous model and one could perhaps argue that in energy bin 2032 MeV, in fact the new model matches the data less closely. This is of no regard and highlights the importance of extracting and fitting all the observables simultaneously. Overall, it can be seen that the new fit better represents the new data, and this is quantified in Table 7.1, showing the values for the reduced χ^2 of the data compared to the model before and after including the new data.

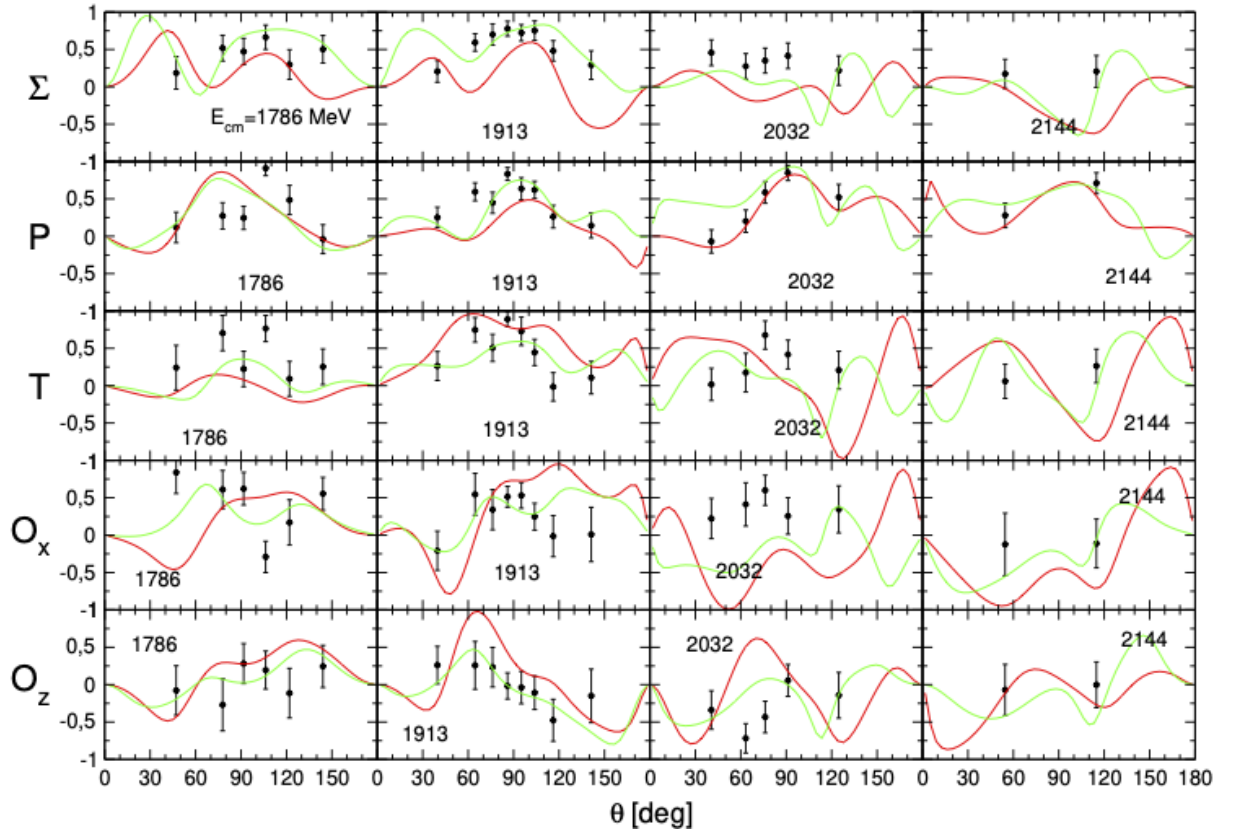


Figure 7.1: Comparison of results against the Juelich-Bonn dynamical coupled channels model. Data points from this work are in black, red line is the model before including the data, and the green line is after including the data. The dependence on θ_{K^0} is shown for each observable for four centre-of-mass energy bins. [81]

	Reduced χ^2	
	Before fitting	After fitting
Σ	4.65	1.32
P	2.82	2.24
T	4.33	1.92
O_x	5.14	1.87
O_z	3.74	0.99

Table 7.1: Reduced χ^2 values before and after the inclusion of the new data. [81]

With the inclusion of the new data from this work, the majority of the physics parameters which were extracted remained stable. This is to be expected as the new data represents only a small percentage of the data included in the fit. However, there were a number of pole positions, pole widths and photon decay amplitudes which were significantly changed in the new fit. In coupled-channel models, such as the Juelich-Bonn model, each resonance is treated as a single object influenced by all reaction channels. The fact that the addition of these 105 data points

to the full set of over 40,000 data points can influence the physics parameters in this way is an indication of the importance of including new observables and channels in the set. Table 7.2 lists the before and after pole positions and widths of two resonant states, $\Delta(1700)$ and $N(2190)$. The pole position of the $\Delta(1700)$ is stable, and there is a slight change (1.3%) change in the position of the $N(2190)$. There is significant change in the width of both resonances. In Table 7.3, the resonances for which there was a significant change to the photon decay amplitudes are listed. The phase is included for reference, but is a quantity which varies greatly between fits and is not of physical significance. The photon decay amplitudes describe the contributions from electric and magnetic multipoles to the expansion of the amplitudes in the scattering matrix and the new data have changed the extracted values by 0.03-0.05 $\text{GeV}^{1/2}$.

	Pole position (MeV)		Width (MeV)	
	Before fitting	After fitting	Before fitting	After fitting
$\Delta(1700) J^P = 3/2^-$	1601	1607	146	172
$N(2190) J^P = 7/2^-$	1994	1968	160.7	141.6

Table 7.2: Pole positions of resonances affected by the new data, before and after fitting. [81]

	Modulus ($\text{GeV}^{-1/2}$)		Phase	
	Before fitting	After fitting	Before fitting	After fitting
$\Delta(1910) J^P = 1/2^+ A_{1/2}$	0.0292	0.0621	7.5°	87.0°
$\Delta(1905) J^P = 5/2^+ A_{1/2}$	-0.09372	-0.04326	83.3°	-64.9°
$\Delta(1905) J^P = 5/2^+ A_{3/2}$	0.2194	0.1704	46.26°	2.46°

Table 7.3: Photon decay amplitudes affected by the new data, before and after fitting. [81]

7.2 Spin Density Matrix Elements for $\vec{\gamma} p \rightarrow p \phi$

We return to the predictions of Vector Meson Dominance (VMD) and examine whether our data confirm or deny the predictions. The predictions are compared below to the results in the Helicity and the Gottfried-Jackson system as shown in Figures 5.25 to 5.27 (Helicity system) and Figures 5.28 to 5.30 (Gottfried-Jackson system). The Adair system is seldom used, therefore the results are included for completeness but are not considered further in this section.

VMD prediction: Only two SDMEs are non-zero: ρ_{1-1}^1 and $\text{Im}\rho_{1-1}^2$

The values of ρ_{00}^0 vary from 0.2 to 0.4 in the Helicity system (Figures 5.25 to 5.27), and from 0.2 to 0.6 in the Gottfried-Jackson system (Figures 5.28 to 5.30), with uncertainties of the order of 0.05. In the 1.8 and 2.0 GeV energy bins several of the other SDMEs predicted to be zero

are distinct from zero in the majority of $\cos(\theta_\phi)$ bins. The trend appears to be that the SDMEs approach zero at higher values of $\cos(\theta_\phi)$.

VMD prediction: The two non-zero SDMEs are related: $\rho_{1-1}^1 = -\text{Im}\rho_{1-1}^2$

Within the uncertainties, this appears to be the case for the majority of bins.

VMD prediction: $\rho_{1-1}^1 = +0.5$ for natural parity exchange via Pomeron exchange and $= -0.5$ for unnatural parity exchange via pseudoscalar meson exchange

In the lowest energy bin, at 1.6 GeV, ρ_{1-1}^1 is consistent with zero or slightly negative. In the higher energy bins, the values generally vary from 0.1 to 0.3, and are consistently higher in the higher energy bin. The trend within each energy bin is that the SDME increases with $\cos(\theta_\phi)$.

We can conclude that the data provide evidence for contributing processes other than vector meson dominance, for example the $s\bar{s}$ knockout mechanism suggested by [18, 19]. The positive value measured for the ρ_{1-1}^1 SDME indicates that the contribution from natural parity exchange outweighs the contribution from unnatural parity exchange. However, the fact that it is considerably less than 0.5 again points to other processes in play other than VMD. Interestingly, under both of the measures (zero value for all but 2 of the SDMEs, and $\rho_{1-1}^1 = +0.5$) there is an approach at higher values of $\cos(\theta_\phi)$ to the values which are consistent with VMD predictions. i.e. in the case of the more forward going ϕ meson, the behaviour becomes similar to the diffractive behaviour at higher energies observed in other studies. At lower energy and backward angles of the ϕ -meson, such as the kinematic regions accessed by this work, the contribution of s -channel resonance production is more significant and the SDMEs could be used in a partial wave analysis to constrain the resonance parameters.

There is also strong evidence for non-helicity conserving processes. Non-zero values for the ρ^0 are indicative of non-conservation of helicity[26]. That is, for helicity conservation $\rho_{00}^0 = \rho_{10}^0 = \rho_{1-1}^0 = 0$. The measured values of ρ_{00}^0 varying from 0.2 to 0.4 in the Helicity system (Figures 5.25 to 5.27) and from 0.15 to 0.55 in the Gottfried-Jackson (Figures 5.28 to 5.30) system point to non-helicity conserving process in both the s -channel and the t -channel. Again, at forward angles of the ϕ meson the trend could be interpreted as heading towards zero, indicative of a higher likelihood of helicity conservation in events with a forward angle meson.

7.3 Next Steps

Two analyses have been performed using similar methods and the same experimental data (known as g8). The status of the first analysis, extraction of polarisation observables for $\vec{\gamma} p \rightarrow$

$K_S^0 \Sigma^+$ is at an advanced stage, having undergone and successfully passed collaboration review. The results have been passed to the Juelich-Bonn theory group and a preliminary fit of the data has been made. The results are ready for publication, in conjunction with a finalised fit being received from Juelich-Bonn. The second analysis, extraction of spin density matrix elements for $\vec{\gamma} p \rightarrow p \phi$ is at an intermediate stage, with results extracted, but no systematic studies having been undertaken. The intended systematic studies are described in Section 5.6. Further investigation into the systematic differences between this work and the result from the previous CLAS measurement[78] should be made. As focus now moves to data taking from the CLAS12 experiment, there could still be useful study to be made of the g8 data. Having performed two analyses using the same data, the procedures and tools are in place for particle ID, simulation and reconstruction particular to the g8 dataset, as well as common analysis tools using sWeights for signal background separation and Markov-Chain Monte-Carlo likelihood sampling to extract the observables. There may well be other reaction channels of interest within the g8 data which would warrant analysis. From early investigation of the $\pi^+ \pi^- \pi^0$ final state, it seemed that there is an easily distinguishable set of events containing the η' meson. Figure 7.2 shows the peak in the $\pi^+ \pi^- \pi^0$ mass at the η' mass of $952 \text{ MeV}/c^2$. The Figure is for data from one coherent peak setting therefore the entire dataset would comprise approximately three times this number.

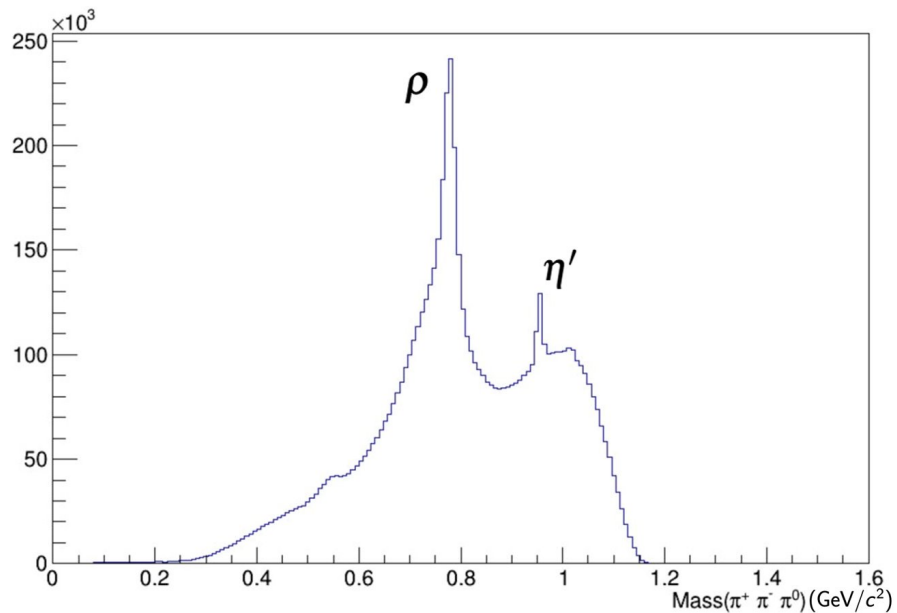


Figure 7.2: Mass ($\pi^+ \pi^- \pi^0$) showing peak at the η' mass of $952 \text{ MeV}/c^2$.

7.4 Conclusion

Hadron spectroscopy is an active field in which many groups of experimentalists and theorists collaborate to extract and analyse the physical observables which can describe the dynamics within the nucleon. Experiments which study reactions caused by exciting the nucleon with an incident beam of polarised photons make an important contribution to the global effort. The CEBAF Large Acceptance Spectrometer (CLAS) at Jefferson laboratory in Virginia provides a facility to perform such experiments. This work has analysed data from CLAS for two reactions, $\gamma p \rightarrow K_S^0 \Sigma^+$ and $\gamma p \rightarrow p \phi$, for which there is a paucity of previous measurements. Nucleon resonances which are predicted by theory but are lacking in evidence may couple to photoproduced states or to states involving strangeness production such as the reactions studied in this work. The measurements obtained in this work will therefore provide a valuable addition to the world data.

In the secondary analysis in this work, the spin density matrix elements (SDMEs) for $\gamma p \rightarrow p \phi$ are extracted and compared to the predictions of the Vector Meson Dominance model (VMD) and of helicity conservation. The results point to deviations from VMD predictions and to non helicity conserving processes. The measurements are the first to extract all nine SDMEs for the full angular range of the ϕ meson production.

The primary analysis in this work, the extraction of polarisation observables for the reaction $\gamma p \rightarrow K_S^0 \Sigma^+$, provides the first measurements of the three of the five polarisation observables, T , O_x and O_z , and the beam asymmetry (Σ) measurement supplements the one previous measurement for this quantity and extends the energy range over which it has been extracted. The measurement of the recoil polarisation, P , is consistent with previous measurements. The data from this analysis has been passed to the Juelich-Bonn theory group for inclusion in their dynamical coupled channel model. Before including the data from this work, only measurements of cross-sections and the recoil polarisation had been included in their fit. The new data caused some changes to the physics parameters derived by the model in a preliminary fit performed by the group [81]. The data had a significant effect on the pole position of the $N(2190)$ resonance, and on the width of the $\Delta(1700)$ and $N(2190)$ resonance. There were also changes in photon decay amplitudes for the $\Delta(1910)$ and $\Delta(1905)$ resonances. These are early fit results from the group but should be incorporated into their next published fit and provide updated information for the Particle Data Group tables, thus contributing to the worldwide program of work to inform theoretical models of hadron physics.

Appendix A

Time-of-flight calibration

A.1 Overview

The CLAS12 Time-of-flight calibration is a multi-step, multi-iteration, multi-pass process which populates the calibration database with tables of values for each of the 540 plastic scintillator paddles in the Forward Time-of-flight (FTOF) detector and the 48 paddles in the Central Time-of-flight (CTOF) detector. These values are then used in the reconstruction software to create the cooked data that will be used for all physics analysis for CLAS12 as described in the reconstruction documentation for FTOF [82] and CTOF [83]. The calibration steps can be split into energy calibration: gain balancing, and attenuation length; and timing calibration: left right adjustment, effective velocity, time walk correction, RF offset, and paddle to paddle offsets. The calibration procedure for FTOF and CTOF are shown in Figures A.1 and A.2. The interdependency between the steps means that the procedure must iterate so that progressively better calibration values feed in to the related steps and the values converge. Once the iterations have converged, this constitutes one pass of the process. These improved calibration values can then feed into the calibration of other detectors, most significantly the tracking detectors, i.e. the Drift Chambers for FTOF and the Central Vertex Tracker (comprising the Silicon Vertex Tracker and the Micromegas detector) for CTOF. The tracking detectors provide independent hit position information which feeds into the time-of-flight calibration. With subsequent passes, the exchange of improved timing calibration and position calibration leads to a fully calibrated system of detectors.

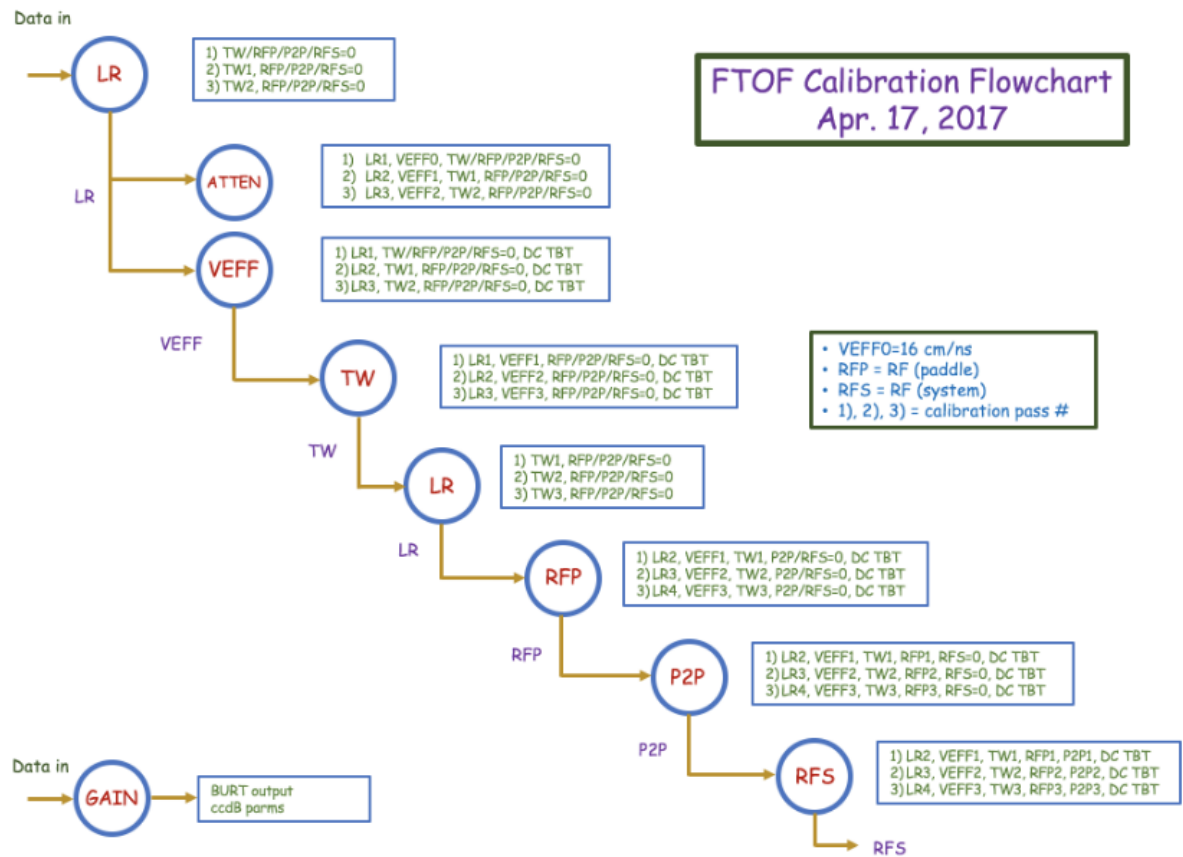


Figure A.1: Calibration procedure for the Forward Time of Flight detector from [84]. Each circle represents a calibration step and the whole process iterates several times, using the output files from the previous iteration (shown in green in the boxes).

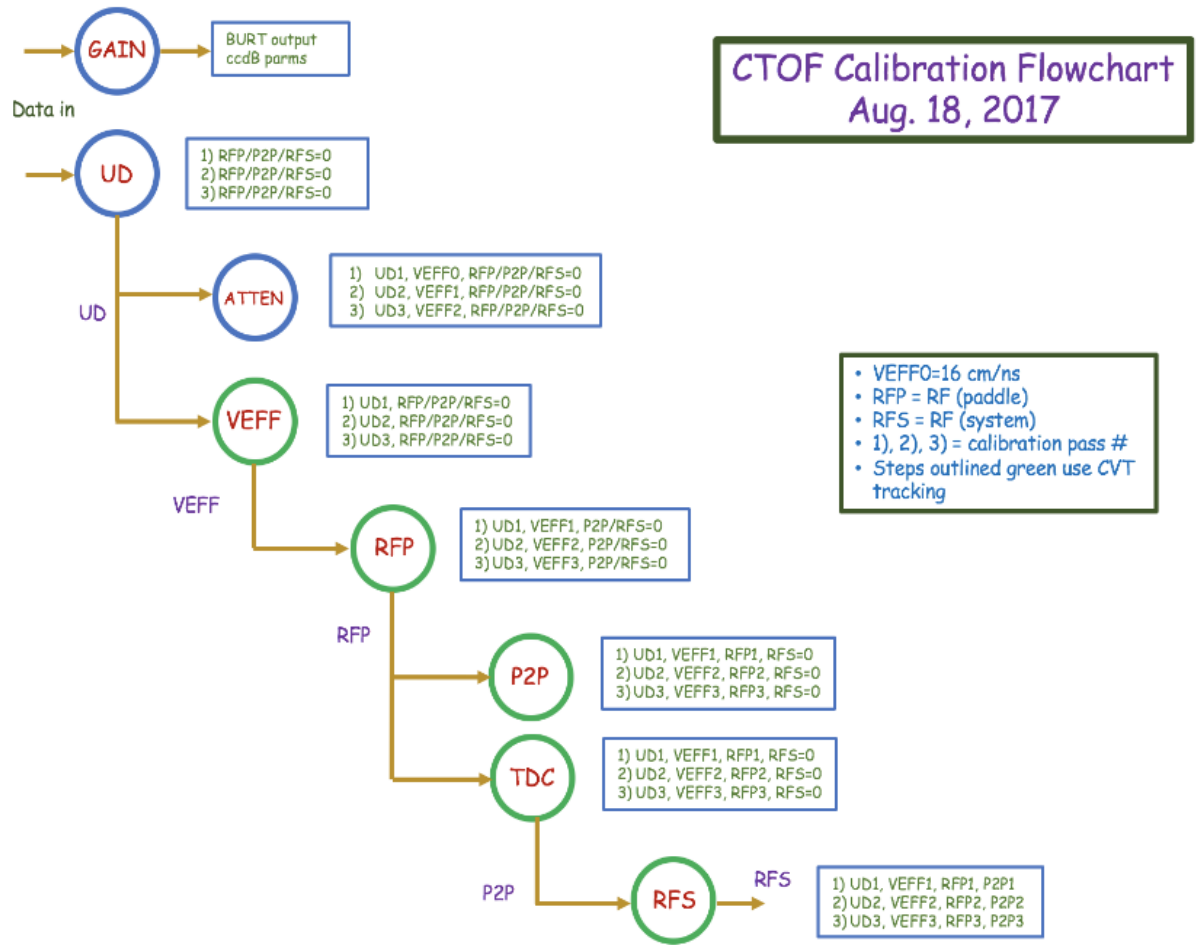


Figure A.2: Calibration procedure for the Central Time of Flight detector [85]. Each circle represents a calibration step and the whole process iterates several times, using the output files from the previous iteration (shown in green in the boxes).

My role was to deliver two complete software suites for each of FTOF and CTOF. This included development of a graphical user interface to run the calibration, and implementation of the calibration algorithms, the process flow and interdependencies. The calibration algorithms evolved as the detectors were tested, and, using experience gained from developing and testing the software, I contributed to the refinement of the calibration algorithms working in conjunction with JLab staff scientists and collaboration members.

A full description of the algorithms for FTOF and CTOF can be found in [84] and [85], and the details of the software development for individual steps are described in the following sections. The software was successfully used by the detector lead at Jefferson Lab to calibrate both the FTOF and CTOF during the Fall 2017 Engineering run and the first physics run in Spring 2018. Some of the success measures of the calibration process are presented in Section

A.11.

A.2 Paddle status

The first step in the calibration process is to identify those paddles which are not functioning in order that the reconstruction software can use alternative methods to derive the hit information. Each PMT for each paddle is classified as fully functioning, no TDC (time to digital convertor) readout, no ADC (analogue to digital convertor), or neither TDC nor ADC functioning. A PMT is regarded as non-functioning if every reading is zero.

A.3 Gain balancing

The aim of the gain balancing calibration is to quantify the gain, i.e. the relationship between the ADC readout and the energy deposition. For this we utilise minimum ionizing particles, which are known to deposit a constant amount of energy in the detector, either cosmic muons, or pions and electrons from beam data. The geometric mean, $A\bar{D}C = \sqrt{ADC_L \cdot ADC_R}$, is a position independent measure of the energy deposited in the paddle, and any imbalance between the left and right readouts, is evident in the log of their ratio, $\ln(ADC_L/ADC_R)$. The dependence of energy on the ADC channel can then be determined. The geometric mean is fitted to a Landau peak on an exponential background and the mean of the distribution is used to quantify the log ratio. Example distributions for an FTOF paddle taken from the calibration software are shown in Fig. A.3.

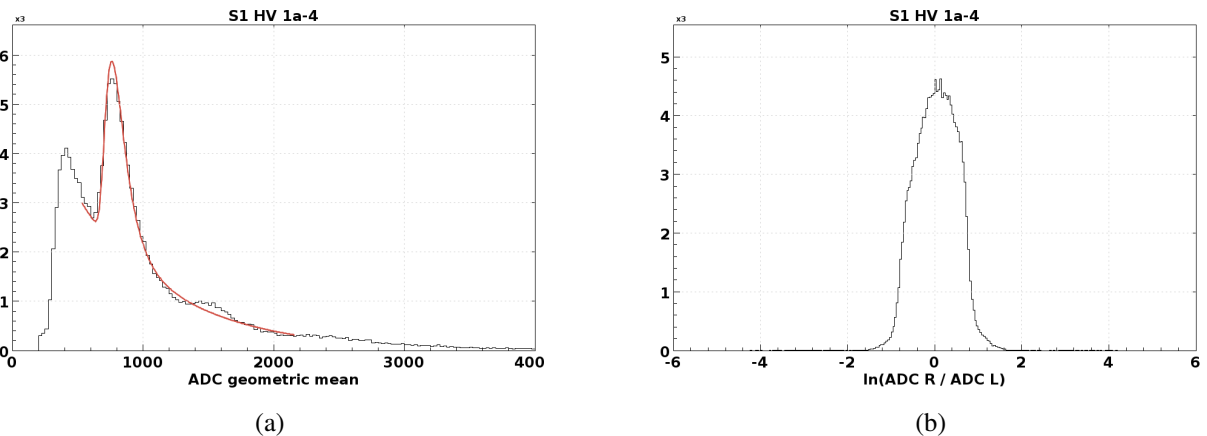


Figure A.3: Example of gain balancing plots for FTOF calibration showing histograms of ADC geometric mean (left) and ADC log ratio (right).

Further to this, the calibration software allows the user to calculate adjusted high-voltage values for the PMTs in order to position the minimum ionizing particle peak in an appropriate channel. The channel is chosen to be sufficiently above pedestal, but low enough to ensure that

higher energy particles such as protons are well within the range of the ADC. Any imbalance in the left and right readouts can be corrected. A change in PMT gain from G_1 to G_2 corresponds to a change in the applied voltage from V_1 to V_2 via $G_1/G_2 = (V_1/V_2)^\alpha$. The power α was determined experimentally for each panel during the FTOF detector refurbishment work described in [86] and typical values fall between 5 and 15. Given the current voltage settings, the new settings can therefore be calculated to place the MIP peak in the desired channel. The software provides the facility to output a script which can be read in by the high-voltage control system to apply the necessary changes.

A.4 Left-right timing alignment

Each hit on a scintillator paddle has an associated TDC left and TDC right readout (TDC upstream and TDC downstream for CTOF) which can be converted to a timing readout using the manufacturer's *ns/channel* conversion factor. Ideally the distribution of the time difference $t_L - t_R$ should be centred around zero, meaning a hit at the centre of the paddle would result in equal timing readings on each side of the paddle. To correct for any discrepancy from this, the left-right/upstream-downstream timing adjustment is calculated for each paddle by finding the centre of the time difference distribution. For FTOF, this can be done by simply taking the mean of the distribution. For CTOF however, the distribution has a bias towards downstream hits due to the positioning of the detector with respect to the target, therefore the centre of the distribution is found by taking the midpoint of the width at a certain fraction of the maximum. Example distributions for FTOF and CTOF are shown in Fig. A.4. The CTOF distribution is significantly off-centre due to the difference in length of the light guides which couple the paddles to the PMTs.

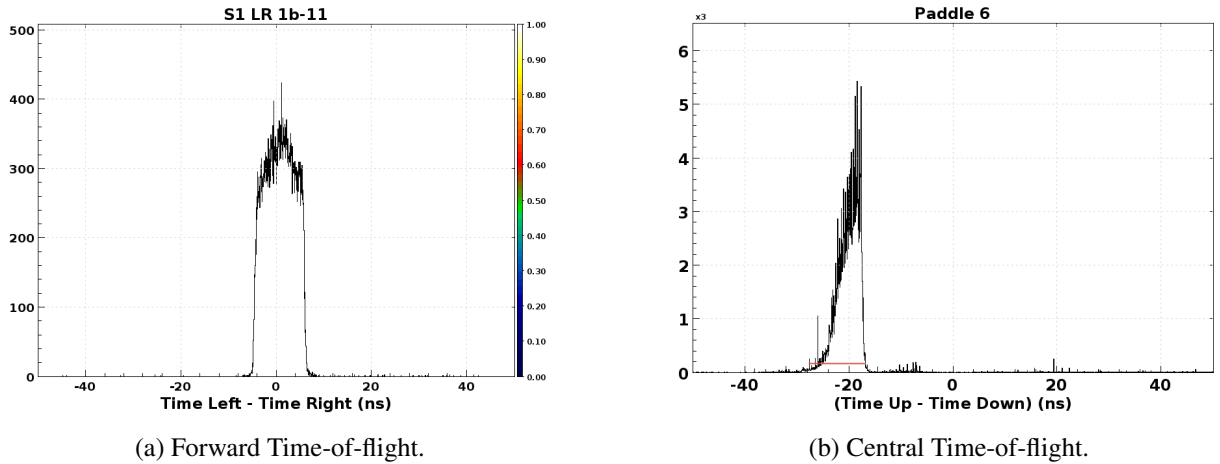


Figure A.4: Time difference distributions for FTOF (left) and CTOF (right) for representative paddles.

A.5 Attenuation length

The scintillation light produced at the hit position will attenuate as it travels along the paddle before being collected at the PMT at each end. The parameter is part of the energy calibration but is included within the timing calibration iteration due to its dependence on the time walk corrections described in Section A.7. The attenuation length, λ for each paddle is derived by plotting the log of the ratio of ADC right to ADC left against the hit position, x , along the paddle. An example distribution is shown in Fig. A.5. The dependency is given by

$$\ln\left(\frac{ADC_R}{ADC_L}\right) = \frac{2 \cdot x}{\lambda} + c$$

The hit position is calculated using the timing difference and the effective velocity of the scintillation light in the paddle. Therefore, the attenuation length step is performed after the Left-right timing adjustment has been obtained and will improve after the paddle effective velocity has been derived. For a first iteration, a default value of 16 cm/ns for the effective velocity can be assumed when calculating the hit position.

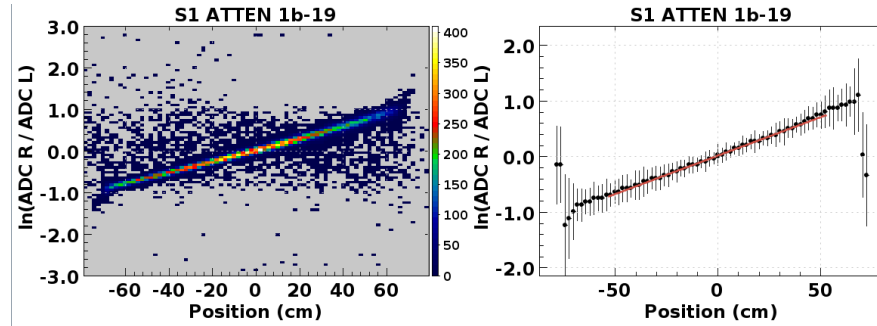


Figure A.5: Example of distribution used to extract attenuation length for FTOF calibration.

A.6 Effective velocity

The effective velocity for each paddle is the speed at which the scintillation light propagates from the hit position to the PMT window and is a property of the scintillation material and the geometry of the paddle. Values of around 16 cm/ns are typical. To derive this, an independent measure of the hit position is required which is taken from tracking information. The position information can also be derived from the TOF information via the relationship

$$y_{hit} = \frac{t_L - t_R}{2} \cdot v_{eff}$$

where y_{hit} is the hit position relative to the paddle (with $y = 0$ defined as the centre of the paddle), t_L and t_R are the timing measurements from TDCs, and v_{eff} is the effective velocity. We therefore plot $(t_L - t_R)/2$ versus the hit position from tracking and derive the effective velocity as $1/\text{gradient}$ for this distribution. A sample distribution is shown in Fig. A.6.

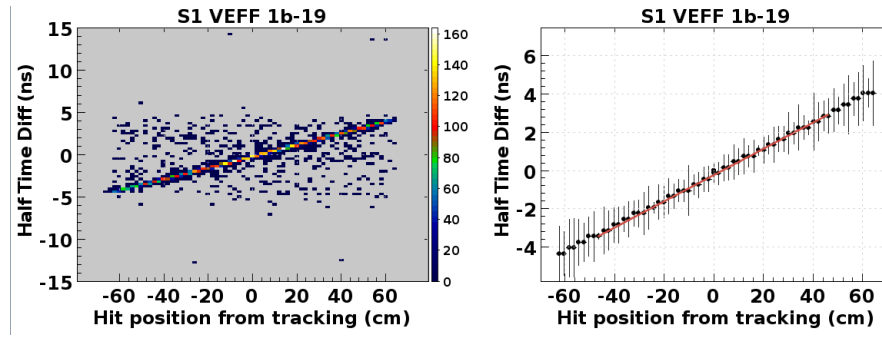


Figure A.6: Example of distribution used to extract effective velocity for FTOF calibration.

A.7 Time walk correction

Time walk corrections are necessary when a leading edge discriminator is used to trigger the TDC readouts based on the ADC pulse shape. A threshold voltage is set at which the timing information is read out, however the rise to the threshold is steeper for larger pulses. This causes the measured time to have a dependence on the ADC channel, with lower channels requiring a larger correction than higher channels. The necessary correction is modelled by the time walk parameters. These corrections are only necessary for the FTOF calibration, since the CTOF uses constant fraction discriminators. In that case, the TDC readout is triggered when the charge collection reaches a threshold fraction of the total charge in the pulse and is therefore independent of the pulse size and ADC channel.

To quantify the time walk correction required for FTOF, the vertex time, $t_{vertex,TOF}$, (calculated by tracing back from the FTOF hit) is compared to the RF signal time, $t_{vertex,RF}$, which signifies the event start time for the whole CLAS12 detector. Starting from the PMT time, the following propagation times in the detector are subtracted. The time for the scintillation light to propagate through the paddle depends on the hit position relative the paddle, y_{hit} , the paddle length l , and the effective velocity as follows.

$$\frac{(l/2) + y_{hit}}{v_{eff}}$$

We then calculate the time taken by the particle from the vertex to the FTOF hit. For this, we need the total distance the particle travels in the detector to reach the FTOF hit position (the path length) and the speed of the particle βc . The path length can be considered in two parts: the curved path taken within the toroidal magnetic field from the vertex to the outer region of the drift chamber, and the straight line path taken from the outer region of the drift chamber to the FTOF detector. The particle mass must also be known in order to calculate the β from the measured momentum. The drift chamber tracking reconstruction data provide the path length to, and the position of the track at the outer region of the drift chamber, and the particle momen-

tum. In earlier studies, the particle mass is usually assumed to be the pion mass as we know this will match with the majority of hits. We can also perform the calibrations assuming electron or proton mass. When reconstructed event data is available, the reconstructed particle mass can be used for each hit.

The necessary timing correction, $\Delta t = t_{vertex,TOF} - t_{vertex,RF}$, as a function of ADC channel can then be plotted and the dependence derived. The ADC channel dependence on the timewalk parameter $tw0$ is modelled as

$$\Delta t = \frac{tw0}{\sqrt{ADC}}$$

An example distribution and fit is shown in Fig. A.7. The distribution is considered within the 2.004 ns beam bucket corresponding to the period of the electron beam from CEBAF. The coarser grained correction in multiples of beam bucket is performed in the paddle-to-paddle corrections described in Section A.9.

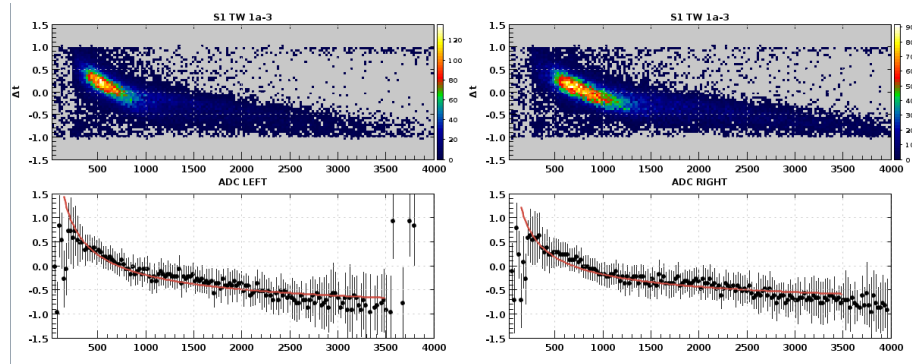


Figure A.7: Example of distribution used to extract time walk correction for FTOF calibration.

An additional adjustment to the time walk correction is required, as it is found to have a dependence on hit position. This can arise as the shape of the pulse depends on the ratio of direct light to reflected light hitting the PMT window. Hits closer to the PMT will have a larger ratio of direct light compared to hits in the centre of the paddle. The Δt versus hit position distribution is parametrized by a second order polynomial in order to calculate the correction required to remove the dependence. An example of this effect is shown in Fig. A.8.

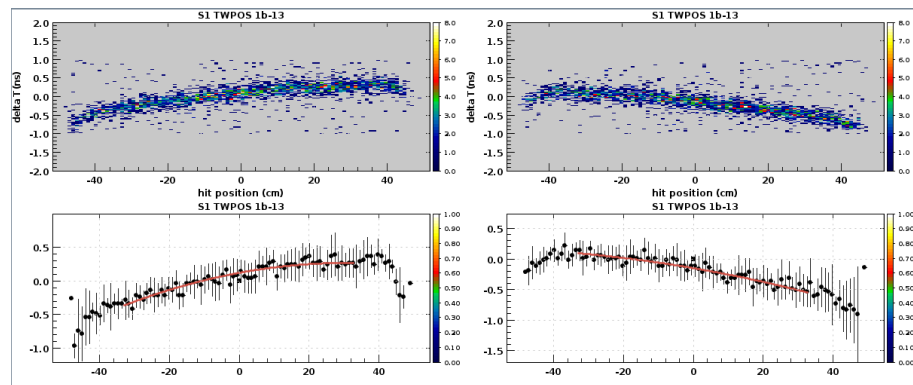


Figure A.8: Example of distribution used to extract time walk correction position dependence for FTOF calibration.

A.8 RF offset

The final step in the calibration process in terms of the fine tuning of the timing information within the beam bucket is the determination of the RF offset and the timing resolution. The vertex time difference is calculated as described in Section A.7, with corrections included from all the previous calibration steps. The peak of this distribution corresponds to the precise offset of each paddle within the 2.004ns beam bucket size from CEBAF. The distribution is fitted to a Gaussian peak on a linear background, an example of which is shown in Fig. A.9. The width of this peak is an important calibration parameter in itself, as it measures the resolution of the detector, and is an indication of the success of the overall calibration process.

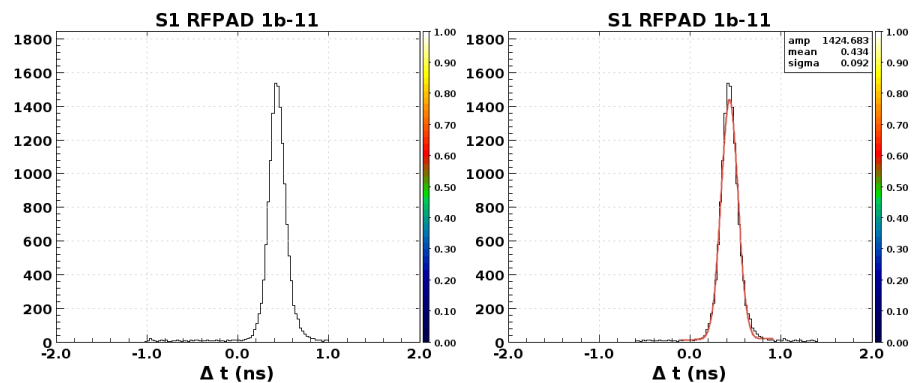


Figure A.9: Example of vertex time difference distribution for FTOF.

A.9 Paddle to paddle corrections

The process described so far has calibrated each individual paddle within the 2.004ns beam bucket size corresponding to the period of the CEBAF beam. However, a step remains to quantify the timing corrections required from one paddle relative to all other paddles, i.e. to

synchronise the timing information from all paddles in order to provide a self-consistent set of measurements for each of the FTOF and CTOF. Since the fine-grained offset has been found for each paddle, it remains to find the paddle to paddle offsets in terms of an integer number of beam buckets. These larger scale offsets arise due mainly to the differences in cable lengths connecting the PMTs to the data acquisition system. Again, the calculated vertex time is used but this time we consider the time difference $t_{vertex,n} - t_{vertex,m}$, where we are calculating for paddle n , and integrating over all other paddles $m \neq n$. After a few iterations, this process converges finding the maximum of the distribution for each paddle.

A.10 Calibration Graphical User Interface

In parallel with the development of the software to implement the calibration algorithms and extract the values for the calibration database, several features were developed within the software suite to allow the calibrator to control the input parameters, perform quality checks, manually adjust fits and parameters, and view summary data.

Before performing an iteration of the calibration process, the calibrator will specify any calibration values from previous steps. These are output at the end of a run and can be read in to the next run independent of database updates and rerunning the reconstruction. Additionally, various parameters can be adjusted for example, the mass assumption to be used in calculations, and limits to the momentum range to be included. To aid the calibrator in their quality checks, summary views are provided: miniature plots of distributions and fits by sector; and graphs of extracted calibration values. The calibration fits can be adjusted by the calibrator by adjusting fit ranges and parameters for individual paddles or by sector and layer.

A.11 Calibration results

As the engineering run and first physics run have progressed, collaboration members have been continually monitoring the performance of the system as a whole, following the calibration and reconstruction of the data. One measure from the FTOF data is the plot of β versus momentum in which we should see the characteristic trajectories of protons, kaons and pions. A recent plot from the calibrated FTOF detector is shown in Fig. A.10.

The timing resolutions for all paddles is also closely monitored as calibrations proceed and improve. This measure is taken from the width of the vertex time difference peak as described in Section A.8. A representative sample of the timing resolutions for CTOF and FTOF are shown in Figure A.11. The timing resolutions are close to the target resolutions. For FTOF the target for the required particle differentiation is 80ps for small angle counters and 150ps for larger

angle counters (i.e. paddle number larger than 40). Some improvement is required in the CTOF timing resolutions in order to meet the target resolution of 60ps.

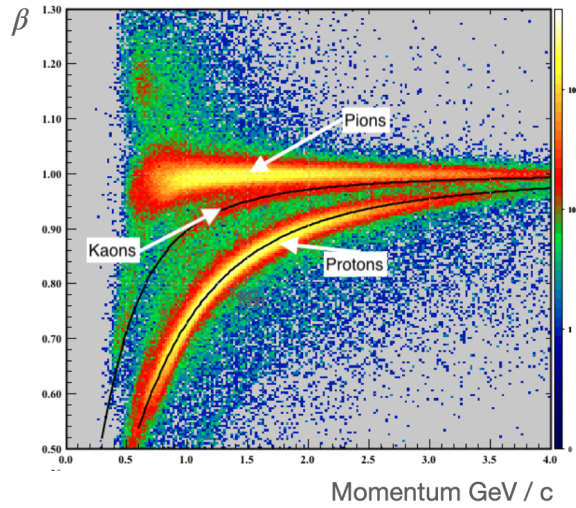
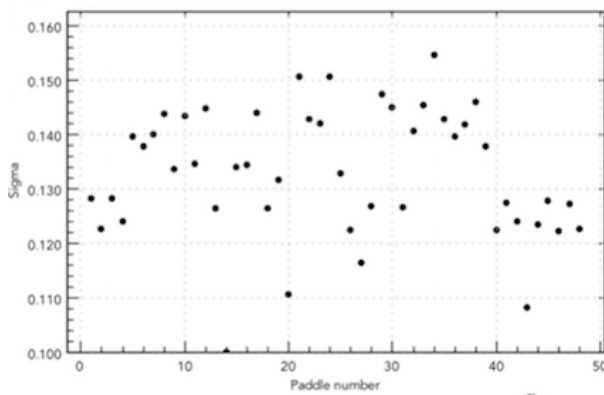
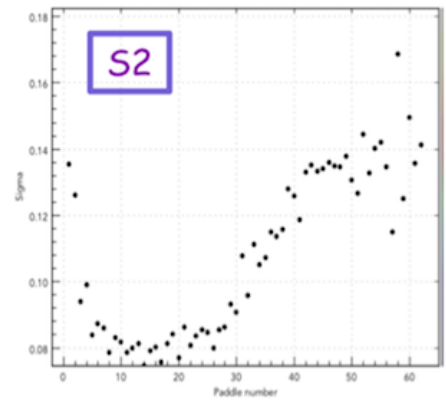


Figure A.10: β vs momentum distribution for calibrated FTOF.



(a) CTOF.



(b) FTOF 1b Sector 2.

Figure A.11: Timing resolution for CLAS12 time-of-flight detectors. CTOF (left) and an example of one sector in panel 1b for FTOF (right)

Appendix B

Run Numbers

The following data runs are used in this analysis:

Peak (GeV)	Setting	Runs
1.3	PARA	48224, 48226, 48227, 48228, 48229, 48230, 48231, 48232, 48235, 48236, 48256, 48257, 48258, 48259, 48260, 48261, 48262, 48278, 48279, 48280, 48281, 48282, 48283, 48284, 48285, 48286, 48309, 48310, 48315, 48316, 48317, 48318, 48319, 48320
1.3	PERP	48240, 48241, 48245, 48246, 48247, 48248, 48249, 48250, 48251, 48268, 48270, 48271, 48272, 48273, 48274, 48276, 48292, 48293, 48294, 48295, 48296, 48297, 48298, 48323, 48326, 48327, 48328, 48329, 48330
1.5	PARA	48418, 48419, 48420, 48421, 48422, 48423, 48424, 48426, 48445, 48446, 48447, 48448, 48449, 48450, 48452, 48454, 48455, 48462, 48463, 48464, 48465, 48501, 48502, 48503, 48504, 48505, 48507, 48508, 48509
1.5	PERP	48431, 48432, 48433, 48434, 48435, 48436, 48437, 48438, 48439, 48440, 48441, 48442, 48443, 48444, 48466, 48467, 48469, 48477, 48478, 48479, 48482, 48483, 48484, 48485, 48486, 48487, 48488
1.7	PARA	48544, 48545, 48546, 48547, 48548, 48549, 48550, 48551, 48552, 48554, 48555, 48556, 48557, 48558, 48561, 48562, 48564, 48565, 48566, 48567, 48568, 48569, 48570, 48571
1.7	PERP	48580, 48581, 48582, 48583, 48584, 48585, 48586, 48587, 48588, 48589, 48590, 48591, 48592, 48593, 48595, 48596, 48597, 48598, 48599, 48601, 48602, 48603, 48605, 48607, 48608, 48609, 48610, 48620, 48623, 48624, 48626, 48628, 48630

Table B.1: Run numbers used for the $E_\gamma = 1.3, 1.5,$ and 1.7 GeV coherent peak settings.

Peak (GeV)	Setting	Runs
1.9	AUTO	48091, 48093, 48095, 48096, 48098, 48099, 48103, 48104, 48105, 48107, 48108, 48110, 48115, 48117, 48120, 48131, 48132, 48134, 48135, 48137, 48146, 48148, 48149, 48150, 48152, 48153, 48154, 48157, 48158, 48159, 48163, 48165, 48171, 48172, 48176, 48178, 48181, 48182, 48185, 48186, 48187, 48189, 48190, 48192, 48195, 48196, 48199, 48200
2.1	PARA	48357, 48358, 48359, 48360, 48361, 48362, 48363, 48364, 48365, 48387, 48388, 48392, 48393, 48394, 48395, 48396, 48397, 48399, 48400, 48405, 48406, 48407, 48408
2.1	PERP	48335, 48337, 48338, 48339, 48340, 48341, 48342, 48343, 48344, 48348, 48349, 48351, 48366, 48367, 48368, 48370, 48371, 48372, 48373, 48374, 48377
Amorphous		48211, 48215-48217, 48237-48239, 48252-48254, 48265-48267, 48287, 48290, 48291, 48299, 48305, 48307, 48308 // 47923, 47927, 47931, 47935, 47939, 47945, 47946, 48413, 48414-48417, 48427-48429, 48456, 48460, 48461, 48489, 48492 // 47951, 47955, 47994, 48023, 48028, 48032, 48037, 48041, 48045, 48073, 48077, 48083, 48528-48531, 48575, 48576, 48578, 48579, 48635, 48636, 48641-48643 // 48092, 48097, 48101, 48106, 48111, 48112, 48114, 48126, 48133, 48138, 48147, 48151, 48155, 48160, 48177, 48183, 48184, 48188, 48193, 48197 // 48352, 48355, 48381-48386

Table B.2: Run numbers used for the 1.9 and 2.1 GeV coherent peak settings, as well as the amorphous radiator runs. The "/" separators in the amorphous runs divide the runs into groups which were performed during the run period for each coherent peak setting.

Appendix C

Tabulated Results for $K_0\Sigma^+$ Polarisation Observables

A systematic uncertainty (upper limit) applies to the results of 6% for energy bins 1.1-1.35 GeV, 1.35-1.6 GeV and 1.6-1.85 GeV, and 7% for energy bin 1.85-2.1 GeV.

Obs	E_γ GeV	$\cos \theta_{K^0}$	Mean	σ	Mode	16th quantile	25th quantile	Median	75th quantile	84th quantile
Σ	1.23	-0.81	0.528	0.185	0.502	0.342	0.402	0.525	0.664	0.725
Σ	1.23	-0.53	0.323	0.199	0.299	0.123	0.194	0.321	0.455	0.516
Σ	1.23	-0.28	0.665	0.163	0.663	0.499	0.561	0.674	0.793	0.839
Σ	1.23	-0.03	0.481	0.177	0.472	0.294	0.358	0.487	0.613	0.665
Σ	1.23	0.21	0.500	0.173	0.518	0.324	0.382	0.503	0.620	0.685
Σ	1.23	0.68	0.203	0.217	0.186	-0.021	0.056	0.201	0.353	0.413
Σ	1.48	-0.78	0.318	0.191	0.290	0.128	0.187	0.312	0.450	0.503
Σ	1.48	-0.44	0.504	0.136	0.482	0.363	0.410	0.505	0.606	0.639
Σ	1.48	-0.24	0.727	0.130	0.752	0.593	0.651	0.743	0.819	0.854
Σ	1.48	-0.09	0.735	0.109	0.723	0.633	0.671	0.741	0.813	0.846
Σ	1.48	0.07	0.749	0.100	0.777	0.654	0.691	0.764	0.819	0.843
Σ	1.48	0.24	0.671	0.143	0.700	0.513	0.574	0.685	0.780	0.822
Σ	1.48	0.43	0.558	0.117	0.594	0.441	0.483	0.562	0.642	0.678
Σ	1.48	0.77	0.209	0.146	0.207	0.062	0.114	0.207	0.304	0.357
Σ	1.73	-0.57	0.212	0.197	0.217	0.011	0.070	0.210	0.351	0.414
Σ	1.73	-0.02	0.440	0.171	0.415	0.272	0.321	0.437	0.562	0.610
Σ	1.73	0.24	0.360	0.168	0.351	0.194	0.244	0.362	0.477	0.524
Σ	1.73	0.45	0.254	0.169	0.275	0.078	0.133	0.261	0.371	0.422
Σ	1.73	0.76	0.487	0.173	0.457	0.317	0.377	0.486	0.600	0.663

Obs	E_γ GeV	$\cos \theta_{K^0}$	Mean	σ	Mode	16th quantile	25th quantile	Median	75th quantile	84th quantile
Σ	1.98	-0.42	0.289	0.213	0.206	0.078	0.142	0.278	0.431	0.503
Σ	1.98	0.58	0.205	0.195	0.173	0.008	0.073	0.199	0.334	0.406
O_x	1.23	-0.81	0.545	0.219	0.555	0.322	0.399	0.561	0.723	0.780
O_x	1.23	-0.53	0.212	0.303	0.170	-0.097	0.014	0.228	0.440	0.523
O_x	1.23	-0.28	-0.231	0.210	-0.291	-0.434	-0.382	-0.261	-0.109	-0.038
O_x	1.23	-0.03	0.572	0.219	0.621	0.341	0.434	0.598	0.741	0.795
O_x	1.23	0.21	0.512	0.255	0.610	0.296	0.391	0.553	0.696	0.750
O_x	1.23	0.68	0.591	0.280	0.838	0.298	0.417	0.652	0.817	0.866
O_x	1.48	-0.78	-0.063	0.364	0.009	-0.446	-0.319	-0.048	0.196	0.292
O_x	1.48	-0.44	0.045	0.276	-0.014	-0.243	-0.152	0.041	0.243	0.344
O_x	1.48	-0.24	0.195	0.179	0.247	0.011	0.080	0.207	0.320	0.374
O_x	1.48	-0.09	0.468	0.171	0.531	0.290	0.363	0.489	0.590	0.641
O_x	1.48	0.07	0.450	0.140	0.515	0.315	0.363	0.466	0.547	0.586
O_x	1.48	0.24	0.260	0.269	0.341	-0.011	0.098	0.299	0.458	0.514
O_x	1.48	0.43	0.386	0.280	0.546	0.127	0.249	0.450	0.588	0.636
O_x	1.48	0.77	-0.094	0.262	-0.208	-0.358	-0.280	-0.107	0.097	0.176
O_x	1.73	-0.57	0.309	0.315	0.345	-0.015	0.112	0.339	0.549	0.632
O_x	1.73	-0.02	0.189	0.244	0.256	-0.083	0.004	0.210	0.366	0.435
O_x	1.73	0.24	0.511	0.201	0.600	0.307	0.391	0.543	0.656	0.706
O_x	1.73	0.45	0.333	0.290	0.412	0.027	0.136	0.358	0.544	0.651
O_x	1.73	0.76	0.182	0.269	0.223	-0.095	0.011	0.198	0.372	0.449
O_x	1.98	-0.42	0.013	0.327	-0.112	-0.332	-0.214	0.012	0.260	0.361
O_x	1.98	0.58	0.002	0.418	-0.124	-0.427	-0.288	-0.020	0.302	0.448
O_z	1.23	-0.81	0.176	0.282	0.244	-0.107	-0.019	0.194	0.368	0.446
O_z	1.23	-0.53	-0.092	0.332	-0.115	-0.442	-0.322	-0.094	0.116	0.227
O_z	1.23	-0.28	0.042	0.254	0.194	-0.234	-0.140	0.065	0.231	0.293
O_z	1.23	-0.03	0.250	0.268	0.281	-0.034	0.071	0.265	0.447	0.532
O_z	1.23	0.21	-0.092	0.349	-0.271	-0.437	-0.357	-0.124	0.145	0.305
O_z	1.23	0.68	-0.143	0.330	-0.078	-0.494	-0.383	-0.126	0.084	0.196
O_z	1.48	-0.78	-0.179	0.358	-0.151	-0.552	-0.460	-0.175	0.075	0.178
O_z	1.48	-0.44	-0.298	0.281	-0.477	-0.571	-0.511	-0.343	-0.112	0.004
O_z	1.48	-0.24	0.001	0.224	-0.109	-0.235	-0.175	0.002	0.181	0.246
O_z	1.48	-0.09	-0.000	0.217	-0.039	-0.214	-0.149	-0.016	0.138	0.230

Obs	E_γ GeV	$\cos\theta_{K^0}$	Mean	σ	Mode	16th quantile	25th quantile	Median	75th quantile	84th quantile
O_z	1.48	0.07	-0.002	0.175	-0.018	-0.172	-0.112	-0.007	0.111	0.173
O_z	1.48	0.24	0.149	0.266	0.233	-0.137	-0.039	0.162	0.352	0.430
O_z	1.48	0.43	0.142	0.320	0.257	-0.209	-0.097	0.176	0.395	0.482
O_z	1.48	0.77	0.329	0.252	0.260	0.081	0.167	0.328	0.500	0.582
O_z	1.73	-0.57	-0.102	0.306	-0.143	-0.431	-0.315	-0.108	0.097	0.201
O_z	1.73	-0.02	-0.014	0.214	0.055	-0.234	-0.161	-0.012	0.130	0.203
O_z	1.73	0.24	-0.417	0.212	-0.433	-0.633	-0.583	-0.428	-0.270	-0.202
O_z	1.73	0.45	-0.627	0.196	-0.718	-0.823	-0.772	-0.655	-0.503	-0.433
O_z	1.73	0.76	-0.358	0.258	-0.340	-0.627	-0.553	-0.367	-0.184	-0.103
O_z	1.98	-0.42	0.024	0.307	-0.003	-0.294	-0.200	0.022	0.248	0.340
O_z	1.98	0.58	-0.084	0.342	-0.071	-0.441	-0.328	-0.078	0.152	0.256
P	1.23	-0.81	-0.010	0.194	-0.039	-0.210	-0.146	-0.019	0.116	0.190
P	1.23	-0.53	0.468	0.196	0.485	0.274	0.348	0.474	0.599	0.663
P	1.23	-0.28	0.839	0.100	0.911	0.739	0.780	0.859	0.916	0.936
P	1.23	-0.03	0.207	0.156	0.247	0.045	0.097	0.214	0.314	0.366
P	1.23	0.21	0.297	0.176	0.273	0.123	0.175	0.294	0.419	0.469
P	1.23	0.68	0.105	0.204	0.117	-0.106	-0.037	0.110	0.247	0.310
P	1.48	-0.78	0.158	0.166	0.143	0.000	0.047	0.151	0.265	0.323
P	1.48	-0.44	0.302	0.151	0.262	0.145	0.199	0.300	0.405	0.453
P	1.48	-0.24	0.625	0.115	0.621	0.512	0.551	0.629	0.708	0.738
P	1.48	-0.09	0.557	0.148	0.636	0.410	0.460	0.569	0.662	0.699
P	1.48	0.07	0.811	0.086	0.834	0.726	0.755	0.820	0.876	0.898
P	1.48	0.24	0.463	0.141	0.448	0.326	0.367	0.465	0.559	0.610
P	1.48	0.43	0.601	0.120	0.594	0.479	0.525	0.607	0.692	0.722
P	1.48	0.77	0.241	0.137	0.252	0.107	0.142	0.240	0.334	0.380
P	1.73	-0.57	0.500	0.173	0.521	0.320	0.390	0.509	0.632	0.679
P	1.73	-0.02	0.816	0.102	0.847	0.711	0.753	0.832	0.893	0.920
P	1.73	0.24	0.534	0.146	0.587	0.379	0.437	0.553	0.633	0.674
P	1.73	0.45	0.184	0.149	0.202	0.037	0.077	0.183	0.280	0.330
P	1.73	0.76	-0.101	0.155	-0.069	-0.246	-0.202	-0.098	0.001	0.055
P	1.98	-0.42	0.660	0.141	0.710	0.513	0.552	0.661	0.774	0.812
P	1.98	0.58	0.250	0.164	0.278	0.082	0.136	0.255	0.364	0.408
T	1.23	-0.81	0.284	0.239	0.253	0.059	0.133	0.280	0.441	0.521

Obs	E_γ GeV	$\cos \theta_{K^0}$	Mean	σ	Mode	16th quantile	25th quantile	Median	75th quantile	84th quantile
T	1.23	-0.53	0.109	0.233	0.092	-0.121	-0.063	0.094	0.261	0.344
T	1.23	-0.28	0.684	0.176	0.765	0.505	0.564	0.703	0.817	0.870
T	1.23	-0.03	0.221	0.238	0.224	-0.027	0.057	0.216	0.386	0.465
T	1.23	0.21	0.541	0.236	0.704	0.280	0.367	0.566	0.730	0.783
T	1.23	0.68	0.189	0.299	0.241	-0.126	-0.029	0.191	0.398	0.490
T	1.48	-0.78	0.135	0.218	0.107	-0.074	-0.016	0.124	0.278	0.347
T	1.48	-0.44	-0.023	0.190	-0.015	-0.211	-0.156	-0.027	0.099	0.157
T	1.48	-0.24	0.401	0.176	0.445	0.221	0.273	0.407	0.530	0.582
T	1.48	-0.09	0.657	0.189	0.728	0.453	0.525	0.679	0.802	0.858
T	1.48	0.07	0.843	0.101	0.891	0.759	0.794	0.861	0.913	0.936
T	1.48	0.24	0.517	0.182	0.506	0.330	0.388	0.520	0.646	0.696
T	1.48	0.43	0.668	0.164	0.747	0.501	0.563	0.687	0.790	0.831
T	1.48	0.77	0.286	0.193	0.264	0.100	0.160	0.284	0.419	0.481
T	1.73	-0.57	0.200	0.254	0.208	-0.055	0.021	0.192	0.359	0.469
T	1.73	-0.02	0.411	0.192	0.417	0.208	0.280	0.411	0.547	0.614
T	1.73	0.24	0.621	0.189	0.678	0.420	0.489	0.639	0.773	0.816
T	1.73	0.45	0.281	0.259	0.174	0.014	0.088	0.263	0.485	0.568
T	1.73	0.76	-0.008	0.216	0.017	-0.228	-0.154	-0.003	0.143	0.211
T	1.98	-0.42	0.246	0.225	0.264	0.014	0.092	0.243	0.382	0.470
T	1.98	0.58	0.095	0.230	0.059	-0.142	-0.063	0.089	0.250	0.327

Table C.1: Values characterising the probability density function for the each observable and bin for the $K_0\Sigma^+$ polarisation observables.

Appendix D

Tabulated Results for ϕ -meson Spin Density Matrix Elements

The following three tables list the extracted values characterising the probability density function for the spin density matrix elements in the Helicity, Gottfried-Jackson, and Adair systems.

D.1 Tabulated Results for ϕ -meson Spin Density Matrix Elements in the Helicity system

Obs	E_γ GeV	$\cos \theta_\phi$	Mean	σ	16th quantile	25th quantile	Median	75th quantile	84th quantile
ρ_{00}^0	1.6	-0.34	0.380	0.043	0.334	0.351	0.380	0.407	0.421
ρ_{00}^0	1.6	0.66	0.282	0.038	0.242	0.253	0.281	0.310	0.321
ρ_{00}^0	1.8	-0.64	0.267	0.038	0.230	0.242	0.265	0.291	0.304
ρ_{00}^0	1.8	-0.1	0.273	0.036	0.236	0.249	0.274	0.299	0.310
ρ_{00}^0	1.8	0.19	0.303	0.039	0.263	0.275	0.303	0.330	0.343
ρ_{00}^0	1.8	0.39	0.370	0.039	0.334	0.345	0.369	0.394	0.408
ρ_{00}^0	1.8	0.54	0.244	0.030	0.213	0.223	0.245	0.265	0.275
ρ_{00}^0	1.8	0.81	0.223	0.033	0.189	0.200	0.224	0.245	0.256
ρ_{00}^0	2.0	-0.64	0.399	0.037	0.359	0.373	0.400	0.423	0.433
ρ_{00}^0	2.0	-0.14	0.369	0.043	0.327	0.339	0.368	0.397	0.411
ρ_{00}^0	2.0	0.1	0.355	0.039	0.315	0.327	0.354	0.382	0.394
ρ_{00}^0	2.0	0.26	0.322	0.033	0.289	0.298	0.322	0.345	0.355
ρ_{00}^0	2.0	0.38	0.332	0.030	0.302	0.312	0.332	0.351	0.360
ρ_{00}^0	2.0	0.46	0.339	0.029	0.311	0.320	0.340	0.358	0.369
ρ_{00}^0	2.0	0.54	0.292	0.030	0.263	0.272	0.292	0.312	0.322

Obs	E_γ GeV	$\cos \theta_\phi$	Mean	σ	16th quantile	25th quantile	Median	75th quantile	84th quantile
ρ_{00}^0	2.0	0.61	0.312	0.028	0.283	0.293	0.311	0.330	0.340
ρ_{00}^0	2.0	0.68	0.217	0.026	0.191	0.199	0.218	0.235	0.243
ρ_{00}^0	2.0	0.86	0.173	0.025	0.149	0.156	0.172	0.190	0.198
$\text{Re} \rho_{10}^0$	1.6	-0.34	-0.035	0.025	-0.060	-0.052	-0.034	-0.017	-0.009
$\text{Re} \rho_{10}^0$	1.6	0.66	-0.091	0.021	-0.112	-0.104	-0.091	-0.076	-0.069
$\text{Re} \rho_{10}^0$	1.8	-0.64	-0.080	0.015	-0.094	-0.090	-0.077	-0.068	-0.065
$\text{Re} \rho_{10}^0$	1.8	-0.1	-0.107	0.027	-0.134	-0.125	-0.106	-0.088	-0.079
$\text{Re} \rho_{10}^0$	1.8	0.19	-0.102	0.018	-0.120	-0.115	-0.104	-0.091	-0.084
$\text{Re} \rho_{10}^0$	1.8	0.39	-0.104	0.017	-0.121	-0.116	-0.103	-0.092	-0.087
$\text{Re} \rho_{10}^0$	1.8	0.54	-0.122	0.017	-0.138	-0.133	-0.123	-0.112	-0.106
$\text{Re} \rho_{10}^0$	1.8	0.81	-0.122	0.017	-0.139	-0.134	-0.123	-0.111	-0.105
$\text{Re} \rho_{10}^0$	2.0	-0.64	-0.096	0.031	-0.125	-0.117	-0.097	-0.077	-0.067
$\text{Re} \rho_{10}^0$	2.0	-0.14	-0.045	0.025	-0.071	-0.062	-0.044	-0.028	-0.020
$\text{Re} \rho_{10}^0$	2.0	0.1	-0.115	0.021	-0.136	-0.130	-0.116	-0.101	-0.093
$\text{Re} \rho_{10}^0$	2.0	0.26	-0.086	0.019	-0.103	-0.098	-0.086	-0.075	-0.069
$\text{Re} \rho_{10}^0$	2.0	0.38	-0.086	0.019	-0.103	-0.097	-0.087	-0.074	-0.068
$\text{Re} \rho_{10}^0$	2.0	0.46	-0.126	0.018	-0.144	-0.139	-0.126	-0.114	-0.109
$\text{Re} \rho_{10}^0$	2.0	0.54	-0.075	0.018	-0.094	-0.088	-0.075	-0.063	-0.057
$\text{Re} \rho_{10}^0$	2.0	0.61	-0.127	0.016	-0.143	-0.138	-0.128	-0.117	-0.111
$\text{Re} \rho_{10}^0$	2.0	0.68	-0.142	0.013	-0.155	-0.151	-0.143	-0.134	-0.130
$\text{Re} \rho_{10}^0$	2.0	0.86	-0.090	0.018	-0.108	-0.102	-0.091	-0.078	-0.073
ρ_{1-1}^0	1.6	-0.34	0.139	0.035	0.105	0.116	0.140	0.163	0.173
ρ_{1-1}^0	1.6	0.66	0.125	0.037	0.090	0.101	0.125	0.149	0.162
ρ_{1-1}^0	1.8	-0.64	-0.133	0.035	-0.167	-0.156	-0.133	-0.110	-0.100
ρ_{1-1}^0	1.8	-0.1	0.016	0.040	-0.023	-0.009	0.014	0.043	0.057
ρ_{1-1}^0	1.8	0.19	0.133	0.035	0.098	0.110	0.134	0.157	0.166
ρ_{1-1}^0	1.8	0.39	0.141	0.023	0.117	0.125	0.143	0.159	0.164
ρ_{1-1}^0	1.8	0.54	0.118	0.030	0.087	0.096	0.118	0.139	0.148
ρ_{1-1}^0	1.8	0.81	0.070	0.030	0.041	0.051	0.072	0.092	0.100
ρ_{1-1}^0	2.0	-0.64	-0.154	0.033	-0.186	-0.176	-0.154	-0.132	-0.121
ρ_{1-1}^0	2.0	-0.14	-0.015	0.038	-0.054	-0.041	-0.016	0.009	0.021
ρ_{1-1}^0	2.0	0.1	0.119	0.030	0.089	0.100	0.119	0.138	0.149
ρ_{1-1}^0	2.0	0.26	0.124	0.025	0.099	0.106	0.124	0.141	0.149

Obs	E_γ GeV	$\cos \theta_\phi$	Mean	σ	16th quantile	25th quantile	Median	75th quantile	84th quantile
ρ_{1-1}^0	2.0	0.38	0.088	0.029	0.060	0.069	0.087	0.106	0.116
ρ_{1-1}^0	2.0	0.46	0.111	0.026	0.083	0.093	0.111	0.128	0.137
ρ_{1-1}^0	2.0	0.54	0.052	0.026	0.025	0.033	0.051	0.071	0.079
ρ_{1-1}^0	2.0	0.61	0.083	0.021	0.063	0.069	0.082	0.098	0.105
ρ_{1-1}^0	2.0	0.68	0.037	0.026	0.011	0.019	0.037	0.056	0.064
ρ_{1-1}^0	2.0	0.86	0.013	0.031	-0.016	-0.008	0.010	0.032	0.044
ρ_{11}^1	1.6	-0.34	-0.069	0.052	-0.121	-0.106	-0.069	-0.033	-0.018
ρ_{11}^1	1.6	0.66	0.017	0.053	-0.032	-0.018	0.018	0.055	0.069
ρ_{11}^1	1.8	-0.64	-0.068	0.060	-0.128	-0.110	-0.067	-0.028	-0.009
ρ_{11}^1	1.8	-0.1	0.040	0.051	-0.009	0.009	0.042	0.074	0.088
ρ_{11}^1	1.8	0.19	0.064	0.049	0.016	0.032	0.066	0.098	0.113
ρ_{11}^1	1.8	0.39	0.065	0.044	0.020	0.034	0.064	0.096	0.109
ρ_{11}^1	1.8	0.54	0.011	0.043	-0.032	-0.018	0.013	0.042	0.055
ρ_{11}^1	1.8	0.81	-0.018	0.041	-0.059	-0.044	-0.018	0.009	0.024
ρ_{11}^1	2.0	-0.64	-0.137	0.062	-0.200	-0.179	-0.139	-0.096	-0.074
ρ_{11}^1	2.0	-0.14	-0.042	0.057	-0.096	-0.079	-0.046	-0.006	0.016
ρ_{11}^1	2.0	0.1	0.159	0.054	0.107	0.123	0.158	0.194	0.213
ρ_{11}^1	2.0	0.26	0.160	0.048	0.110	0.120	0.155	0.198	0.214
ρ_{11}^1	2.0	0.38	0.114	0.043	0.071	0.085	0.113	0.144	0.157
ρ_{11}^1	2.0	0.46	0.063	0.037	0.026	0.036	0.063	0.089	0.101
ρ_{11}^1	2.0	0.54	0.086	0.046	0.043	0.056	0.086	0.117	0.134
ρ_{11}^1	2.0	0.61	0.049	0.044	0.003	0.018	0.050	0.080	0.094
ρ_{11}^1	2.0	0.68	0.081	0.039	0.041	0.054	0.080	0.108	0.120
ρ_{11}^1	2.0	0.86	-0.003	0.047	-0.049	-0.034	-0.005	0.028	0.044
ρ_{00}^1	1.6	-0.34	0.033	0.096	-0.062	-0.030	0.033	0.094	0.122
ρ_{00}^1	1.6	0.66	0.156	0.071	0.082	0.107	0.156	0.205	0.229
ρ_{00}^1	1.8	-0.64	-0.101	0.081	-0.178	-0.151	-0.097	-0.044	-0.020
ρ_{00}^1	1.8	-0.1	-0.075	0.075	-0.148	-0.124	-0.072	-0.027	-0.004
ρ_{00}^1	1.8	0.19	-0.011	0.066	-0.077	-0.051	-0.005	0.036	0.052
ρ_{00}^1	1.8	0.39	-0.023	0.073	-0.093	-0.073	-0.026	0.026	0.048
ρ_{00}^1	1.8	0.54	-0.011	0.062	-0.071	-0.053	-0.012	0.030	0.048
ρ_{00}^1	1.8	0.81	0.038	0.058	-0.019	-0.002	0.035	0.076	0.098
ρ_{00}^1	2.0	-0.64	-0.048	0.096	-0.142	-0.107	-0.050	0.019	0.051

Obs	E_γ GeV	$\cos \theta_\phi$	Mean	σ	16th quantile	25th quantile	Median	75th quantile	84th quantile
ρ_{00}^1	2.0	-0.14	-0.101	0.085	-0.186	-0.158	-0.101	-0.040	-0.015
ρ_{00}^1	2.0	0.1	-0.210	0.081	-0.293	-0.267	-0.214	-0.154	-0.126
ρ_{00}^1	2.0	0.26	-0.026	0.056	-0.086	-0.065	-0.021	0.015	0.033
ρ_{00}^1	2.0	0.38	-0.128	0.070	-0.196	-0.177	-0.128	-0.078	-0.055
ρ_{00}^1	2.0	0.46	-0.041	0.063	-0.104	-0.083	-0.038	0.002	0.021
ρ_{00}^1	2.0	0.54	-0.048	0.069	-0.116	-0.096	-0.048	-0.003	0.022
ρ_{00}^1	2.0	0.61	0.039	0.067	-0.030	-0.010	0.036	0.082	0.106
ρ_{00}^1	2.0	0.68	-0.166	0.050	-0.219	-0.201	-0.166	-0.133	-0.117
ρ_{00}^1	2.0	0.86	-0.088	0.056	-0.144	-0.127	-0.090	-0.049	-0.028
$\text{Re } \rho_{10}^1$	1.6	-0.34	0.044	0.051	-0.007	0.011	0.045	0.077	0.094
$\text{Re } \rho_{10}^1$	1.6	0.66	-0.020	0.039	-0.060	-0.048	-0.020	0.008	0.018
$\text{Re } \rho_{10}^1$	1.8	-0.64	0.170	0.046	0.124	0.140	0.171	0.201	0.216
$\text{Re } \rho_{10}^1$	1.8	-0.1	0.147	0.038	0.112	0.125	0.150	0.174	0.184
$\text{Re } \rho_{10}^1$	1.8	0.19	0.055	0.035	0.019	0.030	0.055	0.079	0.090
$\text{Re } \rho_{10}^1$	1.8	0.39	0.059	0.031	0.026	0.038	0.060	0.080	0.089
$\text{Re } \rho_{10}^1$	1.8	0.54	0.054	0.031	0.022	0.031	0.052	0.074	0.086
$\text{Re } \rho_{10}^1$	1.8	0.81	0.070	0.033	0.037	0.048	0.071	0.093	0.105
$\text{Re } \rho_{10}^1$	2.0	-0.64	0.162	0.061	0.106	0.124	0.162	0.203	0.221
$\text{Re } \rho_{10}^1$	2.0	-0.14	0.055	0.046	0.008	0.023	0.056	0.089	0.102
$\text{Re } \rho_{10}^1$	2.0	0.1	0.171	0.036	0.136	0.147	0.172	0.196	0.207
$\text{Re } \rho_{10}^1$	2.0	0.26	0.168	0.035	0.136	0.149	0.172	0.193	0.201
$\text{Re } \rho_{10}^1$	2.0	0.38	0.006	0.035	-0.029	-0.019	0.005	0.030	0.039
$\text{Re } \rho_{10}^1$	2.0	0.46	0.060	0.037	0.024	0.035	0.060	0.086	0.097
$\text{Re } \rho_{10}^1$	2.0	0.54	0.005	0.038	-0.035	-0.023	0.004	0.031	0.043
$\text{Re } \rho_{10}^1$	2.0	0.61	0.069	0.034	0.036	0.047	0.069	0.092	0.104
$\text{Re } \rho_{10}^1$	2.0	0.68	0.096	0.028	0.066	0.076	0.097	0.116	0.125
$\text{Re } \rho_{10}^1$	2.0	0.86	0.086	0.039	0.047	0.060	0.086	0.112	0.125
ρ_{1-1}^1	1.6	-0.34	-0.070	0.068	-0.138	-0.116	-0.070	-0.024	-0.003
ρ_{1-1}^1	1.6	0.66	-0.023	0.063	-0.085	-0.066	-0.026	0.019	0.038
ρ_{1-1}^1	1.8	-0.64	0.172	0.074	0.094	0.118	0.172	0.222	0.248
ρ_{1-1}^1	1.8	-0.1	0.130	0.061	0.067	0.090	0.131	0.173	0.192
ρ_{1-1}^1	1.8	0.19	0.097	0.059	0.037	0.056	0.097	0.135	0.151
ρ_{1-1}^1	1.8	0.39	0.199	0.049	0.151	0.166	0.201	0.232	0.249
ρ_{1-1}^1	1.8	0.54	0.166	0.055	0.109	0.127	0.165	0.202	0.221

Obs	E_γ GeV	$\cos \theta_\phi$	Mean	σ	16th quantile	25th quantile	Median	75th quantile	84th quantile
ρ_{1-1}^1	1.8	0.81	0.280	0.045	0.234	0.250	0.281	0.312	0.326
ρ_{1-1}^1	2.0	-0.64	0.255	0.068	0.184	0.208	0.259	0.304	0.323
ρ_{1-1}^1	2.0	-0.14	0.224	0.068	0.157	0.179	0.228	0.271	0.291
ρ_{1-1}^1	2.0	0.1	0.326	0.059	0.262	0.289	0.330	0.368	0.385
ρ_{1-1}^1	2.0	0.26	0.274	0.045	0.228	0.245	0.276	0.308	0.320
ρ_{1-1}^1	2.0	0.38	0.316	0.051	0.263	0.280	0.318	0.353	0.369
ρ_{1-1}^1	2.0	0.46	0.157	0.054	0.103	0.123	0.161	0.196	0.211
ρ_{1-1}^1	2.0	0.54	0.248	0.057	0.189	0.210	0.248	0.289	0.306
ρ_{1-1}^1	2.0	0.61	0.228	0.049	0.176	0.194	0.228	0.262	0.278
ρ_{1-1}^1	2.0	0.68	0.333	0.052	0.280	0.298	0.336	0.371	0.385
ρ_{1-1}^1	2.0	0.86	0.310	0.055	0.254	0.272	0.310	0.347	0.364
$\text{Im} \rho_{10}^2$	1.6	-0.34	-0.102	0.049	-0.152	-0.134	-0.102	-0.071	-0.054
$\text{Im} \rho_{10}^2$	1.6	0.66	0.017	0.046	-0.028	-0.013	0.015	0.048	0.062
$\text{Im} \rho_{10}^2$	1.8	-0.64	-0.073	0.044	-0.117	-0.105	-0.075	-0.046	-0.032
$\text{Im} \rho_{10}^2$	1.8	-0.1	-0.026	0.046	-0.074	-0.060	-0.027	0.005	0.021
$\text{Im} \rho_{10}^2$	1.8	0.19	-0.082	0.045	-0.129	-0.114	-0.082	-0.053	-0.037
$\text{Im} \rho_{10}^2$	1.8	0.39	-0.135	0.047	-0.183	-0.167	-0.137	-0.104	-0.089
$\text{Im} \rho_{10}^2$	1.8	0.54	-0.088	0.043	-0.130	-0.116	-0.087	-0.059	-0.045
$\text{Im} \rho_{10}^2$	1.8	0.81	-0.052	0.043	-0.094	-0.081	-0.051	-0.022	-0.010
$\text{Im} \rho_{10}^2$	2.0	-0.64	-0.023	0.056	-0.079	-0.062	-0.026	0.015	0.033
$\text{Im} \rho_{10}^2$	2.0	-0.14	-0.137	0.049	-0.186	-0.171	-0.138	-0.105	-0.088
$\text{Im} \rho_{10}^2$	2.0	0.1	-0.125	0.051	-0.176	-0.161	-0.126	-0.089	-0.072
$\text{Im} \rho_{10}^2$	2.0	0.26	-0.104	0.044	-0.149	-0.133	-0.103	-0.074	-0.061
$\text{Im} \rho_{10}^2$	2.0	0.38	-0.106	0.043	-0.148	-0.135	-0.107	-0.080	-0.065
$\text{Im} \rho_{10}^2$	2.0	0.46	-0.086	0.041	-0.127	-0.113	-0.086	-0.059	-0.046
$\text{Im} \rho_{10}^2$	2.0	0.54	-0.039	0.036	-0.077	-0.064	-0.040	-0.014	-0.002
$\text{Im} \rho_{10}^2$	2.0	0.61	-0.107	0.035	-0.142	-0.131	-0.107	-0.083	-0.073
$\text{Im} \rho_{10}^2$	2.0	0.68	-0.101	0.035	-0.136	-0.125	-0.101	-0.077	-0.066
$\text{Im} \rho_{10}^2$	2.0	0.86	-0.091	0.041	-0.134	-0.120	-0.091	-0.064	-0.050
$\text{Im} \rho_{1-1}^2$	1.6	-0.34	-0.089	0.074	-0.163	-0.141	-0.091	-0.036	-0.013
$\text{Im} \rho_{1-1}^2$	1.6	0.66	-0.054	0.062	-0.116	-0.100	-0.054	-0.009	0.012
$\text{Im} \rho_{1-1}^2$	1.8	-0.64	-0.171	0.069	-0.238	-0.217	-0.173	-0.127	-0.103
$\text{Im} \rho_{1-1}^2$	1.8	-0.1	0.106	0.078	0.028	0.054	0.103	0.160	0.188

Obs	E_γ GeV	$\cos \theta_\phi$	Mean	σ	16th quantile	25th quantile	Median	75th quantile	84th quantile
$\text{Im} \rho_{1-1}^2$	1.8	0.19	-0.159	0.073	-0.230	-0.209	-0.162	-0.113	-0.086
$\text{Im} \rho_{1-1}^2$	1.8	0.39	-0.075	0.065	-0.140	-0.119	-0.075	-0.031	-0.010
$\text{Im} \rho_{1-1}^2$	1.8	0.54	-0.290	0.058	-0.350	-0.332	-0.292	-0.251	-0.233
$\text{Im} \rho_{1-1}^2$	1.8	0.81	-0.163	0.063	-0.226	-0.207	-0.165	-0.121	-0.099
$\text{Im} \rho_{1-1}^2$	2.0	-0.64	0.017	0.079	-0.062	-0.038	0.017	0.071	0.096
$\text{Im} \rho_{1-1}^2$	2.0	-0.14	-0.234	0.065	-0.302	-0.282	-0.236	-0.189	-0.168
$\text{Im} \rho_{1-1}^2$	2.0	0.1	-0.240	0.066	-0.306	-0.284	-0.241	-0.195	-0.176
$\text{Im} \rho_{1-1}^2$	2.0	0.26	-0.155	0.064	-0.219	-0.201	-0.156	-0.114	-0.093
$\text{Im} \rho_{1-1}^2$	2.0	0.38	-0.184	0.054	-0.239	-0.219	-0.183	-0.150	-0.133
$\text{Im} \rho_{1-1}^2$	2.0	0.46	-0.247	0.045	-0.293	-0.278	-0.247	-0.218	-0.204
$\text{Im} \rho_{1-1}^2$	2.0	0.54	-0.238	0.057	-0.292	-0.274	-0.240	-0.203	-0.183
$\text{Im} \rho_{1-1}^2$	2.0	0.61	-0.239	0.050	-0.291	-0.274	-0.240	-0.205	-0.186
$\text{Im} \rho_{1-1}^2$	2.0	0.68	-0.123	0.056	-0.180	-0.158	-0.120	-0.086	-0.067
$\text{Im} \rho_{1-1}^2$	2.0	0.86	-0.107	0.066	-0.172	-0.153	-0.107	-0.062	-0.039

Table D.1: Values characterising the probability density function for each observable and bin for the ϕ -meson spin density matrix elements in the Helicity system.

D.2 Tabulated Results for ϕ -meson Spin Density Matrix Elements in the Gottfried-Jackson system

Obs	E_γ GeV	$\cos \theta_\phi$	Mean	σ	16th quantile	25th quantile	Median	75th quantile	84th quantile
ρ_{00}^0	1.6	-0.34	0.210	0.045	0.163	0.179	0.211	0.243	0.257
ρ_{00}^0	1.6	0.66	0.134	0.043	0.092	0.102	0.132	0.165	0.180
ρ_{00}^0	1.8	-0.64	0.522	0.039	0.485	0.497	0.521	0.547	0.559
ρ_{00}^0	1.8	-0.1	0.428	0.044	0.381	0.397	0.427	0.459	0.474
ρ_{00}^0	1.8	0.19	0.252	0.039	0.213	0.224	0.251	0.279	0.292
ρ_{00}^0	1.8	0.39	0.176	0.028	0.150	0.158	0.174	0.191	0.201
ρ_{00}^0	1.8	0.54	0.166	0.028	0.139	0.147	0.165	0.184	0.195
ρ_{00}^0	1.8	0.81	0.137	0.027	0.112	0.120	0.137	0.155	0.164
ρ_{00}^0	2.0	-0.64	0.579	0.043	0.537	0.550	0.579	0.607	0.623
ρ_{00}^0	2.0	-0.14	0.389	0.039	0.350	0.362	0.389	0.416	0.429
ρ_{00}^0	2.0	0.1	0.316	0.036	0.280	0.291	0.318	0.341	0.352

Obs	E_γ GeV	$\cos \theta_\phi$	Mean	σ	16th quantile	25th quantile	Median	75th quantile	84th quantile
ρ_{00}^0	2.0	0.26	0.251	0.030	0.221	0.230	0.250	0.272	0.282
ρ_{00}^0	2.0	0.38	0.263	0.030	0.232	0.243	0.264	0.285	0.294
ρ_{00}^0	2.0	0.46	0.198	0.030	0.169	0.178	0.198	0.218	0.226
ρ_{00}^0	2.0	0.54	0.272	0.031	0.241	0.252	0.274	0.293	0.302
ρ_{00}^0	2.0	0.61	0.178	0.024	0.154	0.162	0.177	0.194	0.202
ρ_{00}^0	2.0	0.68	0.188	0.026	0.164	0.171	0.187	0.203	0.211
ρ_{00}^0	2.0	0.86	0.218	0.033	0.187	0.196	0.217	0.239	0.250
$\text{Re} \rho_{10}^0$	1.6	-0.34	0.015	0.025	-0.010	-0.003	0.012	0.033	0.042
$\text{Re} \rho_{10}^0$	1.6	0.66	0.053	0.023	0.031	0.039	0.054	0.068	0.075
$\text{Re} \rho_{10}^0$	1.8	-0.64	-0.121	0.025	-0.145	-0.138	-0.122	-0.105	-0.097
$\text{Re} \rho_{10}^0$	1.8	-0.1	0.055	0.025	0.029	0.038	0.055	0.074	0.081
$\text{Re} \rho_{10}^0$	1.8	0.19	0.105	0.018	0.088	0.094	0.106	0.117	0.122
$\text{Re} \rho_{10}^0$	1.8	0.39	0.111	0.012	0.100	0.103	0.111	0.119	0.123
$\text{Re} \rho_{10}^0$	1.8	0.54	0.113	0.017	0.097	0.102	0.113	0.124	0.128
$\text{Re} \rho_{10}^0$	1.8	0.81	0.097	0.020	0.077	0.083	0.097	0.110	0.116
$\text{Re} \rho_{10}^0$	2.0	-0.64	-0.090	0.031	-0.121	-0.111	-0.091	-0.070	-0.061
$\text{Re} \rho_{10}^0$	2.0	-0.14	0.039	0.026	0.014	0.022	0.039	0.057	0.065
$\text{Re} \rho_{10}^0$	2.0	0.1	0.135	0.020	0.114	0.121	0.137	0.151	0.156
$\text{Re} \rho_{10}^0$	2.0	0.26	0.088	0.018	0.070	0.075	0.086	0.103	0.109
$\text{Re} \rho_{10}^0$	2.0	0.38	0.089	0.018	0.070	0.075	0.089	0.102	0.107
$\text{Re} \rho_{10}^0$	2.0	0.46	0.116	0.017	0.099	0.104	0.116	0.127	0.133
$\text{Re} \rho_{10}^0$	2.0	0.54	0.073	0.019	0.054	0.060	0.073	0.086	0.092
$\text{Re} \rho_{10}^0$	2.0	0.61	0.102	0.017	0.086	0.091	0.102	0.114	0.119
$\text{Re} \rho_{10}^0$	2.0	0.68	0.135	0.016	0.119	0.124	0.135	0.146	0.151
$\text{Re} \rho_{10}^0$	2.0	0.86	0.117	0.016	0.101	0.106	0.118	0.128	0.132
ρ_{1-1}^0	1.6	-0.34	0.048	0.032	0.015	0.026	0.048	0.070	0.080
ρ_{1-1}^0	1.6	0.66	0.059	0.034	0.024	0.035	0.058	0.081	0.091
ρ_{1-1}^0	1.8	-0.64	-0.014	0.029	-0.043	-0.033	-0.014	0.005	0.013
ρ_{1-1}^0	1.8	-0.1	0.104	0.034	0.070	0.082	0.105	0.127	0.138
ρ_{1-1}^0	1.8	0.19	0.105	0.033	0.072	0.082	0.105	0.127	0.137
ρ_{1-1}^0	1.8	0.39	0.031	0.029	0.002	0.011	0.030	0.050	0.059
ρ_{1-1}^0	1.8	0.54	0.074	0.033	0.042	0.051	0.073	0.097	0.109
ρ_{1-1}^0	1.8	0.81	0.022	0.029	-0.008	0.001	0.021	0.041	0.050

Obs	E_γ GeV	$\cos \theta_\phi$	Mean	σ	16th quantile	25th quantile	Median	75th quantile	84th quantile
ρ_{1-1}^0	2.0	-0.64	-0.073	0.028	-0.100	-0.092	-0.073	-0.053	-0.045
ρ_{1-1}^0	2.0	-0.14	-0.007	0.031	-0.038	-0.027	-0.005	0.015	0.024
ρ_{1-1}^0	2.0	0.1	0.096	0.029	0.067	0.076	0.096	0.116	0.125
ρ_{1-1}^0	2.0	0.26	0.087	0.027	0.060	0.070	0.089	0.105	0.113
ρ_{1-1}^0	2.0	0.38	0.055	0.026	0.030	0.038	0.056	0.073	0.081
ρ_{1-1}^0	2.0	0.46	0.034	0.028	0.006	0.016	0.034	0.053	0.062
ρ_{1-1}^0	2.0	0.54	0.044	0.029	0.015	0.025	0.044	0.063	0.072
ρ_{1-1}^0	2.0	0.61	0.009	0.026	-0.017	-0.010	0.009	0.027	0.036
ρ_{1-1}^0	2.0	0.68	0.024	0.027	-0.003	0.006	0.025	0.042	0.051
ρ_{1-1}^0	2.0	0.86	0.034	0.027	0.007	0.016	0.034	0.052	0.061
ρ_{11}^1	1.6	-0.34	0.009	0.053	-0.042	-0.025	0.009	0.044	0.062
ρ_{11}^1	1.6	0.66	0.049	0.051	-0.002	0.015	0.048	0.083	0.100
ρ_{11}^1	1.8	-0.64	0.093	0.045	0.045	0.060	0.093	0.124	0.139
ρ_{11}^1	1.8	-0.1	0.104	0.049	0.056	0.072	0.103	0.138	0.153
ρ_{11}^1	1.8	0.19	0.100	0.050	0.052	0.067	0.100	0.132	0.149
ρ_{11}^1	1.8	0.39	0.105	0.041	0.064	0.076	0.106	0.133	0.146
ρ_{11}^1	1.8	0.54	0.054	0.040	0.014	0.028	0.057	0.081	0.092
ρ_{11}^1	1.8	0.81	0.061	0.041	0.019	0.033	0.062	0.089	0.102
ρ_{11}^1	2.0	-0.64	0.035	0.050	-0.018	0.001	0.036	0.071	0.085
ρ_{11}^1	2.0	-0.14	0.050	0.057	-0.008	0.013	0.051	0.088	0.106
ρ_{11}^1	2.0	0.1	0.213	0.044	0.170	0.183	0.212	0.243	0.257
ρ_{11}^1	2.0	0.26	0.258	0.040	0.216	0.230	0.260	0.286	0.297
ρ_{11}^1	2.0	0.38	0.167	0.041	0.126	0.141	0.167	0.196	0.207
ρ_{11}^1	2.0	0.46	0.100	0.045	0.056	0.070	0.099	0.128	0.143
ρ_{11}^1	2.0	0.54	0.143	0.047	0.095	0.110	0.144	0.175	0.190
ρ_{11}^1	2.0	0.61	0.124	0.044	0.080	0.092	0.123	0.154	0.168
ρ_{11}^1	2.0	0.68	0.066	0.042	0.024	0.036	0.065	0.095	0.108
ρ_{11}^1	2.0	0.86	-0.013	0.045	-0.058	-0.042	-0.012	0.017	0.030
ρ_{00}^1	1.6	-0.34	-0.072	0.084	-0.158	-0.132	-0.073	-0.015	0.014
ρ_{00}^1	1.6	0.66	0.058	0.074	-0.019	0.008	0.062	0.110	0.133
ρ_{00}^1	1.8	-0.64	-0.426	0.095	-0.518	-0.492	-0.431	-0.366	-0.331
ρ_{00}^1	1.8	-0.1	-0.218	0.093	-0.311	-0.280	-0.219	-0.155	-0.125
ρ_{00}^1	1.8	0.19	-0.077	0.078	-0.157	-0.132	-0.078	-0.020	0.003
ρ_{00}^1	1.8	0.39	-0.144	0.049	-0.191	-0.177	-0.148	-0.113	-0.097

Obs	E_γ GeV	$\cos \theta_\phi$	Mean	σ	16th quantile	25th quantile	Median	75th quantile	84th quantile
ρ_{00}^1	1.8	0.54	-0.108	0.047	-0.154	-0.141	-0.107	-0.076	-0.061
ρ_{00}^1	1.8	0.81	-0.123	0.046	-0.168	-0.156	-0.126	-0.095	-0.079
ρ_{00}^1	2.0	-0.64	-0.424	0.135	-0.556	-0.517	-0.429	-0.340	-0.293
ρ_{00}^1	2.0	-0.14	-0.318	0.088	-0.404	-0.378	-0.321	-0.262	-0.235
ρ_{00}^1	2.0	0.1	-0.316	0.076	-0.392	-0.368	-0.318	-0.267	-0.240
ρ_{00}^1	2.0	0.26	-0.243	0.058	-0.304	-0.284	-0.244	-0.205	-0.189
ρ_{00}^1	2.0	0.38	-0.220	0.058	-0.284	-0.264	-0.216	-0.179	-0.161
ρ_{00}^1	2.0	0.46	-0.095	0.052	-0.144	-0.130	-0.097	-0.062	-0.046
ρ_{00}^1	2.0	0.54	-0.163	0.071	-0.236	-0.212	-0.162	-0.114	-0.091
ρ_{00}^1	2.0	0.61	-0.117	0.056	-0.173	-0.157	-0.117	-0.078	-0.059
ρ_{00}^1	2.0	0.68	-0.133	0.051	-0.184	-0.168	-0.132	-0.095	-0.081
ρ_{00}^1	2.0	0.86	-0.105	0.072	-0.174	-0.154	-0.105	-0.059	-0.036
$\text{Re} \rho_{10}^1$	1.6	-0.34	-0.019	0.050	-0.070	-0.055	-0.019	0.015	0.031
$\text{Re} \rho_{10}^1$	1.6	0.66	-0.020	0.041	-0.061	-0.050	-0.022	0.006	0.022
$\text{Re} \rho_{10}^1$	1.8	-0.64	0.058	0.053	0.005	0.020	0.057	0.095	0.111
$\text{Re} \rho_{10}^1$	1.8	-0.1	-0.118	0.042	-0.159	-0.146	-0.119	-0.092	-0.077
$\text{Re} \rho_{10}^1$	1.8	0.19	-0.062	0.033	-0.094	-0.085	-0.064	-0.039	-0.027
$\text{Re} \rho_{10}^1$	1.8	0.39	-0.073	0.036	-0.109	-0.097	-0.073	-0.049	-0.037
$\text{Re} \rho_{10}^1$	1.8	0.54	-0.069	0.032	-0.101	-0.091	-0.070	-0.048	-0.035
$\text{Re} \rho_{10}^1$	1.8	0.81	-0.116	0.031	-0.148	-0.137	-0.115	-0.095	-0.084
$\text{Re} \rho_{10}^1$	2.0	-0.64	0.183	0.060	0.124	0.143	0.184	0.224	0.242
$\text{Re} \rho_{10}^1$	2.0	-0.14	0.047	0.056	-0.006	0.011	0.045	0.086	0.105
$\text{Re} \rho_{10}^1$	2.0	0.1	-0.125	0.039	-0.164	-0.153	-0.125	-0.097	-0.085
$\text{Re} \rho_{10}^1$	2.0	0.26	-0.175	0.021	-0.196	-0.189	-0.174	-0.161	-0.155
$\text{Re} \rho_{10}^1$	2.0	0.38	0.000	0.036	-0.036	-0.024	0.001	0.025	0.037
$\text{Re} \rho_{10}^1$	2.0	0.46	-0.060	0.038	-0.098	-0.085	-0.061	-0.033	-0.021
$\text{Re} \rho_{10}^1$	2.0	0.54	-0.046	0.037	-0.080	-0.070	-0.046	-0.020	-0.009
$\text{Re} \rho_{10}^1$	2.0	0.61	-0.106	0.038	-0.144	-0.133	-0.108	-0.081	-0.069
$\text{Re} \rho_{10}^1$	2.0	0.68	-0.081	0.032	-0.113	-0.102	-0.080	-0.060	-0.049
$\text{Re} \rho_{10}^1$	2.0	0.86	-0.107	0.036	-0.144	-0.132	-0.108	-0.081	-0.071
ρ_{1-1}^1	1.6	-0.34	-0.143	0.069	-0.212	-0.194	-0.144	-0.096	-0.074
ρ_{1-1}^1	1.6	0.66	-0.077	0.061	-0.138	-0.119	-0.075	-0.036	-0.017
ρ_{1-1}^1	1.8	-0.64	0.013	0.057	-0.047	-0.027	0.010	0.047	0.069

Obs	E_γ GeV	$\cos \theta_\phi$	Mean	σ	16th quantile	25th quantile	Median	75th quantile	84th quantile
ρ_{1-1}^1	1.8	-0.1	0.037	0.064	-0.026	-0.004	0.037	0.077	0.098
ρ_{1-1}^1	1.8	0.19	0.077	0.062	0.016	0.035	0.078	0.120	0.138
ρ_{1-1}^1	1.8	0.39	0.149	0.054	0.094	0.112	0.150	0.188	0.205
ρ_{1-1}^1	1.8	0.54	0.108	0.054	0.054	0.072	0.107	0.145	0.161
ρ_{1-1}^1	1.8	0.81	0.217	0.054	0.166	0.184	0.219	0.253	0.271
ρ_{1-1}^1	2.0	-0.64	0.084	0.056	0.026	0.045	0.084	0.120	0.140
ρ_{1-1}^1	2.0	-0.14	0.109	0.067	0.041	0.063	0.107	0.156	0.176
ρ_{1-1}^1	2.0	0.1	0.270	0.057	0.213	0.230	0.269	0.311	0.328
ρ_{1-1}^1	2.0	0.26	0.201	0.047	0.154	0.168	0.199	0.233	0.248
ρ_{1-1}^1	2.0	0.38	0.254	0.061	0.193	0.212	0.256	0.298	0.315
ρ_{1-1}^1	2.0	0.46	0.114	0.058	0.053	0.074	0.117	0.155	0.172
ρ_{1-1}^1	2.0	0.54	0.205	0.056	0.150	0.169	0.207	0.243	0.260
ρ_{1-1}^1	2.0	0.61	0.145	0.059	0.084	0.105	0.145	0.183	0.203
ρ_{1-1}^1	2.0	0.68	0.327	0.050	0.277	0.294	0.327	0.360	0.377
ρ_{1-1}^1	2.0	0.86	0.295	0.050	0.245	0.261	0.295	0.330	0.344
$\text{Im} \rho_{10}^2$	1.6	-0.34	0.089	0.056	0.034	0.048	0.084	0.126	0.148
$\text{Im} \rho_{10}^2$	1.6	0.66	0.033	0.043	-0.009	0.005	0.033	0.062	0.077
$\text{Im} \rho_{10}^2$	1.8	-0.64	0.147	0.050	0.097	0.113	0.150	0.183	0.197
$\text{Im} \rho_{10}^2$	1.8	-0.1	-0.058	0.056	-0.115	-0.096	-0.058	-0.020	-0.003
$\text{Im} \rho_{10}^2$	1.8	0.19	0.134	0.054	0.080	0.098	0.135	0.169	0.186
$\text{Im} \rho_{10}^2$	1.8	0.39	0.047	0.043	0.002	0.017	0.047	0.076	0.092
$\text{Im} \rho_{10}^2$	1.8	0.54	0.185	0.037	0.146	0.159	0.186	0.211	0.222
$\text{Im} \rho_{10}^2$	1.8	0.81	0.071	0.043	0.030	0.043	0.073	0.101	0.116
$\text{Im} \rho_{10}^2$	2.0	-0.64	-0.007	0.066	-0.074	-0.050	-0.006	0.035	0.055
$\text{Im} \rho_{10}^2$	2.0	-0.14	0.203	0.053	0.151	0.166	0.204	0.241	0.257
$\text{Im} \rho_{10}^2$	2.0	0.1	0.196	0.043	0.155	0.168	0.197	0.226	0.240
$\text{Im} \rho_{10}^2$	2.0	0.26	0.116	0.046	0.072	0.084	0.117	0.148	0.162
$\text{Im} \rho_{10}^2$	2.0	0.38	0.128	0.043	0.084	0.101	0.130	0.158	0.171
$\text{Im} \rho_{10}^2$	2.0	0.46	0.157	0.031	0.124	0.136	0.158	0.179	0.189
$\text{Im} \rho_{10}^2$	2.0	0.54	0.159	0.038	0.121	0.133	0.157	0.186	0.199
$\text{Im} \rho_{10}^2$	2.0	0.61	0.135	0.036	0.099	0.110	0.136	0.161	0.172
$\text{Im} \rho_{10}^2$	2.0	0.68	0.037	0.039	-0.001	0.009	0.036	0.061	0.074
$\text{Im} \rho_{10}^2$	2.0	0.86	0.015	0.045	-0.031	-0.018	0.015	0.047	0.062
$\text{Im} \rho_{1-1}^2$	1.6	-0.34	-0.110	0.078	-0.187	-0.162	-0.112	-0.057	-0.030

Obs	E_γ GeV	$\cos \theta_\phi$	Mean	σ	16th quantile	25th quantile	Median	75th quantile	84th quantile
$\text{Im} \rho_{1-1}^2$	1.6	0.66	0.010	0.069	-0.061	-0.037	0.011	0.056	0.081
$\text{Im} \rho_{1-1}^2$	1.8	-0.64	0.003	0.065	-0.060	-0.041	0.001	0.049	0.069
$\text{Im} \rho_{1-1}^2$	1.8	-0.1	-0.067	0.065	-0.131	-0.110	-0.065	-0.019	-0.001
$\text{Im} \rho_{1-1}^2$	1.8	0.19	-0.077	0.059	-0.134	-0.117	-0.079	-0.038	-0.018
$\text{Im} \rho_{1-1}^2$	1.8	0.39	-0.188	0.059	-0.247	-0.229	-0.186	-0.146	-0.128
$\text{Im} \rho_{1-1}^2$	1.8	0.54	-0.175	0.053	-0.226	-0.212	-0.177	-0.139	-0.123
$\text{Im} \rho_{1-1}^2$	1.8	0.81	-0.147	0.064	-0.212	-0.192	-0.147	-0.105	-0.086
$\text{Im} \rho_{1-1}^2$	2.0	-0.64	-0.073	0.070	-0.143	-0.124	-0.080	-0.029	-0.005
$\text{Im} \rho_{1-1}^2$	2.0	-0.14	-0.065	0.071	-0.139	-0.116	-0.065	-0.018	0.007
$\text{Im} \rho_{1-1}^2$	2.0	0.1	-0.067	0.070	-0.135	-0.114	-0.068	-0.018	0.004
$\text{Im} \rho_{1-1}^2$	2.0	0.26	-0.130	0.058	-0.189	-0.170	-0.130	-0.090	-0.072
$\text{Im} \rho_{1-1}^2$	2.0	0.38	-0.128	0.055	-0.183	-0.167	-0.131	-0.091	-0.074
$\text{Im} \rho_{1-1}^2$	2.0	0.46	-0.145	0.061	-0.208	-0.187	-0.147	-0.105	-0.086
$\text{Im} \rho_{1-1}^2$	2.0	0.54	-0.092	0.051	-0.141	-0.123	-0.090	-0.058	-0.043
$\text{Im} \rho_{1-1}^2$	2.0	0.61	-0.193	0.055	-0.247	-0.230	-0.194	-0.157	-0.140
$\text{Im} \rho_{1-1}^2$	2.0	0.68	-0.160	0.060	-0.219	-0.199	-0.159	-0.121	-0.103
$\text{Im} \rho_{1-1}^2$	2.0	0.86	-0.140	0.064	-0.202	-0.183	-0.143	-0.099	-0.078

Table D.2: Values characterising the probability density function for each observable and bin for the ϕ -meson spin density matrix elements in the Gottfried-Jackson system.

D.3 Tabulated Results for ϕ -meson Spin Density Matrix Elements in the Adair system

Obs	E_γ GeV	$\cos \theta_\phi$	Mean	σ	16th quantile	25th quantile	Median	75th quantile	84th quantile
ρ_{00}^0	1.6	-0.34	0.178	0.042	0.135	0.149	0.177	0.208	0.222
ρ_{00}^0	1.6	0.66	0.096	0.041	0.056	0.068	0.092	0.121	0.135
ρ_{00}^0	1.8	-0.64	0.595	0.043	0.553	0.566	0.595	0.625	0.638
ρ_{00}^0	1.8	-0.1	0.328	0.041	0.286	0.300	0.327	0.353	0.369
ρ_{00}^0	1.8	0.19	0.136	0.034	0.102	0.112	0.136	0.160	0.171
ρ_{00}^0	1.8	0.39	0.104	0.029	0.074	0.083	0.102	0.123	0.133
ρ_{00}^0	1.8	0.54	0.076	0.021	0.051	0.056	0.080	0.092	0.097
ρ_{00}^0	1.8	0.81	0.084	0.023	0.061	0.069	0.084	0.099	0.106

Obs	E_γ GeV	$\cos \theta_\phi$	Mean	σ	16th quantile	25th quantile	Median	75th quantile	84th quantile
ρ_{00}^0	2.0	-0.64	0.638	0.047	0.592	0.607	0.640	0.669	0.684
ρ_{00}^0	2.0	-0.14	0.334	0.040	0.296	0.308	0.333	0.361	0.374
ρ_{00}^0	2.0	0.1	0.143	0.038	0.106	0.116	0.141	0.167	0.181
ρ_{00}^0	2.0	0.26	0.142	0.033	0.110	0.118	0.137	0.161	0.176
ρ_{00}^0	2.0	0.38	0.180	0.026	0.153	0.161	0.176	0.201	0.212
ρ_{00}^0	2.0	0.46	0.095	0.030	0.065	0.073	0.093	0.114	0.125
ρ_{00}^0	2.0	0.54	0.200	0.034	0.166	0.176	0.200	0.223	0.235
ρ_{00}^0	2.0	0.61	0.107	0.023	0.086	0.092	0.104	0.123	0.133
ρ_{00}^0	2.0	0.68	0.064	0.018	0.043	0.047	0.067	0.078	0.082
ρ_{00}^0	2.0	0.86	0.125	0.026	0.099	0.106	0.125	0.144	0.152
$\text{Re } \rho_{10}^0$	1.6	-0.34	-0.025	0.025	-0.051	-0.043	-0.026	-0.008	0.001
$\text{Re } \rho_{10}^0$	1.6	0.66	0.007	0.023	-0.017	-0.009	0.008	0.023	0.030
$\text{Re } \rho_{10}^0$	1.8	-0.64	-0.052	0.021	-0.073	-0.066	-0.053	-0.036	-0.030
$\text{Re } \rho_{10}^0$	1.8	-0.1	0.097	0.024	0.074	0.083	0.098	0.114	0.120
$\text{Re } \rho_{10}^0$	1.8	0.19	0.060	0.021	0.039	0.045	0.060	0.074	0.081
$\text{Re } \rho_{10}^0$	1.8	0.39	0.001	0.021	-0.020	-0.013	0.002	0.016	0.022
$\text{Re } \rho_{10}^0$	1.8	0.54	0.031	0.019	0.010	0.017	0.031	0.044	0.050
$\text{Re } \rho_{10}^0$	1.8	0.81	0.005	0.021	-0.016	-0.009	0.006	0.020	0.027
$\text{Re } \rho_{10}^0$	2.0	-0.64	-0.026	0.028	-0.053	-0.044	-0.025	-0.006	0.002
$\text{Re } \rho_{10}^0$	2.0	-0.14	0.033	0.023	0.011	0.018	0.032	0.048	0.056
$\text{Re } \rho_{10}^0$	2.0	0.1	0.071	0.021	0.050	0.057	0.072	0.086	0.091
$\text{Re } \rho_{10}^0$	2.0	0.26	0.023	0.020	0.004	0.010	0.023	0.037	0.043
$\text{Re } \rho_{10}^0$	2.0	0.38	0.013	0.020	-0.007	0.001	0.015	0.026	0.031
$\text{Re } \rho_{10}^0$	2.0	0.46	0.006	0.017	-0.011	-0.007	0.006	0.018	0.024
$\text{Re } \rho_{10}^0$	2.0	0.54	0.016	0.020	-0.004	0.003	0.017	0.030	0.036
$\text{Re } \rho_{10}^0$	2.0	0.61	-0.016	0.017	-0.034	-0.028	-0.016	-0.005	0.001
$\text{Re } \rho_{10}^0$	2.0	0.68	0.028	0.017	0.012	0.017	0.028	0.039	0.046
$\text{Re } \rho_{10}^0$	2.0	0.86	0.044	0.018	0.026	0.032	0.045	0.056	0.061
ρ_{1-1}^0	1.6	-0.34	0.049	0.032	0.019	0.028	0.050	0.071	0.080
ρ_{1-1}^0	1.6	0.66	0.044	0.030	0.012	0.022	0.044	0.065	0.076
ρ_{1-1}^0	1.8	-0.64	0.031	0.027	0.003	0.012	0.031	0.051	0.059
ρ_{1-1}^0	1.8	-0.1	0.055	0.037	0.017	0.031	0.054	0.079	0.093
ρ_{1-1}^0	1.8	0.19	0.047	0.035	0.013	0.024	0.047	0.071	0.080
ρ_{1-1}^0	1.8	0.39	-0.008	0.030	-0.039	-0.029	-0.008	0.012	0.022

Obs	E_γ GeV	$\cos \theta_\phi$	Mean	σ	16th quantile	25th quantile	Median	75th quantile	84th quantile
ρ_{1-1}^0	1.8	0.54	0.036	0.028	0.010	0.018	0.035	0.056	0.065
ρ_{1-1}^0	1.8	0.81	0.001	0.030	-0.030	-0.020	0.000	0.020	0.031
ρ_{1-1}^0	2.0	-0.64	-0.048	0.030	-0.079	-0.069	-0.048	-0.027	-0.019
ρ_{1-1}^0	2.0	-0.14	-0.036	0.031	-0.066	-0.056	-0.036	-0.016	-0.005
ρ_{1-1}^0	2.0	0.1	0.009	0.030	-0.022	-0.012	0.009	0.029	0.039
ρ_{1-1}^0	2.0	0.26	0.027	0.032	-0.005	0.005	0.026	0.050	0.060
ρ_{1-1}^0	2.0	0.38	0.005	0.030	-0.025	-0.015	0.005	0.025	0.035
ρ_{1-1}^0	2.0	0.46	-0.019	0.030	-0.049	-0.039	-0.018	0.002	0.011
ρ_{1-1}^0	2.0	0.54	-0.003	0.030	-0.031	-0.022	-0.002	0.018	0.026
ρ_{1-1}^0	2.0	0.61	-0.021	0.027	-0.048	-0.040	-0.022	-0.003	0.006
ρ_{1-1}^0	2.0	0.68	-0.037	0.029	-0.065	-0.056	-0.038	-0.018	-0.008
ρ_{1-1}^0	2.0	0.86	-0.009	0.032	-0.041	-0.030	-0.010	0.013	0.022
ρ_{11}^1	1.6	-0.34	-0.032	0.052	-0.086	-0.069	-0.032	0.003	0.018
ρ_{11}^1	1.6	0.66	0.062	0.046	0.019	0.032	0.062	0.092	0.105
ρ_{11}^1	1.8	-0.64	0.072	0.043	0.028	0.043	0.074	0.102	0.115
ρ_{11}^1	1.8	-0.1	0.025	0.051	-0.027	-0.010	0.024	0.060	0.077
ρ_{11}^1	1.8	0.19	0.055	0.050	0.006	0.021	0.055	0.087	0.104
ρ_{11}^1	1.8	0.39	0.052	0.044	0.008	0.022	0.052	0.083	0.096
ρ_{11}^1	1.8	0.54	0.036	0.046	-0.011	0.003	0.035	0.068	0.084
ρ_{11}^1	1.8	0.81	0.011	0.047	-0.036	-0.021	0.011	0.043	0.059
ρ_{11}^1	2.0	-0.64	0.100	0.045	0.054	0.069	0.102	0.131	0.146
ρ_{11}^1	2.0	-0.14	0.046	0.060	-0.016	0.004	0.048	0.086	0.107
ρ_{11}^1	2.0	0.1	0.098	0.052	0.047	0.064	0.100	0.133	0.150
ρ_{11}^1	2.0	0.26	0.103	0.048	0.056	0.072	0.105	0.138	0.152
ρ_{11}^1	2.0	0.38	0.152	0.049	0.104	0.123	0.155	0.186	0.201
ρ_{11}^1	2.0	0.46	0.043	0.050	-0.007	0.011	0.044	0.075	0.090
ρ_{11}^1	2.0	0.54	0.093	0.045	0.047	0.062	0.095	0.123	0.137
ρ_{11}^1	2.0	0.61	0.056	0.048	0.008	0.021	0.056	0.089	0.106
ρ_{11}^1	2.0	0.68	0.027	0.043	-0.014	-0.001	0.029	0.057	0.070
ρ_{11}^1	2.0	0.86	-0.032	0.048	-0.078	-0.066	-0.034	-0.002	0.017
ρ_{00}^1	1.6	-0.34	-0.024	0.080	-0.106	-0.083	-0.026	0.028	0.054
ρ_{00}^1	1.6	0.66	0.048	0.057	-0.008	0.010	0.049	0.084	0.102
ρ_{00}^1	1.8	-0.64	-0.379	0.108	-0.490	-0.456	-0.380	-0.307	-0.268

Obs	E_γ GeV	$\cos \theta_\phi$	Mean	σ	16th quantile	25th quantile	Median	75th quantile	84th quantile
ρ_{00}^1	1.8	-0.1	-0.058	0.079	-0.139	-0.114	-0.056	-0.003	0.023
ρ_{00}^1	1.8	0.19	0.011	0.060	-0.048	-0.030	0.011	0.052	0.072
ρ_{00}^1	1.8	0.39	-0.047	0.049	-0.094	-0.079	-0.047	-0.013	0.001
ρ_{00}^1	1.8	0.54	-0.018	0.043	-0.062	-0.048	-0.019	0.011	0.028
ρ_{00}^1	1.8	0.81	-0.023	0.042	-0.064	-0.051	-0.024	0.005	0.020
ρ_{00}^1	2.0	-0.64	-0.556	0.129	-0.682	-0.646	-0.556	-0.466	-0.429
ρ_{00}^1	2.0	-0.14	-0.316	0.082	-0.398	-0.373	-0.319	-0.263	-0.231
ρ_{00}^1	2.0	0.1	-0.085	0.073	-0.159	-0.138	-0.087	-0.033	-0.010
ρ_{00}^1	2.0	0.26	0.049	0.060	-0.006	0.007	0.044	0.087	0.105
ρ_{00}^1	2.0	0.38	-0.190	0.063	-0.248	-0.231	-0.195	-0.156	-0.134
ρ_{00}^1	2.0	0.46	0.011	0.059	-0.047	-0.029	0.014	0.053	0.069
ρ_{00}^1	2.0	0.54	-0.076	0.072	-0.149	-0.126	-0.075	-0.025	-0.004
ρ_{00}^1	2.0	0.61	0.021	0.058	-0.040	-0.017	0.025	0.062	0.078
ρ_{00}^1	2.0	0.68	-0.058	0.030	-0.089	-0.080	-0.056	-0.039	-0.029
ρ_{00}^1	2.0	0.86	-0.030	0.057	-0.087	-0.067	-0.029	0.009	0.027
$\text{Re } \rho_{10}^1$	1.6	-0.34	-0.048	0.047	-0.095	-0.080	-0.047	-0.018	0.001
$\text{Re } \rho_{10}^1$	1.6	0.66	-0.042	0.040	-0.083	-0.070	-0.041	-0.014	-0.001
$\text{Re } \rho_{10}^1$	1.8	-0.64	-0.066	0.045	-0.113	-0.098	-0.066	-0.033	-0.021
$\text{Re } \rho_{10}^1$	1.8	-0.1	-0.141	0.042	-0.183	-0.170	-0.143	-0.112	-0.098
$\text{Re } \rho_{10}^1$	1.8	0.19	-0.051	0.038	-0.091	-0.079	-0.052	-0.024	-0.013
$\text{Re } \rho_{10}^1$	1.8	0.39	-0.068	0.037	-0.105	-0.094	-0.069	-0.041	-0.030
$\text{Re } \rho_{10}^1$	1.8	0.54	-0.053	0.034	-0.086	-0.073	-0.052	-0.028	-0.018
$\text{Re } \rho_{10}^1$	1.8	0.81	-0.083	0.035	-0.120	-0.108	-0.083	-0.060	-0.048
$\text{Re } \rho_{10}^1$	2.0	-0.64	0.033	0.059	-0.025	-0.005	0.033	0.071	0.090
$\text{Re } \rho_{10}^1$	2.0	-0.14	-0.062	0.051	-0.112	-0.097	-0.063	-0.027	-0.009
$\text{Re } \rho_{10}^1$	2.0	0.1	-0.135	0.032	-0.169	-0.158	-0.137	-0.113	-0.103
$\text{Re } \rho_{10}^1$	2.0	0.26	-0.169	0.028	-0.196	-0.188	-0.171	-0.153	-0.143
$\text{Re } \rho_{10}^1$	2.0	0.38	-0.031	0.037	-0.068	-0.057	-0.032	-0.006	0.005
$\text{Re } \rho_{10}^1$	2.0	0.46	-0.046	0.036	-0.083	-0.070	-0.046	-0.021	-0.011
$\text{Re } \rho_{10}^1$	2.0	0.54	-0.054	0.039	-0.092	-0.081	-0.054	-0.028	-0.014
$\text{Re } \rho_{10}^1$	2.0	0.61	-0.080	0.037	-0.117	-0.107	-0.082	-0.055	-0.042
$\text{Re } \rho_{10}^1$	2.0	0.68	-0.014	0.032	-0.046	-0.035	-0.013	0.007	0.017
$\text{Re } \rho_{10}^1$	2.0	0.86	-0.045	0.033	-0.079	-0.069	-0.046	-0.021	-0.010
ρ_{1-1}^1	1.6	-0.34	-0.121	0.070	-0.193	-0.168	-0.119	-0.070	-0.050

Obs	E_γ GeV	$\cos \theta_\phi$	Mean	σ	16th quantile	25th quantile	Median	75th quantile	84th quantile
ρ_{1-1}^1	1.6	0.66	-0.072	0.062	-0.131	-0.111	-0.071	-0.029	-0.010
ρ_{1-1}^1	1.8	-0.64	0.037	0.052	-0.016	0.001	0.037	0.075	0.090
ρ_{1-1}^1	1.8	-0.1	0.126	0.068	0.055	0.078	0.126	0.176	0.198
ρ_{1-1}^1	1.8	0.19	0.115	0.065	0.053	0.070	0.115	0.159	0.181
ρ_{1-1}^1	1.8	0.39	0.208	0.061	0.148	0.169	0.208	0.250	0.269
ρ_{1-1}^1	1.8	0.54	0.155	0.059	0.095	0.115	0.157	0.197	0.215
ρ_{1-1}^1	1.8	0.81	0.254	0.056	0.200	0.217	0.254	0.293	0.310
ρ_{1-1}^1	2.0	-0.64	0.016	0.057	-0.041	-0.022	0.019	0.055	0.072
ρ_{1-1}^1	2.0	-0.14	0.134	0.071	0.063	0.089	0.135	0.184	0.204
ρ_{1-1}^1	2.0	0.1	0.387	0.059	0.329	0.347	0.387	0.426	0.443
ρ_{1-1}^1	2.0	0.26	0.309	0.060	0.250	0.271	0.311	0.351	0.369
ρ_{1-1}^1	2.0	0.38	0.300	0.057	0.242	0.260	0.302	0.342	0.360
ρ_{1-1}^1	2.0	0.46	0.173	0.056	0.114	0.134	0.174	0.212	0.230
ρ_{1-1}^1	2.0	0.54	0.212	0.062	0.153	0.172	0.213	0.253	0.271
ρ_{1-1}^1	2.0	0.61	0.220	0.056	0.164	0.182	0.219	0.259	0.278
ρ_{1-1}^1	2.0	0.68	0.363	0.056	0.307	0.326	0.364	0.401	0.419
ρ_{1-1}^1	2.0	0.86	0.317	0.058	0.259	0.278	0.317	0.358	0.376
$\text{Im} \rho_{10}^2$	1.6	-0.34	0.067	0.053	0.014	0.033	0.070	0.105	0.120
$\text{Im} \rho_{10}^2$	1.6	0.66	0.037	0.043	-0.005	0.008	0.037	0.066	0.080
$\text{Im} \rho_{10}^2$	1.8	-0.64	0.134	0.045	0.090	0.104	0.134	0.166	0.181
$\text{Im} \rho_{10}^2$	1.8	-0.1	-0.061	0.056	-0.116	-0.099	-0.063	-0.025	-0.004
$\text{Im} \rho_{10}^2$	1.8	0.19	0.081	0.047	0.034	0.050	0.081	0.113	0.126
$\text{Im} \rho_{10}^2$	1.8	0.39	-0.026	0.043	-0.070	-0.056	-0.026	0.003	0.015
$\text{Im} \rho_{10}^2$	1.8	0.54	0.114	0.038	0.076	0.089	0.114	0.141	0.151
$\text{Im} \rho_{10}^2$	1.8	0.81	0.020	0.043	-0.021	-0.008	0.020	0.050	0.062
$\text{Im} \rho_{10}^2$	2.0	-0.64	-0.050	0.061	-0.108	-0.092	-0.051	-0.011	0.009
$\text{Im} \rho_{10}^2$	2.0	-0.14	0.147	0.053	0.093	0.111	0.149	0.184	0.200
$\text{Im} \rho_{10}^2$	2.0	0.1	0.149	0.042	0.105	0.122	0.152	0.180	0.191
$\text{Im} \rho_{10}^2$	2.0	0.26	0.057	0.047	0.006	0.022	0.056	0.090	0.104
$\text{Im} \rho_{10}^2$	2.0	0.38	0.057	0.039	0.018	0.029	0.057	0.086	0.098
$\text{Im} \rho_{10}^2$	2.0	0.46	0.077	0.034	0.044	0.055	0.079	0.102	0.112
$\text{Im} \rho_{10}^2$	2.0	0.54	0.120	0.041	0.082	0.094	0.120	0.147	0.160
$\text{Im} \rho_{10}^2$	2.0	0.61	0.059	0.036	0.023	0.034	0.059	0.086	0.097
$\text{Im} \rho_{10}^2$	2.0	0.68	0.001	0.034	-0.034	-0.022	0.002	0.026	0.036

Obs	E_γ GeV	$\cos \theta_\phi$	Mean	σ	16th quantile	25th quantile	Median	75th quantile	84th quantile
$\text{Im} \rho_{10}^2$	2.0	0.86	-0.029	0.042	-0.070	-0.055	-0.029	-0.001	0.012
$\text{Im} \rho_{1-1}^2$	1.6	-0.34	-0.133	0.077	-0.206	-0.185	-0.140	-0.082	-0.056
$\text{Im} \rho_{1-1}^2$	1.6	0.66	0.024	0.073	-0.048	-0.023	0.023	0.070	0.095
$\text{Im} \rho_{1-1}^2$	1.8	-0.64	-0.076	0.059	-0.129	-0.114	-0.080	-0.039	-0.018
$\text{Im} \rho_{1-1}^2$	1.8	-0.1	-0.033	0.060	-0.091	-0.073	-0.033	0.007	0.025
$\text{Im} \rho_{1-1}^2$	1.8	0.19	-0.154	0.077	-0.230	-0.206	-0.156	-0.104	-0.077
$\text{Im} \rho_{1-1}^2$	1.8	0.39	-0.195	0.068	-0.262	-0.241	-0.194	-0.148	-0.126
$\text{Im} \rho_{1-1}^2$	1.8	0.54	-0.267	0.059	-0.328	-0.309	-0.267	-0.228	-0.208
$\text{Im} \rho_{1-1}^2$	1.8	0.81	-0.182	0.065	-0.245	-0.227	-0.182	-0.140	-0.118
$\text{Im} \rho_{1-1}^2$	2.0	-0.64	-0.060	0.069	-0.127	-0.106	-0.061	-0.014	0.009
$\text{Im} \rho_{1-1}^2$	2.0	-0.14	-0.201	0.068	-0.272	-0.251	-0.203	-0.148	-0.127
$\text{Im} \rho_{1-1}^2$	2.0	0.1	-0.212	0.068	-0.278	-0.257	-0.213	-0.164	-0.145
$\text{Im} \rho_{1-1}^2$	2.0	0.26	-0.196	0.061	-0.258	-0.239	-0.195	-0.152	-0.135
$\text{Im} \rho_{1-1}^2$	2.0	0.38	-0.208	0.058	-0.266	-0.248	-0.209	-0.169	-0.151
$\text{Im} \rho_{1-1}^2$	2.0	0.46	-0.265	0.059	-0.324	-0.306	-0.267	-0.226	-0.206
$\text{Im} \rho_{1-1}^2$	2.0	0.54	-0.192	0.053	-0.245	-0.228	-0.192	-0.159	-0.139
$\text{Im} \rho_{1-1}^2$	2.0	0.61	-0.248	0.056	-0.303	-0.285	-0.251	-0.211	-0.192
$\text{Im} \rho_{1-1}^2$	2.0	0.68	-0.181	0.054	-0.234	-0.217	-0.182	-0.144	-0.126
$\text{Im} \rho_{1-1}^2$	2.0	0.86	-0.138	0.067	-0.203	-0.180	-0.138	-0.094	-0.074

Table D.3: Values characterising the probability density function for each observable and bin for the ϕ -meson spin density matrix elements in the Adair system.

Bibliography

- [1] P.A. Zyla et al. (Particle Data Group). Review of Particle Physics. Progress of Theoretical and Experimental Physics, 2020 083C01, 2020.
- [2] C. D. Roberts. Hadron Physics and QCD: Just the Basic Facts. Journal of Physics: Conference Series, 630:012051, 2015.
- [3] Contributors to Wikimedia. Wikimedia Commons, 2021. https://commons.wikimedia.org/wiki/Category:Hadron_multiplets.
- [4] R. Koniuk and N. Isgur. Baryon decays in a quark model with chromodynamics. Phys. Rev. D, 21:1868–1886, 1980.
- [5] S. Capstick. Photo- and electroproduction of nonstrange baryon resonances in the relativized quark model. Phys. Rev. D, 46:2864–2881, 1992.
- [6] S. Capstick and W. Roberts. Strange decays of nonstrange baryons. Phys. Rev. D, 58:074011, 1998.
- [7] S. Capstick and W. Roberts. Quark models of baryon masses and decays. Prog. Part. Nucl. Phys., 45:S241–S331, 2000.
- [8] A. Thiel. Light Baryon Spectroscopy, 2021. <http://indico.nucleares.unam.mx/event/1541/session/4/contribution/249/material/slides/0.pdf>.
- [9] K. Schilling, P. Seyboth and G.E. Wolf. On the Analysis of Vector Meson Production by Polarized Photons. Nucl.Phys., B15:397–412, 1970.
- [10] K. Blum. Density Matrix Theory and Applications. Springer, 2012.
- [11] D. Drechsel, S. Kamalov and L. Tiator. Unitary isobar model - MAID2007. European Physical Journal A, 34, 2007.
- [12] Mart et al. KAON-MAID 2000. <https://maid.kph.uni-mainz.de/kaon/kaonmaid.html>.

- [13] A.V. Anisovich et al. Properties of baryon resonances from a multichannel partial wave analysis. The European Physical Journal A, 48(2):15, 2012.
- [14] D. Rönchen, M. Döring and U.-G. Meißner. The impact of $K^+\Lambda$ photoproduction on the resonance spectrum. The European Physical Journal A, 54, 2018.
- [15] A. Thiel, F. Afzal, and Y. Wunderlich. Light Baryon Spectroscopy. Progress in Particle and Nuclear Physics, page 103949, 2022.
- [16] J.J. Sakurai. Theory of strong interactions. Ann. Phys.(NY), 11:1, 1960.
- [17] T.H. Bauer et al. The hadronic properties of the photon in high-energy interactions. Reviews of Modern Physics, 50(2):261, 1978.
- [18] A.I. Titov, Y. Oh, and S.N. Yang. Polarization observables in ϕ -meson photoproduction and the strangeness content of the proton. Physical review letters, 79(9):1634, 1997.
- [19] E.M. Henley, G. Krein and A.G. Williams. Phi production as a measure of the strangeness content of the nucleon. Physics Letters B, 281(3):178–184, 1992.
- [20] A.I. Titov, T. Lee et al. Structure of the ϕ photoproduction amplitude at a few GeV. Physical Review C, 60(3):035205, 1999.
- [21] Y. Oh. Vector Meson Photoproduction Processes near Threshold. Journal of the Korean Physical Society, 43:S20–S26, 2003.
- [22] Q. Zhao, B. Saghai, and J.S. Al-Khalili. Non-diffractive mechanisms in the ϕ -meson photoproduction on nucleons. Physics Letters B, 509(3-4):231–238, 2001.
- [23] P. Cole. Experiment proposal - photoproduction of phi mesons with linearly polarized photons, 1998. https://www.jlab.org/exp_prog/proposals/98/PR98-109.pdf.
- [24] D. Griffiths. Introduction to Elementary Particles. Wiley, 2008.
- [25] F. Krauss. Quarkonium, 2021. https://www.ippp.dur.ac.uk/~krauss/Lectures/QuarksLeptons/QCD/Quarkonium_0.html.
- [26] F.J. Gilman et al. Helicity conservation in diffraction scattering. Physics Letters B, 31(6):387–390, 1970.
- [27] V. Mathieu et al. Vector meson photoproduction with a linearly polarized beam. Phys. Rev. D, 97:094003, 2018.
- [28] O. Bartalini et al. Measurement of π photoproduction on the proton from 550 to 1500 MeV at GRAAL. The European Physical Journal A, 26(3):399–419, 2005.

- [29] K.-H. Kaiser et al. The 1.5GeV harmonic double-sided microtron at Mainz University. Nuclear Instruments and Methods in Physics Research Section A: Accelerators, Spectrometers, Detectors and Associated Equipment, 593(3):159–170, 2008.
- [30] S. Schadmand. Nucleon resonances and meson production with TAPS at MAMI. Acta Physica Polonica B, 31(10-11):2431–2435, 2000.
- [31] B. Mecking et al. The CEBAF large acceptance spectrometer (CLAS). Nuclear Instruments and Methods in Physics Research Section A: Accelerators, Spectrometers, Detectors and Associated Equipment, 503(3):513–553, 2003.
- [32] J. K. Ahn et al. The first operation of laser electron photon facility in SPring-8. In 12th Symposium on Accelerator Science and Technology (SAST'99), pages 141–143, 1999.
- [33] George Washington University. SAID database. <https://gwdac.phys.gwu.edu/>.
- [34] D.G. Ireland, E. Pasyuk and I. Strakovsky. Photoproduction reactions and non-strange baryon spectroscopy. Progress in Particle and Nuclear Physics, 111:103752, 2020.
- [35] A.J.G. Hey and R.L. Kelly. Baryon spectroscopy. Physics Reports, 96(2):71–204, 1983.
- [36] B. Krusche and S. Schadmand. Study of non-strange baryon resonances with meson photoproduction. Progress in Particle and Nuclear Physics, 51(2):399–485, 2003.
- [37] E. Klempt and J.-M. Richard. Baryon spectroscopy. Rev. Mod. Phys., 82:1095–1153, 2010.
- [38] V. Crede and W. Roberts. Progress towards understanding baryon resonances. Reports on Progress in Physics, 76(7):076301, 2013.
- [39] V.D. Burkert et al. The CLAS12 Spectrometer at Jefferson Laboratory. Nuclear Instruments and Methods in Physics Research Section A: Accelerators, Spectrometers, Detectors and Associated Equipment, 959:163419, 2020.
- [40] C.W. Leemann, D.R. Douglas and G.A. Krafft. CEBAF at the Jefferson Laboratory. Annual Review of Nuclear and Particle Science, 51:413–450, 2001.
- [41] F.J. Klein et al. The coherent-bremsstrahlung facility in Hall B at Jefferson Lab, 2005. https://userweb.jlab.org/~fklein/cbf_nim_v2.0.pdf.
- [42] U. Timm. Coherent Bremsstrahlung of Electrons in Crystals. Fortschritte der Physik, 17(12):765–808, 1969.

- [43] D. Lohmann et al. Linearly polarized photons at MAMI (Mainz). Nuclear Instruments and Methods in Physics Research Section A: Accelerators, Spectrometers, Detectors and Associated Equipment, 343(2):494 – 507, 1994.
- [44] K. Livingston. Running the linearly polarized photon beam. CLAS Note 2006-022, 2006.
- [45] D.I. Sober et al. The bremsstrahlung tagged photon beam in Hall B at JLab. Nuclear Instruments and Methods in Physics Research Section A: Accelerators, Spectrometers, Detectors and Associated Equipment, 440(2):263–284, 2000.
- [46] C. A. Paterson. Strangeness photoproduction polarization observables from g8. CLAS Note 2014-010, 2014.
- [47] Jefferson Lab, 2021. <https://www.jlab.org/>.
- [48] M.D. Mestayer et al. The CLAS drift chamber system. Nucl. Instrum. Meth. A, 449:81–111, 2000.
- [49] Y.G. Sharabian et al. A new highly segmented start counter for the clas detector. Nuclear Instruments and Methods in Physics Research Section A: Accelerators, Spectrometers, Detectors and Associated Equipment, 556(1):246–258, 2006.
- [50] A.J. Street et al. Final site assembly and testing of the superconducting toroidal magnet for the CEBAF Large Acceptance Spectrometer (CLAS). IEEE Trans. Magnetics, 32:2074–2076, 1996.
- [51] J. O’Meara et al. A superconducting toroidal magnet for the CEBAF large acceptance spectrometer. IEEE Trans. Magnetics, 25:2, 1989.
- [52] B. Dey. Differential Cross Section and Polarization Extractions for $\gamma p \rightarrow K^+ \Sigma^0$ and $\gamma p \rightarrow \phi p$ using CLAS at Jefferson Lab, Towards a Partial Wave Analysis in Search of Missing Baryon Resonances. PhD thesis, 2011.
- [53] E. Smith et al. The time-of-flight system for CLAS. Nuclear Instruments and Methods in Physics Research Section A: Accelerators, Spectrometers, Detectors and Associated Equipment, 432(2-3):265–298, 1999.
- [54] G. Adams et al. The CLAS Čerenkov detector. Nuclear Instruments and Methods in Physics Research Section A: Accelerators, Spectrometers, Detectors and Associated Equipment, 465(2–3):414–427, 2001.
- [55] M. Amarian et al. The CLAS forward electromagnetic calorimeter. Nuclear Instruments and Methods in Physics Research Section A: Accelerators, Spectrometers, Detectors and Associated Equipment, 460(2-3):239–265, 2001.

- [56] CLAS Collaboration. CLAS12 Technical Design Report, 2008. https://www.jlab.org/Hall-B/clas12_tdr.pdf.
- [57] D.S. Carman et al. The CLAS12 Forward Time-of-Flight system. Nuclear Instruments and Methods in Physics Research Section A: Accelerators, Spectrometers, Detectors and Associated Equipment, 960:163629, 2020.
- [58] D.S. Carman et al. The CLAS12 Central Time-of-Flight system. Nuclear Instruments and Methods in Physics Research Section A: Accelerators, Spectrometers, Detectors and Associated Equipment, 960:163626, 2020.
- [59] D.S. Carman. Forward Time-of-Flight Geometry for CLAS12, 2016. CLAS12-Note 2014-005 https://www.jlab.org/Hall-B/ftof/notes/ftof_geom.pdf.
- [60] V. Baturin and D.S. Carman. Central Time-of-Flight Geometry for CLAS12, 2017. CLAS12-Note 2016-001 https://www.jlab.org/Hall-B/ctof/notes/ctof_geom.pdf.
- [61] M. Pivk and F.R. Le Diberder. sPlots: A statistical tool to unfold data distributions. Nuclear Instruments and Methods in Physics Research, 555(1):356 – 369, 2005.
- [62] A. Rogozhnikov. sPlot: a technique to reconstruct components of a mixture, 2015. <http://arogozhnikov.github.io/2015/10/07/splot.html>.
- [63] M. Baak, CERN. Error calculation for weighted unbinned ML fits (in RooFit), 2009. https://twiki.cern.ch/twiki/pub/Main/RooFit/baak_eventweights.pdf.
- [64] T. Dong, D. An and N.H. Kim. Prognostics 102: Efficient Bayesian-Based Prognostics Algorithm in MATLAB. IntechOpen, 2019.
- [65] K. Livingston. ROOTBEER, 2005. <http://nuclear.gla.ac.uk/~kl/rootbeer/manual/html/>.
- [66] K. Livingston. Polarization from coherent bremsstrahlung enhancement. CLAS Note 2011-020, 2011.
- [67] M. Dugger and B. Ritchie. Consistency corrections to the linear photon polarization for g8b data. CLAS Note 2011-002, 2011.
- [68] M. Dugger et al. Extraction technique for Σ and G for pseudoscalar meson photoproduction. CLAS Note 2009-026, 2009.
- [69] E. Pasyuk. Energy loss corrections for charged particles in CLAS. CLAS Note 2007-016, 2007.

- [70] W. Verkerke and D. Kirkby. RooFit Users Manual, 2006. http://roofit.sourceforge.net/docs/RooFit_Users_Manual_2.07-29.pdf.
- [71] HASPECT Collaboration. EdGen event generator, 2017. <https://github.com/lorenzozana/EdGen>.
- [72] T. Vrancx et al. Incompleteness of complete pseudoscalar-meson photoproduction. Phys. Rev. C, 87:055205, 2013.
- [73] SciPy community. SciPy reference manual, 2022. https://docs.scipy.org/doc/scipy/reference/generated/scipy.stats.gaussian_kde.html#ra3a8695506c7-1.
- [74] C. S. Nepali et al. Transverse polarization of $\Sigma^+(1189)$ in photoproduction on a hydrogen target in CLAS. Phys. Rev. C, 87:045206, 2013.
- [75] V. Crede and F. Gonzalez. Private communication, November 2019.
- [76] R. Ewald et al. Measurement of polarisation observables in $K_S^0\Sigma^+$ photoproduction off the proton. Physics Letters B, 738:268 – 273, 2014.
- [77] R. Ewald. Untersuchung der $\Sigma^+K_S^0$ Photoproduktion am Proton mit dem CBELSA/TAPS-Experiment. PhD thesis, 2010.
- [78] B.Dey et al. Data analysis techniques, differential cross sections, and spin density matrix elements for the reaction $\gamma p \rightarrow \phi p$. Physical Review C, 89(5), 2014.
- [79] W. Chang et al. Measurement of spin-density matrix elements for ϕ -meson photoproduction from protons and deuterons near threshold. Physical Review C, 82(1), 2010.
- [80] K. Mizutani et al. ϕ photoproduction on the proton at $E_\gamma = 1.5 - 2.9$ GeV. Physical Review C, 96(6), 2017.
- [81] D. Rönchen. Private communication, December 2021.
- [82] D.S. Carman. Forward Time-of-Flight Reconstruction for CLAS12, 2017. https://www.jlab.org/Hall-B/ftof/notes/ftof_recon.pdf.
- [83] D.S. Carman. Central Time-of-Flight Reconstruction for CLAS12, 2017. https://www.jlab.org/Hall-B/ctof/notes/ctof_recon.pdf.
- [84] D.S. Carman et al. Description of the Calibration Algorithms for the CLAS12 Forward Time-Of-Flight System, 2018. https://www.jlab.org/Hall-B/ftof/notes/ftof_calib.pdf.

- [85] D.S. Carman et al. Description of the Calibration Algorithms for the CLAS12 Central Time-Of-Flight System, 2018. https://www.jlab.org/Hall-B/ctof/notes/ctof_calib.pdf.
- [86] D.S. Carman. CLAS12 FTOF Panel-1a and Panel-2 Refurbishment and Baseline Test Results, 2013. <https://www.jlab.org/Hall-B/ftof/ftof-1a-2-qa.pdf>.